



Université Catholique de Louvain
Faculté des Sciences Appliquées

Center for Systems Engineering and Applied Mechanics

Micromechanics of inclusion-reinforced
composites in elasto-plasticity and
elasto-viscoplasticity:
modeling and computation

Olivier Pierard

Jury:

Pr C. Bailly, Université Catholique de Louvain, Belgique
Pr I. Doghri, Université Catholique de Louvain, Belgique (Promoteur)
Pr M. Geers, Technische Universiteit Eindhoven, Pays-Bas
Pr J. LLorca, Universidad Politécnica de Madrid, Espagne
Pr T. Pardoën, Université Catholique de Louvain, Belgique
Pr J.-C. Samin, Université Catholique de Louvain, Belgique (Président)
Pr A. Zaoui, Ecole Polytechnique, France

*Thèse présentée en vue de l'obtention du grade
de docteur en sciences appliquées*

Septembre 2006

Acknowledgements

During these four years as a PhD student in Louvain-la-Neuve, I was helped by so many people without whom I wouldn't have been able to come to the end of this study.

First of all, I really would like to thank warmly my supervisor, Pr Issam Doghri. He shares with his team his motivation for research so that we always want to go further on. He always put me on the right path, offered me a high degree of freedom to lead my research and his confidence in me. His hints, openness for discussion and his knowledge of the subject were always an extraordinary source of motivation.

A key period was my three-month stay at the *Universidad Politécnica de Madrid* which undoubtedly enriched my background in micromechanics. Being under the supervision of Pr LLorca and his team was a great experience and an extraordinary opportunity to discover a new subject complementary to the one I was working on in Belgium.

In addition to my work at the office, I had the opportunity to participate to several conferences, graduate courses and workshops during which I met very interesting people. Among them are Pr Zaoui and Dr Renaud Masson who made the pioneering developments of a major subject of this thesis. My discussions with them convinced me that I was on the right way and had to go further.

In Louvain-la-Neuve, I was surrounded by very competent professors. Among them, I couldn't forget the two members of my supervisory committee: Pr Bailly and Pr Pardoën. To finish within the academic context, I would like to thank the other members of my jury: Pr Geers and Pr Samin for their participation to the committee and the precious time they dedicated to this dissertation.

I also would like to thank all the team of e-Xstream engineering, the spin-off company launched by my supervisor. Their numerous advises and a free access to their software improved my work on numerous points.

The so pleasant time I had during these four years is mainly due to all the people I met every day in CESAME, our research center. First of all, I really would like to thank my officemate, Christophe Friebl. He calmly answered

to all my questions, solved so many computer problems and we had plenty of interesting discussions. But, even more importantly, I really discovered a new friend. Even if I really enjoyed being in contact with all the people of the Euler building, I will never forget some of them: Laurent White who was the only one who could understand what traveling by bicycle meant, Olivier and Max with whom I shared most of my lunch times, Brieux for all the strange discussions we had and his help in teaching continuum mechanics, Amine for his friendliness and openness, Laurent Delannay whose door was always open for discussion and advises and finally Michèle for her helpfulness and permanent cheerfulness.

But I couldn't have spent all these years at the university without the support of my family and my parents in particular. They backed me up for so many years and tried to follow my progress even if it was a little bit hard for them to understand all the developments. . . Finally, I really would like to thank my fiancée, Caroline, who showed an extraordinary patience during all this time and who always motivated me to carry on with my work. I really do apologize for spending so many evenings in front of my computer instead of spending time with her.

Olivier.

Contents

1	Introduction	1
2	Scale transition methods	5
2.1	Scale separation	5
2.2	Linking macroscopic and microscopic scales	7
2.2.1	On averages	7
2.2.2	Imposition of the boundary conditions	8
2.2.3	Hill's Lemma	10
2.2.4	Prediction of the macroscopic response	11
2.3	Various approaches to solve the scale transition problem	11
2.3.1	Finite element methods	12
2.3.2	Asymptotic homogenization method	12
2.3.3	Generalized method of cells	13
2.3.4	Fast Fourier transform method	14
2.3.5	Mean-field homogenization schemes	15
2.3.6	Comparison of the various methods	15
3	Finite element simulations at the microscopic level	19
3.1	Two-dimensional unit cells	19
3.1.1	Composites reinforced by long fibers	19
3.1.2	Two-dimensional axisymmetric unit cells	20
3.1.3	Boundary conditions	21
3.2	Three-dimensional unit cells	24
3.2.1	Generation of the geometry	25
3.2.2	Mesh generation	26
3.2.3	Boundary conditions	28
3.2.4	Validation of the unit cell	28
3.3	Conclusions	32

4	Homogenization of linear composites	35
4.1	Constitutive equations	35
4.1.1	Linear thermo-elasticity	35
4.1.2	Linear viscoelasticity	36
4.2	Homogenization of isothermal elastic composites	38
4.2.1	Results of Eshelby and Hill	38
4.2.2	Expressions of localization tensors	40
4.2.3	Various homogenization schemes	41
4.2.4	Some bounds	45
4.3	Homogenization of thermo-elastic composites	46
4.3.1	Homogenization technique	46
4.3.2	Numerical simulations	49
4.4	Homogenization of viscoelastic composites	52
4.4.1	Homogenization technique	52
4.4.2	Numerical simulations	53
4.5	Conclusions	55
5	Homogenization of elasto-plastic composites	57
5.1	Constitutive equations	57
5.2	Homogenization of elasto-plastic composites	58
5.2.1	Secant formulation	59
5.2.2	Incremental formulation	60
5.2.3	Variational formulation	62
5.3	Computation of the macroscopic tangent operator	63
5.3.1	Stiffness reduction of the macroscopic tangent operator	63
5.3.2	Influence of the matrix modulus	64
5.3.3	Isotropic parts of an anisotropic modulus tensor	66
5.3.4	Transversely isotropic parts of an anisotropic modulus tensor	67
5.3.5	Comparison of various local tangent operators	70
5.3.6	Various estimates of the macroscopic tangent operator .	71
5.4	Numerical simulations	72
5.4.1	Effect of the macroscopic tangent operator's computation	72
5.4.2	Microscopic fields analysis	78
5.5	Conclusions	87
6	Homogenization of elasto-viscoplastic composites	93
6.1	Constitutive equations	93
6.2	Homogenization of elasto-viscoplastic composites	95
6.3	The affine formulation	96
6.3.1	From elasto-viscoplasticity to linear thermo-viscoelasticity	96
6.3.2	From linear thermo-viscoelasticity to linear thermo-elasticity	97
6.3.3	Algorithm	98

6.3.4	Prediction of the macroscopic response	101
6.3.5	Main differences with previous implementations	101
6.4	Numerical simulations	102
6.4.1	General simulations	102
6.4.2	Validation against 3D finite element simulations	106
6.5	Conclusions	117
7	Conclusions	119
A	Expressions of the Eshelby's tensor	123
A.1	Isotropic matrix	123
A.2	Transversely isotropic matrix	124
B	Laplace-Carson transform and its inversion	127
B.1	Laplace-Carson transform	127
B.2	Laplace-Carson inversion	127
C	Incremental evaluation of a convolution product	133
D	Computation details of the affine formulation	137
D.1	Solution of the internal variables' constitutive equation	137
D.2	Linear viscoelastic expressions	138
D.3	Linear thermo-elastic expressions	140
D.4	Limit values for the Laplace-Carson inversion	145
D.4.1	The different functions	145
D.4.2	Limit values for $s \rightarrow \infty$	146
D.4.3	Limit values for $s \rightarrow 0$	147
E	Tensile tests	149
E.1	Uniaxial tensile test	149
E.2	Biaxial tensile test	150
F	A short introduction to Affinistan	151
F.1	Input section	151
F.1.1	Toolbar	151
F.1.2	Matrix and inclusions sections	152
F.1.3	Homogenization and loading section	153
F.1.4	Additional parameters section	154
F.2	Post processing section	155
F.2.1	Toolbar	155
F.2.2	Add curve section	155
F.2.3	Set figure layout section	155
G	Notations and units	159

Chapter 1

Introduction

Development of innovative materials has always been one of the most important engineering tasks over the years. In this field, composite materials (i.e. an heterogeneous material made of two or more different constituents) always had an important position and have a much longer history than what we can firstly think of. Wood as such can be considered as a composite material made of very long fibers of cellulose held together by a much weaker substance. The very first composite produced by man was cob: a plastic matrix made of earth is reinforced by plant fibers. More than 4000 years ago, Mongols already produced a sophisticated composite material: a bow made of a wooden frame assembled with horn and tendons. In more recent times, interest for composite materials was permanently growing up. The main interest is to obtain thermo-mechanical properties which are impossible to get with a single homogeneous material. A good example is concrete. The mix of gravel and cement gives a good compressive strength but is much less satisfying in tension. This can be improved by adding metal rods in order to obtain reinforced concrete.

There are two main ways for assembling the different constituents. Several layers made of different materials can be superposed in order to produce a laminated composite. Another possibility is to consider a matrix in which particles are added in order to get a particle-reinforced composite. This work will be limited to the latter type. However, this include a wide range of materials, from fiber-reinforced composites to nanocomposites, from random to perfectly arranged microstructures. An homogeneous material containing holes can also be considered as this type of composite. Even if material properties of all the constituents are well established, predicting the effective response by taking into account geometrical, mechanical and thermal properties is certainly not an easy task. Logically, this strongly depends on the constitutive behavior of each constituent so that different subdivisions can be considered: linear (thermo-)elastic composites, linear viscoelastic composites, elasto-plastic com-

posites, elasto-viscoplastic composites, . . . In this work, we will concentrate our efforts to predict the behavior of materials made of at least one plastic phase. Main applications of such materials include:

- Polymer matrix reinforced with ceramic, glass or Kevlar fibers in order to improve stiffness and strength. Some applications include boat hulls, aircraft wings, sport equipments, car parts, . . .
- Polymer matrix with low modulus rubber particles in order to improve toughness and impact resistance (e.g.: car bumper).
- Metal matrix with ceramic particles or short fibers mainly for high temperature applications.
- Concrete matrix reinforced by elasto-plastic metallic fibers (for better strength in tension or bending) or polymeric fibers (for better ductility, lower density).

Furthermore, rate-dependent plastic effects occur in several types of matrix (e.g.: metallic (aluminum alloy, titanium, . . .), polymer), especially at high temperatures where such effects cannot be neglected. Typical applications include aeronautics (e.g.: aeropropulsion systems). Such composites can be reinforced by elastic inclusions or even elasto-viscoplastic ones.

The range of materials concerned by this study is thus really wide and we are concerned with the prediction of their effective behavior. In order to shorten a long and costly experimental campaign, numerical simulations are of great help. Numerical predictions of such materials represent an extraordinary tool in order to speed up the development of new materials. The main goal of this thesis is to develop efficient numerical methods based on robust algorithms for the prediction of the behavior of elasto-(visco)plastic composites by taking into account geometrical and mechanical aspects. More especially, two approaches will be used throughout this work: finite element simulations and mean-field homogenization schemes. No damage will be considered and all the developments are made in the context of small perturbations.

The structure of the thesis does not rigorously follow the historical developments of the research. This is done in order to get a more logical and readable structure of the text. The first section deals with the scale transition problem from a macroscopic structure to the definition of a representative volume element (RVE) of the heterogeneous microstructure. A boundary value problem is defined over this RVE and several solution methods are suggested. One of these methods, the finite element (FE) one, is presented in chapter 3. Since this technique gives the most accurate predictions, it will be used later as validation tool of other solution methods. This chapter has been the subject of the following publication:

-
- Pierard, O., González, C., Segurado, J., LLorca, J. and Doghri, I. Micromechanics of elasto-plastic materials reinforced with ellipsoidal inclusions. *Mechanics of Materials*, Submitted for publication, 2006.

Subsequent chapters are devoted to the development of mean-field homogenization schemes for a wide range of material constitutive behaviors. This technique relies on simplifying hypotheses so that an approximate solution is found at a much lower computational cost than a corresponding FE simulation. These are introduced in chapter 4 for linear behaviors (isothermal elasticity, thermo-elasticity, viscoelasticity) where analytical solutions are available in most cases. This chapter has been the subject of the following publication:

- Pierard, O., Friebel, C. and Doghri, I. Mean-field homogenization of multi-phase thermo-elastic composites: a general framework and its validation. *Composites Science and Technology*, 64 (2004), 1587-1603.

Mean-field homogenization schemes are later extended to elasto-plastic behaviors where a linearization of the local constitutive laws is required in order to apply homogenization schemes valid in linear elasticity. More precisely, an incremental formulation is introduced in chapter 5 which links at each state of deformation the strain rate to the stress rate. This chapter has been the subject of the following publications:

- Pierard, O. and Doghri, I. A study of various estimates of the macroscopic tangent operator in the incremental homogenization of elasto-plastic composites. *International Journal for Multiscale Computational Engineering*, Accepted for publication, 2006.
- Pierard, O., González, C., Segurado, J., LLorca, J. and Doghri, I. Micromechanics of elasto-plastic materials reinforced with ellipsoidal inclusions. *Mechanics of Materials*, Submitted for publication, 2006.

Finally, one of the main goals of this work is to predict the behavior of heterogeneous elasto-viscoplastic materials, which is introduced in chapter 6. For this, an affine type formulation of the constitutive laws is used to reduce the problem to a linear thermo-viscoelastic one. This chapter has been the subject of the following publications:

- Pierard, O. and Doghri, I. An enhanced affine formulation and the corresponding numerical algorithms for the mean-field homogenization of elasto-viscoplastic composites. *International Journal of Plasticity*, 22 (2006), 131-157.
- Pierard, O., Segurado, J., LLorca, J. and Doghri, I. Micromechanics of particle-reinforced elasto-viscoplastic composites: finite element simulations versus affine homogenization. *International Journal of Plasticity*, Submitted for publication, 2006.

In each chapter, an important part is devoted to the validation of the developed methods.

Chapter 2

Scale transition methods

2.1 Scale separation

Consider a structure made of a composite material. At the level of this structure (macroscopic level), the material is seen as homogeneous. Imposed loads on the structure with prescribed displacements on a part Γ_U of the boundary and prescribed tractions on the remaining part Γ_F induce strain and stress fields in the material. At each macroscopic point, the relation linking local strain and stress depends on the heterogeneous microstructure, which can be seen at a smaller scale only. In order to take into account this heterogeneous microstructure, a representative volume element (RVE) of it is defined at each macroscopic point (see figure 2.1)¹. When linking these scales, several problems arise. Among them: how to load the RVE from the applied macroscopic strain or stress at the corresponding macroscopic point, solve the boundary value problem on the RVE and compute the corresponding macroscopic response. First of all, precisions on the scale separation must be given. For this, following Zaoui [110], let's define various length scales in an ascending order:

- d_0 : lower length bound under which continuum mechanics is no more valid.
- d : characteristic size of the heterogeneities.
- l : size of the RVE.
- λ : fluctuation length of the prescribed mechanical loading over the structure.

¹A simple definition of the RVE was given by Drugan and Willis [28]: “*It is the smallest material volume element of the composite for which the usual spatially constant (overall modulus) macroscopic constitutive representation is a sufficiently accurate model to represent mean constitutive response*”.

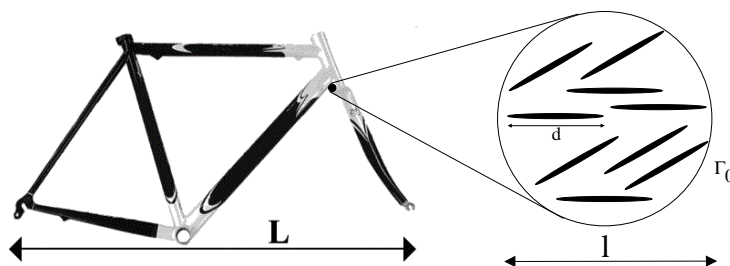


Figure 2.1: Scale separation and characteristic length scales: the material is viewed as homogeneous at the macroscopic level while heterogeneities can be seen at the level of the RVE.

- L : characteristic size of the structure.

In order to consider the structure as a continuum medium, the size of the RVE must be much smaller than the one of the structure (i.e.: $l \ll L$). Furthermore, as a macroscopic point is viewed as the center of the RVE and the response of the boundary value problem is macroscopically homogeneous, characteristic size of the heterogeneities must be much smaller than the size of the RVE (i.e.: $d \ll l$). Moreover, continuum mechanics remains valid at the scale of the RVE so that $d_0 \ll d$. Finally, the size of the RVE must be much smaller than the fluctuation length of the prescribed mechanical loading of the whole body (i.e.: $l \ll \lambda$) so that the use of the classical integral and differential tools of structural analysis remains valid.

Defining the RVE is not an easy task since the microstructure is not necessary known a priori. In the case of random microstructure (figure 2.2a), the property $d \ll l$ is taken into account so that a fictitious random microstructure of the RVE might be generated in order to give a significant response from a statistical point of view. Evidently, when generating a geometry, all the available information of the microstructure must be taken into account (volume fraction of each phase, orientations and shape of the inclusions,...). Periodic microstructures (figure 2.2b) are particularly suitable for numerical simulations on a unit cell. With the help of the geometrical periodicity, one can define a unit cell on which a well-posed problem is solved. In the case of random microstructure, defining the minimum size of the RVE is a crucial problem. Many papers discuss this subject and the minimum required size depends on several factors including the observed property, the geometry, the volume fraction and the mechanical (and thermal) behavior (see Povirk [88] and Kanit *et al.* [50] who define mathematical criteria to fix the cell size). Sometimes, microstructural arrangements (figure 2.2c) enable to strongly reduce the size of the unit cell. If assumptions are required to define such unit cell, different arrangements can sometimes be considered which lead to different predictions of the behavior.

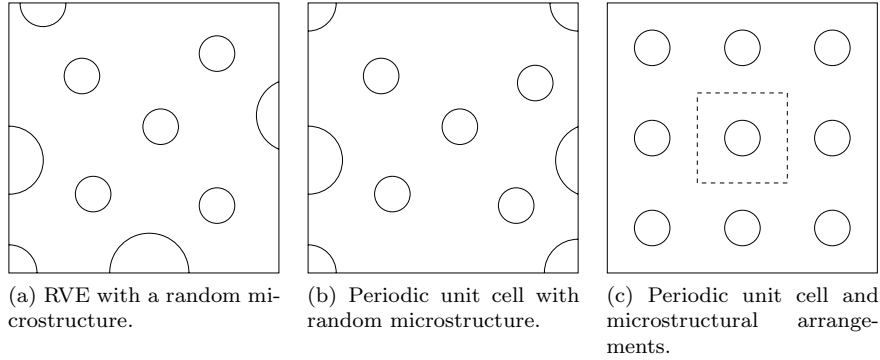


Figure 2.2: Periodicity of the unit cell and the microstructural arrangements.

Also, either on the RVE or the periodic unit cell, various boundary conditions might apply which will also influence the predictions.

2.2 Linking macroscopic and microscopic scales

This section explains how to perform the scale transition between macroscopic and microscopic levels. More precisely, from the load (strain or stress) defined at each point of the macroscopic level (e.g. at integration points of a finite element mesh of the structure), which boundary conditions must be applied to the corresponding RVE. For this, averaging theorems are required and recalled hereafter.

2.2.1 On averages

A macroscopic property can be defined as the volume average of that property over the whole RVE. Mathematically, this reads:

$$\bar{\mathbf{f}} = \langle \mathbf{f}(\mathbf{x}) \rangle_{\omega} = \frac{1}{V} \int_{\omega} \mathbf{f}(\mathbf{x}) dV, \quad (2.1)$$

where \mathbf{x} is the position vector in a local frame attached to the RVE ω of volume V .

Strain averages

Let's define the macroscopic strain as the volume average of the microscopic strain:

$$\bar{\boldsymbol{\varepsilon}} = \langle \boldsymbol{\varepsilon}(\mathbf{x}) \rangle_{\omega} = \frac{1}{V} \int_{\omega} \boldsymbol{\varepsilon}(\mathbf{x}) dV. \quad (2.2)$$

By definition of a strain tensor and using the divergence theorem, the last expression can be rewritten in a Cartesian frame as (dependence of the local fields with respect to \mathbf{x} is omitted for clarity):

$$\bar{\varepsilon}_{ij} = \frac{1}{2V} \int_{\omega} \left(\frac{\partial u_i}{\partial x_j} + \frac{\partial u_j}{\partial x_i} \right) dV = \frac{1}{2V} \int_{\partial\omega} (u_i n_j + u_j n_i) dA. \quad (2.3)$$

Stress averages

Let's define the macroscopic stress as the volume average of the microscopic stress:

$$\bar{\boldsymbol{\sigma}} = \langle \boldsymbol{\sigma}(\mathbf{x}) \rangle_{\omega} = \frac{1}{V} \int_{\omega} \boldsymbol{\sigma}(\mathbf{x}) dV. \quad (2.4)$$

Equilibrium equations without body forces (i.e. the stress field is equilibrated, $\nabla \cdot \boldsymbol{\sigma} = \mathbf{0}$) combined to the divergence theorem enable to rewrite the last expression in a Cartesian frame as (dependence of the local fields with respect to \mathbf{x} is omitted for clarity):

$$\bar{\sigma}_{ij} = \frac{1}{V} \int_{\omega} \frac{\partial(\sigma_{ik} x_j)}{\partial x_k} dV = \frac{1}{V} \int_{\partial\omega} t_i x_j dA. \quad (2.5)$$

2.2.2 Imposition of the boundary conditions

In this section, a coherent scale transition with the averaging theorems is proposed for several boundary conditions imposed on the RVE. Three of them are presented: prescribed displacements, prescribed tractions and periodic boundary conditions which are valid for periodic unit cells (figure 2.2b).

Linear displacements. In the case of prescribed displacement boundary conditions, displacement of each point on the boundary $\partial\omega$ of the RVE is given by:

$$\mathbf{u}_i(\mathbf{x}) = G_{ij} \mathbf{x}_j \text{ with } \mathbf{x} \text{ on } \partial\omega, \quad (2.6)$$

where \mathbf{G} is the displacement gradient tensor so that the strain tensor $\boldsymbol{\varepsilon}$ is its symmetric part: $\boldsymbol{\varepsilon} = \frac{1}{2} (\mathbf{G} + \mathbf{G}^T)$. If a uniform displacement gradient \mathbf{G}^0 corresponding to a strain tensor $\boldsymbol{\varepsilon}^0$ is used to impose the displacements, equation (2.3) reads:

$$\bar{\varepsilon}_{ij} = \frac{1}{2V} \left[\mathbf{G}_{ik}^0 \int_{\partial\omega} x_k n_j dA + \mathbf{G}_{jk}^0 \int_{\partial\omega} x_k n_i dA \right] \quad (2.7)$$

$$\begin{aligned} &= \frac{1}{2V} \left[\mathbf{G}_{ik}^0 \int_{\omega} \frac{\partial x_k}{\partial x_j} dV + \mathbf{G}_{jk}^0 \int_{\omega} \frac{\partial x_k}{\partial x_i} dV \right] \\ &= \varepsilon_{ij}^0. \end{aligned} \quad (2.8)$$

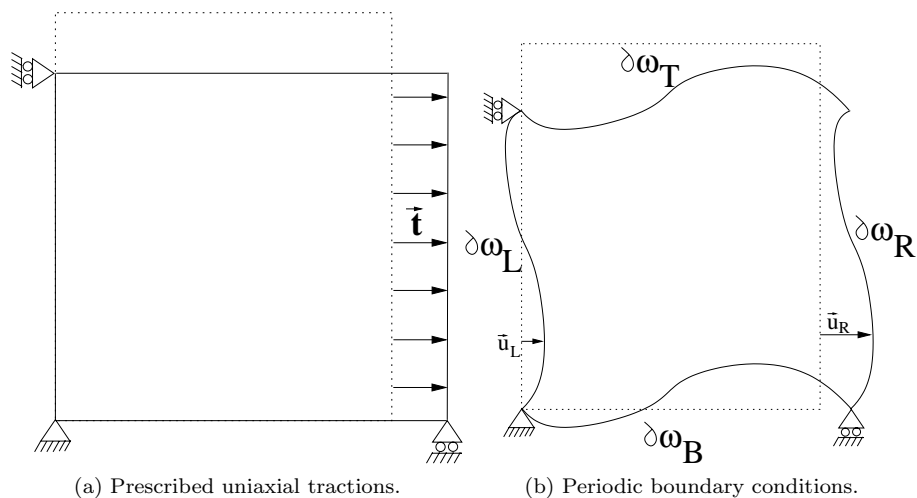


Figure 2.3: Imposition of boundary conditions to a 2D rectangular RVE. Initial configuration is in dots and final one in continuous lines.

Imposing linear displacements indeed satisfies the strain averaging relation (2.2) if $\bar{\epsilon}$ is used to compute the prescribed displacements.

Uniform tractions. For prescribed traction boundary conditions, imposed traction at each point on the boundary of the RVE is given by (see figure 2.3a):

$$\mathbf{t}(\mathbf{x}) = \boldsymbol{\sigma}^T \cdot \mathbf{n}(\mathbf{x}) \text{ with } \mathbf{x} \text{ on } \partial\omega, \quad (2.9)$$

where superscript T stands for transposition and \mathbf{n} for the outer normal at point \mathbf{x} . If a uniform stress tensor $\boldsymbol{\sigma}^0$ is used to impose the tractions, expression (2.5) reads:

$$\bar{\sigma}_{ij} = \frac{1}{V} \sigma_{ik}^0 \int_{\partial\omega} n_k x_j dA = \frac{1}{V} \sigma_{ik}^0 \int_{\omega} \frac{\partial x_j}{\partial x_k} dV = \sigma_{ij}^0. \quad (2.10)$$

Imposing uniform tractions indeed satisfies the stress averaging relation (2.4) if $\bar{\sigma}$ is used to compute the prescribed tractions. If the finite element method is used to solve the problem on the macroscopic structure, prescribed tractions on the boundary of the RVE cannot apply directly since finite element codes are generally strain driven. Furthermore, one has to be careful when using both finite strains and prescribed traction boundary conditions since rotations must be taken into account in order to determine uniquely the corresponding strain (Kouznetsova [51]).

Periodic boundary conditions. A third possibility is to consider periodic boundary conditions. In this case, due to the repetition of the cell in all di-

reactions before and after application of the load, periodic deformations and anti-periodic tractions are applied at each corresponding pair of nodes lying on opposite faces of the RVE boundary (see figure 2.3b):

$$\mathbf{u}_R - \mathbf{u}_L = \mathbf{G} \cdot (\mathbf{x}_R - \mathbf{x}_L), \quad (2.11)$$

$$\mathbf{t}_R = -\mathbf{t}_L. \quad (2.12)$$

Imposing periodic boundary condition also satisfies (2.2) if the displacement gradient \mathbf{G} is computed from $\boldsymbol{\varepsilon} = \bar{\boldsymbol{\varepsilon}}$. The proof is similar to (2.7-2.8) excepted that the integrals must be split into two parts corresponding to the opposite faces.

Solving the RVE boundary value problem with given macroscopic strain or stress does not necessarily give the same response but generally surrounds the correct response. The larger the dimension of the cell is with respect to the size of its constituents, the closest these two responses are. Periodic boundary conditions generally lead to an intermediate and more accurate response, which means that a smaller cell size can be considered. This result is represented schematically on figure 2.4. This is even more true during an analysis of the microscopic fields. Prescribed displacements or tractions on the boundary give an inaccurate response close to the boundaries (e.g.: if uniform tractions are prescribed, the stress will be uniform on the faces which is obviously not correct). On the contrary, when imposing periodic boundary conditions, the treatment of the lateral faces is exactly the same as the one of a section in the middle of the RVE. These facts have been observed numerically in numerous studies, including Kanit *et al.* [50] in linear elasticity, Jiang *et al.* [46, 47] in elasto-plasticity and Ostoja-Starzewski [73] for a wide range of constitutive behaviors.

2.2.3 Hill's Lemma

Given an equilibrated stress field $\boldsymbol{\sigma}$, compatible deformations $\boldsymbol{\varepsilon}$ (i.e.: $\boldsymbol{\varepsilon} = \boldsymbol{\varepsilon}(\mathbf{u})$) and either the stress field, either the strain field satisfies one of the three boundary conditions defined in section 2.2.2, Hill's lemma reads:

$$\langle \boldsymbol{\sigma} : \boldsymbol{\varepsilon} \rangle_\omega = \langle \boldsymbol{\sigma} \rangle_\omega : \langle \boldsymbol{\varepsilon} \rangle_\omega. \quad (2.13)$$

Up to now, no hypothesis has been made on an eventual link between stresses and strains. If they are coupled through a constitutive law, the lemma insures the equality between the average of the microscopic work $\boldsymbol{\sigma} : \boldsymbol{\varepsilon}$ and the macroscopic work $\bar{\boldsymbol{\sigma}} : \bar{\boldsymbol{\varepsilon}}$. This result is commonly called *Hill-Mandel condition* or *macrohomogeneity condition*.

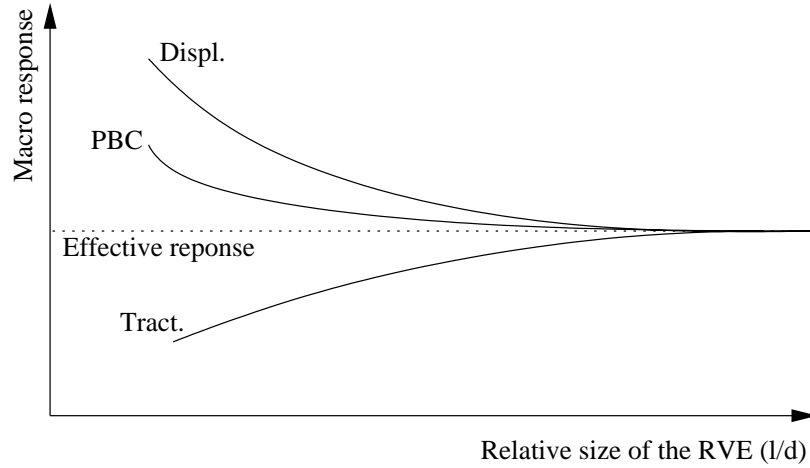


Figure 2.4: Accuracy of the predictions with respect to the RVE size for different boundary conditions (Displ.: prescribed displacements, PBC: periodic boundary conditions, Tract.: prescribed tractions).

2.2.4 Prediction of the macroscopic response

Solving the boundary value problem over the RVE is the core of this work. Several solution methods are proposed in section 2.3. Once this problem is solved, the macroscopic response still must be computed. A coherent manner to predict it is through a volume-average over the RVE so that Hill-Mandel condition is satisfied. If prescribed displacements or periodic boundary conditions are applied, this reads:

$$\bar{\sigma} = \frac{1}{V} \int_{\omega} \sigma(x) dV. \quad (2.14)$$

If prescribed traction boundary conditions are applied, the macroscopic strain is computed as:

$$\bar{\varepsilon} = \frac{1}{V} \int_{\omega} \varepsilon(x) dV. \quad (2.15)$$

2.3 Various approaches to solve the scale transition problem

The micro/macro problem being defined, the boundary value problem over the RVE must still be solved. For this, several approaches have been proposed over the years, some of them being reported hereafter. Several criteria must be taken

into account when choosing a solution method: arrangement and periodicity of the microstructure, computational cost, desired information on the local fields, accuracy of the predictions, . . . A comparison of all the presented methods is given at the end of this section.

2.3.1 Finite element methods

Solving the boundary value problem on a RVE can be done by a classical finite element approach. If periodic microstructure is assumed, unit cells are considered and periodic boundary conditions can apply. This method gives good results for both the global response and the local fields but has several disadvantages. One of them is, as most methods, the impossibility of taking into account of size effects. Also, generating good meshes for complex microstructures is difficult and its computational cost, especially if this problem is coupled to another one on the macroscopic structure, can be very high. Simplifications are sometimes required. One of them is to reduce the real three dimensional (3D) RVE to a simplified two dimensional (2D) axisymmetric or planar one. Since this method is the most accurate one, it has been adopted as validation tool in this work so that an entire chapter is dedicated to it (chapter 3). An alternative if difficulties in modeling the microstructure arise is the Voronoi cell finite element method. This approach initiated by Ghosh [35] is based on a Dirichlet tessellation of the microstructure into a network of multi-sided Voronoi polygons (see figure 2.5). This method is frequently used to represent the microstructure of polycrystals and sometimes for the one of two-phase materials (Kanit *et al.* [50]). In both cases, either regular or irregular meshes can be used, the latter being far better. Formulations in linear and some non-linear regimes have been developed for these elements and applied to various constitutive behaviors. Another approach is the extended finite element approach (XFEM) for which shape functions are enriched so that it enables to deal with discontinuities of the displacement field. Main advantage is the generation of a more structured mesh since it does not have to fit boundaries of the heterogeneities.

2.3.2 Asymptotic homogenization method

The asymptotic homogenization method is an elegant technique for predicting both microscopic and macroscopic properties of heterogeneous media and was developed by Bensoussan *et al.* [6] and Sanchez-Palencia [89]. This method relies on a distinction between a characteristic length of the RVE (l) and the one of the real structure (L) so that the ratio of these lengths gives a very small number $\varepsilon = l/L$. Starting from the fact that a high level of heterogeneity in a periodic microstructure causes rapid variation of strains and stresses in a small neighborhood ε of a macroscopic point \bar{x} , all variables are assumed to exhibit

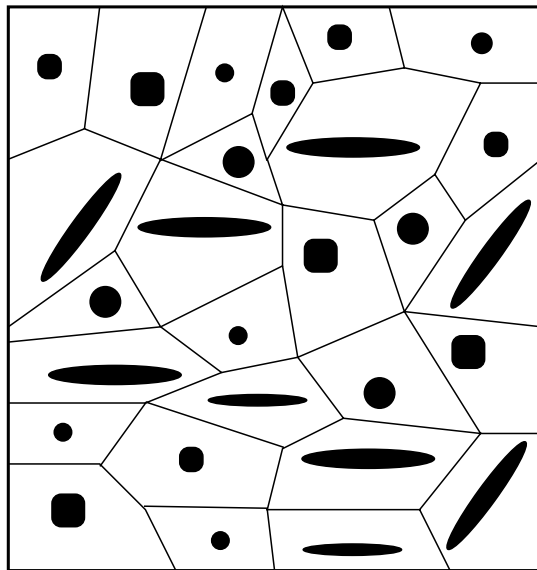


Figure 2.5: Tessellation of the microstructure into Voronoi cells.

dependence on both length scales of coordinates $\bar{\mathbf{x}}$ at the macroscopic level and $\bar{\mathbf{x}}/\varepsilon$ at the microscopic one (Ghosh *et al.* [36]). Asymptotical expansions of displacement and stress fields with respect to ε are introduced into equilibrium and constitutive relations. This leads to a set of partial differential equations with periodic boundary conditions which must be solved numerically (e.g. by Finite Element algorithms). This method has been applied successfully on linear elastic materials and is still under investigation for inelastic materials and damage. For a historical review of the method, see Chung *et al.* [21] and references therein. Notice that a combination of Voronoi cell tessellation and asymptotic homogenization methods has also been developed (Ghosh *et al.* [36]).

2.3.3 Generalized method of cells

The generalized method of cells enables to compute both microscopic and macroscopic properties of heterogeneous inelastic materials undergoing multi-axial mechanical loading as well as a spatially constant thermal loading. Following the review of Bednarczyk *et al.* [5], this method introduced by Aboudi [2], Paley and Aboudi [74] and Dvorak [29] (called the transformation field analysis) divides a repeating unit cell into an arbitrary number of generic cells,

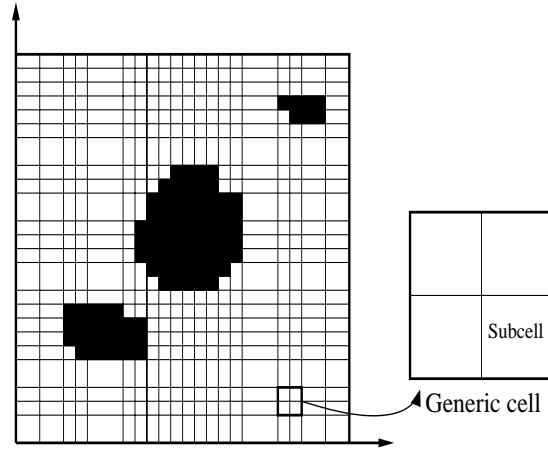


Figure 2.6: Typical discretization of a repeating unit cell, generic cell and subcell of the generalized method of cells.

themselves being divided into 4 (or 8) rectangular (or parallelepipedal) subcells and each one may contain a distinct homogeneous material (see figure 2.6). Basic assumption is that the displacement vector in each subcell varies linearly with the local subcell coordinates. Continuity of displacements and tractions between adjacent subcells and repeating unit cells is imposed. Global response is computed by a classical volume average. This method is very efficient in an algorithmic point of view and present a very good accuracy for the global response. However, due to the linear assumption of the displacement fields, quality of the local fields is not that high. In order to better capture the nonlinearities, the high-fidelity general method of cells (Aboudi *et al.* [3, 4]) has been developed. Higher order displacement fields are used so that additional equations are needed to solve the system: the zeroth, first and second moments of the local (subcell) equilibrium equations must be satisfied in a volumetric sense. This induces a much higher computational cost than the original cell method but still lower than an equivalent finite element simulation. However, due to the imposed rectangular shape of the subcells, finite element methods generally still give a better accuracy of the microfields.

2.3.4 Fast Fourier transform method

This meshless method introduced by Moulinec and Suquet [70, 71] makes use of the fast Fourier transform to solve the problem at the microscopic level. Periodic boundary conditions are applied to the RVE so that the method is

limited to periodic microstructure. The RVE is digitalized into a given number of pixels (2D) or voxels (3D), different mechanical properties can be given to each of them. The method is thus particularly suitable for analyses of digital images of the real and eventually complex microstructure (clustering, percolation, ...). Constitutive and equilibrium equations can be written as an integral equation in which the Green tensor is introduced. Fourier transform of this expression is easily obtained so that an iterative process over the stress tensor (if macroscopic strain is prescribed) to solve a nonlinear periodic equation (the Lippmann-Schwinger equation) in the Fourier space is used. The adopted discretization is appropriate for the use of fast Fourier transform packages. Solution is obtained at each pixel (or voxel) of the microstructure at a lower computational cost than a corresponding finite element simulation. Extensions to nonlinear behaviors require additional hypotheses. One possibility is the use of the generalized method of cells. This induces an additional subdivision of the phases and increases significantly the computational cost.

2.3.5 Mean-field homogenization schemes

Semi-analytical mean-field homogenization methods started several decades ago when computational cost was a real challenge. Based on assumptions of the interaction laws between the different phases (which define the homogenization scheme), they enable to give a macroscopic response as well as basic information on the state of deformation within the phases (i.e.: mean-field information). However, they are unable to predict any strain or stress localization on the contrary to other numerical approaches. Also, clustering, percolation and size effects cannot be taken into account. Most of these homogenization schemes are based on the Eshelby result [30], which is valid for ellipsoidal inclusions only and assume a perfect bonding between the constituents. Mean-field homogenization schemes were first developed for linear constituents and later extended to inelastic materials. They enable to get predictions of the macroscopic behavior as well as derivation of bounds. For nonlinear materials, a linearization of the local constitutive laws is required (formulation of the problem) in order to apply homogenization schemes valid in linear (thermo-)elasticity. The method is very efficient on a computational point of view and some models have a good accuracy in the linear elastic regime for both inclusion-reinforced materials and polycrystals. Extension of mean-field homogenization schemes to rate independent and dependent elasto-plastic behaviors is the main challenge of this work.

2.3.6 Comparison of the various methods

Here is a summary of the different capabilities and levels of accuracy offered by the homogenization methods presented above. Comparison is made over

several criteria, among them:

- Complex geometries: possibility of the method to deal with complex microstructures.
- Ease of discretization: most methods require a discretization of the RVE, which can be tricky in some cases.
- Accuracy of the macroscopic response: this is the main goal of the homogenization methods, so its accuracy is of first importance.
- Accuracy of the microfields: some methods, in addition to the prediction of the macroscopic response can give an accurate information about microfields as well.
- Computational cost: varies from a fraction of second to several hours on a multiprocessor computer so that it might be a huge limitation for applications of the method in practice.
- Nonlinear behaviors: the difficulty of extensions to nonlinear behavior greatly depend on the method.

An overview of the different methods is reported in table 2.1. Notice that by no way the list of the methods is exhaustive. Even if a lot of care has been taken to complete this table, some evaluations are still the subject of debate, especially when a method offers several variants. Furthermore, these evaluations are somehow subjective, a better solution would be to compare them on several benchmarks.

Homogenization method	2DFE	3DFE	2DVCFE	AHM
Complex geometries	+	+	+	+
Ease of discretization	++	+	+++	++
Accuracy macro response	++	+++	++	++
Accuracy microfields	+ / ++	+++	+	++
Computational cost	++	+	++	+
Nonlinear behaviors	+++	+++	+++	++
Homogenization method	GMC	HFGMC	FFTM	MFHM
Complex geometries	++	++	+++	++
Ease of discretization	++	++	+++	+++
Accuracy macro response	+++	+++	++	++
Accuracy microfields	+	++	++	+
Computational cost	++	+	+	+++
Nonlinear behaviors	+++	+++	++	++

Table 2.1: Comparison of different homogenization methods over various criteria. 2DFE: two-Dimensional Finite Element method, 3DFE: three-Dimensional Finite Element method, 2DVCFE: two-Dimensional Voronoi Cell Finite Element method, AHM: Asymptotic Homogenization Method, FFTM: Fast Fourier Transform Method, GMC: Generalized Method of Cells, HFGC: High Fidelity Generalized Method of Cells and MFHM: Mean-Field Homogenization Method. Evaluations are: +: weak, ++: fair, +++: good.

Chapter 3

Finite element simulations at the microscopic level

¹ Finite element simulations are an efficient homogenization method in terms of accuracy. For this, a RVE or unit cell must be defined, meshed and loaded so that the final response can be computed. All these aspects are examined in this chapter for different unit cells: 2D, 2D axisymmetric and 3D ones.

3.1 Two-dimensional unit cells

In some cases, three-dimensional geometries can be represented by two-dimensional unit cells. Two possibilities are considered here: composite reinforced by aligned fibers and axisymmetric geometries.

3.1.1 Composites reinforced by long fibers

For composites reinforced by aligned long fibers, the knowledge of the geometry of a cross section perpendicular to the fibers is enough. This geometry is described by the arrangements of the fibers within the matrix. Two possibilities will be examined in the numerical section: square and hexagonal array of fibers (see figure 3.1). Of course, in order to model the long fibers, plane strain (i.e. deformation in the longitudinal direction is zero) or generalized plane strain (i.e. deformation in the longitudinal direction is constant) elements are used. With the help of the symmetries, the dashed unit cell can be reduced to only one quarter of it (continuous lines of figure 3.1). If the cell periodicity

¹Some developments of this chapter led to the publication “Micromechanics of elastoplastic materials reinforced with ellipsoidal inclusions”, Pierard O., González C., Segurado J., LLorca J. and Doghri I., *Mechanics of Materials*, submitted for publication [81].

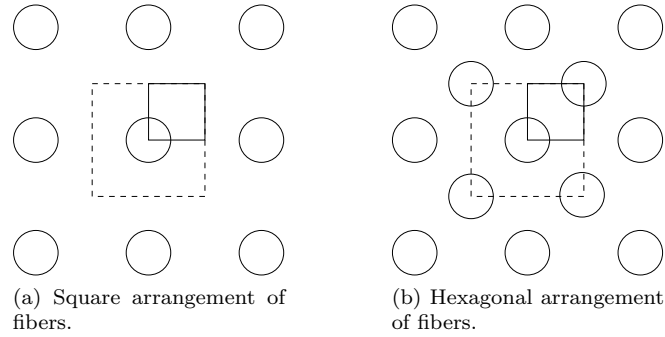


Figure 3.1: Unit cells with different arrangements of fibers.

is required (e.g.: asymptotic homogenization or prescribed periodic boundary conditions over the unit cell), symmetries cannot be taken into account and only the entire unit cell can be considered. A main limitation of using 2D unit cells to represent 3D geometries is that it is not possible to simulate all the loading possibilities (e.g.: shear in the longitudinal direction). It is well known that the considered unit cell might have a significant impact on the global response, especially in the non-linear regime (see Hom [44], Doghri and Friebel [25]). Several authors have already discussed this subject, e.g. Böhm and Han [9] for two-phase isothermal composites and Weissenbek *et al.* [104] for two-phase thermo-elastic(-plastic) composites. Tucker and Liang [100] also made various FE calculations based on different unit cells. This is illustrated on several examples in the different numerical simulation sections of this work (e.g.: section 5.4.1).

3.1.2 Two-dimensional axisymmetric unit cells

As done in several works (e.g.: Christman *et al.* [20], LLorca and Segurado [64]), a classical approach is an approximation of the 3D microstructure by a 2D axisymmetric unit cell as illustrated on figure 3.2. Space is supposed filled by prisms with a hexagonal basis which represent the matrix, each prism being reinforced by a spherical inclusion in its middle. To take advantage of symmetry of the unit cell, the prism is approximated by a cylinder. The unit cell can then be reduced to a 2D axisymmetric one.

Boundary conditions for a uniaxial tension test are the following. For symmetry reasons, no vertical (axial) displacement is allowed on bottom side (1 on figure 3.2) and no horizontal (radial) one on the left side (3). Also, the right side (4) must remain vertical, so that all the horizontal displacements are the same. Displacements are imposed gradually on the top side (2) to reach the required strain at the end of the simulation. Three-node linear axisymmetric

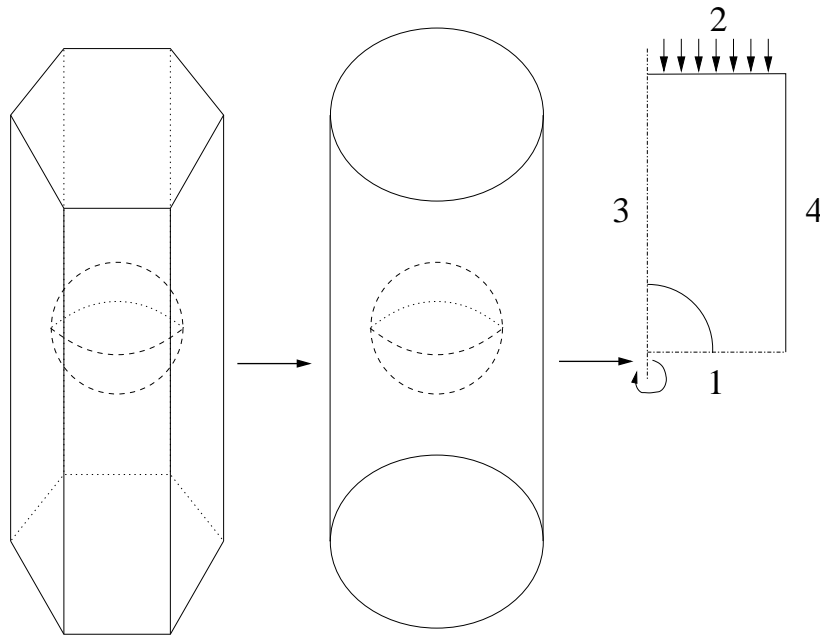


Figure 3.2: Reduction to a 2D axisymmetric unit cell of a sphere-reinforced composite material.

triangles (CAX3 in ABAQUS [1]) or six-node quadratic axisymmetric triangles (CAX6) are used to mesh the surface and about 10000 elements give a sufficiently refined mesh.

3.1.3 Boundary conditions

In section 2.2.2, various boundary conditions to the boundary value problem over the RVE have been presented which include uniform traction, linear displacement and periodic boundary conditions. This section explains how to use these boundary conditions with the FE method. Also, prediction of the macroscopic response can be done in a more efficient way than from a volume average of the fields as in (2.2) or (2.4).

Linear displacement boundary conditions

If linear displacements are applied on the boundary, the macroscopic stress response can be computed from a volume average of the stress tensor given at

each integration point over the volume:

$$\bar{\boldsymbol{\sigma}} = \frac{1}{V} \sum_{k=1}^{k=N_k} \boldsymbol{\sigma}_k V_k, \quad (3.1)$$

where $\boldsymbol{\sigma}_k$ is the stress acting at the integration point k , V_k is the representative volume of the integration point k and N_k is the number of integration points within the volume.

More simply, with the help of (2.5), this can be computed by an average of the resulting tractions acting on the boundary:

$$\bar{\boldsymbol{\sigma}} = \frac{1}{V} \sum_{p=1}^{p=N_p} \mathbf{t}_p \otimes \mathbf{x}_p, \quad (3.2)$$

where N_p is the number of nodes over the boundary of the RVE, \mathbf{t}_p are the resulting tractions at node p and \mathbf{x}_p is the position vector at this node.

In the case of a uniaxial tensile test in direction 1, the macroscopic normal stress component in this direction becomes:

$$\bar{\sigma}_{11} = \frac{1}{S} \sum_{p=1}^{p=N_{p1}} t_1, \quad (3.3)$$

where S is the area of the surface on which tractions are imposed and N_{p1} is the number of nodes lying on that surface.

Uniform traction boundary conditions

If uniform tractions are applied, the macroscopic strain response can also be computed either from a volume average of the strain tensor given at all the integration points over the volume:

$$\bar{\boldsymbol{\varepsilon}} = \frac{1}{V} \sum_{k=1}^{k=N_k} \boldsymbol{\varepsilon}_k V_k. \quad (3.4)$$

Equivalently, with the help of (2.3), this can be computed by an average of the resulting displacements on the boundary:

$$\bar{\boldsymbol{\varepsilon}} = \frac{1}{2V} \sum_{p=1}^{p=N_p} (\mathbf{u}_p \otimes \mathbf{n}_p + \mathbf{n}_p \otimes \mathbf{u}_p), \quad (3.5)$$

where \mathbf{u}_p is the resulting displacement at the boundary node p and \mathbf{n}_p is the normal vector to the boundary at this node.

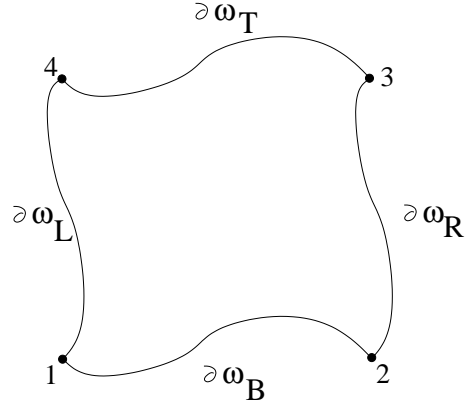


Figure 3.3: Definition of the boundaries, master node (node 1) and slave nodes (nodes 2 and 4) for periodic boundary conditions used in the FE method.

Periodic boundary conditions

Application of the conditions In addition to the microstructural periodicity, meshes are supposed to be the same on opposite faces so that initial positions of every corresponding pair of nodes are related through (see figure 3.3 for notations):

$$\begin{aligned} \mathbf{x}_R - \mathbf{x}_L &= \mathbf{x}_2 - \mathbf{x}_1, \\ \mathbf{x}_T - \mathbf{x}_B &= \mathbf{x}_4 - \mathbf{x}_1, \end{aligned} \quad (3.6)$$

where \mathbf{x}_s lies on $\partial\omega_s$, $s = R, L, T, B$. \mathbf{x}_1 is the master node and \mathbf{x}_2 and \mathbf{x}_4 are the slave nodes. With the help of equation (2.11) and for a given macroscopic strain $\bar{\boldsymbol{\varepsilon}}$ ($\bar{\boldsymbol{\varepsilon}} = \frac{1}{2}(\bar{\mathbf{G}} + \bar{\mathbf{G}}^T)$), this can be rewritten in term of displacements as:

$$\begin{aligned} \mathbf{u}_R - \mathbf{u}_L &= \bar{\mathbf{G}} \cdot (\mathbf{x}_R - \mathbf{x}_L) = \bar{\mathbf{G}} \cdot (\mathbf{x}_2 - \mathbf{x}_1), \\ \mathbf{u}_T - \mathbf{u}_B &= \bar{\mathbf{G}} \cdot (\mathbf{x}_T - \mathbf{x}_B) = \bar{\mathbf{G}} \cdot (\mathbf{x}_4 - \mathbf{x}_1). \end{aligned} \quad (3.7)$$

If following displacements are applied to the master and slave nodes:

$$\mathbf{u}_1 = \bar{\mathbf{G}} \cdot \mathbf{x}_1, \quad (3.8)$$

$$\mathbf{u}_2 = \bar{\mathbf{G}} \cdot \mathbf{x}_2, \quad (3.9)$$

$$\mathbf{u}_4 = \bar{\mathbf{G}} \cdot \mathbf{x}_4, \quad (3.10)$$

periodic boundary conditions may be rewritten as:

$$\mathbf{u}_R - \mathbf{u}_L = \mathbf{u}_2 - \mathbf{u}_1, \quad (3.11)$$

$$\mathbf{u}_T - \mathbf{u}_B = \mathbf{u}_4 - \mathbf{u}_1. \quad (3.12)$$

The set of equations (3.11-3.12) completely defines the application of periodic boundary displacements. Equation (2.12) still requires anti-periodic tractions on the boundary. Imposition of the displacements (3.8-3.10) at master and slave nodes induces resulting external forces at these nodes. Furthermore, tying conditions (3.11-3.12) induce tying tractions at the nodes on the boundary. Imposing a zero virtual work at the tied nodes enables to prove that the resulting tying tractions are opposite to each others at every pair of nodes on the boundary (detailed proof in Kouznetsova [51]). Condition (2.12) is thus trivially satisfied.

It should be kept in mind that imposing equations (3.11-3.12) can strongly increase the bandwidth of the system. If a direct solver is used, a much higher computational cost can be expected. On the other hand, using periodic boundary conditions gives better microscopic fields, especially in the surroundings of the inclusions close to the sides of the RVE.

Computation of the macroscopic response Computation of the macroscopic stress tensor from the external and tying tractions on the boundary (equation (2.5)) enable to strongly simplify the result (details in Kouznetsova [51]):

$$\bar{\sigma}_{ij} = \frac{1}{V}(t_{1_i}x_{1_j} + t_{2_i}x_{2_j} + t_{4_i}x_{4_j}), \quad (3.13)$$

where \mathbf{t}_1 , \mathbf{t}_2 and \mathbf{t}_4 are the resulting external tractions at the master and slave nodes.

This approach is limited to moderate strain/stress gradients otherwise the scale separation hypotheses ($d \ll l$, see figure 2.1) does no apply anymore. In this case, highly localized deformation might occur and precision of the classical FE method cannot be guaranteed. This led to the development of the second-order computational homogenization method which takes into account of the gradient of the macroscopic deformation gradient tensor into the scale transition procedure (Kouznetsova *et al.* [52, 53]). This approach gives an higher-order constitutive response without additional assumptions at the macroscopic level.

3.2 Three-dimensional unit cells

In this section, generation of three-dimensional unit cells reinforced by similarly-shaped, non-overlapping and randomly dispersed ellipsoids of revolution is examined. At first, generation of the geometry and the mesh as well as the application of the boundary conditions are presented and followed by an analysis of the unit cell (homogeneity, isotropy, required minimum number of inclusions).

3.2.1 Generation of the geometry

For inclusions aligned with their revolution axis and a constant aspect ratio Ar , the considered unit cell is a parallelepiped of size $(ArL \times L \times L)$ in order to have the same number of inclusions in all directions. If they are randomly oriented, a cubic unit cell is considered.

At first, the size of the inclusions must be defined (same size is considered for all of them). For a given volume fraction of inclusions v_1 and a number of aligned inclusions N within the cell (see in section 3.2.4 how to fix N), dimensions of all the ellipsoids' semi-axes can be easily found. Semi-axis length along the revolution axis is $r \times Ar$, while the other two semi-axes have the same length $r = L(3v_1/4\pi N)^{1/3}$. For randomly oriented inclusions, the semi-axis length is: $r = L(3v_1/4\pi NAr)^{1/3}$.

The final particle arrangement must be non-overlapping and suitable for finite element discretization. Similarly to unit cells filled with spheres, the Random Sequential Adsorption (RSA) algorithm (Widom [106]) is used to generate sequentially the coordinates of the particle centers. For this, consider a new particle E_i with a randomly generated center (and orientation if needed). Geometric and discretization conditions that E_i must verify in order to be accepted are:

1. Minimum distance between ellipsoid E_i and all the previously generated ellipsoids.
2. Surface of particle E_i should not be too close to the unit cell faces, edges or corners to prevent the presence of distorted finite elements during meshing.

The minimal distance between two ellipsoids is computed with an iterative algorithm proposed by Lin and Han [63]. As illustrated in 2D on figure 3.4, consider that the minimal distance between ellipsoids E_1 and E_2 must be determined. At the k^{th} iteration, the two closest points are: $x(k) \in \partial E_1$ and $y(k) \in \partial E_2$, where ∂E means 'the boundary of E '. A ball $B(c_1, r_1)$ is constructed completely inside the ellipsoid E_1 and tangent to E_1 at $x(k)$, and a ball $B(c_2, r_2)$ completely inside the ellipsoid E_2 and tangent to E_2 at $y(k)$. If the line segment $[c_1, c_2]$ between the two centers is entirely contained in $E_1 \cup E_2$, then the two ellipsoids have a nonempty intersection and the distance $d(E_1, E_2) = 0$; otherwise, the new point $x(k+1)$ is found as the intersection of the line segment $[c_1, c_2]$ with the boundary ∂E_1 , and the new point $y(k+1)$ as the intersection of the same segment with the boundary ∂E_2 . Convergence is achieved once the angle between the segment $[x(k+1), y(k+1)]$ and the segment $[c_1(k+1), x(k+1)]$ is smaller than a given tolerance ($c_1(k+1)$ is the center of the new ball tangent to the ellipsoid at $x(k+1)$). A similar test holds for the second ellipsoid. Convergence of the method is guaranteed to the unique solution of the problem. If the minimal distance between the two ellipsoids is

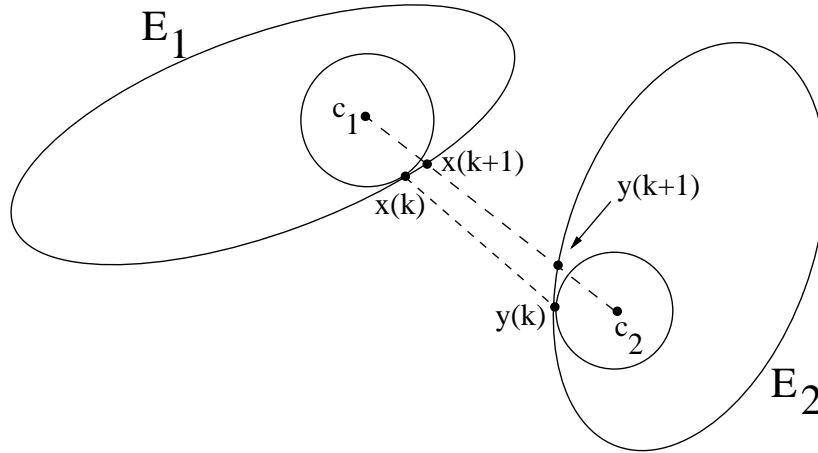


Figure 3.4: One iteration of the algorithm to find the minimal distance between two ellipsoids.

smaller than a given value (typically $3.5 \cdot 10^{-2} \times Ar \times r$), this ellipsoid must be rejected.

The second condition is the imposition of a minimal distance between the ellipsoid and faces, edges and corners of the parallelepiped; i.e., the distance has to be checked with respect to planes, lines and points. For the distance between an ellipsoid and a plane, an analytical formula is available ([91]). The other two tests are checked by a modification of the iterative algorithm presented above. If the ellipsoid is too close to a face (or an edge, or a corner) or just slightly crosses it, it must be rejected. Commonly used tolerance for this minimal distance is $5 \cdot 10^{-2} \times Ar \times r$. An example of such unit cell generation is illustrated on figure 3.5 for aligned inclusions.

The main limitation of this approach is that only moderate volume fractions of inclusions can be reached. These are reported in table 3.1 for typical values of N and tolerances. For higher volume fractions, Segurado and LLorca [92] proposed an algorithm for sphere reinforced unit cells which enables to reach up to 50% of inclusions. This can be easily extended to ellipsoid-reinforced unit cells. Anyway, for the composites studied in this work, such extension is not required.

3.2.2 Mesh generation

If periodic boundary conditions are applied (section 3.1.3), the microstructure must also be periodic so that particles which cut faces of the unit cell are split into the appropriate number of parts (two parts if across one face, four if

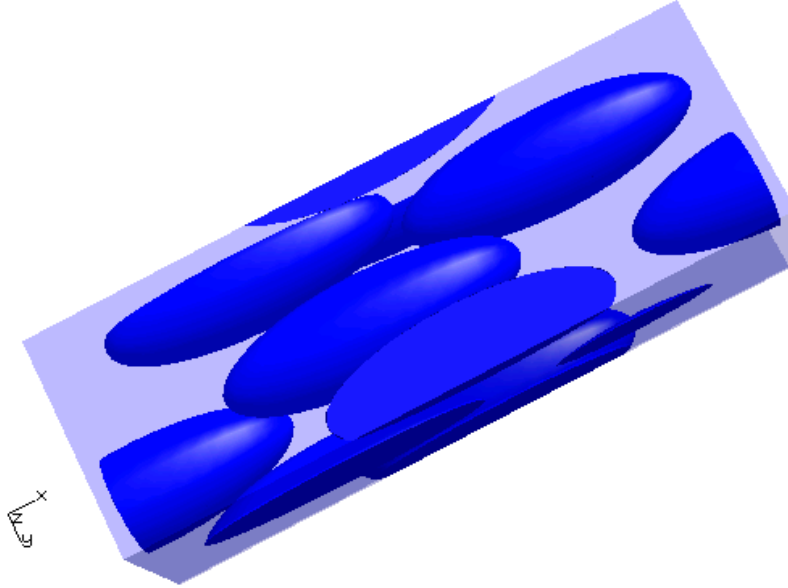


Figure 3.5: Unit cell containing 25% of aligned inclusions ($N=5$, $Ar=3$).

Ar	v_1 max. [%]		
	aligned	2D random	v_1 3D random
1	36	36	36
3	28	28	26
5	26	20	18
10	20	12	10

Table 3.1: Maximum volume fraction of inclusions (v_1) reached with the RSA algorithm for various aspect ratios of 30 aligned, 2D randomly dispersed and 3D randomly dispersed inclusions. Typical tolerances on the minimal distances are used.

across two, eight if across three) and copied on the opposite side. The unit cell is meshed with second-order tetrahedra by the software NETGEN [72]. This mesher has very good optimizing properties so that the number of distorted elements is reduced to only a few (less than 5). It also enables to deal with periodic boundary conditions. If the distance between two inclusions is close to the imposed limit, the mesh is refined in this region in order to generally

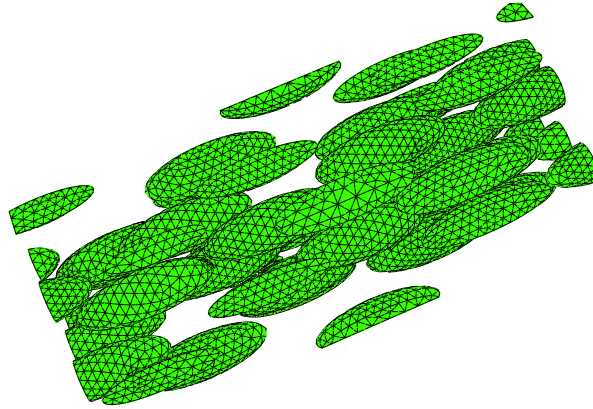


Figure 3.6: Unit cell containing 25% of meshed inclusions.

have a minimum of two elements between these two heterogeneities. Resolution of the problem is done with ABAQUS [1] and 10-node modified tetrahedron (C3D10M) elements are used. Additional degrees of freedom offered by this modified element capture the deformation gradients better than the classical one. For cells reinforced with 30 spheres, a sufficiently refined mesh contains about 90000 nodes and for the same number of ellipsoids ($Ar=3$), about 110000 nodes are required. A typical mesh for ellipsoidal inclusions can be seen on figure 3.6.

3.2.3 Boundary conditions

Application of boundary conditions and resulting simplifications to compute the response of the material have already been examined in section 3.1.3 for 2D unit cells. This can be easily extended to 3D and will not be developed here.

3.2.4 Validation of the unit cell

Three validations of the cells containing ellipsoids ($Ar = 3$) generated by the proposed method are examined. As geometrical tests, homogeneity and isotropy of the cell are analyzed. Determination of the minimal required number of inclusions is also done.

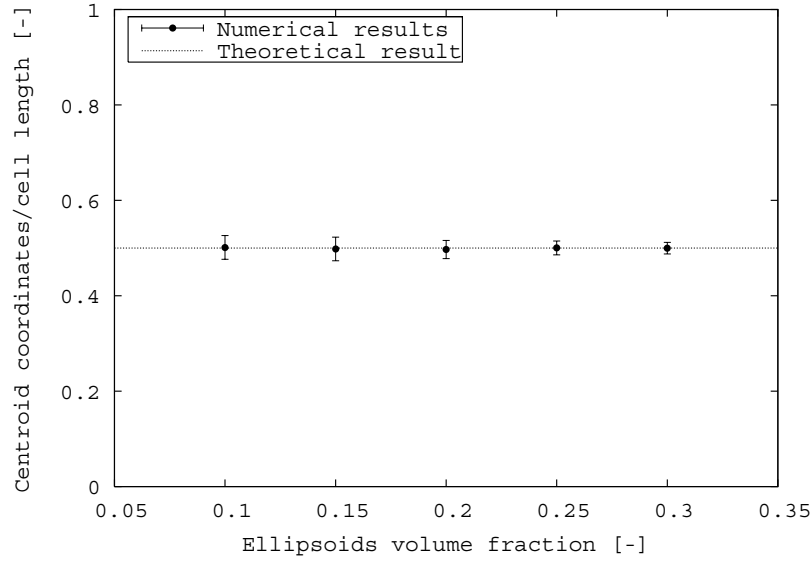


Figure 3.7: Average position and standard deviation of the center of mass of 100 unit cells generated at various volume fractions.

Geometrical analysis

The first test checks the homogeneity of the generated cells. For several volume fractions of inclusions, 100 cells containing 30 ellipsoids are generated for each of them. For each cell, the position of the center of mass is computed (it is supposed that only inclusions have non-zero density) as well as the average position and standard deviation for a given volume fraction. This is illustrated on figure 3.7. Of course, for a perfectly homogeneous distribution of inclusions, the center of mass should be at the half-length of the cell in each direction. On the figure, the average position always coincides with the reference result while the standard deviation remains very small and logically decreases as the volume fraction of inclusions increases.

In order to check the transverse isotropy of the cell, three moments of inertia with respect to the three perpendicular axes at the center of the cell are computed numerically. For this, the cell is decomposed into many small cubes which have a non-zero mass if they mainly contain part of an ellipsoid. Average and standard deviations with respect to a direction parallel to the revolution axis of the inclusions are plotted on figure 3.8. Theoretical moment of inertia obtained with a homogeneous prism whose mass is equal to the one of the ellipsoids in the random arrangements is given in the direction x by: $v_1 V(L_y^2 + L_z^2)\rho/12$,

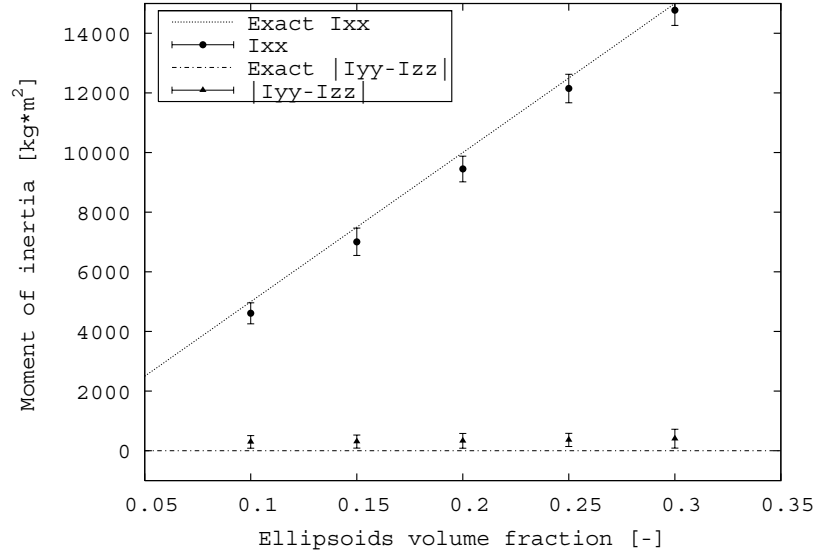


Figure 3.8: Average and standard deviation of the longitudinal (dir. x) and transverse (dir. y and z) moments of inertia for 100 unit cells generated at various volume fractions v_1 . V is the volume of the RVE, L_y and L_z the lengths in directions y and z of the RVE and I_{yy} and I_{zz} the moments of inertia with respect to axes y and z .

where ρ is the density of the inclusions (considered as equal to one). This result is also reported on the figure and a good agreement is found with numerical results. In addition, for each cell, the moments of inertia with respect to the two others axes should be the same. Their difference in absolute value is also plotted on the figure and remains very small.

These two tests thus show that our method used to generate unit cells containing ellipsoids gives homogeneous and transversely isotropic cells for a wide range of volume fractions of inclusions.

Numerical analysis

A crucial issue for the accuracy of the FE predictions is to determine the required minimum number of inclusions N within the unit cell. Advantage of small N is that a lower number of elements is required during meshing so that simulations are faster. On the other hand, as we will see, a too small N does not lead to accurate enough predictions. In order to find a compromise, two tests are made. For these, an elasto-plastic matrix (J_2 constitutive model

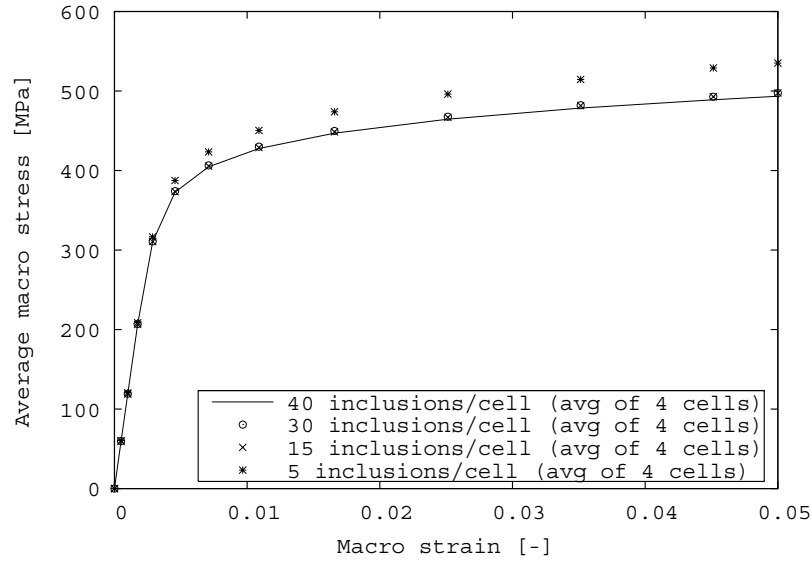


Figure 3.9: FE average response of 4 unit cells for a various number of inclusions within the unit cell. The loading direction is aligned with the ellipsoids.

(see section 5.1), $E = 70$ GPa, $\nu = 0.33$, $\sigma_Y = 1.5924$ MPa, $k = 400$ MPa and $n = 0.05$) is reinforced by elastic inclusions ($E = 400$ GPa and $\nu = 0.2$). All cells contain 25 % of randomly located aligned ellipsoids ($Ar = 3$) and the uniaxial tension direction is along the revolution axis of the ellipsoids.

A first test illustrated on figure 3.9 checks the accuracy of the FE average response obtained for several values of N (5, 15, 30 or 40 inclusions), 4 cells being generated for each N . Of course, even for a small N , the average response on dozens of different cells would increase the accuracy of the average response but an excessive computation time would be needed. Clearly, 5 inclusions within each cell are not enough since the obtained response is quite far from the reference value (the one corresponding to 40 inclusions). Logically, increasing N reduces this error, the response obtained with 15 inclusions being already very good.

A second test, and maybe even more crucial, is to check the standard deviation of the responses obtained for the different values of N . Again, 4 unit cells are generated for each N and results are reported on figure 3.10. As expected, a high scattering is observed (up to 5% of the average value) for a low number of inclusions while this reduces as N increases, the standard deviation for 30

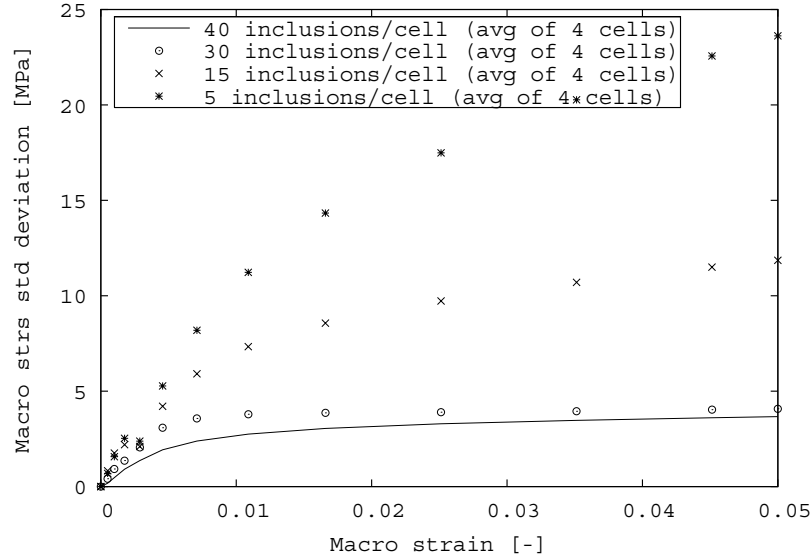


Figure 3.10: FE standard deviation of the average response of 4 unit cells for a various number of inclusions within the cell. The loading direction is aligned with the ellipsoids.

inclusions being already very low.

The analysis of average and standard deviations of FE responses shows that a low number of inclusions leads to an inaccurate average response and a too high standard deviation. For these reasons, we advise to use 30 inclusions within each cell. For such value, corresponding meshes have about 110.000 nodes and 75.000 elements. Mesh refinement has also been successfully checked against a refined one containing more than 200.000 nodes.

3.3 Conclusions

In this chapter, we used the finite element method to solve the boundary value problem defined on a representative volume element of heterogeneous materials. For this, various unit cells are proposed, including 2D, 2D axisymmetric and 3D ones. For random distribution of the inclusions, 3D cells with randomly dispersed ellipsoids are generated and meshed with second order tetrahedron. Homogeneity and isotropy of these cells have been checked. Finally, the application of different boundary conditions has been examined. Periodic boundary conditions are studied in depth since they are known to give the most accurate

macroscopic and microscopic predictions. In addition, imposition of these conditions to parallelepipedic cells and computation of the macroscopic response can be done in a simplified way. When using 3D cells and periodic boundary conditions, a minimum of 30 ellipsoidal inclusions ($Ar=3.$) within the cell has been adopted in order to limit the standard deviation of the macroscopic response obtained with different cells.

Chapter 4

Homogenization of linear composites

¹ Mean-field homogenization schemes are an efficient way to predict the behavior of heterogeneous materials. Based on assumptions of the interaction laws between the different phases, they enable to get a prediction of the macroscopic response as well as some information on the per-phase state of deformation and stress. In comparison with the FE method, this approach is infinitely much faster. Various mean-field homogenization schemes are presented in this section and their application to linear (visco)elastic composites is examined. Furthermore, some theoretical bounds of the real response can be developed which enable to check some approximations made by the predictive methods. At first, constitutive models of the homogeneous materials are presented.

4.1 Constitutive equations

4.1.1 Linear thermo-elasticity

Consider a homogeneous linear thermo-elastic material of elastic stiffness \mathbf{C} and thermal expansion $\boldsymbol{\alpha}$. At each point \mathbf{x} of the material, for a given total strain $\boldsymbol{\varepsilon}$ and a change in temperature ΔT , the stress is given by:

$$\boldsymbol{\sigma}(\mathbf{x}) = \mathbf{C} : (\boldsymbol{\varepsilon}(\mathbf{x}) - \boldsymbol{\varepsilon}^{th}(\mathbf{x})), \quad \boldsymbol{\varepsilon}^{th}(\mathbf{x}) = \boldsymbol{\alpha}\Delta T(\mathbf{x}) \quad (4.1)$$

$$= \mathbf{C} : \boldsymbol{\varepsilon}(\mathbf{x}) + \boldsymbol{\beta}\Delta T(\mathbf{x}), \quad \boldsymbol{\beta} = -\mathbf{C} : \boldsymbol{\alpha}, \quad (4.2)$$

¹Some developments of this chapter led to the publication “Mean-field homogenization of multi-phase thermo-elastic composites: a general framework and its validation”, Pierard O., Friebel C. and Doghri I., *Composites, Science and Technology*, 64 (2004), pp. 1587-1603 [80].

or equivalently,

$$\boldsymbol{\varepsilon}(\mathbf{x}) = \mathbf{C}^{-1} : \boldsymbol{\sigma}(\mathbf{x}) + \boldsymbol{\varepsilon}^{th}(\mathbf{x}), \quad (4.3)$$

where $\boldsymbol{\varepsilon}^{th}$ is the thermal strain tensor and the double dot $(:)$ designates a tensor product contracted over two indices. The total strain $\boldsymbol{\varepsilon}$ is the sum of the mechanical and thermal strains. The latter is thus a stress free eigenstrain since a variation in temperature does not induce a stress variation. For a general material with no particular symmetry and since the conservation laws must be satisfied, the fourth-order stiffness tensor and the second-order tensor of thermal expansion have only 21 and 6 degrees of freedom, respectively.

For some materials, physical symmetries can be taken into account. A widely encountered material symmetry is transverse isotropy (the material has an axis of isotropy around which any rotation is indistinguishable). In this case, respectively 5 and 2 scalars are necessary to define the stiffness and thermal expansion tensors.

In the particular case of isotropic materials (no preferential direction), stiffness and thermal expansion tensors are depending of only two and one scalars, respectively. Equations (4.1-4.3) are then simplified to:

$$\begin{aligned} \boldsymbol{\sigma}(\mathbf{x}) &= \lambda[\text{tr}(\boldsymbol{\varepsilon}(\mathbf{x}) - \boldsymbol{\varepsilon}^{th}(\mathbf{x}))]\mathbf{1} + 2\mu(\boldsymbol{\varepsilon}(\mathbf{x}) - \boldsymbol{\varepsilon}^{th}(\mathbf{x})), \quad (4.4) \\ \text{where } \boldsymbol{\varepsilon}^{th}(\mathbf{x}) &= \alpha\Delta T(\mathbf{x})\mathbf{1}, \end{aligned}$$

or equivalently,

$$\boldsymbol{\varepsilon}(\mathbf{x}) = \frac{1+\nu}{E}\boldsymbol{\sigma}(\mathbf{x}) - \frac{\nu}{E}[\text{tr}(\boldsymbol{\sigma}(\mathbf{x}))]\mathbf{1} + \boldsymbol{\varepsilon}^{th}(\mathbf{x}), \quad (4.5)$$

where $\mathbf{1}$ is the second-order unit tensor, tr is the trace of a tensor, λ and μ are the Lamé coefficients and α is the coefficient of thermal expansion (CTE). Of course, these are related to the other coefficients classically used in isotropic linear elasticity, i.e. the Young's modulus E , the Poisson's ratio ν , the bulk modulus κ and the shear modulus $G = \mu$.

4.1.2 Linear viscoelasticity

Linear viscoelasticity is another class of linear behavior. A main difference with linear thermo-elasticity is the presence in the response of the material of an explicit time dependence due to a fading memory effect so that it is the sum of an instantaneous initial response and a time-dependent integral. If the initial state is defined at $t = 0$, the constitutive model of linear viscoelasticity reads at each point \mathbf{x} of the homogeneous material:

$$\begin{aligned} \boldsymbol{\sigma}(\mathbf{x}, t) &= \mathbf{G}(t) : \boldsymbol{\varepsilon}(\mathbf{x}, 0) + \int_0^t \mathbf{G}(t - \tau) : \dot{\boldsymbol{\varepsilon}}(\mathbf{x}, \tau) d\tau \\ &= \mathbf{G}(t) : \boldsymbol{\varepsilon}(\mathbf{x}, 0) + \dot{\boldsymbol{\varepsilon}}(\mathbf{x}) \otimes \mathbf{G}, \quad (4.6) \\ \text{where } \boldsymbol{\varepsilon}(\mathbf{x}, 0) &= \lim_{t \rightarrow 0^+} \boldsymbol{\varepsilon}(\mathbf{x}, t) \end{aligned}$$

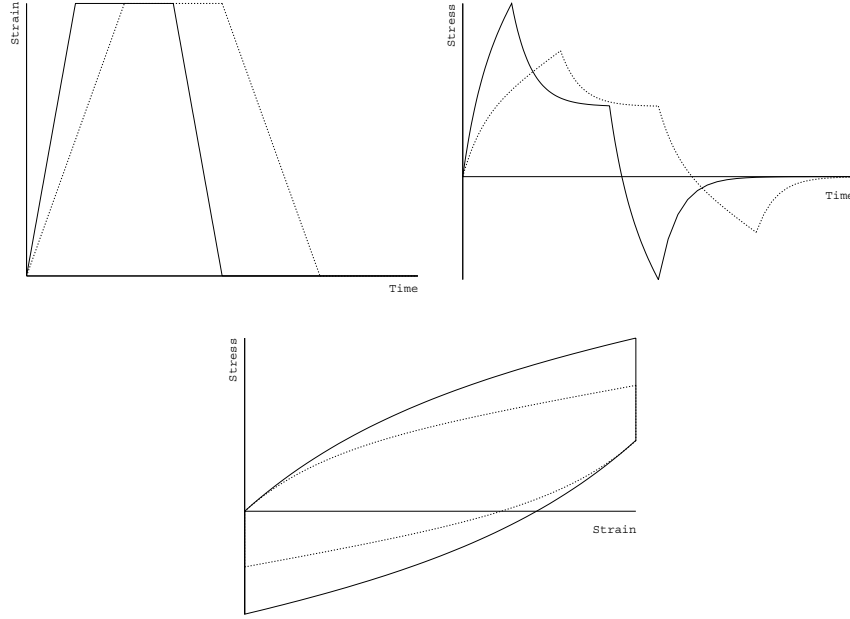


Figure 4.1: Response to a given strain loading path for a linear viscoelastic material.

or equivalently,

$$\begin{aligned}
 \varepsilon(\mathbf{x}, t) &= \mathbf{J}(t) : \boldsymbol{\sigma}(\mathbf{x}, 0) + \int_0^t \mathbf{J}(t - \tau) : \dot{\boldsymbol{\sigma}}(\mathbf{x}, \tau) d\tau \\
 &= \mathbf{J}(t) : \boldsymbol{\sigma}(\mathbf{x}, 0) + \dot{\boldsymbol{\sigma}}(\mathbf{x}) \otimes \mathbf{J}, \quad (4.7) \\
 \text{where } \boldsymbol{\sigma}(\mathbf{x}, 0) &= \lim_{t \rightarrow 0^+} \boldsymbol{\sigma}(\mathbf{x}, t)
 \end{aligned}$$

where \mathbf{G} is the fourth order relaxation tensor, \mathbf{J} the fourth-order creep tensor and \otimes is the classical convolution product which for two scalar functions f and g is defined by:

$$f \otimes g = \int_0^t f(\tau)g(t - \tau)d\tau. \quad (4.8)$$

Once again, simplified expressions of the relaxation and creep tensors exist for isotropic materials (Friebe *et al.* [33]). One-dimensional linear viscoelastic constitutive law and influence of the strain rate are illustrated on figure 4.1 for two different loading paths.

The correspondence principle is a classical way to solve expressions of the form (4.6/4.7) by making use of the Laplace-Carson transform (see appendix

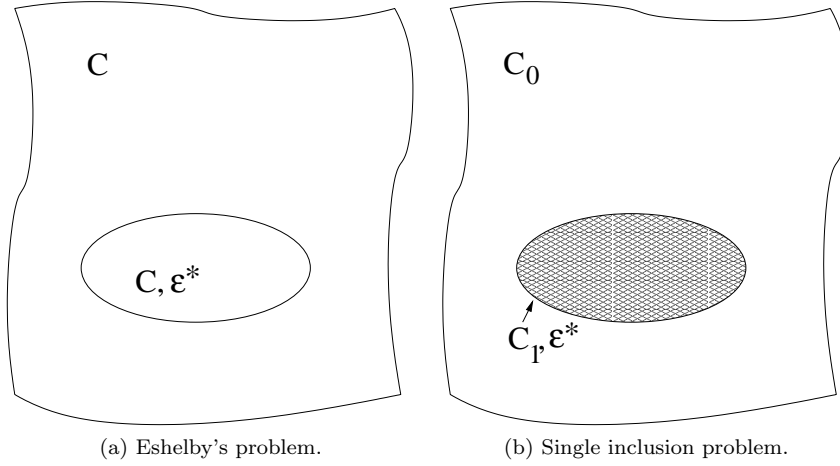


Figure 4.2: Illustration of the results of Eshelby and Hill.

B.1). This enables to eliminate the dependence with respect to $\varepsilon(0)$ and to rewrite these expressions under a linear elastic formalism:

$$\begin{aligned}\sigma^*(s) &= \mathbf{G}^*(s) : \varepsilon^*(s), \\ \varepsilon^*(s) &= \mathbf{J}^*(s) : \sigma^*(s),\end{aligned}\tag{4.9}$$

where f^* is the Laplace-Carson transform of the function f and s is the Laplace variable. If not singular, tensors \mathbf{G}^* and \mathbf{J}^* are inverse of each other.

4.2 Homogenization of isothermal elastic composites

In order to take into account some important geometrical properties (e.g.: shape and orientation of inclusions), several useful homogenization schemes are based on the solution of the Eshelby problem. From this result, the symmetric Hill's tensor is introduced which enables to guarantee some important properties of other tensors. Localization tensors are presented afterwards, from which various homogenization schemes are defined.

4.2.1 Results of Eshelby and Hill

Let us consider a homogeneous linear elastic material of stiffness \mathbf{C} in which an embedded ellipsoidal inclusion made of the same material undergoes an eigenstrain ε^* (figure 4.2a). Eshelby [30] proved that the resulting strain field

inside the inclusion (ε_1) is uniform and related to the eigenstrain through the fourth-order *Eshelby's tensor* \mathcal{E} :

$$\varepsilon_1 = \mathcal{E} : \varepsilon^*. \quad (4.10)$$

In general, \mathcal{E} possesses the minor but not the major symmetries ($\mathcal{E}_{ijkl} = \mathcal{E}_{jikl} = \mathcal{E}_{ijlk}; \mathcal{E}_{ijkl} \neq \mathcal{E}_{klij}$). Analytical formulae of the Eshelby's tensor were introduced by Eshelby [30] for isotropic materials and spheroids (expressions can be found in appendix A.1). Later, Withers [108] extended this result to transversely isotropic medium, with the restriction that the direction of anisotropy is aligned with the revolution direction of the spheroid (see appendix A.2). In all other cases, a numerical evaluation of the tensor is necessary and was implemented by Gavazzi and Lagoudas [34].

The homogeneous stress field σ_1 inside the inclusion is given by:

$$\sigma_1 = \mathbf{C} : \varepsilon_1 + \tau, \quad \tau = -\mathbf{C} : \varepsilon^*. \quad (4.11)$$

The second-order tensor τ is called the *polarization tensor* and is symmetric by construction. Introducing this new tensor into (4.10) gives:

$$\varepsilon_1 = -\mathbf{P} : \tau, \quad \mathbf{P} = \mathcal{E} : \mathbf{C}^{-1}. \quad (4.12)$$

The fourth-order tensor \mathbf{P} is called *Hill's tensor* and relates the eigenstress due to ε^* to the strain in the inclusions.

Let's now consider a single inclusion of stiffness \mathbf{C}_1 undergoing an eigenstrain embedded in a matrix with a different stiffness ($\mathbf{C}_0 = \mathbf{C}_1 - \Delta\mathbf{C}$), see figure 4.2b. Stress and strain are still related through the classical relations:

$$\begin{aligned} \sigma_0 &= \mathbf{C}_0 : \varepsilon_0 \text{ in the matrix,} \\ \sigma_1 &= \mathbf{C}_1 : \varepsilon_1 + \tau_1 \text{ in the inclusion.} \\ &= \mathbf{C}_0 : \varepsilon_1 + \tau_0, \end{aligned} \quad (4.13)$$

where $\tau_0 = \Delta\mathbf{C} : \varepsilon_1 + \tau_1$. Following the hypothesis of Hill that ε_1 is uniform in the inclusions, this relation is form similar to the homogeneous Eshelby's one so that the solution of this inhomogeneous problem is given by:

$$\varepsilon_1 = -\mathbf{P}(\mathbf{C}_0) : \tau_0 \Rightarrow -\tau_1 = (\mathbf{C}^* + \mathbf{C}_1) : \varepsilon_1; \quad \mathbf{C}^* = \mathbf{P}^{-1} - \mathbf{C}_0. \quad (4.14)$$

This new fourth-order tensor \mathbf{C}^* is called *Hill's constraint tensor* and characterizes the stress acting on an inclusion by the infinite medium independently of the properties of the inclusion: $\sigma_1 = -\mathbf{C}^* : \varepsilon_1$. Tensor \mathbf{C}^* possesses the minor symmetries by construction. In order to prove the major symmetries of this tensor, let's consider two different systems of loads (forces by unit of area) $F_i^{(1)}$ and $F_i^{(2)}$ acting of the interface inclusion/matrix of the single inclusion problem (figure 4.2b). These loads induce two different displacement fields, $u_i^{(1)}$ and

$u_i^{(2)}$, respectively. The Maxwell-Betti theorem gives the following equivalence of works:

$$\int_{\partial\omega} F_i^{(1)} u_i^{(2)} dS = \int_{\partial\omega} F_i^{(2)} u_i^{(1)} dS, \quad (4.15)$$

where $\partial\omega$ is the interface surface. By using the definition of the constraint tensor, expression (4.15) can be rewritten as:

$$\int_{\partial\omega} -C_{ijkl}^* \epsilon_{lk}^{(1)} n_j u_i^{(2)} dS = \int_{\partial\omega} -C_{ijkl}^* \epsilon_{lk}^{(2)} n_j u_i^{(1)} dS. \quad (4.16)$$

Since \mathbf{C}^* has the minor symmetries, following relations hold:

$$\begin{aligned} \int_{\partial\omega} -C_{ijkl}^* \epsilon_{lk}^{(1)} n_j u_i^{(2)} dS &= \int_{\omega} -C_{ijkl}^* \epsilon_{lk}^{(1)} \frac{\partial u_i^{(2)}}{\partial x_j} dV \\ &= \int_{\omega} -C_{jikl}^* \epsilon_{lk}^{(1)} \frac{\partial u_j^{(2)}}{\partial x_i} dV. \end{aligned} \quad (4.17)$$

Expression (4.16) can be rewritten as:

$$\begin{aligned} \int_{\omega} C_{ijkl}^* \epsilon_{lk}^{(1)} \epsilon_{ij}^{(2)} dV &= \int_{\omega} C_{ijkl}^* \epsilon_{lk}^{(2)} \epsilon_{ij}^{(1)} \\ &= \int_{\omega} C_{klij}^* \epsilon_{lk}^{(1)} \epsilon_{ij}^{(2)} dV. \end{aligned} \quad (4.18)$$

Last relation is true for any load system $F^{(1)}$ and $F^{(2)}$. So, in order to satisfy this last relation, major symmetries are required:

$$C_{ijkl}^* = C_{klij}^*. \quad (4.19)$$

Consequently, \mathbf{P} is also fully symmetric.

4.2.2 Expressions of localization tensors

In sections 2.1 and 2.2, the definition of a representative volume element has been given as well as a presentation of various boundary conditions to apply if either macroscopic stress or macroscopic strain is given. Localization expressions in linear elasticity are examined and resulting macroscopic relations are obtained accordingly. Developments in this section follow Zaoui [110].

Concentration tensors enable to link a local property to the corresponding macroscopic one. For example, given a macroscopic strain, the corresponding macroscopic stress writes:

$$\bar{\boldsymbol{\sigma}}(\bar{\boldsymbol{\varepsilon}}) = \langle \boldsymbol{\sigma}(\boldsymbol{\varepsilon}(\mathbf{x})) \rangle = \langle \boldsymbol{\sigma}(\mathbf{D}^\varepsilon(\mathbf{x}) : \bar{\boldsymbol{\varepsilon}}) \rangle, \quad (4.20)$$

where the strain concentration tensor \mathbf{D}^ε relates the local strain at any point of the RVE to the macroscopic one:

$$\varepsilon(\mathbf{x}) = \mathbf{D}^\varepsilon(\mathbf{x}) : \bar{\varepsilon}. \quad (4.21)$$

Each point of the RVE belongs to phase r whose behavior is given by a linear elastic relation as:

$$\boldsymbol{\sigma}(\mathbf{x}) = \mathbf{C}_r : \varepsilon(\mathbf{x}), \quad (4.22)$$

where point \mathbf{x} belongs to phase r of uniform stiffness \mathbf{C}_r .

For any heterogeneous material made of linear elastic constituents, the following macroscopic relation holds (proved by using the Hill's Lemma):

$$\bar{\boldsymbol{\sigma}} = \mathbf{C}^{\text{eff}} : \bar{\varepsilon}, \quad (4.23)$$

where \mathbf{C}^{eff} is the effective stiffness tensor. The macroscopic stress computed from the volume average of the stress microfield becomes:

$$\bar{\boldsymbol{\sigma}} = \langle \boldsymbol{\sigma}(\mathbf{x}) \rangle = \langle \mathbf{C}_r : \varepsilon(\mathbf{x}) \rangle = \langle \mathbf{C}_r : \mathbf{D}^\varepsilon(\mathbf{x}) \rangle : \bar{\varepsilon} = \bar{\mathbf{C}} : \bar{\varepsilon}. \quad (4.24)$$

Hypothesis on the strain concentration tensors \mathbf{D}^ε give a $\bar{\mathbf{C}}$ which is either an estimation or a bound of the effective stiffness \mathbf{C}^{eff} and represents a macroscopically homogeneous material with an equivalent behavior to the one of the heterogeneous RVE.

4.2.3 Various homogenization schemes

In this section, a two-phase isothermal linear elastic composite with a uniform stiffness \mathbf{C}_0 for the matrix and \mathbf{C}_1 for the inclusions (subscript 0 always refers to the matrix and 1 to the inclusions) is considered. The RVE is subjected to linear boundary displacements corresponding to a macroscopic strain $\bar{\varepsilon}$ so that per phase strain averages are related between each others and to $\bar{\varepsilon}$ through a (still unknown) strain concentration tensor \mathbf{B}^ε :

$$\begin{aligned} \langle \varepsilon \rangle_{\omega_1} &= \mathbf{B}^\varepsilon : \langle \varepsilon \rangle_{\omega_0}, & \langle \varepsilon \rangle_{\omega_1} &= \mathbf{A}^\varepsilon : \bar{\varepsilon}, \\ \mathbf{A}^\varepsilon &= \mathbf{B}^\varepsilon : (v_1 \mathbf{B}^\varepsilon + (1 - v_1) \mathbf{I})^{-1}, & \mathbf{B}^\varepsilon &= (1 - v_1) \mathbf{A}^\varepsilon : (\mathbf{I} - v_1 \mathbf{A}^\varepsilon)^{-1}, \end{aligned} \quad (4.25)$$

where \mathbf{I} designates the fourth-order symmetric identity tensor and \mathbf{A}^ε is the strain concentration tensor linking the average strain in the inclusions to the macroscopic one. For any homogenization model defined by \mathbf{B}^ε , the macroscopic stiffness is given by:

$$\bar{\mathbf{C}} = [v_1 \mathbf{C}_1 : \mathbf{B}^\varepsilon + (1 - v_1) \mathbf{C}_0] : [v_1 \mathbf{B}^\varepsilon + (1 - v_1) \mathbf{I}]^{-1} \quad (4.26)$$

$$= [v_1 (\mathbf{C}^* + \mathbf{C}_1)^{-1} + (1 - v_1) (\mathbf{C}^* + \mathbf{C}_0)^{-1}]^{-1} - \mathbf{C}^*, \quad (4.27)$$

$$= \mathbf{C}_0 + v_1 (\mathbf{C}_1 - \mathbf{C}_0) : \mathbf{A}^\varepsilon. \quad (4.28)$$

Since the Hill's constraint tensor \mathbf{C}^* is fully symmetric, expression (4.27) imposes that the macroscopic tangent operator is also fully symmetric. This is a very important property since, as we will see in elasto-plastic simulations, some approximations of the matrix modulus might lead to the loss of major symmetries and finally give non physical results. Hypothesis on the strain concentration tensor defines an homogenization scheme so that the composite behavior can be predicted. On the contrary to basic models of Voigt and Reuss, more elaborated mean-field homogenization schemes rely on the solution of the Eshelby's problem. In addition to the volume fraction of each phase, they take into account of the shape and the orientation of the RVE constituents. However, due to the Eshelby's hypothesis, the inclusions must have an ellipsoidal shape as well as the same aspect ratio and orientation². Otherwise, the composite is considered as a multi phase material (Pierard *et al.* [80]).

Voigt and Reuss models

Assuming a uniform strain within the RVE, the following results are immediately found:

$$\mathbf{B}^\varepsilon = \mathbf{I}, \quad \bar{\mathbf{C}} = v_1 \mathbf{C}_1 + (1 - v_1) \mathbf{C}_0. \quad (4.29)$$

This is known as the Voigt homogenization model and the effective moduli are thus the volume average of the per phase uniform local stiffnesses. Even with such a big approximation, the Voigt model gives good predictions in the longitudinal direction of materials reinforced by long fibers.

Another obvious hypothesis is to consider uniform stress within the RVE. Consequently, the following expressions are found:

$$\mathbf{B}^\varepsilon = \mathbf{C}_1^{-1} : \mathbf{C}_0, \quad \bar{\mathbf{C}} = [v_1 \mathbf{C}_1^{-1} + (1 - v_1) \mathbf{C}_0^{-1}]^{-1}. \quad (4.30)$$

This result is known as the Reuss homogenization model and the effective compliance is thus simply the volume average of the per phase uniform ones.

Mori-Tanaka model

The Mori-Tanaka model tries to take into account interactions between the inclusions. Since this model is intensively used in the numerical simulations of this work, derivation of the strain concentration tensor is briefly recalled.

Let's define a companion problem to the original one over the RVE in which the inclusions are made of the same material as the one of the matrix and undergo an eigenstrain ε^* (figure 4.3b). This fictitious material, as in the original problem, is subjected to linear displacements imposed at infinity which

²Note that we consider the same inclusion geometry in the original material and the associated single inclusion problem without taking into account the inclusions spatial distribution (see Bornert [11] and Ponte Castañeda and Willis [87] for more details).

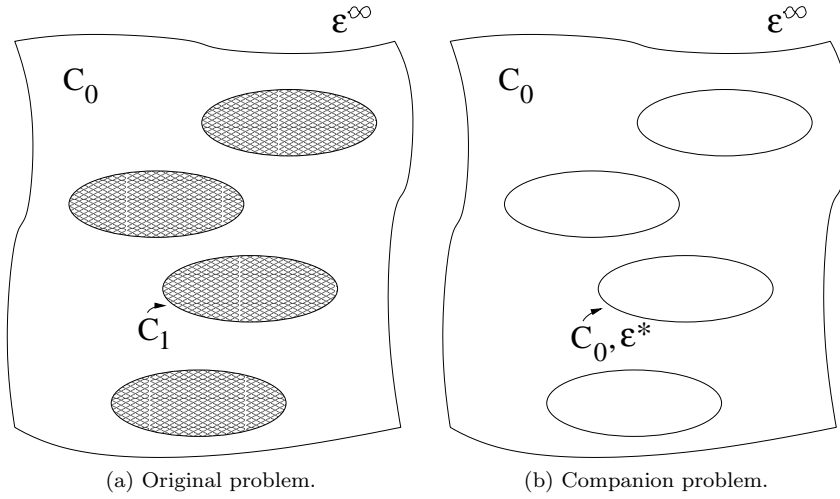


Figure 4.3: The two problems of the Mori-Tanaka homogenization scheme.

induce a uniform strain within both matrix and inclusions. With the help of the Eshelby's result and superposition principle, strain and stress in the inclusions of the companion problem are given by:

$$\boldsymbol{\varepsilon}_1 = \boldsymbol{\varepsilon}^\infty + \boldsymbol{\mathcal{E}} : \boldsymbol{\varepsilon}^* + \boldsymbol{\varepsilon}'(\mathbf{x}), \quad \boldsymbol{\sigma}_1 = \mathbf{C}_0 : (\boldsymbol{\varepsilon}^\infty + \boldsymbol{\mathcal{E}} : \boldsymbol{\varepsilon}^* + \boldsymbol{\varepsilon}'(\mathbf{x}) - \boldsymbol{\varepsilon}^*), \quad (4.31)$$

where $\boldsymbol{\varepsilon}'(\mathbf{x})$ is the sum of all the strain fields caused by the presence of each inclusion. Strain and stress equivalence in both phases between the companion and the original problem (inclusion's stiffness \mathbf{C}_1 and no eigenstrain, figure 4.3a) is satisfied if the same strain in the inclusions of both problems is imposed and:

$$\mathbf{C}_0 : (\boldsymbol{\varepsilon}^\infty + \boldsymbol{\mathcal{E}} : \boldsymbol{\varepsilon}^* + \boldsymbol{\varepsilon}'(\mathbf{x}) - \boldsymbol{\varepsilon}^*) = \mathbf{C}_1 : (\boldsymbol{\varepsilon}^\infty + \boldsymbol{\mathcal{E}} : \boldsymbol{\varepsilon}^* + \boldsymbol{\varepsilon}'(\mathbf{x})). \quad (4.32)$$

Such condition cannot be fulfilled at each point of the material. However, a solution exists if an average over all the inclusions is considered:

$$\mathbf{C}_0 : (\boldsymbol{\varepsilon}^\infty + \boldsymbol{\mathcal{E}} : \boldsymbol{\varepsilon}^* + \langle \boldsymbol{\varepsilon}'(\mathbf{x}) \rangle_{\omega_1} - \boldsymbol{\varepsilon}^*) = \mathbf{C}_1 : (\boldsymbol{\varepsilon}^\infty + \boldsymbol{\mathcal{E}} : \boldsymbol{\varepsilon}^* + \langle \boldsymbol{\varepsilon}'(\mathbf{x}) \rangle_{\omega_1}).$$

Equivalence is fulfilled for the following expression of the eigenstrain:

$$\boldsymbol{\varepsilon}^* = - [(\mathbf{C}_0^{-1} : \mathbf{C}_1 - \mathbf{I})^{-1} + \boldsymbol{\mathcal{E}}]^{-1} : (\boldsymbol{\varepsilon}^\infty + \langle \boldsymbol{\varepsilon}'(\mathbf{x}) \rangle_{\omega_1}). \quad (4.33)$$

Combining this expression with the one of the average strain in the inclusions gives:

$$\langle \boldsymbol{\varepsilon} \rangle_{\omega_1} = \left[\mathbf{I} - \boldsymbol{\mathcal{E}} : ((\mathbf{C}_0^{-1} : \mathbf{C}_1 - \mathbf{I})^{-1} + \boldsymbol{\mathcal{E}})^{-1} \right] : (\boldsymbol{\varepsilon}^\infty + \langle \boldsymbol{\varepsilon}'(\mathbf{x}) \rangle_{\omega_1}). \quad (4.34)$$

This expression is valid if Eshelby's tensor is the same for all the inclusions, i.e. all the inclusions are similarly shaped and aligned. Due to the infinite number of inclusions randomly dispersed in the RVE, we can say that the disturbance field $\boldsymbol{\varepsilon}'(\mathbf{x})$ is, on average, the same in the inclusions and in the matrix so that average strain in the matrix can be rewritten as:

$$\langle \boldsymbol{\varepsilon} \rangle_{\omega_0} = \boldsymbol{\varepsilon}^\infty + \langle \boldsymbol{\varepsilon}'(\mathbf{x}) \rangle_{\omega_0} = \boldsymbol{\varepsilon}^\infty + \langle \boldsymbol{\varepsilon}'(\mathbf{x}) \rangle_{\omega_1}. \quad (4.35)$$

Inserting this result into (4.34), expression of the strain concentration tensor linking the average strain in the inclusion to the one in the matrix is given by:

$$\begin{aligned} \mathbf{B}^\varepsilon &= [\mathbf{I} + \boldsymbol{\varepsilon} : (\mathbf{C}_0^{-1} : \mathbf{C}_1 - \mathbf{I})]^{-1} = \mathbf{B}_{\text{M-T}}(\mathbf{C}_0, \mathbf{C}_1) \\ &= [\mathbf{I} + \mathbf{P} : (\mathbf{C}_1 - \mathbf{C}_0)]^{-1} \end{aligned} \quad (4.36)$$

$$= (\mathbf{C}^* + \mathbf{C}_1)^{-1} : (\mathbf{C}^* + \mathbf{C}_0). \quad (4.37)$$

This is the same result as the one obtained for a matrix reinforced by a single inclusion undergoing uniform strain at infinity. Consequently, Benveniste [7] proposed the following interpretation: "each inclusion behaves like an isolated inclusion in the matrix seeing $\langle \boldsymbol{\varepsilon} \rangle_{\omega_0}$ as a far-field strain". The Mori-Tanaka model is particularly suitable for particle reinforced composite materials up to moderate volume fractions (25-30%).

For higher volume fractions, Lielens [62] proposed an extension of this model which combines a nonlinear interpolation between the original Mori-Tanaka model and the one considering reverse material properties (which corresponds to the second Hashin-Shtrikman-Willis bound [107], see section 4.2.4). The strain concentration tensor then reads:

$$\mathbf{B}^\varepsilon = [(1 - f(v_1))\mathbf{B}_{\text{M-T}}^{-1}(\mathbf{C}_0, \mathbf{C}_1) + f(v_1)\mathbf{B}_{\text{M-T}}(\mathbf{C}_1, \mathbf{C}_0)]^{-1}. \quad (4.38)$$

The proposed interpolative function is $f(v_1) = (v_1 + v_1^2)/2$. This homogenization scheme is called Lielens' *interpolative model*.

Self-consistent model

The self-consistent model (S-C) assumes that each inclusion is isolated and embedded in a fictitious homogeneous matrix possessing the composite's unknown stiffness $\bar{\mathbf{C}}$ seeing $\bar{\boldsymbol{\varepsilon}}$ as a far-field strain. This problem thus becomes similar to the one of the single inclusion problem and the strain concentration reads:

$$\langle \boldsymbol{\varepsilon} \rangle_{\omega_1} = \mathbf{B}_{\text{M-T}}(\bar{\mathbf{C}}, \mathbf{C}_1) : \bar{\boldsymbol{\varepsilon}} = \mathbf{A}^\varepsilon(\bar{\mathbf{C}}, \mathbf{C}_1) : \bar{\boldsymbol{\varepsilon}}. \quad (4.39)$$

The localization problem becomes implicit ($\bar{\mathbf{C}}$ is computed from the strain concentration tensor \mathbf{A}^ε , see (4.28)) and requires an additional iterative loop in order to determine $\bar{\mathbf{C}}$. Strain concentration tensors are given by:

$$\mathbf{B}^\varepsilon = (1 - v_1)\mathbf{A}^\varepsilon : (\mathbf{I} - v_1\mathbf{A}^\varepsilon)^{-1}, \quad \mathbf{A}^\varepsilon = [\mathbf{I} + \boldsymbol{\varepsilon} : (\bar{\mathbf{C}}^{-1} : \mathbf{C}_1 - \mathbf{I})]^{-1}. \quad (4.40)$$

The self-consistent model generally gives good predictions for polycrystals but is less satisfying in the case of two-phase composites.

4.2.4 Some bounds

All the previous models give estimates for the effective moduli of the equivalent homogeneous material. However, given information on the phase modulus and geometry of the microstructure, bounds can be derived from the minimum principle for elastic media. Following Zaoui [110], if linear displacement boundary conditions are imposed, among all the strain fields $\boldsymbol{\varepsilon}^*$ which satisfy these conditions, the average microscopic work of the real solution $\boldsymbol{\varepsilon}$ to the boundary value problem is always smaller (position dependence is omitted for clarity):

$$\langle \boldsymbol{\varepsilon}^* : \mathbf{C} : \boldsymbol{\varepsilon}^* \rangle \geq \langle \boldsymbol{\varepsilon} : \mathbf{C} : \boldsymbol{\varepsilon} \rangle. \quad (4.41)$$

Similarly, if uniform tractions are imposed, this reads:

$$\langle \boldsymbol{\sigma}^* : \mathbf{S} : \boldsymbol{\sigma}^* \rangle \geq \langle \boldsymbol{\sigma} : \mathbf{S} : \boldsymbol{\sigma} \rangle. \quad (4.42)$$

Making use of Hill's lemma and introducing the strain concentration tensor \mathbf{D}^ε ($\boldsymbol{\varepsilon}^*(x) = \mathbf{D}^\varepsilon(x) : \bar{\boldsymbol{\varepsilon}}$) and the stress concentration tensor \mathbf{D}^σ ($\boldsymbol{\sigma}^*(x) = \mathbf{D}^\sigma(x) : \bar{\boldsymbol{\sigma}}$), these two equations can be rewritten as:

$$\begin{aligned} \bar{\boldsymbol{\varepsilon}} : (\langle \mathbf{D}^{\varepsilon^T} : \mathbf{C} : \mathbf{D}^\varepsilon \rangle - \mathbf{C}^{eff}) : \bar{\boldsymbol{\varepsilon}} &\geq 0 \quad \forall \bar{\boldsymbol{\varepsilon}}, \\ \bar{\boldsymbol{\sigma}} : (\langle \mathbf{D}^{\sigma^T} : \mathbf{S} : \mathbf{D}^\sigma \rangle - \mathbf{S}^{eff}) : \bar{\boldsymbol{\sigma}} &\geq 0 \quad \forall \bar{\boldsymbol{\sigma}}. \end{aligned} \quad (4.43)$$

From these expressions, bounds can be derived. A basic hypothesis is to consider a uniform strain field which respects linear displacement boundary conditions. This leads to the Voigt bound on the effective moduli:

$$\bar{\boldsymbol{\varepsilon}} : (\langle \mathbf{C} \rangle - \mathbf{C}^{eff}) : \bar{\boldsymbol{\varepsilon}} \geq 0 \quad \forall \bar{\boldsymbol{\varepsilon}}. \quad (4.44)$$

Similarly, for a uniform stress field which respects uniform traction boundary conditions, the Reuss bound is found:

$$\bar{\boldsymbol{\sigma}} : (\langle \mathbf{S} \rangle - \mathbf{S}^{eff}) : \bar{\boldsymbol{\sigma}} \geq 0 \quad \forall \bar{\boldsymbol{\sigma}}. \quad (4.45)$$

If materials are isotropic, these relations can be reduced to much more interesting bounds on the effective shear (μ^{eff}) and bulk (κ^{eff}) moduli:

$$\langle \mu^{-1} \rangle^{-1} \leq \mu^{eff} \leq \langle \mu \rangle, \quad \langle \kappa^{-1} \rangle^{-1} \leq \kappa^{eff} \leq \langle \kappa \rangle. \quad (4.46)$$

Voigt/Reuss bounds can be improved, as shown in Hashin and Shtrikman [38] for overall isotropic materials. This was later extended to anisotropic constituents, anisotropic phase arrangements and/or aligned non spherical arrangements (Walpole [102], Willis [107]). In general, the Mori-Tanaka estimate

correspond to one of the extended Hashin-Shtrikman bounds for two-phase materials (Weng [105]). The other one can be obtained with a Mori-Tanaka estimate of a fictitious material with reverse material properties. Better bounds have been developed, but this requires additional hypotheses on the geometry (Bornert *et al.* [12], Hervé and Zaoui [39, 40]). A more recent work which gives very close bounds is the second-order method of Torquato [99].

4.3 Homogenization of thermo-elastic composites

4.3.1 Homogenization technique

Consider a two-phase composite, where the matrix has uniform properties \mathbf{C}_0 and $\boldsymbol{\alpha}_0$, and the inclusions have the same aspect ratio, orientation and properties \mathbf{C}_1 and $\boldsymbol{\alpha}_1$. Relations (4.1-4.3) hold for each phase; our aim is to write similar macroscopic relations for the whole composite. In order to determine the macroscopic properties $\bar{\mathbf{C}}$ and $\bar{\boldsymbol{\alpha}}$, one can re-derive a homogenization model taking into account thermo-elastic behavior instead of isothermal elasticity. A better alternative is proposed in Lielens [61]. Its major interest is that given any homogenization model which is defined in the isothermal case by its strain concentration tensor \mathbf{B}^ϵ (or \mathbf{A}^ϵ), general expressions of the macroscopic thermo-elastic properties can be found³. For this, linear displacement boundary conditions corresponding to a macroscopic total strain $\bar{\boldsymbol{\epsilon}} = \langle \boldsymbol{\epsilon} \rangle$ and uniform temperature change ΔT are assumed. The proof is based on the following three-step approach.

First step

In this step, the composite is subjected to linear boundary displacements corresponding to the final total strain $\boldsymbol{\epsilon}^{s1} = \bar{\boldsymbol{\epsilon}}$ and to zero change in temperature $\Delta T^{s1} = 0$. This step corresponds to a classical isothermal transformation whose solution is given in section 4.2.3. The per phase strain averages are found as follows:

$$\langle \boldsymbol{\epsilon}^{s1} \rangle_{\omega_1} = \mathbf{A}^\epsilon : \bar{\boldsymbol{\epsilon}}, \quad v_1 \langle \boldsymbol{\epsilon}^{s1} \rangle_{\omega_1} + (1 - v_1) \langle \boldsymbol{\epsilon}^{s1} \rangle_{\omega_0} = \bar{\boldsymbol{\epsilon}}, \quad (4.47)$$

where \mathbf{A}^ϵ is given by equation (4.25) and its expression depends on the chosen homogenization model. The stress averages are given by:

$$\langle \boldsymbol{\sigma}^{s1} \rangle_{\omega_1} = \mathbf{C}_1 : \langle \boldsymbol{\epsilon}^{s1} \rangle_{\omega_1}, \quad \langle \boldsymbol{\sigma}^{s1} \rangle_{\omega_0} = \mathbf{C}_0 : \langle \boldsymbol{\epsilon}^{s1} \rangle_{\omega_0}. \quad (4.48)$$

³An alternative if the macroscopic stiffness is known consists of using the Levin's theorem [55]: $\bar{\boldsymbol{\beta}} = ((1 - v_1)\boldsymbol{\beta}_0 + v_1\boldsymbol{\beta}_1) + (\bar{\mathbf{C}} - (1 - v_1)\boldsymbol{\beta}_0 - v_1\boldsymbol{\beta}_1) : (\mathbf{C}_1 - \mathbf{C}_0)^{-1} : (\boldsymbol{\beta}_1 - \boldsymbol{\beta}_0)$.

Second step

In this step, the RVE witnesses a uniform temperature increment equal to the final temperature change $\Delta T^{s2} = \Delta T$, and incremental boundary linear displacements corresponding to a macroscopic strain increment $\Delta \bar{\epsilon}^{s2}$ are imposed so that uniform strain and stress increments are obtained:

$$\Delta \sigma^{s2} = \mathbf{C}_0 : \Delta \bar{\epsilon}^{s2} + \beta_0 \Delta T = \mathbf{C}_1 : \Delta \bar{\epsilon}^{s2} + \beta_1 \Delta T. \quad (4.49)$$

This allows to compute the uniform total strain increment:

$$\Delta \bar{\epsilon}^{s2} = -(\mathbf{C}_1 - \mathbf{C}_0)^{-1} : (\beta_1 - \beta_0) \Delta T. \quad (4.50)$$

Third step

In this step, the composite is subjected to linear boundary displacements corresponding to a macroscopic total strain increment $\Delta \bar{\epsilon}^{s3}$ and to zero temperature increment $\Delta T^{s3} = 0$. This is a classical isothermal transformation whose solution is given in section 4.2.3 as follows:

$$\langle \Delta \epsilon^{s3} \rangle_{\omega_1} = \mathbf{A}^\epsilon : \Delta \bar{\epsilon}^{s3}, \quad v_1 \langle \Delta \epsilon^{s3} \rangle_{\omega_1} + (1 - v_1) \langle \Delta \epsilon^{s3} \rangle_{\omega_0} = \Delta \bar{\epsilon}^{s3},$$

where \mathbf{A}^ϵ is given by equation (4.25). The per-phase stress averages are given by:

$$\langle \Delta \sigma^{s3} \rangle_{\omega_1} = \mathbf{C}_1 : \langle \Delta \epsilon^{s3} \rangle_{\omega_1}, \quad \langle \Delta \sigma^{s3} \rangle_{\omega_0} = \mathbf{C}_0 : \langle \Delta \epsilon^{s3} \rangle_{\omega_0}. \quad (4.51)$$

Superposition

Using the superposition theorem, it is seen that at the end of the three steps, the per-phase strain averages are given by:

$$\langle \epsilon \rangle_{\omega_1} = \mathbf{A}^\epsilon : (\bar{\epsilon} + \Delta \bar{\epsilon}^{s3}) + \Delta \bar{\epsilon}^{s2} \quad (4.52)$$

$$v_1 \langle \epsilon \rangle_{\omega_1} + (1 - v_1) \langle \epsilon \rangle_{\omega_0} = \bar{\epsilon} + \Delta \bar{\epsilon}^{s2} + \Delta \bar{\epsilon}^{s3}, \quad (4.53)$$

where $\Delta \bar{\epsilon}^{s2}$ is given by equation (4.50). At the end of the three steps, the RVE is subjected to a uniform temperature change ΔT and linear boundary displacements corresponding to a macroscopic total strain $\bar{\epsilon} + \Delta \bar{\epsilon}^{s2} + \Delta \bar{\epsilon}^{s3}$. However, the latter value should be equal to $\bar{\epsilon}$, therefore we have:

$$\Delta \bar{\epsilon}^{s3} = -\Delta \bar{\epsilon}^{s2}. \quad (4.54)$$

Consequently, the per-phase strain averages can be computed from equations (4.50) and (4.52-4.53), the per-phase stress averages from equations (4.48 - 4.49) and (4.51), and the stress average over the RVE by superposition,

$$\begin{aligned} \langle \sigma \rangle &= \Delta \sigma^{s2} + (1 - v_1) (\langle \sigma^{s1} \rangle_{\omega_0} + \langle \Delta \sigma^{s3} \rangle_{\omega_0}), \\ &+ v_1 (\langle \sigma^{s1} \rangle_{\omega_1} + \langle \Delta \sigma^{s3} \rangle_{\omega_1}). \end{aligned} \quad (4.55)$$

Final expressions

Carrying out the computations and rearranging terms, the following expressions for the total strain averages are found:

$$\begin{aligned} \langle \boldsymbol{\varepsilon} \rangle_{\omega_1} &= \mathbf{A}^\varepsilon : \bar{\boldsymbol{\varepsilon}} + \mathbf{a}^\varepsilon \Delta T, \\ \mathbf{a}^\varepsilon &= (\mathbf{A}^\varepsilon - \mathbf{I}) : (\mathbf{C}_1 - \mathbf{C}_0)^{-1} : (\boldsymbol{\beta}_1 - \boldsymbol{\beta}_0), \end{aligned} \quad (4.56)$$

$$v_1 \langle \boldsymbol{\varepsilon} \rangle_{\omega_1} + (1 - v_1) \langle \boldsymbol{\varepsilon} \rangle_{\omega_0} = \bar{\boldsymbol{\varepsilon}}, \quad (4.57)$$

where \mathbf{A}^ε is defined in equation (4.25). Similarly to (4.2), it is found that the macroscopic thermo-elastic response is written under the following format:

$$\langle \boldsymbol{\sigma} \rangle = \bar{\mathbf{C}} : \bar{\boldsymbol{\varepsilon}} + \bar{\boldsymbol{\beta}} \Delta T; \quad \bar{\boldsymbol{\beta}} = (1 - v_1)\boldsymbol{\beta}_0 + v_1\boldsymbol{\beta}_1 + v_1(\mathbf{C}_1 - \mathbf{C}_0) : \mathbf{a}^\varepsilon, \quad (4.58)$$

where the macroscopic stiffness $\bar{\mathbf{C}}$ is given by the isothermal expression (4.26), \mathbf{a}^ε by equation (4.56) and the macroscopic thermal expansion $\bar{\boldsymbol{\alpha}}$ is defined as follows:

$$\bar{\boldsymbol{\alpha}} = -\bar{\mathbf{C}}^{-1} : \bar{\boldsymbol{\beta}}. \quad (4.59)$$

In conclusion, generic expressions for thermo-elastic properties are obtained for any homogenization model defined in the isothermal case by its strain concentration tensor \mathbf{B}^ε (or equivalently \mathbf{A}^ε).

Special case.

When the two phases have identical stiffness operators ($\mathbf{C}_0 = \mathbf{C}_1 \equiv \mathbf{C}$), equations (4.56) and (4.58) become invalid. Lielens [61] suggests the following solution. In the previous three-step method, step 1 remains unchanged and steps 2 and 3 are replaced by one single step in which the RVE is subjected to a uniform temperature change $\Delta T^{s2} = \Delta T$ and zero boundary displacements corresponding to zero macroscopic total strain $\Delta \bar{\boldsymbol{\varepsilon}}^{s2} = 0$. The average stress is then:

$$\begin{aligned} \langle \Delta \boldsymbol{\sigma}^{s2} \rangle &= (1 - v_1) \langle \mathbf{C} : \Delta \boldsymbol{\varepsilon}^{s2} + \boldsymbol{\beta}_0 \Delta T \rangle_{\omega_0} \\ &\quad + v_1 \langle \mathbf{C} : \Delta \boldsymbol{\varepsilon}^{s2} + \boldsymbol{\beta}_1 \Delta T \rangle_{\omega_1} \\ &= \mathbf{C} : \Delta \bar{\boldsymbol{\varepsilon}}^{s2} + [(1 - v_1)\boldsymbol{\beta}_0 + v_1\boldsymbol{\beta}_1] \Delta T \\ &= ((1 - v_1)\boldsymbol{\beta}_0 + v_1\boldsymbol{\beta}_1) \Delta T. \end{aligned} \quad (4.60)$$

Superposition of steps 1 and 2 shows then that:

$$\langle \boldsymbol{\sigma} \rangle = \bar{\mathbf{C}} : \bar{\boldsymbol{\varepsilon}} + \bar{\boldsymbol{\beta}} \Delta T; \quad \bar{\boldsymbol{\beta}} = (1 - v_1)\boldsymbol{\beta}_0 + v_1\boldsymbol{\beta}_1. \quad (4.61)$$

where the macroscopic stiffness $\bar{\mathbf{C}}$ is given by the isothermal expression (4.26).

4.3.2 Numerical simulations

In this section, macroscopic predictions are compared with experimental data and FE results obtained either on a RVE or a unit cell.

Influence of the inclusion's shape

Consider a thermo-elastic composite made of a polymer matrix ($E_0 = 3.0$ GPa, $\nu_0 = 0.35$ and $\alpha_0 = 70 \times 10^{-6} K^{-1}$) reinforced with aligned inclusions ($E_1 = 172.0$ GPa, $\nu_1 = 0.2$ and $\alpha_1 = 10^{-6} K^{-1}$). Notice the high contrast between Young's moduli and CTEs. A uniaxial traction test is simulated in the direction of the revolution axis of the inclusions.

M-T predictions of the CTE are confronted with those of van Es [101]. The latter model is based on a simplified two-phase composite which is a superposition of a layer made of the matrix material and another one made of the inclusions material. The interaction between the inclusions is thus not directly taken into account. However, in this formulation appears the homogenized stiffness tensor of linear elasticity which might be calculated previously through a classical M-T approach. Results of the predictions of the macroscopic CTE in the longitudinal direction are reported on figure 4.4 for various volume fractions of the inclusions and various aspect ratios. Both methods give very similar results. Logically, since the matrix has a higher CTE than the inclusions, the longitudinal CTE will be higher for platelets (i.e. small Ar) than for fibers (i.e. high Ar).

Comparison of various predictive methods

Short glass fiber reinforced composite is now considered ($E_1 = 72.5$ GPa, $\nu_1 = 0.2$, $\alpha_1 = 4.9 \times 10^{-6} K^{-1}$, $A_r = 35.58$ and $v_1 = 8\%$). The matrix characteristics are: $E_0 = 1.57$ GPa, $\nu_0 = 0.335$ and $\alpha_0 = 108.3 \times 10^{-6} K^{-1}$.

A uniaxial tension test is performed in a direction aligned with the fibers. Predictions with the M-T and interpolative models of the macroscopic longitudinal and transverse Young's moduli and CTE are confronted with experimental data found in Lusti *et al.* [65]. In that paper, several simplified methods are also used and recalled hereafter. McCullough's model predicts the macroscopic characteristics directly. Two microscopic approaches were proposed by Takao and Taya [98]. The first one is a simple second order average of the longitudinal and transverse CTE (noted hereafter Takao-Taya/aggregate). The second one, proposed by Tandon and Weng tried to include elastic constraints. This approach is noted Tandon-Weng/laminate hereafter. Comparison of all these approaches with our mean-field homogenization predictions of the macroscopic properties is reported in table 4.1. Note that for the predictions made with homogenization schemes, aspect ratios of the fibers are multiplied by 1.25 in order to try to model the cylinders by spheroids, as proposed by Li and Ponte

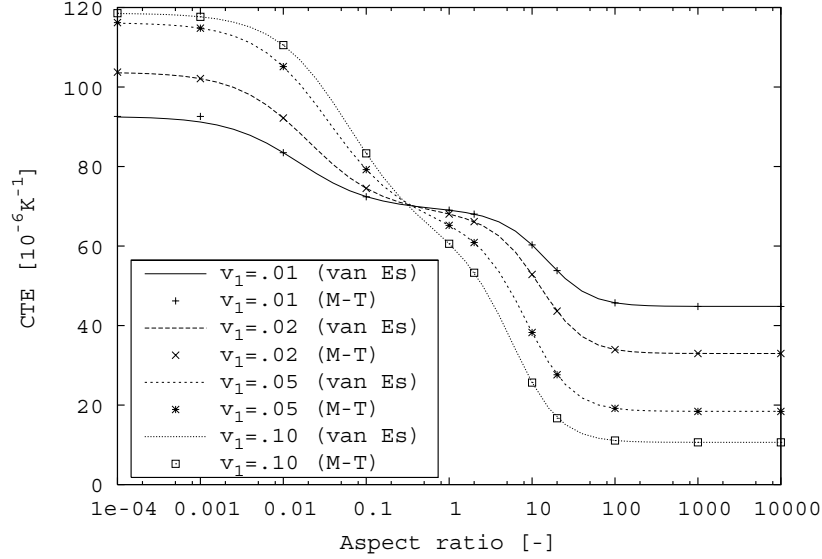


Figure 4.4: Influence of the aspect ratio on the macroscopic thermal expansion coefficient for different volume fractions of a linear thermo-elastic composite.

Castañeda [57]. Table 4.1 shows that our predictions with both homogenization models are very close to experimental results and this generally leads to slightly better predictions than with simplified models. These predictions also agree with Palmyra [75] 3D FE results (using first-order tetrahedra and periodic boundary conditions) while our procedure is much less time-consuming.

Transversely isotropic inclusions

A graphite fiber-reinforced composite is now considered. The main difference with the previous cases is that the inclusion's material is not isotropic anymore but transversely isotropic (subscript L denotes the longitudinal direction -the one of anisotropy- and T a transverse one). A slight modification of the method in order to take into account this particularity is proposed hereafter.

Since Eshelby's tensor only depends on the matrix properties and the shape of the inclusions, it will not be modified when used in M-T. However, when storing the tensors (accordingly with the traditional storage of strain and stress tensors⁴), stiffness matrix and the thermal expansion vector must be written

$${}^4[\boldsymbol{\sigma}] = [\sigma_{11} \quad \sigma_{22} \quad \sigma_{33} \quad \sigma_{23} \quad \sigma_{13} \quad \sigma_{12}]^T, [\boldsymbol{\varepsilon}] = [\varepsilon_{11} \quad \varepsilon_{22} \quad \varepsilon_{33} \quad 2\varepsilon_{23} \quad 2\varepsilon_{13} \quad 2\varepsilon_{12}]^T$$

Model	\bar{E}_L [GPa]	\bar{E}_T [GPa]	$\bar{\alpha}_L$ [10^{-6}K^{-1}]	$\bar{\alpha}_T$ [10^{-6}K^{-1}]
Experiment [65]	5.99		27.7 ± 1.7	121 ± 1
M-T	6.097	1.929	30.1	120.6
M-T($A_r \times 1.25$)	6.401	1.932	28.9	121.0
Interpol. model	6.136	1.938	30.0	120.1
Interpol. model ($A_r \times 1.25$)	6.432	1.941	28.8	120.5
FE [65]			29.3 ± 0.1	119 ± 0.1
Takao-Taya/aggregate [65]			32.0	120
Tandon-Weng/laminate [65]			29.4	119
McCullough [65]	< 5.89		31.4	121

Table 4.1: Short glass fiber reinforced composite: predictions of the macroscopic thermo-mechanical properties by using various homogenization schemes and comparison with several predictive formulae [65].

under the following form, using the direction 1 as the direction of the aligned fibers:

$$\mathbf{C}_1 = \begin{pmatrix} \frac{1}{E_L} & -\frac{\nu_{LT}}{E_T} & -\frac{\nu_{LT}}{E_T} & 0 & 0 & 0 \\ -\frac{\nu_{LT}}{E_T} & \frac{1}{E_T} & -\frac{\nu_T}{E_T} & 0 & 0 & 0 \\ -\frac{\nu_{LT}}{E_L} & -\frac{\nu_T}{E_T} & \frac{1}{E_T} & 0 & 0 & 0 \\ 0 & 0 & 0 & \frac{2(1+\nu_T)}{E_T} & 0 & 0 \\ 0 & 0 & 0 & 0 & \frac{1}{\mu_{LT}} & 0 \\ 0 & 0 & 0 & 0 & 0 & \frac{1}{\mu_{LT}} \end{pmatrix}^{-1},$$

$$\boldsymbol{\alpha}_1 = (\alpha_L \quad \alpha_T \quad \alpha_T \quad 0 \quad 0 \quad 0)^T.$$

For this test, two materials are considered for the matrix: 930/934 epoxy ($E_0 = 0.63$ GPa, $\nu_0 = 0.37$ and $\alpha_0 = 24.4 \times 10^{-6} \text{ K}^{-1}$) and PMR15 polyimide ($E_0 = 0.50$ GPa, $\nu_0 = 0.35$ and $\alpha_0 = 20.0 \times 10^{-6} \text{ K}^{-1}$), and two kinds of graphite fibers: C6000 ($E_{1,L} = 33.8$ GPa, $E_{1,T} = 3.35$ GPa, $\mu_{1,LT} = 1.30$ GPa, $\nu_{1,LT} = 0.20$, $\nu_{1,T} = 0.40$ and $A_{r_1} = \infty$) and P75 ($E_{1,L} = 79.8$ GPa, $E_{1,T} = 1.38$ GPa, $\mu_{1,LT} = 1.00$ GPa, $\nu_{1,LT} = 0.20$, $\nu_{1,T} = 0.40$ and $A_{r_1} = \infty$) where $-\nu_{LT}$ represents the ratio of the strain in the transverse direction over the strain in the longitudinal direction in a uniaxial tension test along the fibers. Predictions by using the M-T homogenization scheme are confronted to several experimental results, some well-known analytical predictions for the CTE and FE results assuming generalized plane strain on square and hexagonal arrays of fibers (Bowles and Tompkins [13]). These are reported in table 4.2. Note that the Schapery's predictive formula, which exists for the longitudinal and transverse directions, is only valid for isotropic constituents and so it does not

Composite - CTE	Exp.	FE	FE	M-T	SH	RH
		(Hex)	(Sq)			
P75/934 - $\bar{\alpha}_L$	-0.584	-0.512	-0.512	-0.512	-0.537	-0.512
P75/934 - $\bar{\alpha}_T$	19.18	19.07	19.06	18.92	19.70	18.90
P75/930 - $\bar{\alpha}_L$	-0.598	-0.627	-0.625	-0.627	-0.644	-0.627
P75/930 - $\bar{\alpha}_T$	17.62	14.04	14.00	13.90	14.80	13.90
C6000/PMR15 - $\bar{\alpha}_L$	-0.118	-0.104	-0.099	-0.104	-0.125	-0.104
C6000/PMR15 - $\bar{\alpha}_T$	12.46	12.56	12.36	12.54	14.30	12.40

Table 4.2: Transversely isotropic graphite fibers-reinforced composites: prediction of the longitudinal and transverse macroscopic CTE ($[10^{-6}\text{K}^{-1}]$) with direct predictive formulae [13] (Shapery (SH), Rosen and Hashin (RH)), FE on a hexagonal (Hex) or square (Sq) fibers arrangement [13], homogenization scheme (M-T) and experimental results (Exp.). Volume fraction of fibers are: 0.48 for P75/934, 0.65 for P75/930 and 0.63 for C6000/PMR15.

account for the different values of the CTE of the inclusions in different directions. Good predictions are observed with mean-field homogenization schemes, especially for the transverse macroscopic CTE which is much more dependent on the predictive technique used.

4.4 Homogenization of viscoelastic composites

4.4.1 Homogenization technique

Consider a two-phase linear viscoelastic composite, each phase obeying a constitutive law of the form (4.6/4.7). By using the Laplace-Carson transform (see appendix B.1), the convolution product becomes a single contraction without rate dependence anymore so that constitutive laws can be rewritten in the Laplace domain as:

$$\begin{aligned}
 \boldsymbol{\sigma}^*(s) &= \mathbf{G}^*(s) : \boldsymbol{\varepsilon}^*(s), \\
 \text{or equivalently } \boldsymbol{\varepsilon}^*(s) &= \mathbf{J}^*(s) : \boldsymbol{\sigma}^*(s), \\
 \text{with } \mathbf{G}^*(s) &= [\mathbf{J}^*(s)]^{-1}.
 \end{aligned} \tag{4.62}$$

These equations are similar to those of linear isothermal elasticity. Of course, they are fictitious constitutive equations since they are defined in the Laplace-Carson domain. However, one can apply the homogenization schemes valid in linear isothermal elasticity in order to obtain the homogenized modulus $\bar{\mathbf{G}}^*$ or

$\bar{\mathbf{J}}^*$:

$$\begin{aligned}\bar{\boldsymbol{\sigma}}^*(s) &= \bar{\mathbf{G}}^*(s) : \bar{\boldsymbol{\varepsilon}}^*(s), \\ \text{or equivalently } \bar{\boldsymbol{\varepsilon}}^*(s) &= \bar{\mathbf{J}}^*(s) : \bar{\boldsymbol{\sigma}}^*(s), \\ \text{with } \bar{\mathbf{G}}^*(s) &= [\bar{\mathbf{J}}^*(s)]^{-1}.\end{aligned}\quad (4.63)$$

Using a numerical inversion of the Laplace-Carson transform (see appendix B.2) to find the corresponding time dependent operators, the following expressions enable to compute the macroscopic response:

$$\begin{aligned}\bar{\boldsymbol{\sigma}}(t) &= \bar{\mathbf{G}}(t) : \bar{\boldsymbol{\varepsilon}}(0) + \int_0^t \bar{\mathbf{G}}(t - \tau) : \dot{\bar{\boldsymbol{\varepsilon}}}(\tau) d\tau, \\ \bar{\boldsymbol{\varepsilon}}(t) &= \bar{\mathbf{J}}(t) : \bar{\boldsymbol{\sigma}}(0) + \int_0^t \bar{\mathbf{J}}(t - \tau) : \dot{\bar{\boldsymbol{\sigma}}}(\tau) d\tau.\end{aligned}\quad (4.64)$$

For the numerical inversion, the use of 20 collocation points is recommended. Those are chosen as equispaced on a logarithmic scale containing at least all the relaxation times of the homogeneous materials. If the relaxation functions of the phases are particularly simple, a lower number of points may be considered (5 to 10).

4.4.2 Numerical simulations

As seen later in this work, homogenization of linear viscoelastic composites is a subproblem of the affine formulation developed for homogenization of elastoviscoplastic composites. Accuracy of this subproblem is thus of first importance. As basic validation for homogenization of linear viscoelastic composites, the following material defined by Prony series is considered. Time dependent Young's modulus of the matrix is $E_0 = 3 + 17e^{-t}$ and its Poisson's ratio is $\nu_0 = 0.38$. For the long fibers, these parameters are: $E_1 = 3 + 17e^{-t/10}$ and $\nu_1 = 0.38$. Given the high volume fraction of inclusions (50%), the interpolative homogenization scheme is used. This composite was studied numerically by asymptotic homogenization in the Laplace domain (asymptotic homogenization method and 2D plane strain FE simulations are used as numerical method, square arrangement of the fibers is considered) in Yeong-Moo Yi *et al.* [109] and the time response is obtained by a Laplace numerical inversion method similar to the one used in this work (see appendix B.2). Predictions by mean-field homogenization schemes are available in Friebel *et al.* [33]. Our goal here is to reproduce homogenization results and check their accuracy against FE.

Prediction of the homogenized transverse plane strain tensile modulus is illustrated on figure 4.5. Plane strain tensile modulus (E_T^{PE}) is computed from a tensile test in a transverse direction with respect to the fibers so that the stress in the other transverse direction and deformation in the longitudinal

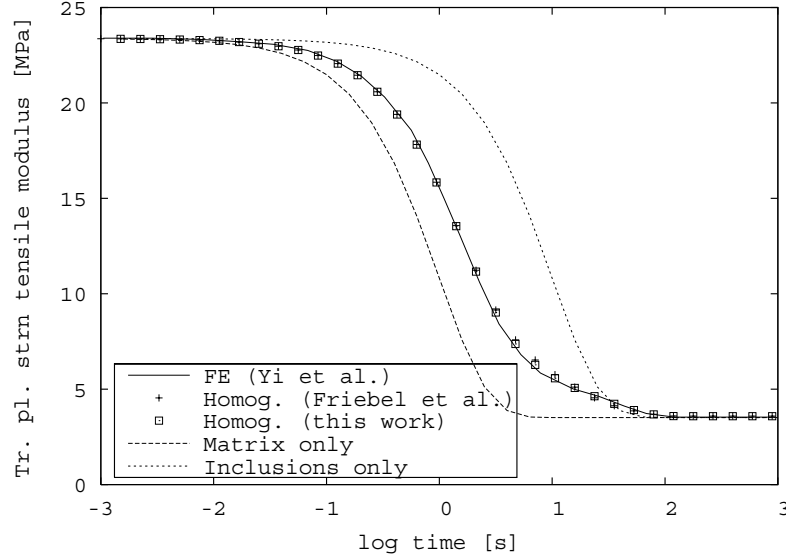


Figure 4.5: Prediction of the homogenized transverse plane strain tensile modulus of a two-phase linear viscoelastic composite.

direction are prevented. This can be computed from the components of the relaxation modulus in the Laplace-Carson domain as (direction 1 is aligned with the fibers):

$$E_T^{PE*} = G_{3333}^* - \frac{G_{3322}^* G_{3322}^*}{G_{2222}^*}, \quad \sigma_{33}^* = E_T^{PE*} \varepsilon_{33}^*. \quad (4.65)$$

Our predictions are compared to the available results. Almost no difference can be seen between the two results obtained by mean-field homogenization (in both cases, 10 collocation points are used for the numerical Laplace inversion). Furthermore, a very good agreement is observed between homogenization and FE results.

Macroscopic response to a loading test can be computed with the help of equation (4.64). On figure 4.6, mean-field homogenization results for a uniaxial displacement test in the transverse direction to the fibers is illustrated. These results are confronted to 2D plane strain finite element simulations. For this, a quarter of unit cell corresponding to hexagonal array fibers arrangement is considered (see section 3.1). A very good agreement is observed for various strain rates. This means that the numerical inversion of the Laplace transform is done correctly as well as the computation of the convolution product. For a given loading path, evaluation of this convolution product is done incrementally

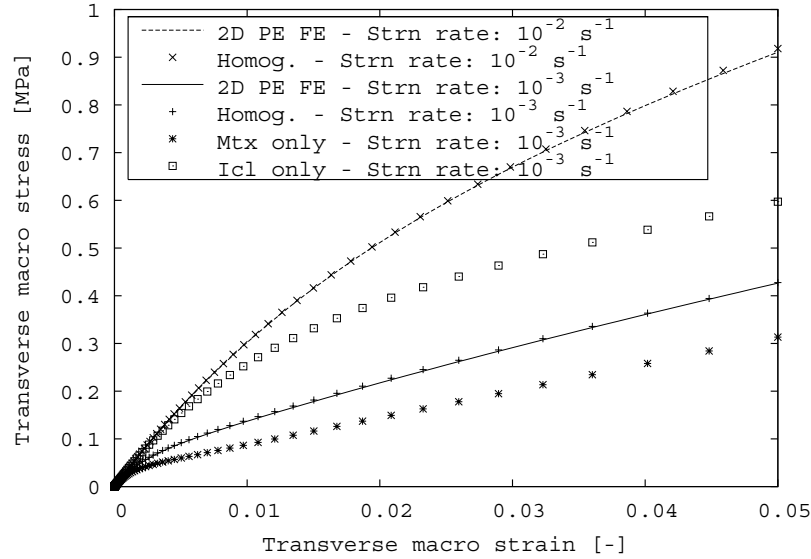


Figure 4.6: Prediction of the macroscopic response of a two-phase linear viscoelastic composite under uniaxial displacements.

in time from only the solution at the last time-step and given data over the increment, see appendix C for more details.

4.5 Conclusions

In this chapter, we focused on three subjects and presented their theory in detail. Firstly, major mean-field homogenization schemes for two-phase isothermal linear elastic composites are presented. Secondly, a general method allows to formulate the thermo-elastic version of any homogenization model defined by its isothermal strain concentration tensors. Thirdly, the problem of linear elastic composites is examined. All these homogenization schemes must be highly accurate since they are used as subproblems in the homogenization of nonlinear materials. For this reason, the predictions have been extensively validated against experimental data or FE results for numerous composite systems.

For thermo-elastic composites, we compared our predictions of the CTE with experimental data, either when each phase is isotropic or when the fibers present a transversely isotropic behavior. In both cases, the longitudinal and transverse values of the CTE were in excellent agreement with target results.

For linear viscoelastic composites, validations are done in both Laplace and

time domains. Predictions of a composite whose behavior is defined by Prony series are in excellent agreement with FE results. This guarantees the quality of the adopted homogenization scheme and of the numerical calculus (Laplace inversion, incremental evaluation of a convolution product).

Chapter 5

Homogenization of elasto-plastic composites

¹ Mean-field homogenization schemes previously developed in the context of linear elasticity are now extended to nonlinear behaviors and firstly to elasto-plasticity. After a brief review of the constitutive equations, these are linearized so that homogenization schemes apply and allow the computation of the effective response.

5.1 Constitutive equations

The J_2 elasto-plastic model described hereafter is presented in Doghri [24] and relies on the von Mises equivalent stress which is the second invariant of the deviatoric stress tensor. In elasto-plasticity, the Hookean law and the additive decomposition of the total strain are given by:

$$\boldsymbol{\sigma} = \mathbf{C} : \boldsymbol{\varepsilon}^e, \quad \boldsymbol{\varepsilon} = \boldsymbol{\varepsilon}^e + \boldsymbol{\varepsilon}^p, \quad (5.1)$$

where \mathbf{C} is the Hookean elastic stiffness tensor, $\boldsymbol{\varepsilon}$ is the total strain tensor, $\boldsymbol{\varepsilon}^e$ is the elastic part and $\boldsymbol{\varepsilon}^p$ the plastic one. A yield function f defines an elastic region ($f \leq 0$) and a yield surface ($f = 0$) as:

$$f(\boldsymbol{\sigma}, p) = \sigma_{eq} - \sigma_Y - R(p), \quad (5.2)$$

¹Some developments of this chapter led to two publications: “A study of various estimates of the macroscopic tangent operator in the incremental homogenization of elasto-plastic composites”, Pierard O. and Doghri I., *International Journal for Multiscale Computational Engineering*, accepted for publication [79] and “Micromechanics of elasto-plastic materials reinforced with ellipsoidal inclusions”, Pierard O., González C., Segurado J., LLorca J. and Doghri I., *Mechanics of Materials*, submitted for publication [81].

where σ_Y is the initial yield stress and $R(p)$ the hardening function. It is commonly written as a power law function: $R(p) = kp^n$, where k is the hardening modulus and n is the hardening exponent. The plastic flow rule governs the evolution of the plastic strain as:

$$\dot{\epsilon}^p = \dot{\gamma} \frac{\partial f}{\partial \boldsymbol{\sigma}}, \quad (5.3)$$

where the scalar $\dot{\gamma} \geq 0$ is the plastic multiplier. Its sign is positive if $f = 0$ and $\dot{f} = 0$ (yielding in plasticity) or nil if $f < 0$ (elasticity) or $f = 0$ and $\dot{f} < 0$ (unloading).

The accumulated plasticity p is an internal variable of the model which keeps track of the past history undergone by the material and is linked to the viscoplastic law as:

$$p(t) = \int_0^t \dot{p} d\tau, \quad \dot{p} = \left(\frac{2}{3} \dot{\epsilon}^p : \dot{\epsilon}^p \right)^{1/2} = \dot{\gamma}, \quad (5.4)$$

where $\dot{\epsilon}^p$ is the plastic strain rate.

5.2 Homogenization of elasto-plastic composites

Homogenization models developed for non-linear composite materials rely on the definition of a linear comparison composite (LCC). This fictitious composite has the same geometry as the original one but the non-linear constitutive laws of its various phases are linearized in such a way that mean-field homogenization schemes valid in linear (thermo-)elasticity apply. The different linearizations lead to various formulations of the local behavior.

First attempt of homogenization for elasto-plastic composites was made by Kröner [54] (and followed in the same time by Budiansky and Wu [16]) who proposed a self-consistent model for polycrystals in which interactions between the phases are only elastic. This led to too stiff responses. Another approach was proposed by Hill [42] who linearized the local constitutive laws written in rate form and introduced an instantaneous elasto-plastic tangent modulus to compute the mechanical response of elasto-plastic materials through a step-by-step iterative procedure. However, when dealing with high non-linearities, predictions become very close to a far upper bound. Berveiller and Zaoui [8] proposed an isotropic interaction law instead of the anisotropic one used by Hill.

Four different formulations are presented here. The secant one relates directly the total strain to the total stress. The version used in this work has been implemented by González and LLorca [37]. The incremental formulation, which will be studied in-depth theoretically and numerically, is written in a rate form. For exhaustiveness purpose, a short introduction is given to the

variational formulation which is based on energy concepts and involves an optimization step. However, this formulation is limited to constitutive laws which derive from a single potential. A last linearization, the affine formulation, will be presented in the elasto-viscoplastic section (chapter 6) since we use it only for this class of composites.

For linear homogeneous materials, stiffness and compliance tensors remain uniform within a phase, even if strain and stress fields are not. This is not true anymore with non-linear materials for which instantaneous (secant or tangent) stiffness and compliance tensors are defined at each point of a phase. This fact leads to a crucial problem when solving the homogenization step of the LCC since an infinity of phases is present. One way to circumvent it is to define a reference state for each constituent which enables to have representative moduli of this phase. Generally, the average stress or strain in the phase are considered as the reference state. However, especially when strong gradients occur, such definition of the reference state is not that accurate. Another one based on the second order moment of the stress tensor is presented for the secant formulation in section 5.2.1.

5.2.1 Secant formulation

The secant formulation determines for each phase a secant operator which links the total strain to the total stress. Implementation of the present version is due to González and LLorca [37] for two-phase elasto-plastic material. For a better coherence with subsequent sections, the algorithm described hereafter is written in a strain driven way even if its dual form has been implemented. However, these two approaches are rigorously equivalent (Suquet [95]).

Strains and stresses of an elasto-plastic phase r are related through a secant stiffness tensor \mathbf{C}_r^s as:

$$\boldsymbol{\sigma}_r = \mathbf{C}_r^s : \boldsymbol{\varepsilon}_r \quad \text{with} \quad \mathbf{C}_r^s = 3\kappa_r \mathbf{I}^{vol} + 2\mu_r^s(\tilde{\boldsymbol{\varepsilon}}_r^{eq}) \mathbf{I}^{dev}, \quad (5.5)$$

where μ_r^s is the secant shear modulus, which is a function of the per phase reference equivalent strain $\tilde{\boldsymbol{\varepsilon}}_r^{eq}$.

The equivalent macroscopic relation makes use of the effective stiffness tensor $\bar{\mathbf{C}}$ as:

$$\bar{\boldsymbol{\sigma}} = \bar{\mathbf{C}}(\tilde{\boldsymbol{\varepsilon}}_0^{eq}, \tilde{\boldsymbol{\varepsilon}}_1^{eq}) : \bar{\boldsymbol{\varepsilon}}, \quad (5.6)$$

where $\tilde{\boldsymbol{\varepsilon}}_0^{eq}$ and $\tilde{\boldsymbol{\varepsilon}}_1^{eq}$ are the reference equivalent strains in the matrix and inclusions, respectively. These have to be computed from either the first or the second order moment of the strain tensor in each phase as indicated below.

$\bar{\mathbf{C}}$ can be determined assuming any linear homogenization scheme defined by its strain concentration tensor (equation (4.28) for two-phase materials). Homogenization of elasto-plastic composites is thus reduced to solving a set of non-linear algebraic equations in $\tilde{\boldsymbol{\varepsilon}}_0^{eq}$. For each value of the applied strain $\bar{\boldsymbol{\varepsilon}}$,

a secant effective stiffness tensor of the composite is determined so that the effective response of the composite can be computed through equation (5.6). From the practical viewpoint, this set is solved using a fixed point algorithm, which begins with a trial value of the secant stiffness tensor of the matrix (the one computed in the previous loading step).

In order to define the reference state of each phase, two methods are proposed. In the classical approach (or first order method), the reference equivalent strain in phase r is determined from the deviatoric part of the average strain tensor $\langle \boldsymbol{\varepsilon} \rangle_r^{dev}$ of that phase:

$$\tilde{\boldsymbol{\varepsilon}}_r^{eq} = \left[\frac{2}{3} \langle \boldsymbol{\varepsilon} \rangle_{\omega_r}^{dev} : \langle \boldsymbol{\varepsilon} \rangle_{\omega_r}^{dev} \right]^{1/2}, \quad (5.7)$$

while in the modified (or second order method) it is computed from the second order moment of the effective strain in the phase as in Ponte Castañeda [83] and Suquet [94]:

$$\tilde{\boldsymbol{\varepsilon}}_r^{eq} = \left[\frac{2}{3} \mathbf{I}^{dev} :: \langle \boldsymbol{\varepsilon} \otimes \boldsymbol{\varepsilon} \rangle_{\omega_r} \right]^{1/2}, \quad (5.8)$$

and an analytical expression of $\langle \boldsymbol{\varepsilon} \otimes \boldsymbol{\varepsilon} \rangle_{\omega_r}$ was proposed by Buryachenko [17] and given in Suquet [95] for sphere-reinforced composite. This is valid in linear elasticity for a given homogenization scheme. However, when dealing with non linear behaviors, it can be used on the LCC. The extension to ellipsoidal inclusions is done at a higher computational cost and requires the computation of the derivatives of the Eshelby's tensor with respect to the Poisson's ratio (details in Pierard *et al.* [81]).

5.2.2 Incremental formulation

The incremental approach is another option to predict both macroscopic and per-phase responses of non-linear materials. This is done incrementally over several time-steps. The implementation of this formulation is more involved than the secant first-order one but enables to deal with any elasto-plastic model in any phase and a wider range of loading paths (e.g.: non-proportional and cyclic loadings) since it follows the deformation history.

The rate form of the elasto-plastic behavior of phase r reads:

$$\dot{\boldsymbol{\sigma}}_r = \mathbf{C}_r^{ep} : \dot{\boldsymbol{\varepsilon}}_r, \quad (5.9)$$

where \mathbf{C}_r^{ep} is the so-called continuum elasto-plastic tangent operator. When considering finite time increments for numerical implementation, a discretization in time over each time interval gives:

$$\Delta \boldsymbol{\sigma}_r \approx \mathbf{C}_r^{alg} : \Delta \boldsymbol{\varepsilon}_r, \quad (5.10)$$

where $\Delta\boldsymbol{\sigma}_r$ and $\Delta\boldsymbol{\varepsilon}_r$ are stress and strain increments of phase r over the time interval and \mathbf{C}_r^{alg} is the algorithmic tangent operator. It is emphasized that the two tangent operators are different in general and become close for vanishingly small plastic strain increments.

Both continuum and consistent tangent operators can be computed analytically for most constitutive models. For the J_2 elasto-plastic model considered in this study, they read:

$$\mathbf{C}_r^{alg} = \mathbf{C}_r^{ep} - (2\mu_r)^2 \frac{\Delta p_r}{\sigma_r^{eq,tr}} \left(\frac{3}{2} \mathbf{I}^{dev} - \mathbf{N}_r \otimes \mathbf{N}_r \right), \quad (5.11)$$

$$\mathbf{C}_r^{ep} = \mathbf{C}_r - \frac{(2\mu_r)^2}{3\mu_r + \frac{d\sigma_r^{eq}}{dp_r}} \mathbf{N}_r \otimes \mathbf{N}_r, \quad \mathbf{N}_r = \frac{3}{2} \frac{\boldsymbol{\sigma}_r^{dev}}{\sigma_r^{eq}}, \quad (5.12)$$

where $\sigma_r^{eq,tr}$ is an elastic predictor of the equivalent stress of phase r at the end of the considered time step and \mathbf{N}_r is the normal to the yield surface in stress space of phase r . Both tangent operators are anisotropic during a plastic increment even for isotropic materials.

Equation (5.10-5.12) written for each phase thus define a set of linearized constitutive equations over the time step. Given the state of deformation at the beginning of the time step, homogenization models valid in linear elasticity can apply over this time interval so that the effective relation reads:

$$\Delta\bar{\boldsymbol{\sigma}} = \bar{\mathbf{C}}(\tilde{\sigma}_0^{eq}, \tilde{\sigma}_1^{eq}) : \Delta\bar{\boldsymbol{\varepsilon}}, \quad (5.13)$$

where $\bar{\mathbf{C}}$ is the macroscopic tangent operator. In this approach, the considered reference equivalent stresses in the phases are computed from the average stress tensor. Extension of the incremental approach by taking into account the second order moment of the stress tensor is still an open subject. Similarly to developments valid for the secant approaches, the effective tangent operator $\bar{\mathbf{C}}$ can be evaluated once a homogenization scheme is assumed and is given by (4.28). The strain concentration tensors are the ones used in the context of linear elasticity (section 4.2.3) but their arguments are the elasto-plastic tangent operators in each phase. This set of equations is solved in a strain driven way. Given a macroscopic strain increment over the time step, a trial value of the average strain increment in the inclusions is computed. A fixed point iterative scheme converges to average strain values in the phases from which the effective stiffness and the macroscopic response can be computed. Various results obtained with this formulation are presented in Doghri and Ouaar [26] for spherical reinforcements and in Doghri and Friebel [25] for other inclusion shapes. As presented in section 5.3, various computations of the macroscopic tangent stiffness are possible by considering isotropic or transversely isotropic extraction of the tangent modulus of the matrix.

5.2.3 Variational formulation

Developments presented hereafter follow the review paper of Ponte Castañeda [86], who made the major developments of this formulation. This approach is valid for heterogeneous hyperelastic materials for which, at each point, the local constitutive law derives from a single potential:

$$\boldsymbol{\sigma} = \frac{\partial w}{\partial \boldsymbol{\varepsilon}}(\boldsymbol{\varepsilon}). \quad (5.14)$$

For a strain tensor field $\boldsymbol{\varepsilon}$ within the set of kinematically admissible ones \mathcal{K} , the macroscopic stress can be determined from the effective energy function $\bar{\mathbf{W}}(\bar{\boldsymbol{\varepsilon}})$ as (Hill [41]):

$$\bar{\boldsymbol{\sigma}} = \frac{\partial \bar{\mathbf{W}}}{\partial \bar{\boldsymbol{\varepsilon}}}, \quad \bar{\mathbf{W}}(\bar{\boldsymbol{\varepsilon}}) = \min_{\boldsymbol{\varepsilon} \in \mathcal{K}} [(1 - v_1) \langle w_0(\boldsymbol{\varepsilon}) \rangle_{\omega_0} + v_1 \langle w_1(\boldsymbol{\varepsilon}) \rangle_{\omega_1}]. \quad (5.15)$$

A dual form exists and both are exactly equivalent.

Similarly to the other formulations, the effective energy function cannot be determined easily and approximations must be made. The local potential can be approximated by the sum of a Taylor expansion w_r^T of w_r around a reference strain $\tilde{\boldsymbol{\varepsilon}}_r$ and a per phase constant corrector function V_r ²:

$$\begin{aligned} w_r(\boldsymbol{\varepsilon}) &\approx w_r^T(\boldsymbol{\varepsilon}) + V_r(\tilde{\boldsymbol{\varepsilon}}_r, \mathbf{L}_r^0), \\ w_r^T(\boldsymbol{\varepsilon}) &= w_r(\tilde{\boldsymbol{\varepsilon}}_r) + \frac{\partial w_r}{\partial \boldsymbol{\varepsilon}}(\tilde{\boldsymbol{\varepsilon}}_r) : (\boldsymbol{\varepsilon} - \tilde{\boldsymbol{\varepsilon}}_r) + \frac{1}{2}(\boldsymbol{\varepsilon} - \tilde{\boldsymbol{\varepsilon}}_r) : \mathbf{L}_r^0 : (\boldsymbol{\varepsilon} - \tilde{\boldsymbol{\varepsilon}}_r), \\ V_r(\tilde{\boldsymbol{\varepsilon}}_r, \mathbf{L}_r^0) &= \underset{\hat{\boldsymbol{\varepsilon}}_r}{stat} [w_r(\hat{\boldsymbol{\varepsilon}}_r) - w_r^T(\hat{\boldsymbol{\varepsilon}}_r)], \end{aligned} \quad (5.16)$$

where \mathbf{L}_r^0 is a uniform modulus tensor and *stat* means optimizing with respect to the relevant variable. A volume average over the composite enables to get an approximation of the effective potential:

$$\begin{aligned} \bar{\mathbf{W}}(\bar{\boldsymbol{\varepsilon}}) &\approx \bar{\mathbf{W}}^T(\bar{\boldsymbol{\varepsilon}}; \tilde{\boldsymbol{\varepsilon}}_s, \mathbf{L}_s^0) + \sum_{r=1}^N v_r V_r(\tilde{\boldsymbol{\varepsilon}}_r, \mathbf{L}_r^0), \\ \bar{\mathbf{W}}^T(\bar{\boldsymbol{\varepsilon}}, \tilde{\boldsymbol{\varepsilon}}_s, \mathbf{L}_s^0) &= \min_{\boldsymbol{\varepsilon} \in \mathcal{K}} \langle w^T(\boldsymbol{\varepsilon}) \rangle, \end{aligned} \quad (5.17)$$

where w^T is the volume average of the approximated local potentials w_r^T . An optimization process over the variables $\boldsymbol{\varepsilon}_r$ and \mathbf{L}_r^0 which depends on the choice of the corrector function enables to derive various estimates and bounds.

A first choice reduces the stationary condition in (5.16) to finding a maximum (Ponte Castañeda [83]) which leads to a linear elastic comparison composite so that a secant effective constitutive relation can be written (deBotton

²Such approximation of the potential corresponds to a fictitious linear thermo-elastic material since $\boldsymbol{\sigma}_r(\boldsymbol{\varepsilon}) \approx \frac{\partial w_r}{\partial \boldsymbol{\varepsilon}}(\tilde{\boldsymbol{\varepsilon}}_r) + \mathbf{L}_r^0 : (\boldsymbol{\varepsilon} - \tilde{\boldsymbol{\varepsilon}}_r) = \mathbf{L}_r^0 : \boldsymbol{\varepsilon} + \left(\frac{\partial w_r}{\partial \boldsymbol{\varepsilon}}(\tilde{\boldsymbol{\varepsilon}}_r) - \mathbf{L}_r^0 : \tilde{\boldsymbol{\varepsilon}}_r \right)$.

and Ponte Castañeda [22]). Bounds and estimates can be found for non-linear materials by using the models developed for linear ones on the linear comparison composite. This method takes into account the second-order moment of the fields.

Another approach consists of choosing $\hat{\epsilon}_r = \tilde{\epsilon}_r$, which cancels the corrector function V_r in equation (5.16) (Ponte Castañeda [84]). This method makes use of the tangent moduli of the phases and is called accordingly the tangent second-order estimates because it reproduces exactly to the second-order terms of the asymptotic expansions of Suquet and Ponte Castañeda [97]. The optimizing process lead to per phase reference strains $\tilde{\epsilon}_r$ equal to the average strain in that phase. This method has the drawback of a duality gap (i.e.: the dual formulation does not lead to the same linear comparison composite and thus a different prediction) and cannot provide bounds. The affine formulation (see section 6.3) is a particular case of this formulation.

A recent improvement of this second-order method takes into account the second-order moment of the stress tensor so that its accuracy is much higher when strong heterogeneities of the fields occur (Ponte Castañeda [85]). This method is called the generalized secant one since it leads to intermediate modulus between the tangent and secant ones.

5.3 Computation of the macroscopic tangent operator

In this section, different computations of the macroscopic tangent modulus are examined. These evaluations have a great impact on the final prediction of the incremental formulation. A theoretical study will first determine relations between the different operators thus computed. This will be later analyzed numerically for various composite materials.

5.3.1 Motivation for a stiffness reduction of the macroscopic tangent operator

Predictions of the classical incremental formulation are known to be too stiff and this is illustrated on the following example. Consider a longitudinal uniaxial tension test performed on an elasto-plastic aluminum matrix ($E=71.3$ GPa, $\nu=0.3$, $\sigma_Y=246.9$ MPa, $k=133$ MPa and $m=0.37$) reinforced by elastic SiC whiskers ($E=485$ GPa, $\nu=0.2$, $v_1=22$ % and $Ar=4.1$). Experimental results and 3D FE simulations are taken from Levy and Papazian [56]. Results of the incremental formulation implemented as in section 5.2.2 are also reported on figure 5.1 and are effectively very stiff.

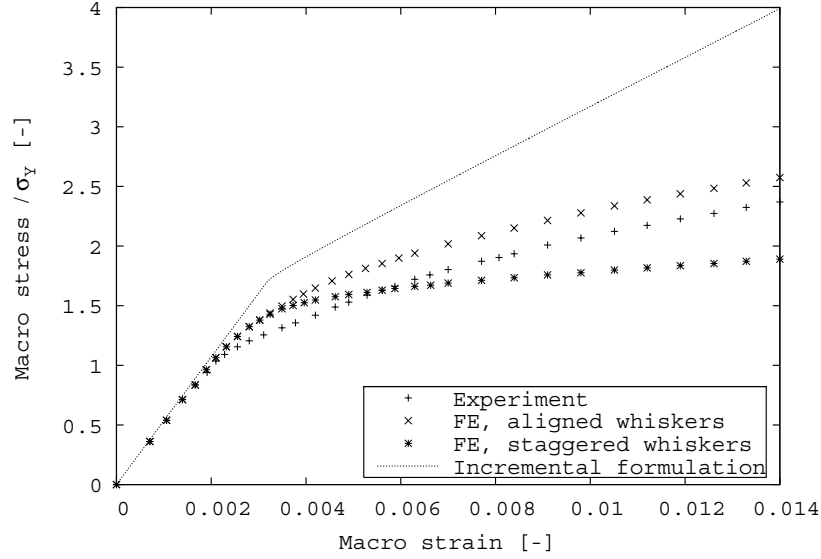


Figure 5.1: Aluminum matrix with SiC whiskers. Longitudinal macroscopic tension test. Illustration of the too stiff response of the incremental formulation.

In the subsequent sections, various attempts to soften the response are presented. The key idea is to consider tensors other than \mathbf{C}_0 in the computation of the Eshelby, Hill and effective tensors. This can be done by modifying the tensor \mathbf{C}_0 and extracting its isotropic or transversely isotropic part (\mathbf{C}_0 is anisotropic during plastic yielding even if the matrix is isotropic). Comparisons between all these tensors are made and their influence on the final response is examined.

5.3.2 Influence of the matrix modulus

A fourth-order tensor \mathbf{C} is positive definite (noted $\mathbf{C} > 0$) if for all non-nil symmetric second-order tensors $\boldsymbol{\varepsilon}$,

$$\boldsymbol{\varepsilon} : \mathbf{C} : \boldsymbol{\varepsilon} > 0. \quad (5.18)$$

By using this quadratic form, two fourth-order tensors can be compared. Notation $\mathbf{C} > \mathbf{D}$ means that for all non-nil second-order tensors $\boldsymbol{\varepsilon}$, $\boldsymbol{\varepsilon} : \mathbf{C} : \boldsymbol{\varepsilon} > \boldsymbol{\varepsilon} : \mathbf{D} : \boldsymbol{\varepsilon}$.

An important application of positive definite tensors is when \mathbf{C} represents

a macroscopic stiffness $\bar{\mathbf{C}}$ and $\bar{\boldsymbol{\varepsilon}}$ a strain tensor. If $\bar{\mathbf{C}}^{(1)} > \bar{\mathbf{C}}^{(2)}$, it means that:

$$\forall \bar{\boldsymbol{\varepsilon}} \neq 0, \bar{\boldsymbol{\varepsilon}} : \underbrace{\bar{\mathbf{C}}^{(1)}}_{\bar{\boldsymbol{\sigma}}^{(1)}} : \bar{\boldsymbol{\varepsilon}} > \bar{\boldsymbol{\varepsilon}} : \underbrace{\bar{\mathbf{C}}^{(2)}}_{\bar{\boldsymbol{\sigma}}^{(2)}} : \bar{\boldsymbol{\varepsilon}}. \quad (5.19)$$

So, during a uniaxial test, following relations are guarantee $\bar{\sigma}_{11}^{(1)} > \bar{\sigma}_{11}^{(2)}$ if $\bar{\varepsilon}_{11} > 0$ and $\bar{\sigma}_{11}^{(1)} < \bar{\sigma}_{11}^{(2)}$ otherwise.

In this section the dependence of the macroscopic tangent, the Hill's and the Hill's constraint tensors with respect to \mathbf{C}_0 is analyzed. Our main goal is the following. If $\mathbf{C}_0^{(1)} > \mathbf{C}_0^{(2)}$, does the relation $\bar{\mathbf{C}}^{(1)} > \bar{\mathbf{C}}^{(2)}$ hold?

Let $\mathbf{C}_0 > 0$ and $\Delta\mathbf{C} > 0$. Bornert [10] proved the following relations:

$$\begin{aligned} \mathbf{P}(\mathbf{C}_0 + \Delta\mathbf{C}) &< \mathbf{P}(\mathbf{C}_0), \\ \mathbf{C}^*(\mathbf{C}_0) &< \mathbf{C}^*(\mathbf{C}_0 + \Delta\mathbf{C}). \end{aligned} \quad (5.20)$$

Hill's tensor \mathbf{P} is thus decreasing with \mathbf{C}_0 for a given geometry of inclusions on the contrary to Hill's constraint tensor \mathbf{C}^* which is an increasing function of \mathbf{C}_0 .

Given a fourth-order tensorial variable \mathbf{A} , one can prove that the following function f is increasing with \mathbf{A} (Bornert [10]):

$$f : \mathbf{A} \rightarrow [v_1(\mathbf{A} + \mathbf{C}_1)^{-1} + (1 - v_1)(\mathbf{A} + \mathbf{C}_0)^{-1}]^{-1} - \mathbf{A}. \quad (5.21)$$

Expression (4.27) of the macroscopic tangent operator is form-similar to (5.21). $\bar{\mathbf{C}}$ is thus increasing with \mathbf{C}^* and therefore with \mathbf{C}_0 :

$$\bar{\mathbf{C}}(\mathbf{C}_0 + \Delta\mathbf{C}) > \bar{\mathbf{C}}(\mathbf{C}_0), \quad \Delta\mathbf{C} > 0. \quad (5.22)$$

Furthermore, the dependence of $\bar{\mathbf{C}}$ with respect to \mathbf{P} is analyzed. By using relations (4.26) and (4.36), the macroscopic tangent operator can be rewritten as:

$$\begin{aligned} \bar{\mathbf{C}} &= (v_1\mathbf{C}_1 : \mathbf{B}^\varepsilon + (1 - v_1)\mathbf{C}_0) : (v_1\mathbf{B}^\varepsilon + (1 - v_1)\mathbf{I})^{-1} \\ &= \mathbf{C}_0 + v_1(\mathbf{C}_1 - \mathbf{C}_0) : \mathbf{B}^\varepsilon : (v_1\mathbf{B}^\varepsilon + (1 - v_1)\mathbf{I})^{-1} \\ &= \mathbf{C}_0 + v_1(\mathbf{C}_1 - \mathbf{C}_0) : (v_1\mathbf{I} + (1 - v_1)\mathbf{B}^{\varepsilon^{-1}})^{-1} \\ &= \mathbf{C}_0 + v_1[(\mathbf{C}_1 - \mathbf{C}_0)^{-1} + (1 - v_1)\mathbf{P}]^{-1}. \end{aligned} \quad (5.23)$$

Since \mathbf{P} is decreasing with \mathbf{C}_0 and, if in this last expression, \mathbf{P} is computed either with \mathbf{C}_0 or $\mathbf{C}_0 + \Delta\mathbf{C}$, and the rest of $\bar{\mathbf{C}}$ is computed with \mathbf{C}_0 , the following relation holds:

$$\bar{\mathbf{C}}(\mathbf{P}(\mathbf{C}_0 + \Delta\mathbf{C}), \mathbf{C}_0) > \bar{\mathbf{C}}(\mathbf{P}(\mathbf{C}_0), \mathbf{C}_0), \quad \Delta\mathbf{C} > 0. \quad (5.24)$$

5.3.3 Isotropic parts of an anisotropic modulus tensor

Any fourth-order isotropic tensor can always be written under the form (Suquet and Bornert *et al.* [96]):

$$\mathbf{C}^{iso} = 3\kappa\mathbf{I}^{vol} + 2\mu\mathbf{I}^{dev} = (\mathbf{I}^{vol} :: \mathbf{C}^{iso})\mathbf{I}^{vol} + \frac{1}{5}(\mathbf{I}^{dev} :: \mathbf{C}^{iso})\mathbf{I}^{dev}, \quad (5.25)$$

where κ and μ are the bulk and shear moduli, respectively, $\mathbf{I}^{vol} = \frac{1}{3}\mathbf{1} \otimes \mathbf{1}$ and $\mathbf{I}^{dev} = \mathbf{I} - \mathbf{I}^{vol}$ are the spherical and deviatoric operators, respectively, $\mathbf{1}$ is the second-order identity tensor and $' :: '$ is a tensor product contracted over four indices.

Extracting an isotropic part \mathbf{C}^{iso} from an anisotropic modulus tensor \mathbf{C}^{ani} consists in finding two scalars κ_t and μ_t so that the isotropic tensor is written as:

$$\mathbf{C}^{iso} = 3\kappa_t\mathbf{I}^{vol} + 2\mu_t\mathbf{I}^{dev}. \quad (5.26)$$

Two extraction methods are proposed hereafter: a general one valid for any anisotropic tensor and a special one.

General method This method proposed by Bornert [11] consists of a projection of the anisotropic tangent operator \mathbf{C}^{ani} onto the subspace of isotropic ones so that we get:

$$3\kappa_t = \mathbf{I}^{vol} :: \mathbf{C}^{ani}, \quad 10\mu_t = \mathbf{I}^{dev} :: \mathbf{C}^{ani}. \quad (5.27)$$

In all the simulations, the J_2 elasto-plastic model is used. It is thus interesting to apply this projection method in this particular case. An application of equation (5.27) to \mathbf{C}^{alg} gives an isotropic projection \mathbf{C}^{IsoGen} defined by

$$\kappa_t = \kappa, \quad \mu_t = \mu - \frac{3}{5}\mu^2 \left(\frac{1}{h} + 4\frac{\Delta p}{\sigma_{eq}^{tr}} \right). \quad (5.28)$$

Special method Another method was proposed by Ponte Castañeda [84]. It is applicable when the anisotropic tangent operator can be cast under the form:

$$\mathbf{C}^{ani} = 3k_1\mathbf{I}^{vol} + 2k_2(\mathbf{I}^{dev} - \frac{2}{3}\mathbf{N} \otimes \mathbf{N}) + 2k_3 \left(\frac{2}{3}\mathbf{N} \otimes \mathbf{N} \right), \quad (5.29)$$

with $N_{ii} = 0$ and $\mathbf{N} : \mathbf{N} = \frac{3}{2}$. The method is based on the following fundamental assumption:

$$\text{dev}(\dot{\boldsymbol{\varepsilon}}) // \mathbf{N}, \quad (5.30)$$

where $' // '$ means 'is collinear with'. It then follows that:

$$\dot{\boldsymbol{\sigma}} = \mathbf{C}^{ani} : \dot{\boldsymbol{\varepsilon}} = \mathbf{C}^{IsoSpe} : \dot{\boldsymbol{\varepsilon}}, \quad (5.31)$$

where \mathbf{C}^{IsoSpe} is a special isotropic operator defined by:

$$\kappa_t = k_1, \quad \mu_t = k_3. \quad (5.32)$$

Chaboche *et al.* [18, 19] made the interesting observation that the special isotropic extraction corresponds to a stiffness reduction of \mathbf{C}^{ani} in a direction orthogonal to \mathbf{N} . Indeed, since $(\mathbf{I}^{dev} - \frac{2}{3}\mathbf{N} \otimes \mathbf{N}) : \mathbf{N} = \mathbf{0}$, and using (5.30), we have:

$$\dot{\boldsymbol{\sigma}} = \mathbf{C}^{ani} : \dot{\boldsymbol{\epsilon}} = \left[\mathbf{C}^{ani} + \alpha(\mathbf{I}^{dev} - \frac{2}{3}\mathbf{N} \otimes \mathbf{N}) \right] : \dot{\boldsymbol{\epsilon}} = \mathbf{C}^{IsoSpe} : \dot{\boldsymbol{\epsilon}}. \quad (5.33)$$

With the conditions $2k_3 - 2k_2 - \alpha = 0$ and $2\mu_t = 2k_2 + \alpha$, we do retrieve $\mu_t = k_3$.

For J_2 elasto-plastic model, both anisotropic tangent operators follow equation (5.29) and assumption (5.30) is always valid if $\dot{\mathbf{N}} = \mathbf{0}$. An application of equation (5.32) gives:

$$\kappa_t = \kappa, \quad \mu_t = \mu \left(1 - \frac{3\mu}{h} \right). \quad (5.34)$$

Chaboche *et al.* [18, 19] also note that μ_t thus obtained is softer than with the general projection when \mathbf{C}^{ep} is considered. We generalize this observation and prove that \mathbf{C}^{IsoGen} is stiffer than \mathbf{C}^{IsoSpe} for both \mathbf{C}^{ep} and \mathbf{C}^{alg} :

$$\mathbf{C}^{IsoGen} - \mathbf{C}^{IsoSpe} = \frac{12\mu^2}{5} \left(\frac{1}{h} - \frac{\Delta p}{\sigma_{eq}^{tr}} \right) \mathbf{I}^{dev} > 0, \quad (5.35)$$

the scalar factor between brackets being positive (Doghri and Ouaar [26]).

5.3.4 Transversely isotropic parts of an anisotropic modulus tensor

Similarly to the general method for isotropic extraction, a projection is proposed for extracting the transversely isotropic part of an anisotropic fourth-order tensor. The method presented here was first proposed by Walpole [103] and described in Frederico *et al.* [31].

Any transversely isotropic second-order tensor \mathbf{c} can be written as a combination of two basis tensors \mathbf{a} and \mathbf{b} :

$$\mathbf{c} = c^a \mathbf{a} + c^b \mathbf{b}, \quad (5.36)$$

where:

$$\mathbf{a} = \mathbf{w} \otimes \mathbf{w}, \quad \mathbf{b} = \mathbf{1} - \mathbf{a},$$

\mathbf{w} being the direction of anisotropy. Any fourth-order transversely isotropic tensor \mathbf{T} with a direction of anisotropy \mathbf{w} can be written as (Bornert [10]):

$$\begin{aligned} \mathbf{T} = & (\mathbf{B}_1 :: \mathbf{T})\mathbf{B}_1 + (\mathbf{B}_2 :: \mathbf{T})\mathbf{B}_2 + \frac{1}{2}(\mathbf{B}_3 :: \mathbf{T})\mathbf{B}_3 \\ & + \frac{1}{2}(\mathbf{B}_4 :: \mathbf{T})\mathbf{B}_4 + \frac{1}{2}(\mathbf{B}_5 :: \mathbf{T})\mathbf{B}_6 + \frac{1}{2}(\mathbf{B}_6 :: \mathbf{T})\mathbf{B}_5, \end{aligned} \quad (5.37)$$

where the six fourth-order basis tensors \mathbf{B}_i are constructed as follows:

$$\begin{aligned} (\mathbf{B}_1)_{ijkl} &= \frac{1}{2}b_{ij}b_{kl}, & (5.38) \\ (\mathbf{B}_2)_{ijkl} &= a_{ij}a_{kl}, \\ (\mathbf{B}_3)_{ijkl} &= \frac{1}{2}(b_{ik}b_{jl} + b_{jk}b_{il} - b_{ij}b_{kl}), \\ (\mathbf{B}_4)_{ijkl} &= \frac{1}{2}(b_{ik}a_{jl} + b_{il}a_{jk} + b_{jl}a_{ik} + b_{jk}a_{il}), \\ (\mathbf{B}_5)_{ijkl} &= a_{ij}b_{kl}, \\ (\mathbf{B}_6)_{ijkl} &= b_{ij}a_{kl}. \end{aligned} \quad (5.39)$$

The first four tensors have minor and major symmetries while the last two ones have only the minor symmetries. One can notice that if $T_5 = T_6$ ($T_i = \mathbf{B}_i :: \mathbf{T}$), the tensor \mathbf{T} is fully symmetric ($B_5_{ijkl} = B_6_{klij}$). In this particular case, the problem is reduced to finding five independent components as expected in the case of transversely isotropic modulus operators. If the first four components T_i are positive, then the tensor \mathbf{T} is positive definite.

Let's now consider an arbitrary anisotropic fourth-order tensor \mathbf{C}^{ani} which has the minor symmetries. In this case, application of the double contractions in (5.37) on \mathbf{C}^{ani} instead of \mathbf{T} give the projection of \mathbf{C}^{ani} onto the subspace generated by \mathbf{B}_i , to obtain a transversely isotropic tensor with a direction of anisotropy \mathbf{w} :

$$\begin{aligned} \mathbf{C}^{TrIso} = & (\mathbf{B}_1 :: \mathbf{C}^{ani})\mathbf{B}_1 + (\mathbf{B}_2 :: \mathbf{C}^{ani})\mathbf{B}_2 + \frac{1}{2}(\mathbf{B}_3 :: \mathbf{C}^{ani})\mathbf{B}_3 \\ & + \frac{1}{2}(\mathbf{B}_4 :: \mathbf{C}^{ani})\mathbf{B}_4 + \frac{1}{2}(\mathbf{B}_5 :: \mathbf{C}^{ani})\mathbf{B}_6 + \frac{1}{2}(\mathbf{B}_6 :: \mathbf{C}^{ani})\mathbf{B}_5 \end{aligned} \quad (5.40)$$

Application of this method to the tangent operator \mathbf{C}^{ep} (equation (5.12)) of the J_2 elasto-plastic model gives (direction of anisotropy is along axis 1 and

$T_i = \mathbf{B}_i :: \mathbf{C}^{ani}$):

$$\begin{aligned}
 T_1 &= 2\kappa + \frac{2}{3}\mu - \frac{1}{2}(N_{22}^2 + N_{33}^2 + 2N_{22}N_{33})\frac{(2\mu)^2}{h}, \\
 T_2 &= \kappa + \frac{4}{3}\mu - N_{11}^2\frac{(2\mu)^2}{h}, \\
 T_3 &= 2\mu - \frac{1}{4}(N_{22}^2 + N_{33}^2 - 2N_{22}N_{33} + 2N_{23}^2)\frac{(2\mu)^2}{h}, \\
 T_4 &= 2\mu - \frac{1}{2}(2N_{12}^2 + 2N_{13}^2)\frac{(2\mu)^2}{h}, \\
 T_5 &= \kappa - \frac{2}{3}\mu - \frac{1}{2}(N_{11}N_{22} + N_{11}N_{33})\frac{(2\mu)^2}{h}, \\
 T_6 &= T_5,
 \end{aligned} \tag{5.41}$$

where $h = 3\mu + \frac{d\sigma^{eq}}{dp}$. With these notations, engineering moduli are given by:

$$E_L = T_2 - \frac{T_5^2}{2T_1}, \tag{5.42}$$

$$\nu_{LT} = \frac{T_5}{2T_1}, \quad \nu_T = \frac{T_5^2 - (2T_1 - T_3)T_2}{T_6^2 - (2T_1 + T_3)T_2}, \tag{5.43}$$

$$\mu_{LT} = \frac{T_3}{4}, \quad \mu_T = \frac{T_4}{4}, \tag{5.44}$$

where E_L is the Young's modulus in the longitudinal direction (the one of anisotropy), ν_{LT} is the Poisson's ratio for a traction test in the longitudinal direction, ν_T is the Poisson's ratio in the transverse plane, μ_{LT} is the shear modulus along the longitudinal direction and μ_T is the shear modulus in the transverse plane.

For the J_2 elasto-plastic model under monotonic loading, assumption (5.30) is verified and therefore equation (5.31) always holds and gives an isotropic tangent operator. Nevertheless, based on the fact that the special method for extracting the isotropic part of a tensor gives a softer tangent, we propose the following more compliant approximation of the anisotropic tangent:

$$\mathbf{C}^{AniSpe} = \mathbf{C}^{ani} - K\frac{(2\mu)^2}{h}\mathbf{N} \otimes \mathbf{N}, \tag{5.45}$$

where $K > 1$ is a softening factor. Applying the general transversely isotropic extraction on this modified tensor will give a new transversely isotropic tensor. This approach will be called the special transversely isotropic method. The particular case of $K = 1$ (no softening added) is called the general transversely isotropic method.

5.3.5 Comparison of various local tangent operators

In this section, the various local tangent operators of the J_2 plasticity model are compared in the meaning of the quadratic forms. Doghri and Ouaar [26] already proved that

$$\mathbf{C}^{ep} \geq \mathbf{C}^{alg} \geq \mathbf{C}^{IsoSpe}. \quad (5.46)$$

Our next goal is to find similar relations involving \mathbf{C}^{IsoGen} . The results hereafter hold for both \mathbf{C}^{alg} ($\Delta p > 0$) and \mathbf{C}^{ep} (by setting $\Delta p \rightarrow 0$) so that the anisotropic tangent operator is denoted \mathbf{C}^{ani} . Results of section 5.3.3 give:

$$\mathbf{C}^{IsoGen} - \mathbf{C}^{ani} = -H \left[\mathbf{I}^{dev} - \frac{10}{3} \mathbf{N} \otimes \mathbf{N} \right], \quad H = \frac{6}{5} \mu^2 \left(\frac{1}{h} - \frac{\Delta p}{\sigma_{eq}^{tr}} \right) > 0. \quad (5.47)$$

The proof for $H > 0$ is given in Doghri and Ouaar [26]. Unfortunately, the tensor might be not positive definite. However, some interesting relations are found in the following case:

$$\boldsymbol{\sigma} = [a \quad b \quad b \quad 0 \quad 0 \quad 0]^T, \quad (5.48)$$

where the scalars a and b are of opposite signs. Under these conditions and if fourth-order tensors are stored under the usual engineering way, following result is obtained:

$$\mathbf{C}^{IsoGen} - \mathbf{C}^{ani} = H \begin{pmatrix} 8/3 & -4/3 & -4/3 & 0 & 0 & 0 \\ -4/3 & 1/6 & 7/6 & 0 & 0 & 0 \\ -4/3 & 7/6 & 1/6 & 0 & 0 & 0 \\ 0 & 0 & 0 & -1 & 0 & 0 \\ 0 & 0 & 0 & 0 & -1 & 0 \\ 0 & 0 & 0 & 0 & 0 & -1 \end{pmatrix}. \quad (5.49)$$

For stresses given by equation (5.48), the strains have the following form:

$$\boldsymbol{\varepsilon} = [\varepsilon_{11} \quad \varepsilon_{22} \quad \varepsilon_{33} \quad 0 \quad 0 \quad 0]^T, \quad (5.50)$$

where $sign(\varepsilon_{11}) = sign(a)$; $sign(\varepsilon_{22}) = sign(\varepsilon_{33}) = -sign(a)$. For these strains, we obtain:

$$\begin{aligned} \boldsymbol{\varepsilon} : (\mathbf{C}^{IsoGen} - \mathbf{C}^{ani}) : \boldsymbol{\varepsilon} &= H \left(\frac{8}{3} \varepsilon_{11}^2 + \frac{1}{6} \varepsilon_{22}^2 + \frac{1}{6} \varepsilon_{33}^2 - \frac{8}{3} \varepsilon_{11} \varepsilon_{22} \right. \\ &\quad \left. + \frac{7}{3} \varepsilon_{22} \varepsilon_{33} - \frac{8}{3} \varepsilon_{11} \varepsilon_{33} \right) > 0. \end{aligned} \quad (5.51)$$

In this particular case, following relation holds:

$$\mathbf{C}^{IsoGen} > \mathbf{C}^{ani}, \quad \mathbf{C}^{ani} = \mathbf{C}^{ep} \quad \text{or} \quad \mathbf{C}^{alg}. \quad (5.52)$$

It is rather surprising and unexpected to find that \mathbf{C}^{IsoGen} is stiffer than \mathbf{C}^{ani} . Given the form of the stress tensor (5.48), this result is valid for each plastic phase of the composite if a macroscopic tension test is applied. The particular case $b = 0$ corresponds to uniaxial tension in a phase.

5.3.6 Various estimates of the macroscopic tangent operator

Hill's tensor (\mathbf{P}), the strain concentration tensor (\mathbf{B}^ε) and the macroscopic tangent operator ($\bar{\mathbf{C}}$) make use of \mathbf{C}_0 as indicated in section 4.2.1 for Mori-Tanaka homogenization scheme. In order to extend the latter model to elasto-plasticity, tangent operators $\mathbf{C}_r(t)$ which are homogeneous per phase and defined at a reference equivalent stress $\tilde{\sigma}^{eq}$ are needed:

$$\dot{\boldsymbol{\sigma}}(\mathbf{x}, t) = \mathbf{C}_r(t, \tilde{\sigma}^{eq}) : \dot{\boldsymbol{\varepsilon}}(\mathbf{x}, t), \quad \forall \mathbf{x} \in \omega_r. \quad (5.53)$$

For simplicity, subsequent developments focus on the matrix phase and assume that it obeys J_2 elasto-plastic model. A reference tangent operator $\mathbf{C}_0^{ani}(t)$ is computed by sending average matrix strain and strain increments to the J_2 elasto-plastic model. If all computations are made with \mathbf{C}_0^{ani} which is anisotropic, this is known to lead to too stiff predictions (see section 5.1). Variations may include evaluation of Eshelby's tensor \mathcal{E} , Hill's tensor \mathbf{P} or all the macroscopic operator $\bar{\mathbf{C}}$ with different approximations of \mathbf{C}_0^{ani} . In the previous sections, the following instantaneous matrix operators have been defined:

1. Anisotropic operators \mathbf{C}_0^{ani} , either "continuum" (\mathbf{C}_0^{ep} , equation (5.12)) or "algorithmic" (\mathbf{C}_0^{alg} , equation (5.11)).
2. Isotropic part \mathbf{C}_0^{IsoGen} using a general projection method - equation (5.27).
3. Isotropic part \mathbf{C}_0^{IsoSpe} using a special method - equation (5.32).
4. Transversely isotropic part $\mathbf{C}_0^{TrIsoGen}$ using a general projection method (obtained by setting $\mathbf{C}^{ani} = \mathbf{C}_0^{ep}$ in equation (5.40)).
5. Transversely isotropic part $\mathbf{C}_0^{TrIsoSpe}$ using a special method (obtained by computing \mathbf{C}_0^{AniSpe} from equation (5.45) and setting $\mathbf{C}^{ani} = \mathbf{C}_0^{AniSpe}$ in equation (5.40)).

For the computation of various estimates of the macroscopic tangent, the following procedure is proposed.

$$\mathbf{P} = \mathcal{E}(\mathbf{E}_0) : \mathbf{D}_0^{-1}, \quad (5.54)$$

$$\mathbf{B}^\varepsilon = [\mathbf{I} + \mathbf{P} : (\mathbf{C}_1 - \mathbf{C}_0)]^{-1}, \quad (5.55)$$

$$\bar{\mathbf{C}} = (v_1 \mathbf{C}_1 : \mathbf{B}^\varepsilon + (1 - v_1) \mathbf{C}_0) : (v_1 \mathbf{B}^\varepsilon + (1 - v_1) \mathbf{I})^{-1}. \quad (5.56)$$

\mathbf{C}_0 , \mathbf{D}_0 and \mathbf{E}_0 are various instantaneous operators for the reference matrix discussed above. The classical (but too stiff) case corresponds to the following choice:

$$\mathbf{E}_0 = \mathbf{D}_0 = \mathbf{C}_0 = \mathbf{C}_0^{ani} = \mathbf{C}_0^{ep}. \quad (5.57)$$

Softer and better predictions were obtained by Doghri and Ouair [26] and Doghri and Friebel [25] by taking:

$$\mathbf{E}_0 = \mathbf{C}_0^{IsoGen} \text{ or } \mathbf{C}_0^{IsoSpe}; \mathbf{D}_0 = \mathbf{C}_0 = \mathbf{C}_0^{ani} = \mathbf{C}_0^{alg}. \quad (5.58)$$

Chaboche *et al.* [18, 19] obtained good predictions with the following case:

$$\mathbf{E}_0 = \mathbf{D}_0 = \mathbf{C}_0^{IsoSpe}; \mathbf{C}_0 = \mathbf{C}_0^{ani} = \mathbf{C}_0^{ep}. \quad (5.59)$$

Several other variants will be tested in the numerical section.

Notice that evaluation of the Eshelby's tensor is analytical only if \mathbf{E}_0 is isotropic or transversely isotropic with the restriction that the direction of anisotropy is aligned with the direction of the reinforcements. Expressions in these two cases are different and presented in appendix A. In all other cases, a numerical evaluation is required (Gavazzi and Lagoudas [34]).

5.4 Numerical simulations

5.4.1 Effect of the macroscopic tangent operator's computation

Throughout this section, comparisons are made between the different predictions obtained with various versions of the macroscopic tangent operator of the incremental formulation. Table 5.1 explains which operator is used to compute Eshelby's tensor, Hill's tensor and finally the macroscopic tangent operator.

For all the simulations, the J_2 plasticity model is used and notations of the corresponding parameters were presented in section 5.1. Inclusion's shape is described by the aspect ratio Ar . Subscript 0 refers to the matrix and 1 to the inclusions.

Aluminum matrix with SiC whiskers

Example of section 5.3.1 is picked up again. Confrontation of reference results with different evaluations of Hill's tensor \mathbf{P} is reported on figure 5.2a. The extracting method to get the isotropic part of \mathbf{C}_0 has a considerable impact on the macroscopic prediction. In this case, the special method ($P IsoSpe$) gives acceptable results, the general one being much too stiff ($P IsoGen$). This fact has already been reported by Chaboche *et al.* [19]. Logically, in this test, computing \mathbf{P} with the transversely isotropic part or the anisotropic version gives almost the same results, which are both too stiff.

Predictions obtained with a macroscopic tangent operator computed entirely from the same tangent operator of the matrix are reported on figure

Case	Notations	\mathbf{E}_0 (for \mathcal{E} in eq.(5.54))	\mathbf{D}_0 (for \mathbf{P} in eq. (5.54))	\mathbf{C}_0 (for $\bar{\mathbf{C}}$ in eqs. (5.55-5.56))
1	Esh IsoGen	\mathbf{C}_0^{IsoGen}	\mathbf{C}_0^{ani}	\mathbf{C}_0^{ani}
2	Esh IsoSpe	\mathbf{C}_0^{IsoSpe}	\mathbf{C}_0^{ani}	\mathbf{C}_0^{ani}
3	P IsoGen	\mathbf{C}_0^{IsoGen}	\mathbf{C}_0^{IsoGen}	\mathbf{C}_0^{ani}
4	P IsoSpe	\mathbf{C}_0^{IsoSpe}	\mathbf{C}_0^{IsoSpe}	\mathbf{C}_0^{ani}
5	P TrIsoGen	$\mathbf{C}_0^{TrIsoGen}$	$\mathbf{C}_0^{TrIsoGen}$	\mathbf{C}_0^{ani}
6	P TrIsoSpe	$\mathbf{C}_0^{TrIsoSpe}$	$\mathbf{C}_0^{TrIsoSpe}$	\mathbf{C}_0^{ani}
7	all IsoGen	\mathbf{C}_0^{IsoGen}	\mathbf{C}_0^{IsoGen}	\mathbf{C}_0^{IsoGen}
8	all IsoSpe	\mathbf{C}_0^{IsoSpe}	\mathbf{C}_0^{IsoSpe}	\mathbf{C}_0^{IsoSpe}
9	all TrIsoGen	$\mathbf{C}_0^{TrIsoGen}$	$\mathbf{C}_0^{TrIsoGen}$	$\mathbf{C}_0^{TrIsoGen}$
10	all Ani	\mathbf{C}_0^{ani}	\mathbf{C}_0^{ani}	\mathbf{C}_0^{ani}

Table 5.1: Notations for the various computations of the macroscopic tangent operator.

5.2b. In this case only the predictions obtained with the special isotropic tangent operator give realistic results. The three other predictions are too stiff, especially with the general isotropic operator !

One can note that it has been proven that $\bar{\mathbf{C}}$ is a monotonic function of the tangent operator of the matrix used for the computation of \mathbf{P} (see equation (5.24)), which is well in accordance with figure 5.2a. On the other hand, $\bar{\mathbf{C}}$ is also a monotonic function of \mathbf{C}_0 if $\mathbf{E}_0 = \mathbf{D}_0 = \mathbf{C}_0$, as observed on figure 5.2b. Finally, figure 5.2a shows that *Esh IsoGen* and *Esh IsoSpe* give almost the same results. This is almost always observed and is due to the property of homogeneity of degree zero of \mathcal{E} with respect to \mathbf{C}_0 (Suquet and Bornert [96]).

Aluminum alloy matrix with long stiff aluminum fibers

Once again, a ductile aluminum alloy matrix ($E=68.9$ GPa, $\nu=0.32$, $\sigma_Y=94$ MPa, $k=578.25$ MPa and $m=0.53$) reinforced this time by long stiff alumina fibers ($E=344.5$ GPa, $\nu=0.26$, $v_1=55$ % and $Ar=1000$) is considered.

Figure 5.3 illustrates the various predictions in a longitudinal macroscopic tension test and are compared to 2D FE simulations with an hexagonal arrangement of fibers (Jansson [45]). All the predictions which compute \mathbf{P} with different matrix operators ($\mathbf{E}_0 \neq \mathbf{D}_0$) give non physical results. In fact, this inconsistency gives a non symmetric \mathbf{P} , which is unacceptable (see section 4.2.1). The overall stiffness is not symmetric either and the transverse response in terms of strains and stresses was found to lose its symmetry.

However, all other predictions (with $\mathbf{E}_0 = \mathbf{D}_0$) give almost the same results

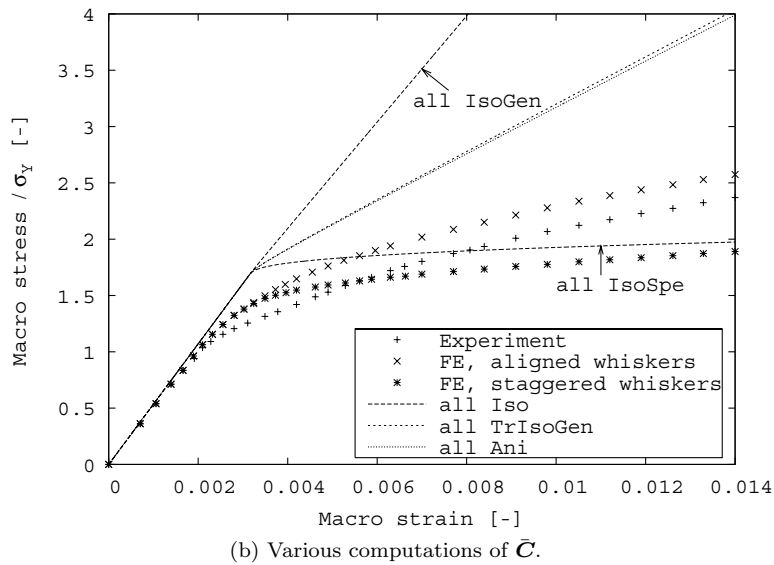
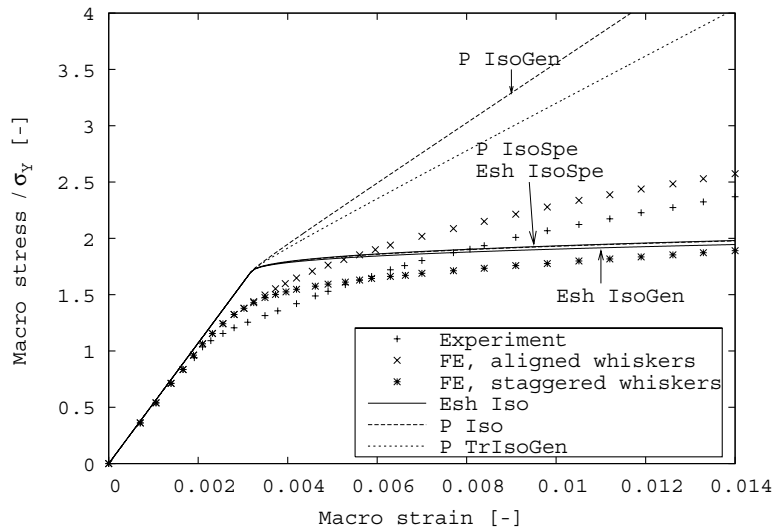


Figure 5.2: Aluminum matrix with SiC whiskers. Longitudinal macroscopic tension test.

as the finite element simulations, excepted *all IsoGen* which is a little bit too

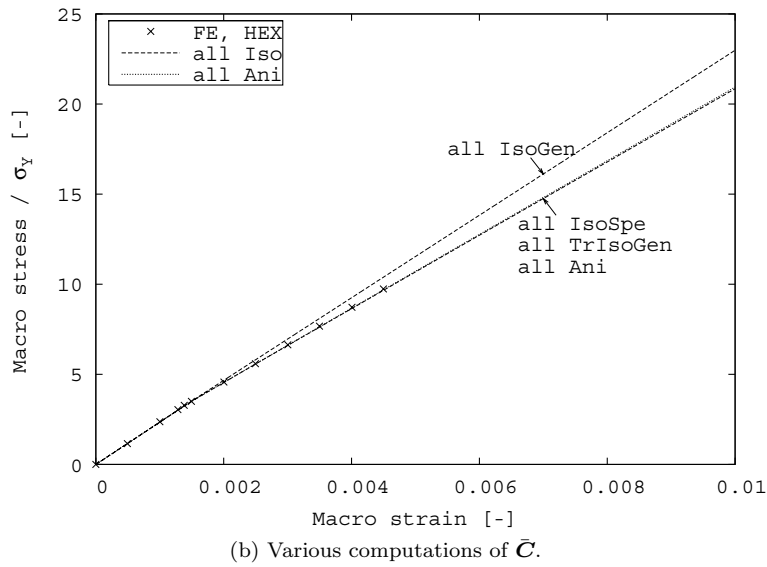
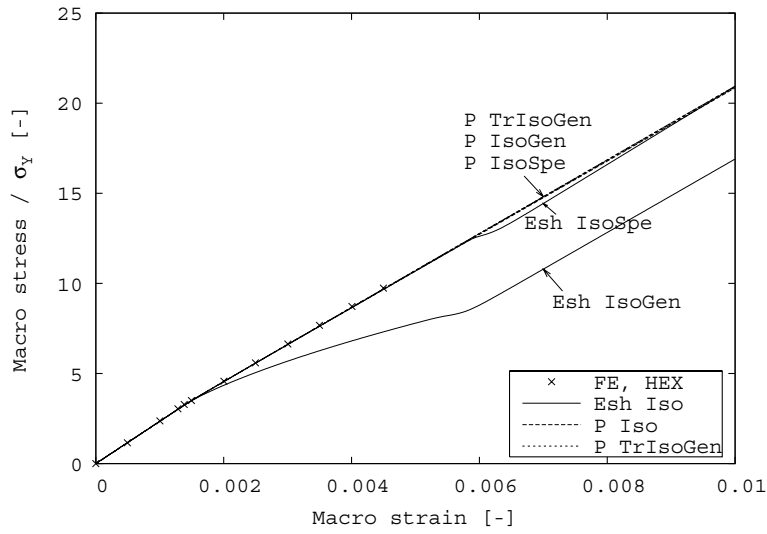


Figure 5.3: Aluminum alloy matrix with long stiff aluminum fibers. Longitudinal macroscopic tension test.

stiff.

Aluminum matrix with fibers

In this simulation, an aluminum alloy matrix ($E=70$ GPa, $\nu=0.33$, $\sigma_Y=200$ MPa, $k=2000$ MPa and $m=1$) is reinforced with δ -Al₂O₃ fibers ($E=300$ GPa, $\nu=0.2$, $v_1=10$ % and $Ar=20$). The behavior of such a material was simulated with FE by Kang and Gao [49]. In a tension test in the longitudinal direction, figures 5.4a and 5.4b illustrate the predictions obtained with different evaluations of \mathbf{P} and $\bar{\mathbf{C}}$, respectively. Note that even if *Esh IsoGen* gives the smallest error, the hardening rate is not predicted accurately so that the most accurate predictions are obtained when making use of the special isotropisation technique. The general transversely isotropic and anisotropic predictions are almost superposed and also too stiff. However, making use of the special transversely isotropic extraction -equations (5.40) and (5.45)- such as illustrated on figure 5.5 softens the response and can even give the best predictions with a relatively small value of the softening coefficient K .

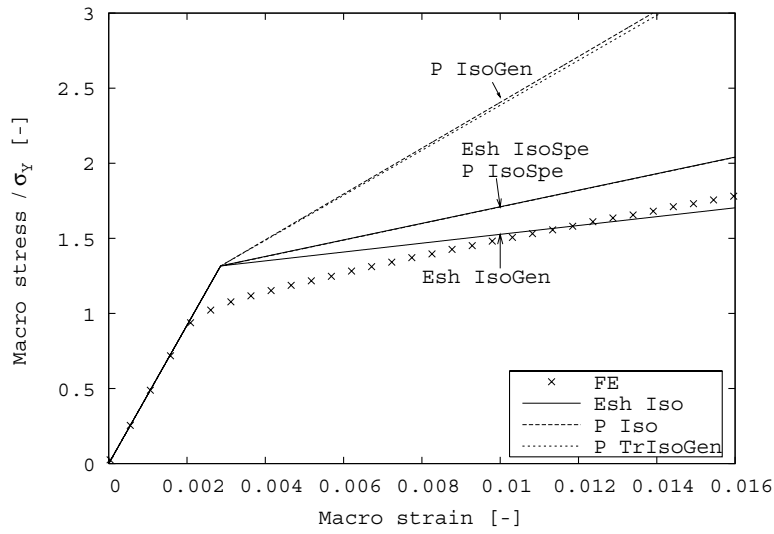
Predictions for a tension test in the transverse direction are reported on figures 5.6a and 5.6b. Interpretation given for the longitudinal case remains valid except that *all TrIsoGen* is much stiffer than *all Ani*. The last one being quite close to the reference solution. Again, with a well chosen value of the softening coefficient, one can get very reliable predictions (see figure 5.7). This is even lower than for longitudinal traction.

MMC under cyclic strain

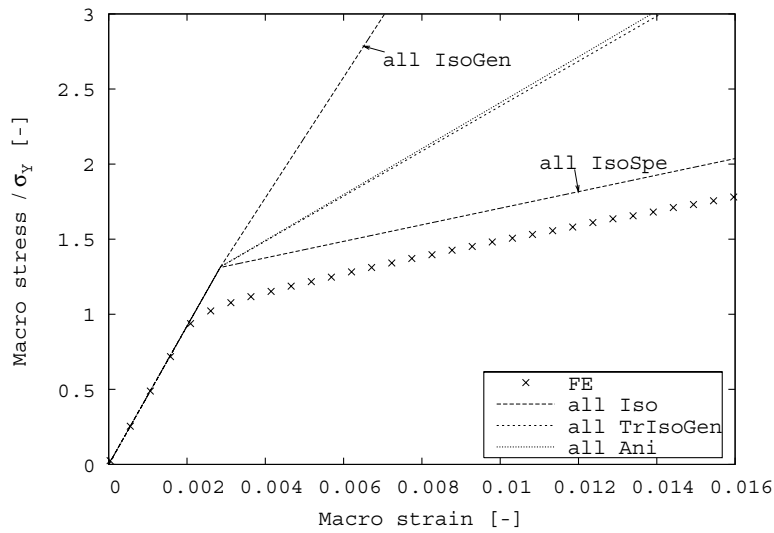
Different predictions of a metal matrix composite (MMC) (matrix: $E=75$ GPa, $\nu=0.30$, $\sigma_Y=75$ MPa, $k=416$ MPa and $m=0.39$; inclusions: $E=400$ GPa, $\nu=0.20$, $v_1=30$ % and $Ar=1$) under cyclic strain are illustrated on figure 5.8 and compared to FE predictions (2D axisymmetric unit cell) of Doghri and Ouaar [26]. Once again this test shows large differences between the different evaluations of the macroscopic tangent operator. Only *Esh Iso* (general and special), *P IsoSpe* and *all IsoSpe* give acceptable results. But once use of the general isotropic extraction of \mathbf{C}_0 or the anisotropic tangent operator is made in \mathbf{P} or $\bar{\mathbf{C}}$, results are much stiffer.

MMC under transverse shear

The response of the same MMC (but with 15% of long fibers) undergoing a transverse shear test is confronted to 2D plane strain FE simulations and illustrated on figure 5.9a. As in tensile tests, predictions which make use of the general isotropic extraction (excepted *Esh IsoGen*) or only the anisotropic tangent operator are too stiff while the special methods give much more realistic results. Several predictions with the transversely isotropic extraction are illustrated on figure 5.9b. The too stiff general transversely isotropic prediction can



(a) Various computations of \mathbf{P} .



(b) Various computations of $\bar{\mathbf{C}}$.

Figure 5.4: Aluminum matrix with fibers. Longitudinal macroscopic tension test.

be corrected with the help of the softening coefficient so that predictions be-

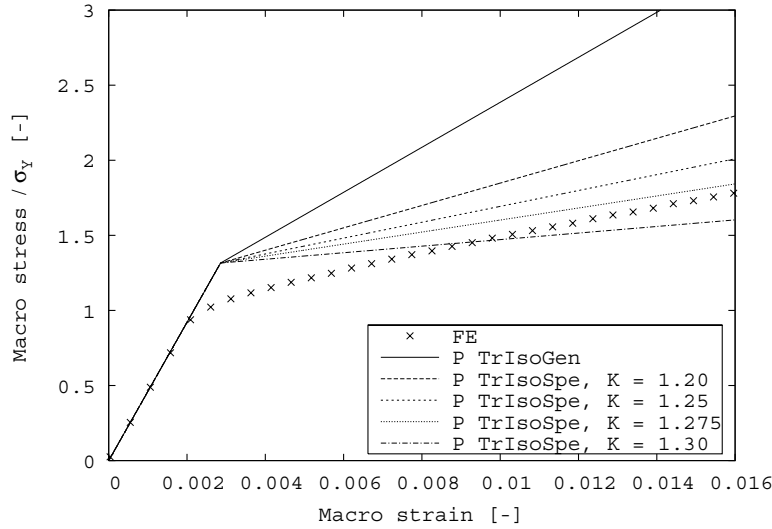


Figure 5.5: Aluminum matrix with fibers. Longitudinal macroscopic tension test. Various computations of \mathbf{P} with the general and special transversely isotropic extraction method.

come much more realistic and can even give the best one among all the different computations.

5.4.2 Microscopic fields analysis

This section focuses on the accuracy of the microscopic fields and their influence on the macroscopic predictions. For this, three models are compared: first order secant formulation, second order secant formulation (results of these two models are provided by González and LLorca [81]) and the incremental formulation (obtained with DIGIMAT [23]). The latter always uses an isotropic extraction of the matrix modulus to compute the Eshelby's tensor only in order to soften the effective tangent operator (section 5.3). Throughout this section, the same composite is considered and consists of an elasto-plastic matrix ($E_m = 70$ GPa, $\nu_m = 0.33$, $\sigma_Y = 0$ MPa, hardening power law and $k = 400$ MPa) reinforced with ellipsoidal elastic inclusions ($E_i = 400$ GPa and $\nu_i = 0.20$) with small aspect ratio ($Ar = 3$). Two different values of the hardening exponent of the matrix are used: $n = 0.05$ and $n = 0.40$. Uniaxial traction tests are performed in both longitudinal and transverse directions. Such analysis enables to better evaluate homogenization schemes. Also, knowing the accuracy of the microscopic fields is a crucial issue since these govern damage initiation.

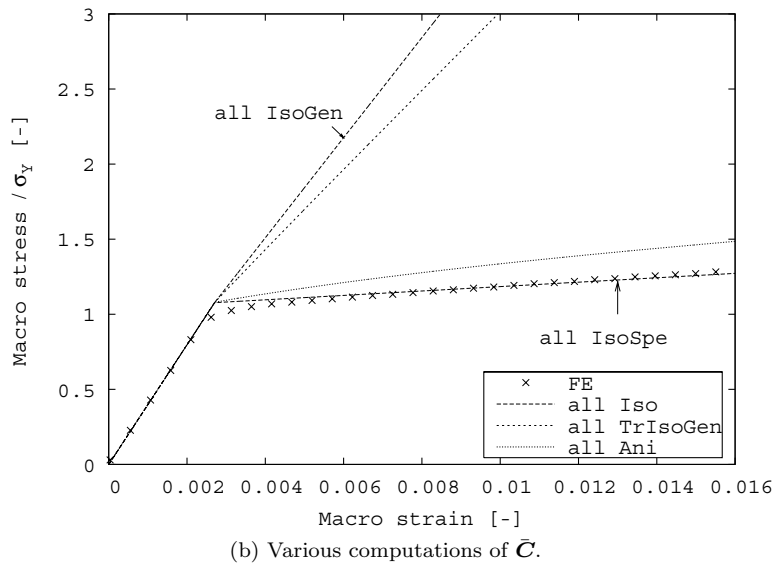
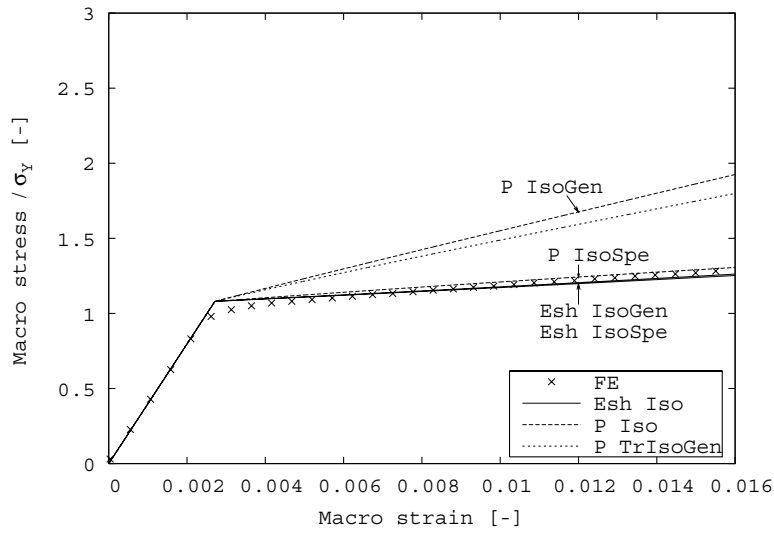


Figure 5.6: Aluminum alloy with fibers. Transverse macroscopic tension test.

For validation purpose, predictions of mean-field homogenization schemes are confronted with FE simulations on 3D periodic unit cells (section 3.2).

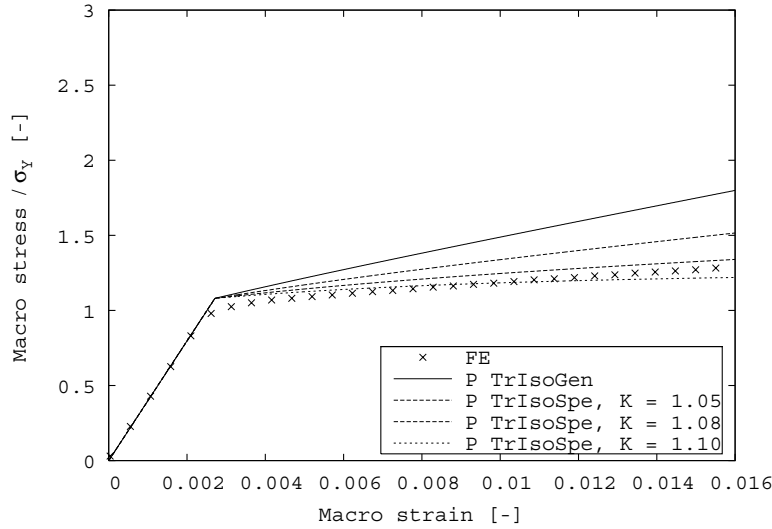
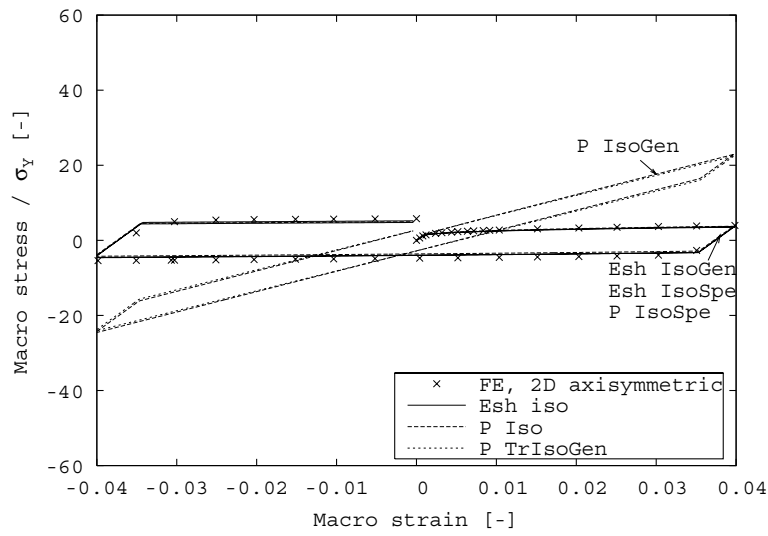


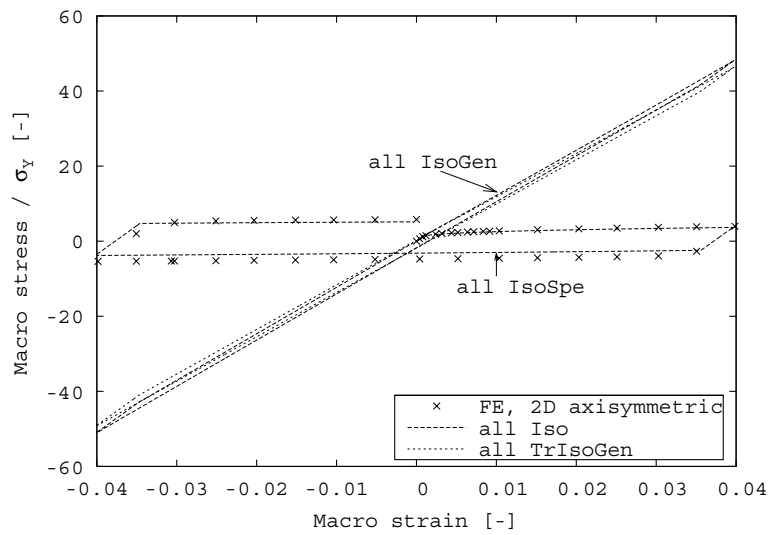
Figure 5.7: Aluminum alloy with fibers. Transverse macroscopic tension test. Various computations of \mathbf{P} with the general and special transversely isotropic extraction method.

To check the accuracy of the FE simulations, four cells were generated and for each value of n , four traction tests were simulated in the longitudinal direction and eight in the transverse one. The scattering between these curves was generally very low, from a fraction of percent to a few percent. This being higher in the transverse direction and for $n = 0.05$. The quasi-exact reference prediction is obtained by averaging the four (or eight) curves.

Macroscopic results of mean-field homogenization and FE simulations are plotted on figures 5.10 and 5.11 for tension tests in both directions and for the two values of the hardening exponent. First-order secant method is generally the stiffest prediction while the second-order secant is the softest among the three homogenization schemes. The incremental formulation has intermediate predictions. It is interesting to notice that accuracy depends on the direction and the hardening. Differences being more pronounced for the longitudinal traction test and the low value of the hardening exponent. For the traction direction, this result was expected since curvature edges of the ellipsoids are higher in the longitudinal direction than the transverse one, where reinforcements behaves much more like spheres. This fact is illustrated on figure 5.12 where the accumulated plastic strain field is illustrated for both traction tests for a corresponding macro strain of 5% and $n = 0.05$. Heterogeneities are clearly



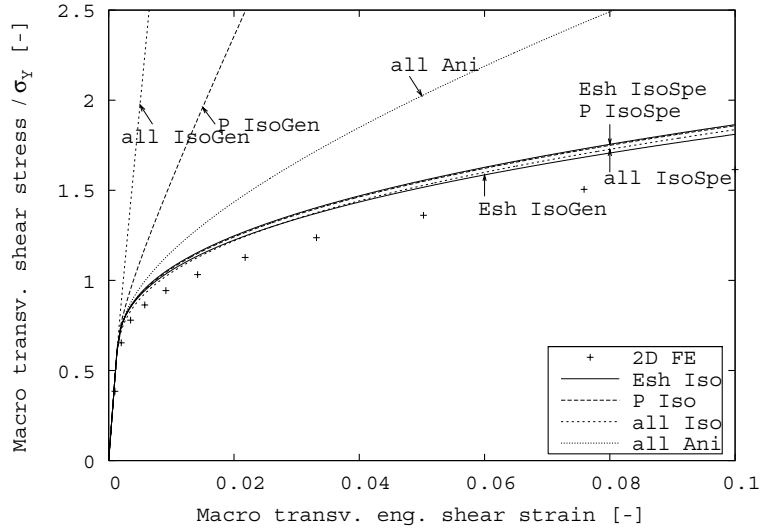
(a) Various computations of P .



(b) Various computations of \bar{C} .

Figure 5.8: MMC under cyclic strain.

more pronounced in the case of a longitudinal traction test. Furthermore, high levels of plasticity are found along the loading direction and especially between



(a) Various computations of the macroscopic tangent operator.

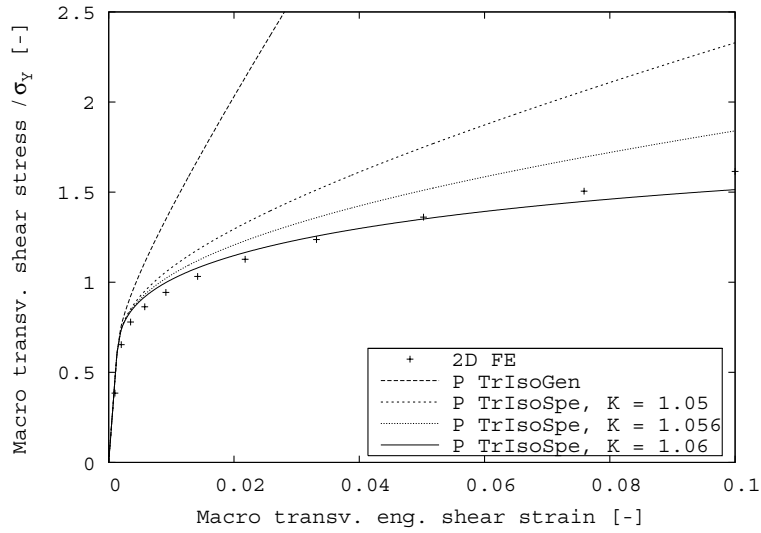
(b) Various computations of \mathbf{P} with the general and special transversely isotropic extraction method.

Figure 5.9: MMC under transverse shear.

ellipsoids closely packed to each others. In order to measure the heterogeneity

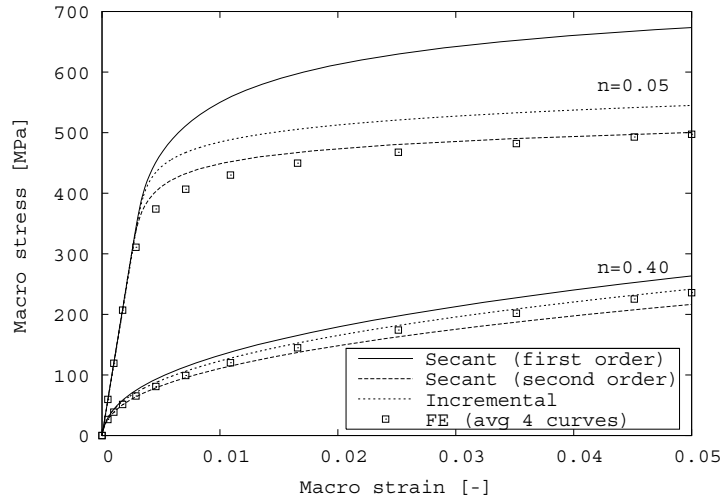


Figure 5.10: Predictions of the tensile stress-strain curves in the longitudinal direction for the composite reinforced with 25% of aligned ellipsoids.

of the accumulated plastic strain field, curves on figure 5.13 show the cumulative probability that the plastic strain is smaller than a given value. In order to compute it, magnitude of the plastic strain at each Gauss point of the matrix is considered as well as the corresponding volumes of these points. A perfectly homogeneous field would give a step function. The widest distribution is found for the longitudinal traction test and $n = 0.05$ while the field is much more homogeneous for the transverse traction test and a high value of the matrix hardening exponent. Such analysis is important in order to understand the behavior of homogenization schemes. Effectively, these rely on the definition of a per phase reference state (see section 5.2.1 for the secant formulation and section 5.2.2 for the incremental one) so that the average equivalent stress can be evaluated in an approximate way only. First order secant and incremental methods compute it from the per phase average stress tensor and this is known for being less accurate when high heterogeneity of the fields occur. The second order secant homogenization scheme relies on the second order moment of the stress tensor. However, all these values can be computed from the FE

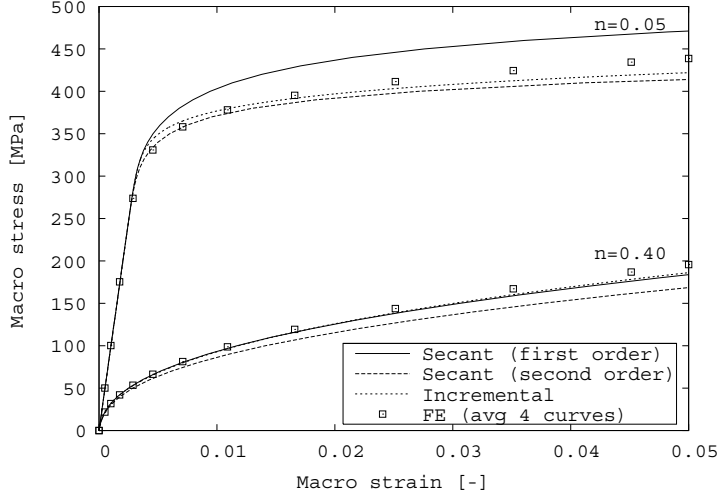


Figure 5.11: Predictions of the tensile stress-strain curves in the transverse direction for the composite reinforced with 25% of aligned ellipsoids.

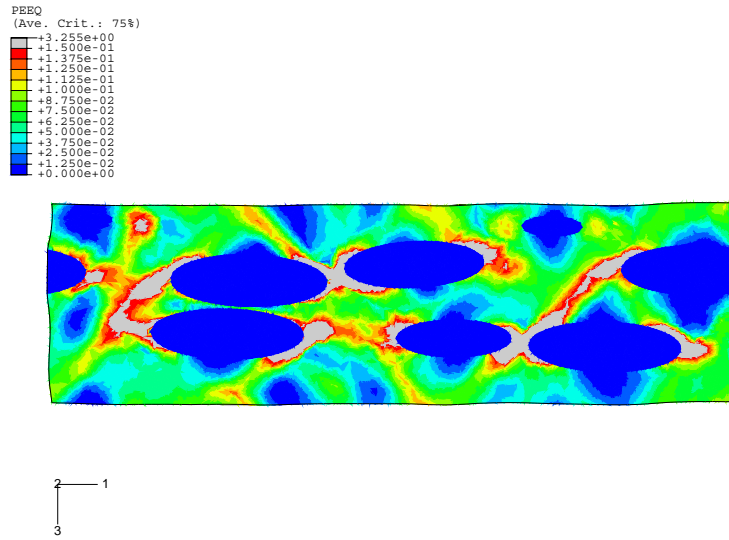
simulations as (González *et al.* [37]):

$$\langle \sigma^{eq} \rangle_{\omega_0} = \left[\sum_k \sigma_k^{eq} V_k \right] / \sum_k V_k, \quad (5.60)$$

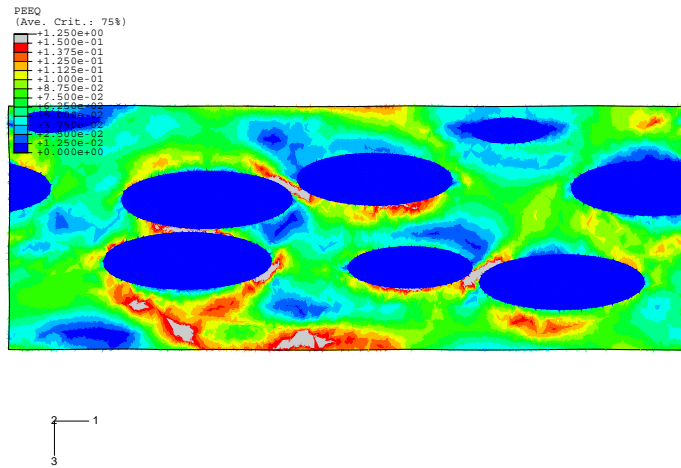
$$\langle \sigma \rangle_{\omega_0} = \left[\sum_k \sigma_k V_k \right] / \sum_k V_k, \quad (5.61)$$

$$\langle \sigma \otimes \sigma \rangle_{\omega_0} = \left[\sum_k (\sigma_k \otimes \sigma_k) V_k \right] / \sum_k V_k, \quad (5.62)$$

where σ_k is the stress tensor at the Gauss point k and V_k is its corresponding volume. Equation (5.60) gives the average equivalent stress and equations (5.61-5.62) give first and second order moments. These enable to compute the reference equivalent stress used in the first order and second order secant methods (equations (5.7-5.8)). Average of the equivalent stress and the two reference values obtained by FE at a macroscopic deformation state of 5% are plotted on figure 5.14. Equivalent stresses computed from the second order moment of the stress tensor are extremely close to the reference result while the one computed from the average stress tensor is always lower. This fact being more pronounced for low hardening exponent and in the longitudinal direction. These lower reference equivalent stresses of the matrix for the first order secant approach lead



(a) Longitudinal traction.



(b) Transverse traction.

Figure 5.12: Contour plot of the accumulated plastic strain in the matrix after tensile deformation up to 5% in the composite with $n = 0.05$.

to much higher equivalent stresses in the inclusions than ones obtained by the second order method and finally give too stiff macroscopic predictions as shown

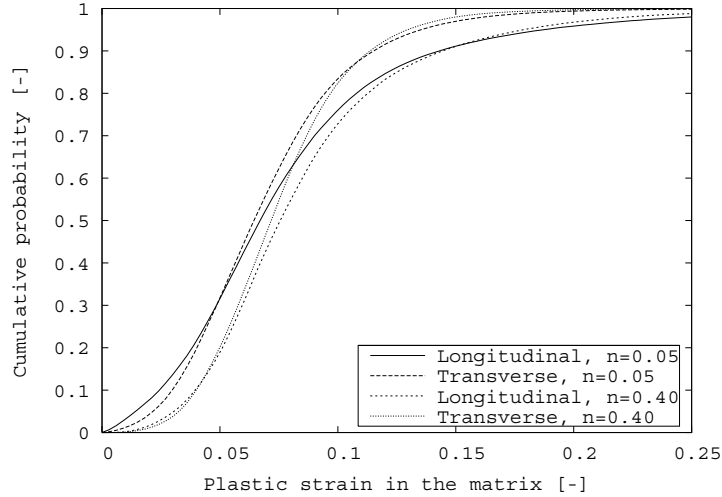


Figure 5.13: Cumulative probabilities of the plastic strain in the matrix as a function of the loading direction and of the matrix strain hardening exponent at a far-field applied strain of 5%.

on figures 5.10 and 5.11. After the study of the influence of the reference state on the macroscopic predictions, let's now examine the accuracy of the different homogenization schemes at the microscopic level. Effectively, even if a model provides a good estimation of the macroscopic behavior, this is not necessary true for the microscopic fields. This is illustrated on figure 5.15 for a traction test in the longitudinal direction and a high hardening exponent. Evolution of the matrix plastic strain is plotted with respect to the macroscopic strain (figure 5.15a). Plastic strain in the matrix is always underestimated by the mean-field homogenization schemes so that elastic effects dominate and the matrix hardening rate will be overestimated. This can be corrected either by using the second order secant method or the incremental one with a stiffness reduction of the matrix tangent operator. However, such approach decreases the accuracy of the von Mises equivalent stress in the inclusions (figure 5.15b), best prediction being then obtained with first order secant method. When looking at the components of the stress tensor in the phases, some surprises appear. For example, in the same simulation, the incremental method predicts a triaxial tension state in the inclusions and a compression in the direction of traction in the matrix even if the equivalent stress in both phases is not that far from the reference value. This illustrates the need for improvements in the per phase predictions of homogenization schemes, especially for modeling dam-

age by either inclusions fracture or interface debonding. For such tests, FE simulations are, by far, the best predictive method. FE simulations to model damage modeling are given by LLorca and Segurado [64] and Segurado and LLorca [93].

5.5 Conclusions

In this chapter, various formulations of the local elasto-plastic constitutive laws were reviewed. The incremental formulation, which links over a time step the strain increment to the stress increment through a tangent operator has been studied in depth. For simplicity, we focused on the matrix phase, assumed that it obeys classical J_2 elasto-plasticity and considered the Mori-Tanaka homogenization scheme. A key issue in Eshelby-based nonlinear homogenization is to define a homogeneous tangent operator $\mathbf{C}_0(t)$ for a fictitious reference matrix. The tangent operator is anisotropic (and designated by \mathbf{C}_0^{ani}) and computing the overall tangent operator $\bar{\mathbf{C}}$ with \mathbf{C}_0^{ani} leads to predictions which are too stiff and unacceptable. A known workaround is to compute the tensors of Eshelby (\mathcal{E}) or Hill (\mathbf{P}) with an isotropic part \mathbf{C}_0^{iso} of \mathbf{C}_0^{ani} and the rest of $\bar{\mathbf{C}}$ with \mathbf{C}_0^{ani} , but this method has been criticized as being unjustified or even wrong. Our opinion is that ideally $\bar{\mathbf{C}}$ should be computed with a given reference matrix tangent \mathbf{C}_0 . The fact that \mathbf{C}_0^{ani} leads to bad predictions means that it is a bad approximation to \mathbf{C}_0 . In the absence of an appropriate expression for \mathbf{C}_0 , the workaround consisting of computing part of $\bar{\mathbf{C}}$ (e.g. \mathcal{E} or \mathbf{P}) with \mathbf{C}_0^{iso} and the rest with \mathbf{C}_0^{ani} is acceptable as long as it leads to good predictions and is no less legitimate than computing all of $\bar{\mathbf{C}}$ with \mathbf{C}_0^{ani} . In this work, we chose to examine different variants for the computation of $\bar{\mathbf{C}}$ and understand why some work better than others by studying some of their mathematical properties. Some key points are recalled and discussed hereafter.

Hill's tensor (\mathbf{P}) and the overall tangent ($\bar{\mathbf{C}}$) are decreasing and increasing functions of \mathbf{C}_0 , respectively:

$$\mathbf{P}(\mathbf{C}_0 + \Delta\mathbf{C}) < \mathbf{P}(\mathbf{C}_0), \quad \bar{\mathbf{C}}(\mathbf{C}_0 + \Delta\mathbf{C}) > \bar{\mathbf{C}}(\mathbf{C}_0), \quad \Delta\mathbf{C} > 0. \quad (5.63)$$

A similar result for $\bar{\mathbf{C}}$ holds when only the argument of \mathbf{P} is changing:

$$\bar{\mathbf{C}}(\mathbf{P}(\mathbf{C}_0 + \Delta\mathbf{C}), \mathbf{C}_0) > \bar{\mathbf{C}}(\mathbf{P}(\mathbf{C}_0), \mathbf{C}_0), \quad \Delta\mathbf{C} > 0. \quad (5.64)$$

Two isotropic extractions of \mathbf{C}_0^{ani} exist: a general projection method (giving \mathbf{C}_0^{IsoGen}) and a special method (\mathbf{C}_0^{IsoSpe}). The following relations hold:

$$\mathbf{C} > \mathbf{C}_0^{ani} \geq \mathbf{C}_0^{IsoSpe}. \quad (5.65)$$

Therefore $\bar{\mathbf{C}}$ computed with the isotropic operator \mathbf{C}_0^{IsoSpe} is softer than the one computed with anisotropic operators \mathbf{C}_0^{ani} , i.e.

$$\bar{\mathbf{C}}(\mathbf{C}_0^{IsoSpe}) < \bar{\mathbf{C}}(\mathbf{C}_0^{ani}), \quad \bar{\mathbf{C}}(\mathbf{P}(\mathbf{C}_0^{IsoSpe}), \mathbf{C}_0) < \bar{\mathbf{C}}(\mathbf{P}(\mathbf{C}_0^{ani}), \mathbf{C}_0). \quad (5.66)$$

However, we found that in some cases (e.g., macro tension) the following result holds:

$$\mathbf{C}_0^{IsoGen} > \mathbf{C}_0^{ani}, \quad (5.67)$$

which means that the isotropic operator \mathbf{C}_0^{IsoGen} is stiffer than the anisotropic one, and this implies that:

$$\bar{\mathbf{C}}(\mathbf{C}_0^{IsoGen}) > \bar{\mathbf{C}}(\mathbf{C}_0^{ani}), \quad \bar{\mathbf{C}}(\mathbf{P}(\mathbf{C}_0^{IsoGen}), \mathbf{C}_0) > \bar{\mathbf{C}}(\mathbf{P}(\mathbf{C}_0^{ani}), \mathbf{C}_0). \quad (5.68)$$

This surprising and unexpected result may be interpreted physically following Chaboche *et al.* [18], [19]. Indeed, the special method (at least under proportional loading) corresponds to a stiffness reduction of \mathbf{C}_0^{ani} in a direction orthogonal to that of the reference flow direction (\mathbf{N}). Moreover the stiffness reduction effect is much more important with the special method than with the general one.

In this chapter, we also extracted transversely isotropic parts of \mathbf{C}_0^{ani} using a general projection method (giving $\mathbf{C}_0^{TrIsoGen}$) or a special one ($\mathbf{C}_0^{TrIsoSpe}$). In summary, in addition to \mathbf{C}_0^{ani} , we considered two isotropic projections (\mathbf{C}_0^{IsoGen} and \mathbf{C}_0^{IsoSpe}) and two transversely isotropic ones ($\mathbf{C}_0^{TrIsoGen}$ and $\mathbf{C}_0^{TrIsoSpe}$). Designating anyone of these five operators by \mathbf{C}_0 , \mathbf{D}_0 or \mathbf{E}_0 , we studied different variants of the incremental formulation by computing Hill's tensor as:

$$\mathbf{P} = \mathcal{E}(\mathbf{E}_0) : \mathbf{D}_0^{-1} \quad (5.69)$$

and the rest of $\bar{\mathbf{C}}$ with \mathbf{C}_0 . We conducted a series of validated numerical simulations for a variety of composites with different types of inclusions (long or short fibers, spherical particles) under various loads (longitudinal or transverse tension, transverse shear). The main conclusions are listed hereafter.

The sets which work best in most cases are the following:

$$\mathbf{E}_0 = \mathbf{C}_0^{IsoGen} \text{ or } \mathbf{C}_0^{IsoSpe}, \quad \mathbf{D}_0 = \mathbf{C}_0 = \mathbf{C}_0^{ani}. \quad (5.70)$$

In some cases, they fail and give physically unacceptable results, which is especially noticeable for materials reinforced with long fibers. This corresponds to \mathbf{P} losing diagonal (major) symmetry. When this happens, the following set gives good results:

$$\mathbf{E}_0 = \mathbf{D}_0 = \mathbf{C}_0^{IsoSpe}, \text{ i.e. } \mathbf{P}(\mathbf{C}_0^{IsoSpe}), \quad \mathbf{C}_0 = \mathbf{C}_0^{ani}. \quad (5.71)$$

It also leads to good predictions in most cases. However the choice $\mathbf{P}(\mathbf{C}_0^{IsoGen})$ leads to bad (too stiff) predictions. Another set which works in many cases is the following:

$$\mathbf{E}_0 = \mathbf{D}_0 = \mathbf{C}_0 = \mathbf{C}_0^{IsoSpe}, \text{ i.e. } \mathbf{P}(\mathbf{C}_0^{IsoSpe}) \text{ and } \bar{\mathbf{C}}(\mathbf{C}_0^{IsoSpe}). \quad (5.72)$$

Unfortunately, the use of \mathbf{C}_0^{IsoSpe} is limited to constitutive models for which the anisotropic tangent operator can be cast under the particular form (5.29).

If this is not the case and if the use of \mathbf{C}_0^{IsoGen} in (5.70) gives bad results, we advice to use the special method of the transversely isotropic projection with the following set:

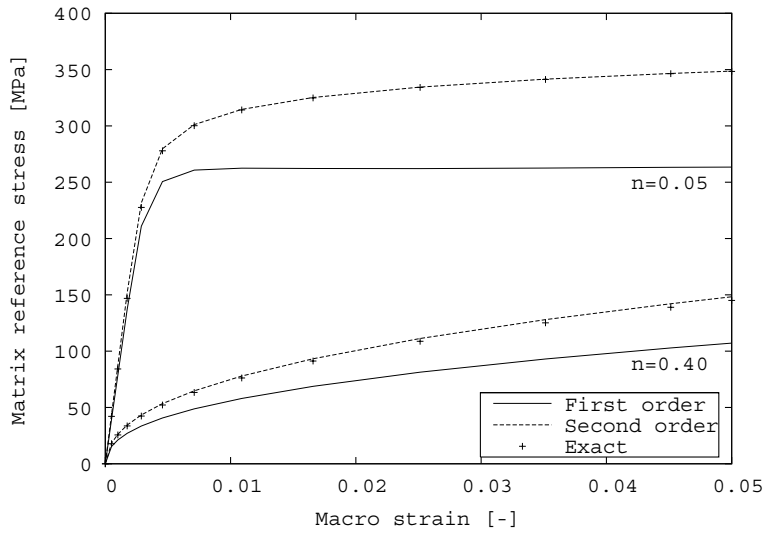
$$\mathbf{E}_0 = \mathbf{D}_0 = \mathbf{C}_0^{TrIsoSpe}, \text{ i.e. } \mathbf{P}(\mathbf{C}_0^{TrIsoSpe}), \quad \mathbf{C}_0 = \mathbf{C}_0^{ani}. \quad (5.73)$$

The case $\mathbf{P}(\mathbf{C}_0^{TrIsoGen})$ gives extremely stiff predictions. This means that $\mathbf{C}_0^{TrIsoGen}$ is too stiff. Similarly to isotropic projections, this might be explained by the fact that the general transversely isotropic projection is a mathematical definition with no physical basis. Other sets studied, namely $\bar{\mathbf{C}}(\mathbf{C}_0^{IsoGen})$, $\bar{\mathbf{C}}(\mathbf{C}_0^{TrIsoGen})$ and $\bar{\mathbf{C}}(\mathbf{C}_0^{ani})$ all lead in general to unacceptably stiff predictions.

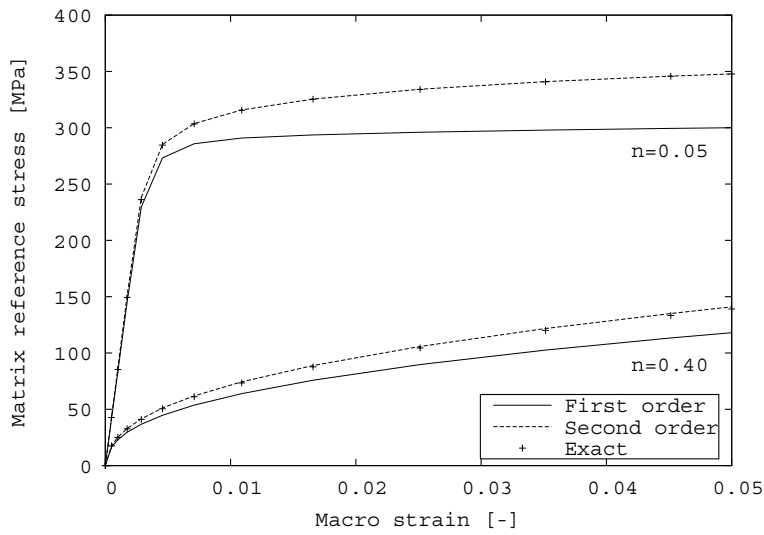
In the future, one could improve some points. For instance, in the transversely isotropic projection, try an anisotropy direction other than the ellipsoids' revolution axis or find a better special stiffness reduction method with no arbitrary coefficient K . Real progress in Eshelby-based nonlinear homogenization is possible only with new approaches in computing reference matrix tangent operator $\mathbf{C}_0(t)$, for instance with phase-averaged second-order moments of stress or strain. However, extending the latter approach to an incremental formulation and to sophisticated micro constitutive models remains an open question.

In order to analyze the influence of the per phase reference state and compare different formulations of the constitutive laws, the first order incremental formulation was confronted to both first and second order secant formulations and to FE simulations. The considered composite for this analysis was made of a matrix reinforced by 25% of aligned and randomly distributed ellipsoidal inclusions ($Ar=3$) and the Mori-Tanaka homogenization scheme was used. Different matrix strain hardening were considered and uniaxial traction tests were performed in both longitudinal and transverse directions.

For the overall predictions, best ones were obtained by the incremental and the second order secant formulations while the first order secant method gave generally too stiff results. The incremental tended to overestimate the composite flow stress when the localization of the plastic strain in the matrix was maximum, which occurred for the longitudinal tension test and a low matrix hardening exponent. Comparison of the volumetric-average fields in each phase showed that accurate predictions of the effective properties by the homogenization methods did not guarantee the same accuracy at the phase level.

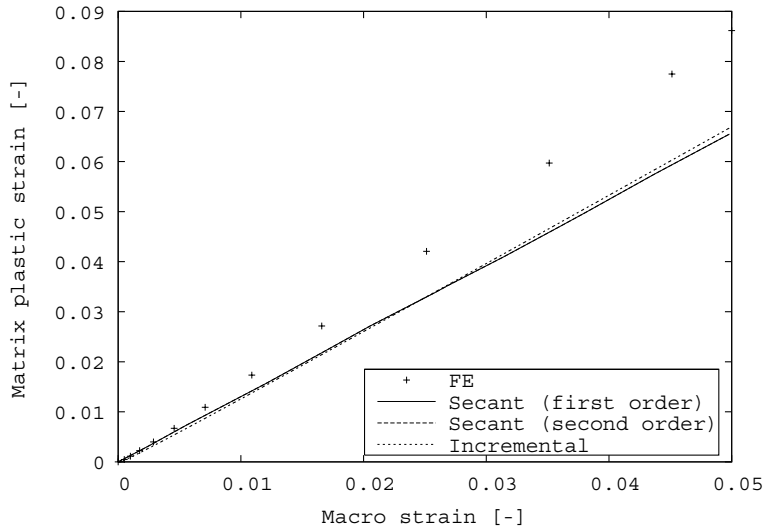


(a) Longitudinal deformation.

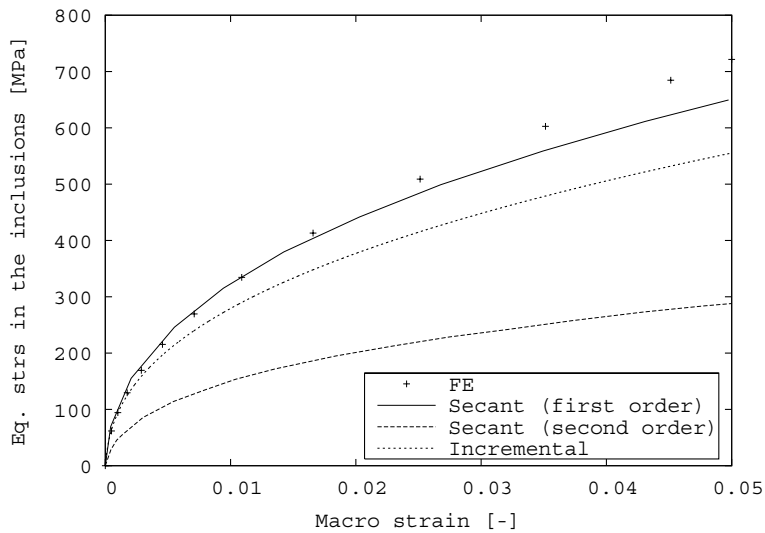


(b) Transverse deformation.

Figure 5.14: Evolution of the actual volume-averaged reference stress in the matrix ($\bar{\sigma}_m^{eq}$) as a function of the applied strain and of the estimation based on the volume-averaged first ($\hat{\sigma}_m^{eq}$) and second-order ($\hat{\hat{\sigma}}_m^{eq}$) moment of the matrix stress tensor.



(a) Evolution of the plastic strain the matrix as a function of the applied strain.



(b) Evolution of the von Mises equivalent stress in the ellipsoids as a function of the applied strain.

Figure 5.15: The composite is loaded in the longitudinal direction (matrix strain hardening exponent is 0.40).

Chapter 6

Homogenization of elasto-viscoplastic composites

¹ In this section, another type of behavior for the constitutive phases of the composite is examined. More precisely, in addition to the elasto-plastic nature of the phases, the plastic regime exhibits a dependence with the loading rate. Such phenomena appear especially at high temperatures.

6.1 Constitutive equations

The Perzyna-type elasto-viscoplastic constitutive model is used for all the simulations presented in this work. However, the proposed homogenization technique for elasto-viscoplastic composites is not restricted to this single model. The following developments are limited to isotropic hardening in each phase.

The Perzyna-type constitutive model

The additive decomposition of the total strain gives an elastic part and an inelastic one, so that the time derivative of the Hookean's law can be rewritten

¹Some developments of this chapter led to two publications “An enhanced affine formulation and the corresponding numerical algorithms for the mean-field homogenization of elasto-viscoplastic composites”, Pierard O. and Doghri I., *International Journal of Plasticity*, 22 (2006), pp.131-157 [78] and “Micromechanics of particle-reinforced elasto-viscoplastic composites: finite element simulations versus affine homogenization”, Pierard O., LLorca J., Segurado J. and Doghri I., *International Journal of Plasticity*, submitted for publication [82].

as:

$$\dot{\boldsymbol{\sigma}} = \mathbf{C} : (\dot{\boldsymbol{\varepsilon}} - \dot{\boldsymbol{\varepsilon}}^{in}). \quad (6.1)$$

As in elasto-plasticity, the inelastic strain rate is governed by a plastic flow rule:

$$\dot{\boldsymbol{\varepsilon}}^{in} = g_v \frac{\partial f}{\partial \boldsymbol{\sigma}} = \frac{3}{2} \frac{g_v}{\sigma_{eq}} \boldsymbol{\sigma}^{dev}, \quad (6.2)$$

where $g_v(\sigma_{eq}, p)$ is a viscoplastic function (see hereafter) which is equal to the plastic multiplier $\dot{\gamma}$ introduced for elasto-plasticity, f is the yield function ($f(\sigma_{eq}, p) = \sigma_{eq} - \sigma_Y - R(p)$) and is positive during plastic loading in the case of rate-dependent materials, σ_{eq} is the von Mises equivalent stress, σ_Y is the initial yield stress, $R(p)$ is the hardening stress (see hereafter), $\boldsymbol{\sigma}^{dev}$ is the deviatoric part of the stress tensor and p is the accumulated plasticity defined by (5.4). Combining these two relations leads to an equation linking stress and strain rates:

$$\dot{\boldsymbol{\sigma}} = \mathbf{C} : \left(\dot{\boldsymbol{\varepsilon}} - g_v(\sigma_{eq}, p) \frac{\partial f}{\partial \boldsymbol{\sigma}} \right). \quad (6.3)$$

Given this constitutive elasto-viscoplastic model, it is possible, for a homogeneous material, to predict the elasto-viscoplastic response. In order to compute the response of that material over a time step (the problem is supposed solved until the beginning of this time step) given either strain or stress increment, an algorithm is needed (e.g., (Doghri [24])) to solve two scalar equations by a Newton-Raphson scheme.

Hardening function

As in elasto-plasticity, the only hardening function considered in the subsequent simulations is a power-law model which is defined as:

$$R(p) = kp^n \text{ if } p > 0, 0 \text{ otherwise,} \quad (6.4)$$

where $k [Pa]$ is the hardening modulus and $n [-]$ the hardening exponent.

Viscoplastic function

The two viscoplastic functions defined hereafter require two parameters: the viscoplastic modulus ($\eta [Pa.s]$ or $\kappa [1/s]$) and the viscoplastic exponent $m [-]$.

- Norton's viscoplastic power law:

$$g_v(\sigma_{eq}, p) = \frac{\sigma_Y}{\eta} \left(\frac{\sigma_{eq} - \sigma_Y - R(p)}{\sigma_Y} \right)^m \text{ if } f > 0, 0 \text{ otherwise.} \quad (6.5)$$

- Viscoplastic power law as defined in ABAQUS [1]:
This law is obtained by a slight modification of Norton's power law. Implementation of this law is useful for validation purposes.

$$g_v(\sigma_{eq}, p) = \kappa \left(\frac{\sigma_{eq} - \sigma_Y - R(p)}{\sigma_Y + R(p)} \right)^m \quad \text{if } f > 0, 0 \text{ otherwise.} \quad (6.6)$$

6.2 Homogenization of elasto-viscoplastic composites

In elasto-viscoplasticity, there is no one-to-one correspondence between stress and strain rates through a so-called continuum tangent operator \mathbf{C}^{ep} such as it exists in elasto-plasticity. It results that the incremental formulation of elasto-plastic composites (Hill [43]) cannot rigorously be used. However, when considering finite strain and stress increments instead of infinitesimal ones, an algorithmic tangent operator \mathbf{C}^{alg} derived from a consistent linearization of the time-discretized constitutive equations exists in elasto-viscoplasticity (Ju [48], Doghri [24]):

$$\dot{\boldsymbol{\sigma}} \neq \mathbf{C}^{in} : \dot{\boldsymbol{\varepsilon}}, \quad \mathbf{C}^{alg} = \frac{\partial(\Delta\boldsymbol{\sigma})}{\partial(\Delta\boldsymbol{\varepsilon})}. \quad (6.7)$$

It is thus tempting to use a Hill-type incremental formulation nevertheless, but based on \mathbf{C}^{alg} . Unfortunately, as observed in various simulations, such an approach gives too stiff responses. Such as done nowadays in elasto-plasticity, some adjustments should be done in order to get accurate predictions with an incremental formulation (e.g.: Doghri and Ouaar [26], Doghri and Friebel [25], Doghri and Tinel [27]). In some cases, using the latter formulation in elasto-viscoplasticity with algorithmic tangent operators \mathbf{C}^{alg} gives acceptable predictions (an example is given in section 6.4.1). Another widely used formulation is the secant one. Li and Weng [58, 59, 60] performed various interesting simulations by making use of a secant viscosity in the local constitutive laws. However, the secant formulation cannot handle some important cases such as unloading, cyclic loading and otherwise non-proportional loading histories. A non-classical formulation is thus needed and the so-called affine formulation adopted in this work transforms the problem into a fictitious linear thermo-elastic one which can be homogenized according to classical homogenization schemes. This approach was introduced by Molinari *et al.* [69] and improved by Masson [66].

In order to predict the overall behavior, a homogenization scheme is used. Such an approach is much faster than a purely numerical method (e.g.: finite elements), especially when dealing with real structures for which two meshes are needed at different scales. However, in order to validate this model, FE simulations performed on unit cells are also carried out.

6.3 The affine formulation

In this section, the affine homogenization introduced by Masson [66] is presented. Main steps of the linearization, predictions of the final response as well as an algorithm are detailed. Finally, a special attention is paid to the differences with previous implementations of this method.

The affine formulation relies on a linearization in time of the constitutive equations of the strain rate and the rate of internal variables. For clarity of the development, a single scalar internal variable p , not yet specified, is considered. When dealing with hereditary behaviors (such as in elasto-viscoplasticity), a direct prediction of the response is impossible and a discretization into time steps is required. During all the linearization procedure described hereafter, the problem is considered over a time step, for which the solution is supposed already found up to the beginning of the time step (t_n). For this, the constitutive model has to be written under the general form:

$$\dot{\boldsymbol{\varepsilon}}(t) = \underbrace{\mathbf{S} : \dot{\boldsymbol{\sigma}}(t)}_{\dot{\boldsymbol{\varepsilon}}^{el}(t)} + \dot{\boldsymbol{\varepsilon}}^{in}(\boldsymbol{\sigma}(t), p(t)), \quad (6.8)$$

$$\dot{p}(t) = \dot{p}(\boldsymbol{\sigma}(t), p(t)), \quad (6.9)$$

with $\dot{\boldsymbol{\varepsilon}}(t)$ the total strain rate, $\dot{\boldsymbol{\sigma}}(t)$ the Cauchy stress rate, $\dot{\boldsymbol{\varepsilon}}^{el}$ and $\dot{\boldsymbol{\varepsilon}}^{in}$ the elastic and inelastic strain rates, respectively, and \mathbf{S} the elastic compliance tensor.

6.3.1 From elasto-viscoplasticity to linear thermo-viscoelasticity

The first step in the theory is a linearization of equations (6.8-6.9) around time t_n :

$$\dot{\boldsymbol{\varepsilon}}^{in}(t) = \dot{\boldsymbol{\varepsilon}}^{in}(t_n) + \mathbf{m}(\tau) : [\boldsymbol{\sigma}(t) - \boldsymbol{\sigma}(t_n)] + \mathbf{n}(\tau)[p(t) - p(t_n)], \quad (6.10)$$

$$\dot{p}(t) = \dot{p}(t_n) + \mathbf{l}(\tau) : [\boldsymbol{\sigma}(t) - \boldsymbol{\sigma}(t_n)] + q(\tau)[p(t) - p(t_n)], \quad (6.11)$$

in which four derivatives are introduced:

$$m_{ijkl} = \frac{\partial \dot{\boldsymbol{\varepsilon}}_{ij}^{in}}{\partial \sigma_{kl}}, \quad n_{ij} = \frac{\partial \dot{\boldsymbol{\varepsilon}}_{ij}^{in}}{\partial p}, \quad l_{kl} = \frac{\partial \dot{p}}{\partial \sigma_{kl}}, \quad q = \frac{\partial \dot{p}}{\partial p}. \quad (6.12)$$

These derivatives are evaluated at time τ , which belongs to the time interval $[t_n; t]$. Analytical expressions of these derivatives are available once the constitutive model is defined.

For the Perzyna-type constitutive model (section 6.1), these derivatives are

nil if the yield function is negative or nil. If $f > 0$, they are given by:

$$\begin{aligned} m_{ijkl} &= \frac{\partial g_v}{\partial \sigma_{eq}} N_{kl} N_{ij} + g_v \frac{\partial N_{ij}}{\partial \sigma_{kl}} \quad , \quad n_{ij} = \frac{\partial g_v}{\partial p} N_{ij}, \\ l_{kl} &= \frac{\partial g_v}{\partial \sigma_{eq}} N_{kl} \quad , \quad q = \frac{\partial g_v}{\partial p}, \end{aligned} \quad (6.13)$$

where:

$$\frac{\partial N_{ij}}{\partial \sigma_{kl}} = \frac{1}{\sigma_{eq}} \left[\frac{3}{2} I_{ijkl}^{dev} - N_{ij} N_{kl} \right]. \quad (6.14)$$

Derivative q is always negative, which is logical. If p increases, $R(p)$ increases also and since the stress is considered constant in this partial derivative, $f(\boldsymbol{\sigma}_{eq}, p)$ decreases. Thus, the viscoplastic function $g_v(\boldsymbol{\sigma}_{eq}, p)$ and \dot{p} decrease so that $q = \frac{\partial g_v}{\partial p}$ is negative.

As shown in appendix D.1, the solution of equation (6.11) can be given under the integral form:

$$p(t) - p(t_n) = \hat{p}(\tau, t) + \int_0^t e^{(t-u)q(\tau)} \mathbf{l}(\tau) : \boldsymbol{\sigma}(u) du, \quad (6.15)$$

where:

$$\begin{aligned} \hat{p}(\tau, t) &= q^{-1}(\tau) [e^{(t-t_n)q(\tau)} - 1] [\dot{p}(t_n) - \mathbf{l}(\tau) : \boldsymbol{\sigma}(t_n)] \\ &\quad - \int_0^{t_n} e^{(t-u)q(\tau)} \mathbf{l}(\tau) : \boldsymbol{\sigma}(u) du. \end{aligned} \quad (6.16)$$

By inserting result (6.15) in equation (6.10) and after some mathematical manipulations (detailed proof in appendix D.2), the problem (6.10-6.11) is rewritten as:

$$\dot{\boldsymbol{\epsilon}}(t) = \frac{d}{dt} \left[\int_0^t \mathbf{S}_\tau(\tau, t-u) : \dot{\boldsymbol{\sigma}}(u) du \right] + \dot{\boldsymbol{\epsilon}}^0(\tau, t) = [\mathbf{S}_\tau \odot \dot{\boldsymbol{\sigma}}]_{(\tau, t)} + \dot{\boldsymbol{\epsilon}}^0(\tau, t), \quad (6.17)$$

in which the Stieljes-type convolution product denoted by \odot is introduced. Semi-analytical expressions of tensors $\mathbf{S}_\tau(\tau, t)$ and $\dot{\boldsymbol{\epsilon}}^0(\tau, t)$ are reported in appendix D.2.

Rewriting local constitutive equations as (6.17) is remarkable as they become similar to linear viscoelastic ones, with an additive eigenstrain rate term. Classically, this problem is solved with the help of the Laplace-Carson transform as presented in the next section.

6.3.2 From linear thermo-viscoelasticity to linear thermo-elasticity

Similarly to the solution method proposed for linear viscoelastic materials (section 4.4.1), the Laplace-Carson transform (appendix B.1) is used to write equation (6.17) in a linear elastic form. Under this transformation, the Stieljes-type

convolution product becomes a single contraction so that the linearized constitutive law reads:

$$\dot{\boldsymbol{\varepsilon}}^*(s) = \mathbf{S}_\tau^*(\tau, s) : \dot{\boldsymbol{\sigma}}^*(s) + \dot{\boldsymbol{\varepsilon}}^{0*}(\tau, s), \quad (6.18)$$

$$\text{or equivalently } \dot{\boldsymbol{\sigma}}^*(s) = \mathbf{C}_\tau^*(\tau, s) : (\dot{\boldsymbol{\varepsilon}}^*(s) - \dot{\boldsymbol{\varepsilon}}^{0*}(\tau, s)), \quad (6.19)$$

$$\text{with } \mathbf{C}_\tau^*(\tau, s) = [\mathbf{S}_\tau^*(\tau, s)]^{-1},$$

where an asterisk in exponent means the Laplace-Carson transform and s is the Laplace variable. \mathbf{S}_τ^* and $\dot{\boldsymbol{\varepsilon}}^{0*}$ are given by (proof in appendix D.3):

$$\mathbf{S}_\tau^*(\tau, s) = \mathbf{S} + \frac{\mathbf{m}(\tau)}{s} + \frac{\mathbf{n}(\tau) \otimes \mathbf{l}(\tau)}{s(s - q(\tau))}, \quad (6.20)$$

$$\begin{aligned} \dot{\boldsymbol{\varepsilon}}^{0*}(\tau, s) &= \dot{\boldsymbol{\varepsilon}}^{in}(t_n)e^{-s\tau} + s \int_0^{t_n} \dot{\boldsymbol{\varepsilon}}^{in}(t)e^{-st} dt \\ &\quad - s\mathbf{m}(\tau) : \int_0^{t_n} \boldsymbol{\sigma}(t)e^{-st} dt - \mathbf{m}(\tau) : \boldsymbol{\sigma}(t_n)e^{-st_n} \\ &\quad - q^{-1}(\tau)\dot{p}(t_n) \frac{se^{-st_n}}{q(\tau) - s} \mathbf{n}(\tau) \\ &\quad + q^{-1}(\tau) \left[\frac{s}{q(\tau) - s} + 1 \right] \mathbf{l}(\tau) : \boldsymbol{\sigma}(t_n)e^{-st_n} \mathbf{n}(\tau) \\ &\quad + q^{-1}(\tau)\mathbf{l}(\tau) : \boldsymbol{\sigma}(t_n)e^{-st_n} \mathbf{n}(\tau) \\ &\quad - q^{-1}(\tau)\dot{p}(t_n)e^{-st_n} \mathbf{n}(\tau) \\ &\quad + \frac{s}{q(\tau) - s} \mathbf{n}(\tau) : \mathbf{l}(\tau) \int_0^{t_n} \boldsymbol{\sigma}(t)e^{-st} dt \\ &\quad + \widehat{\boldsymbol{\varepsilon}}^{0*}(\tau, s, \boldsymbol{\sigma}(0)), \end{aligned} \quad (6.21)$$

$$\widehat{\boldsymbol{\varepsilon}}^{0*}(\tau, s, \boldsymbol{\sigma}(0)) = \mathbf{m}(\tau) : \boldsymbol{\sigma}(0) - \mathbf{n}(\tau)q^{-1}(\tau) \left(1 - \frac{s}{s - q(\tau)} \right) \mathbf{l}(\tau) : \boldsymbol{\sigma}(0).$$

A proof of these expressions is given in appendix D.3. A special attention is paid to the computation at a low memory cost of these integrals so that they are always evaluated from variables at the end of the previous time step, which requires to decompose the integrals. Some details are given in appendices C and D. These equations are similar to those of linear thermo-elasticity. Of course, they are fictitious constitutive equations since they are defined in the Laplace-Carson domain. Classical homogenization schemes valid in linear thermo-elasticity can thus apply.

6.3.3 Algorithm

Consider now a two-phase elasto-viscoplastic composite for which constitutive equations of each phase can be linearized over a time interval as (6.19). Simi-

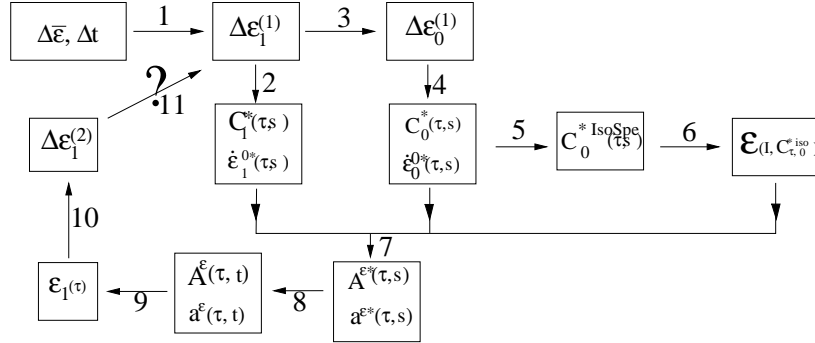


Figure 6.1: Iterative procedure to find the correct strain increments in the phases. Labels 1, . . . , 11 refer to the step numbers in the algorithm of section 6.3.3.

larly to linear thermo-elasticity, localization equation can be written as:

$$\langle \dot{\boldsymbol{\varepsilon}}^*(s) \rangle_{\omega_1} = \mathbf{A}^{\varepsilon^*}(\tau, s) : \dot{\boldsymbol{\varepsilon}}^*(s) + \mathbf{a}^{\varepsilon^*}(\tau, s), \quad (6.22)$$

Corresponding relation in the time domain writes:

$$\langle \boldsymbol{\varepsilon}(t) \rangle_{\omega_1} = \langle \boldsymbol{\varepsilon}(0) \rangle_{\omega_1} + [\mathbf{A}^\varepsilon \otimes \dot{\boldsymbol{\varepsilon}}]_{(\tau,t)} + \int_0^t \mathbf{a}^\varepsilon(\tau, u) du, \quad (6.23)$$

where \mathbf{A}^ε and \mathbf{a}^ε are the strain localization tensors defined for the homogenization of two-phase linear thermo-elastic composites. In this section, an iterative procedure to determine strain increments in each phase over a time step is proposed. For this, consider the problem solved until the beginning of this time step, all local variables being known at that time. Over the time step $[t_n, t_{n+1}]$, a macro strain increment $\Delta \bar{\boldsymbol{\varepsilon}}$ is given. The algorithm is illustrated schematically on figure 6.1, main steps being described hereafter.

1. Initialization of the average strain increment $\Delta \boldsymbol{\varepsilon}_1$ in the inclusions with the converged value at the previous time step weighted by a possible variation of the time increment: $\Delta \boldsymbol{\varepsilon}_1 = \frac{t_{n+1} - t_n}{t_n - t_{n-1}} (\boldsymbol{\varepsilon}_1(t_n) - \boldsymbol{\varepsilon}_1(t_{n-1}))$.
2. Computation of the affine stiffness modulus $\mathbf{C}_1^*(\tau, s)$ and the eigenstrain tensor $\dot{\boldsymbol{\varepsilon}}_1^{0*}(\tau, s)$ in (6.19) in the reference inclusions' phase. For this, the response of the phase has first to be computed according to the constitutive model of the inclusions with $\Delta \boldsymbol{\varepsilon}_1$ as input. Secondly, one has to compute the derivatives of the evolution laws of inelastic strain rates and rate of plasticity with respect to their parameters (6.12). These are evaluated at time $\tau = t_{n+1}$. The discretization is done implicitly so that the

derivatives are evaluated at t_{n+1} . Finally, the required $\mathbf{C}_1^*(\tau, s)$ is computed by taking the inverse of expression (6.20) and $\dot{\boldsymbol{\varepsilon}}_1^{0*}(\tau, s)$ by using (6.21).

3. Evaluation of the corresponding strain increment in the matrix:

$$\Delta \boldsymbol{\varepsilon}_0 = \frac{1}{v_0} (\Delta \bar{\boldsymbol{\varepsilon}} - v_1 \Delta \boldsymbol{\varepsilon}_1).$$
4. As in step 2, computation of the tensors $\mathbf{C}_0^*(\tau, s)$ and $\dot{\boldsymbol{\varepsilon}}_0^{0*}(\tau, s)$ for the matrix phase.
5. Extraction of the special isotropic part of $\mathbf{C}_0^*(\tau, s)$ as done for the incremental formulation in elasto-plasticity (section 5.3.3) - noted $\mathbf{C}_0^{*IsoSpe}(\tau, s)$.
6. Computation of Eshelby's tensor $\mathcal{E}(I, \mathbf{C}_0^{*IsoSpe}(\tau, s))$ with $\mathbf{C}_0^{*IsoSpe}(\tau, s)$ and the inclusions shape (I) (appendix A.1).
7. Computation of the strain concentration tensors $\mathbf{A}^{\varepsilon*}(\tau, s)$ and $\mathbf{a}^{\varepsilon*}(\tau, s)$ in the Laplace domain (equations (4.25, 4.56b), \mathbf{B}^ε is given by the adopted homogenization scheme - see section 4.2.3).
8. Numerical Laplace inversion (see appendix B.2) of $\mathbf{A}^{\varepsilon*}(\tau, s)$ and $\mathbf{a}^{\varepsilon*}(\tau, s)$. To perform this operation, the strain concentration tensors of step 7 must be evaluated at several collocation points s_i in the Laplace-Carson domain. Limit values of these functions are needed for the inversion and are given in appendix D.4.
9. Evaluation of a new value of the average strain in the inclusions at $t = t_{n+1}$ according to relation (6.23). When using a collocation method as advocated for the numerical Laplace inversion, the corresponding time function is under a serial decomposition form so that the convolution product and the integral can be evaluated analytically (not too difficult for the integral and see appendix C for the incremental computation of the convolution product).
10. Computation of the average strain increment in the inclusions.
11. Comparison of this new value with the one at the beginning of this iteration. If it deviates too much, a new iteration is performed with this new value. Otherwise, the estimates per phase are accepted and the overall macroscopic response is computed as explained in section 6.3.4.

This algorithm is the core of the “Affinistan” software developed in the context of this thesis. A short presentation is given in appendix F.

6.3.4 Prediction of the macroscopic response

Once the average strain increments in each phase are found by the algorithm presented in section 6.3.3, there are two different ways to compute the macroscopic stress response corresponding to a macro strain increment.

The first method considers that the macroscopic stress is the spatial average of the local stresses, i.e. sum of the average stresses in the phases weighted by the corresponding volume fraction of that phase. This is easily done at a low computation cost.

The second method is based on a macroscopic linear viscoelastic relation. Indeed, in the linearization procedure, linear viscoelastic constitutive relations exist for each phase at each time step so that the macroscopic one at a given time step is form-similar:

$$\bar{\sigma}(t_{n+1}) = \bar{\sigma}(0) + \int_0^{t_{n+1}} \bar{C}_\tau(\tau, t_{n+1} - u) : (\dot{\epsilon}(u) - \dot{\epsilon}^0(t_{n+1}, u)) du. \quad (6.24)$$

At first, computation of the homogenized tensors ($\bar{C}^*(\tau, s)$ and $\dot{\epsilon}^{0*}(\tau, s)$) in thermo-elasticity are needed. The numerical Laplace inversion back to the time domain (see appendix B.2) of these tensors give serial decompositions so that the convolution product can be computed analytically, and finally, the macroscopic stress response is computable.

This second approach is more time-consuming and requires two additional numerical inversions of the Laplace-Carson transform. Since some numerical errors appear in this inversion and the method is sensitive to the choice of the collocation points (see appendix B.2), the quality of the final prediction might be better with the first method. For example, using (6.24) introduces some fictitious plasticity during elastic unloading or reloading. The two methods have been implemented and with a minimum of care with the numerical Laplace inversions, no significant differences on the predictions have been observed. Logically, for performance reasons, the first option is the default one.

If there are constraints on the corresponding macroscopic stress tensor (e.g.: uniaxial tension, biaxial tension, shear, . . .), an additive iterative loop is necessary and is described in appendix E. For this purpose, several components of the macroscopic tangent operator are needed. This is done with a perturbation method.

6.3.5 Main differences with previous implementations

The major differences in our implementation with previous ones (Brenner *et al.* [15], Masson and Zaoui [68], Masson *et al.* [67]) are the following:

- A full treatment of the evolution laws of internal variables, e.g.: accumulated plasticity for composite materials or resistances of the slip systems

for polycrystals. This consideration adds a great deal of complexity to the mathematical developments of the affine formulation.

- This work is focused on two-phase composites, on the contrary to Masson [66] who studied various crystalline symmetries and especially Zirconium's alloys modeled as polycrystals. The fact that we consider a different microstructure does not have an impact on the development of the affine formulation itself, but on the constitutive models of the phases and most importantly on the numerical algorithms which have to be robust in order to handle different constitutive models and contrasts between phase materials.
- An extensive validation of the method. Up to now, very few validations were available.
- Simulations are performed under various loading cases. To our knowledge, no one has performed cyclic loading tests with an affine formulation before.

It should be noted that two extensions of the affine formulation have been developed by Brenner *et al.* [14]. First one deals with a simplified numerical Laplace-Carson transform. Such approach enables to reduce the required computation time for this operation and is especially useful for polycrystals due to the numerous different grains. The other extension takes into account the second order moment of the stress tensor in the definition of the reference state. This is done for polycrystals which exhibit a power law constitutive law. In this case, the secant and affine moduli are linked in a simple way so that the evaluation of the second order moment of the stress tensor can be obtained in a semi analytical fashion.

6.4 Numerical simulations

6.4.1 General simulations

In this first part of the numerical simulations of the affine formulation, a wide range of loading paths, homogenization methods and comparisons with another formulation are presented. In the description of the material properties, subscript 0 refers to the matrix and 1 to the inclusions.

Effect of the homogenization formulation In the past, the incremental formulation has been criticized for giving too stiff predictions. Extracting the isotropic part of the algorithmic tangent modulus leads to much more realistic predictions in the elasto-plastic regime (Doghri and Ouaar [26]). As mentioned

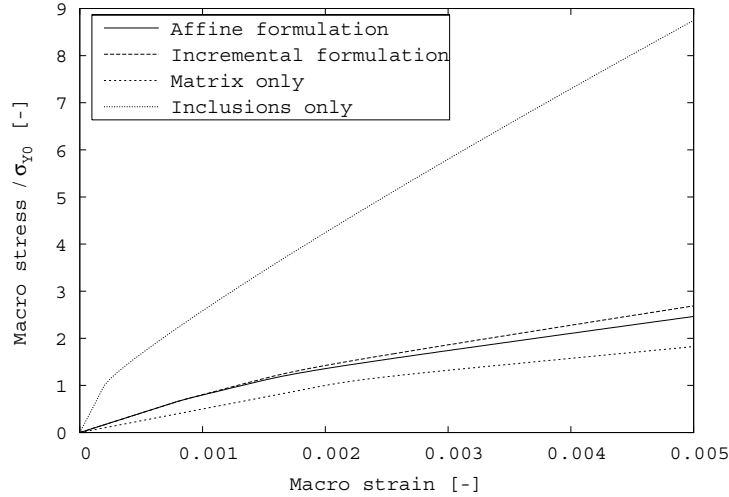


Figure 6.2: Uniaxial tension test. Comparison of the affine and incremental formulations.

in section 6.2, the incremental formulation cannot rigorously be used in the rate-dependent case because of the absence of continuum tangent operators relating strain and stress rates. Nevertheless, since an algorithmic tangent operator \mathbf{C}^{alg} -equation (6.7b)- can be defined, the idea in this section is to run the incremental formulation in elasto-viscoplasticity with \mathbf{C}^{alg} although there is no constitutive justification for \mathbf{C}^{alg} . The predictions will be compared to those of the affine formulation.

Material properties of the considered two-phase composite are the following (Norton's viscoplastic power law is used): $E_0 = 50$ GPa, $\nu_0 = 0.3$, $\sigma_{Y_0} = 100$ MPa, $k_0 = 50$ GPa, $n_0 = 1.0$, $\eta_0 = 30.0$ GPa.s and $m_0 = 1.0$ for the matrix which is reinforced by 30% of spherical inclusions with the following properties: $E_1 = 500$ GPa, $\nu_1 = 0.3$, $\sigma_{Y_1} = 100$ MPa, $k_1 = 100$ GPa, $n_1 = 0.85$, $\eta_1 = 10.0$ GPa.s and $m_1 = 1.0$. This composite undergoes a uniaxial tension test at a constant strain rate of 10^{-3} s^{-1} .

Predictions obtained with the two formulations are reported on figure 6.2, as well as responses of individual phases alone. As expected, this test shows that the prediction of the affine formulation is softer than that of the incremental one, although in this example the difference is not too pronounced.

Effect of the inclusions shape A major advantage of Eshelby-based homogenization schemes is that they can predict the influence of the shape of the inclusions. In this test, predictions of two composites made of the same

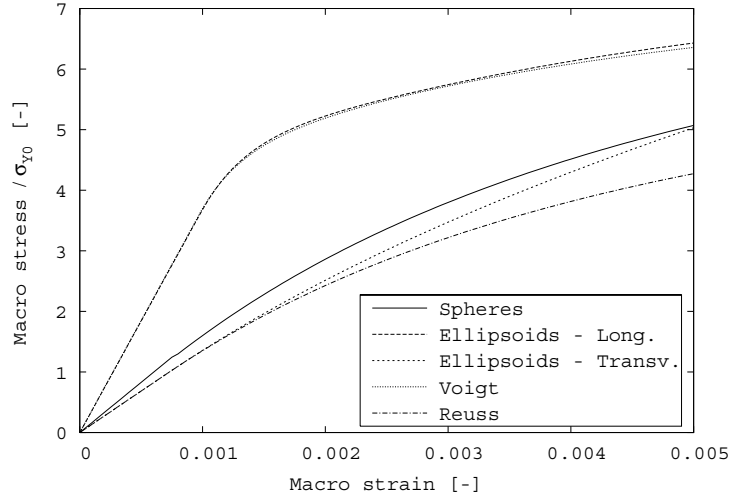


Figure 6.3: Uniaxial tension test in the longitudinal and transverse directions. Influence of the reinforcements shape.

materials are compared, one being reinforced with spheres, the other by long fibers. These results are confronted to the bounds of Reuss and Voigt (which are independent of the reinforcements shape).

In this test, the contrast between the phases is more pronounced : $E_0 = 100$ GPa, $\nu_0 = 0.3$, $\sigma_{Y_0} = 100$ MPa, $E_1 = 1000$ GPa, $\nu_1 = 0.3$ and $\sigma_{Y_1} = 1000$ MPa. Both phases obey a power law hardening function and Norton's viscoplastic law ($k = 10$ GPa, $n = 1$, $\eta = 300$ GPa.s and $m = 1$). The uniaxial tension test is performed at a constant strain rate of 10^{-3} s^{-1} . For both composites, the volume fraction of the inclusions is 30%.

Logically, as illustrated on figure 6.3, the composite made with fibers has, in the longitudinal direction, a much better resistance to this traction test than the composite reinforced by spheres. On the contrary, the response in the transverse direction of the composite reinforced by fibers is softer than the one of the composite made with spheres. One can note that the response of the long fiber composite predicted with Mori-Tanaka in the direction of the fibers is slightly stiffer than with Voigt! This is due to some small numerical errors occurring in the Laplace inversion as explained in appendix B.2. The Reuss and Voigt schemes avoid these problems since inversions of the constant strain concentration tensors are obvious.

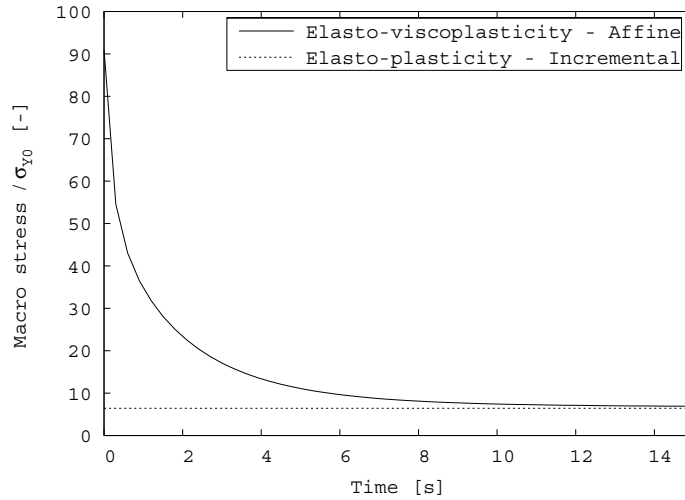


Figure 6.4: Uniaxial relaxation test of a long fiber reinforced composite in the longitudinal direction. Illustration of the viscous effects.

Relaxation test In this relaxation test, the influence of the viscous effects is illustrated. Transient viscous effects of the studied composite is compared to the rate independent response of this composite.

The properties of this composite are the following: $E_0 = 100$ GPa, $\nu_0 = 0.2$ and $\sigma_{Y_0} = 100$ MPa for the matrix, $E_1 = 500$ GPa, $\nu_1 = 0.3$ and $\sigma_{Y_1} = 500$ MPa for the inclusions. For both phases, the power law hardening model is defined by $k = 10$ GPa and $n = 1$. The Norton's viscoplastic laws have different parameters for each phase: $\eta_0 = 300$ GPa.s, $n_0 = 1.1$ for the matrix and $\eta_1 = 500$ GPa.s, $n_1 = 1.8$ for the long fibers. The composite is reinforced by long fibers (20% of volume fraction) aligned with the direction of uniaxial relaxation.

On figure 6.4, initial stress response of the rate-dependent composite is the homogenized elastic one. Furthermore, it is observed at long times that the response of the composite tends to the instantaneous elasto-plastic one, which is obtained by the commercial software DIGIMAT [23]. This result is also obtained with homogenization methods but with an incremental formulation in elasto-plasticity.

Effect of the loading strain rate This simulation illustrates the influence of the loading strain rate in a shear test. For decreasing strain rates, responses become softer and should tend to the rate independent one.

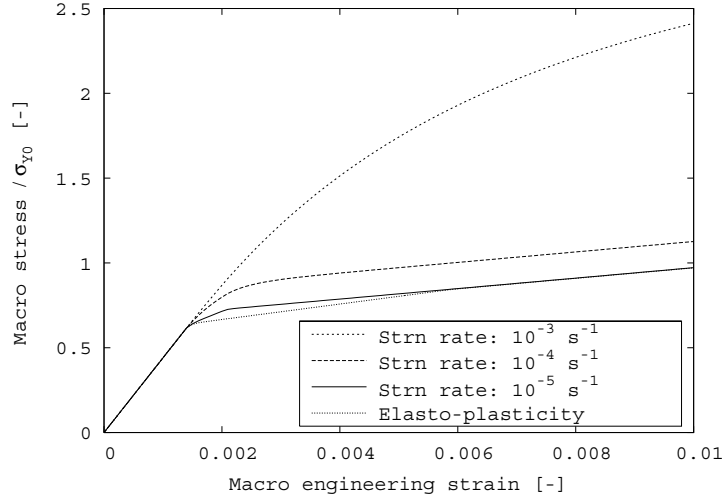


Figure 6.5: Sphere-reinforced composite under a shear test. Influence of the loading strain rate.

The two phases of this composite obey to power law hardening model and Norton's viscoplastic law. Mechanical properties are the following: $E_0 = 100$ GPa, $E_1 = 200$ GPa, $\nu_0 = \nu_1 = 0.3$, $\sigma_{Y_0} = 100$ MPa, $\sigma_{Y_1} = 200$ MPa, $k_0 = k_1 = 10$ GPa, $n_0 = n_1 = 1$, $\eta_0 = \eta_1 = 300$ GPa.s and $m_0 = m_1 = 1$. The volume fraction of spherical inclusions is 20 %.

Responses of the rate-dependent composite at various strain rates are plotted on figure 6.5. For comparison, the rate independent response computed with the commercial program DIGIMAT [23] is also reported. Simulation at the lowest strain rate (10^{-5} s^{-1}) is almost identical to the elasto-plastic response since hardening introduced by the strain rate is negligible while at higher strain rates, the response becomes logically stiffer. At low strain rates, the prediction doesn't drop below this rate independent limit, even if these two responses are obtained with two completely different approaches. However, at very low strain rates (order of 10^{-10} s^{-1}), numerical instabilities arise and a lack of precision is observed in the affine formulations.

6.4.2 Validation against 3D finite element simulations

As second part of the numerical validations of the affine formulation, confrontations are made against 3D FE simulations. Per phase analysis is also performed in order to better understand the limits of the method.

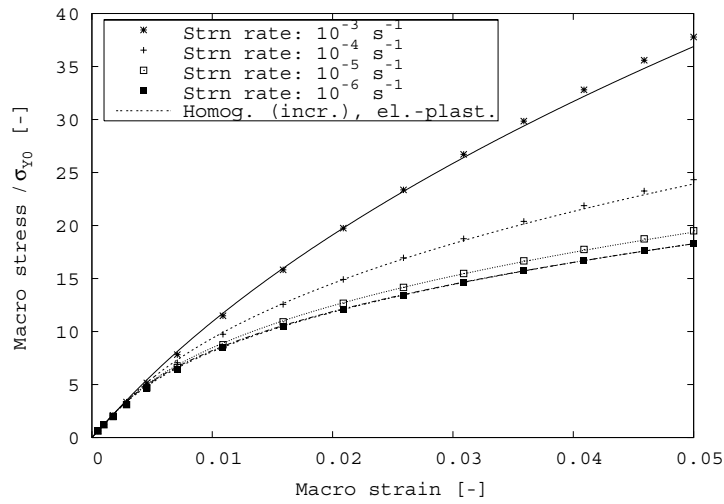
Throughout this section, only one material is considered in order to get more

relevant interpretations. This is a two-phase elasto-viscoplastic composite with a hardening power law (section 6.1) and the rate-dependent power law defined in ABAQUS (section 6.1). According to the notations previously introduced, the parameters are the following: $E_0 = 70$ GPa, $\nu_0 = 0.33$, $\sigma_{Y0} = 70$ MPa, $k_0 = 4$ GPa, $n_0 = 0.4$, $\kappa_0 = 3 \cdot 10^{-4} \text{ s}^{-1}$ and $m_0 = 1.5$ for the matrix and $E_1 = 400$ GPa, $\nu_1 = 0.286$, $\sigma_{Y1} = 400$ MPa, $k_1 = 8$ GPa, $n_1 = 0.4$, $\kappa_1 = 2 \cdot 10^{-4} \text{ s}^{-1}$ and $m_1 = 1.5$ for the spherical inclusions.

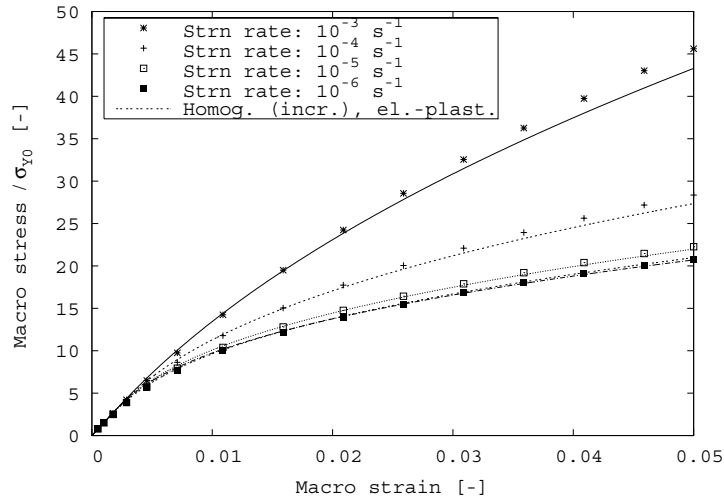
Finite element simulations are performed on 3D unit cells reinforced by several dozens of spheres. These are randomly distributed in the unit cell and periodic boundary conditions are enforced. Isotropy of the cells and low scattering between predictions obtained on several cells have been checked. Computation time was much higher than for an elasto-plastic matrix reinforced by elastic inclusions: about six hours on a HP RX-4640 with four processors and 8 Gb of RAM instead of one and an half hour.

Effect of the volume fraction and strain rate Predictions at different strain rates on a cell containing 15% of reinforcements are illustrated on figure 6.6a. For this, 6 FE simulations are performed at an average strain rate and conditions (cell and tension direction) of the closest response to the average one are used at the other strain rates. The response obtained by the incremental formulation for rate independent elasto-plastic materials is also reported. As previously, simulation at the lowest strain rate (10^{-6} s^{-1}) is almost identical to the elasto-plastic response. One can observe that at low strain rates, predictions with the affine formulation coincide almost perfectly with the FE simulations. At higher strain rates, the final response diverges a little bit from the reference results, predictions with the homogenization scheme being a little bit softer. This underestimation, which is unusual for homogenization schemes, is partly due to the use of the isotropic extraction of the affine modulus of the matrix (\mathbf{S}_τ^{*-1}) to compute the Eshelby's tensor. As illustrated on figure 6.6b, comments for cells containing twice more reinforcements (30%) are similar, the difference at high strain rates being more pronounced while predictions at low strain rates remain very good. Increasing the volume fraction or the strain rate thus decreases the accuracy of the predictions by the affine formulation of homogenization.

Effect of triaxiality In this section, the influence of the triaxiality level is examined: shear, uniaxial tension or biaxial tension test. Since the affine homogenization scheme considers only average strain and stress fields to define the state of each phase, these will always be isotropic under a triaxial tension test on a cell reinforced by spheres (if the same tension is applied in the three directions). Since the Perzyna-type constitutive model considered here is based on the von Mises equivalent stress, no plasticity will appear. Obviously, this



(a) Cell reinforced by 15% of stiff elasto-viscoplastic spherical inclusions.



(b) Cell reinforced by 30% of stiff elasto-viscoplastic spherical inclusions.

Figure 6.6: Uniaxial tension test. Comparison between direct 3D FE analysis (points) and affine homogenization formulation (straight lines) for various strain rates.

is not correct. Indeed, some stress concentration will occur in the surrounding of the inclusions which will not be under a triaxial tension, so that plasticity

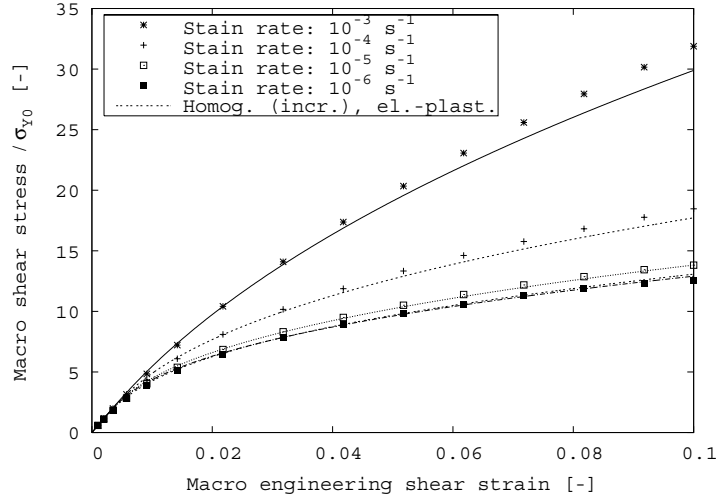


Figure 6.7: Shear test - cell reinforced by 30% of stiff elasto-viscoplastic spherical inclusions. Comparison between direct 3D FE analysis of RVE (points) and affine homogenization formulation (straight lines).

might develop. A good way to improve the model would be to take into account the second-order moment of the stress tensor which gives additional information on the heterogeneity of the stress field. For the other loading cases, it is interesting to know the triaxiality levels at which homogenization schemes give good predictions.

Let's consider at first shear tests at different strain rates. Results are reported on figure 6.7 for a cell reinforced by 30% of spheres. As in previous observations, good predictions are obtained at low strain rates and the relative difference between homogenization and reference FE results reaches about 5% as the strain rate increases. Similar results and interpretation are obtained for biaxial tension tests as illustrated on figure 6.8.

In order to check the accuracy of the triaxiality effect, von Mises equivalent stress versus equivalent strain is plotted for the different loading cases. These are computed as:

$$\sigma_{eq} = \left(\frac{3}{2} \boldsymbol{\sigma}^{dev} : \boldsymbol{\sigma}^{dev} \right)^{1/2}, \quad \varepsilon_{eq} = \left(\frac{2}{3} \boldsymbol{\varepsilon}^{dev} : \boldsymbol{\varepsilon}^{dev} \right)^{1/2}, \quad (6.25)$$

where $\boldsymbol{\varepsilon}^{dev}$ is the deviatoric strain tensor. In FE, these values are computed from the volume average of the equivalent strain and equivalent stress fields. The comparison is reported on figure 6.9 for the different loading cases at

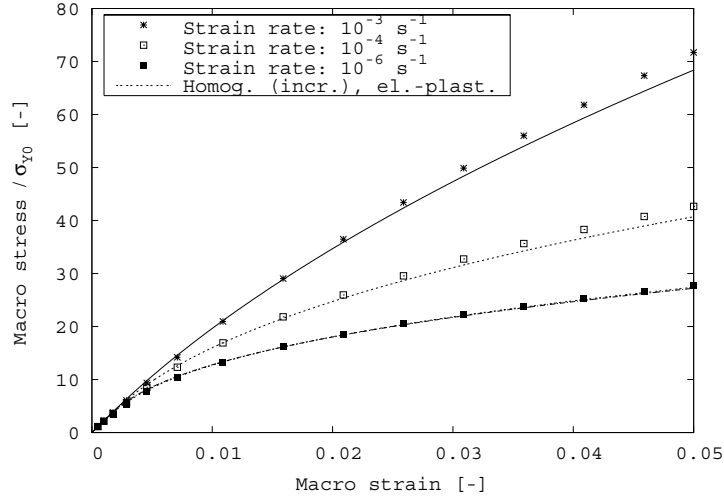


Figure 6.8: Biaxial tension test - cell reinforced by 30% of stiff elasto-viscoplastic spherical inclusions. Comparison between direct 3D FE analysis of RVE (points) and affine homogenization formulation (straight lines).

the highest strain rate ($10^{-3} s^{-1}$). Results do not have to be compared in a quantitative way but only the relative errors at the end of the simulations, which are at the last FE result of each curve: shear: 6.1%, uniaxial tension: 6.3% and biaxial tension: 3.9%. All these values are quite similar and by no way a deterioration of the predictions is observed as the level of triaxiality increases.

Effect of Cyclic loading In this section, strain rate effect is studied over a complete cycle of uniaxial loading/unloading/compression/reloading. The maximum macro strain at the end of loading, compression and reloading is $\pm 5\%$. On the contrary to homogenization schemes based on the secant formulation, the affine one enables such a non-monotonic loading.

Figure 6.10 reports simulations at two different strain rates over a complete cycle. The first loading path is exactly the same as the previously studied monotonic uniaxial loading case. During unloading and reloading, results at low strain rate of homogenization schemes and FE are almost identical, which is a pretty impressive result for such a high volume fraction of inclusions (30%). On the contrary, at high strain rates, the difference already observed at the end of the first loading path continues to increase during unloading and reloading.

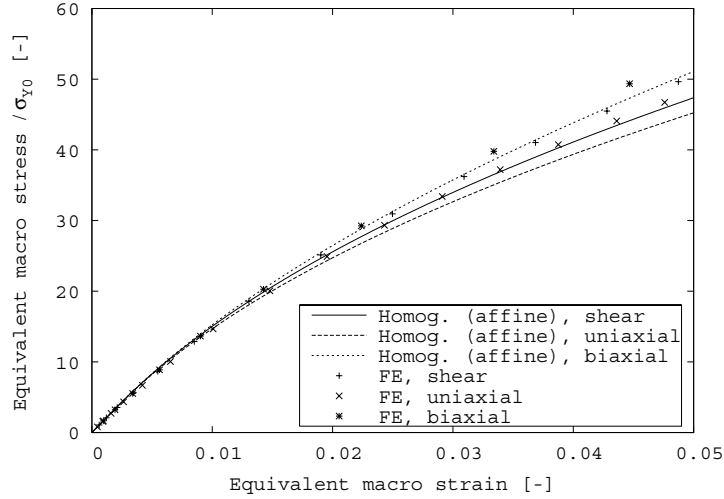


Figure 6.9: Influence of triaxiality - comparison of various loading tests (30% of inclusions).

One can observe that this difference does increase only during plastic increments but not during the elastic transitions.

Per phase analysis Even if a very good accuracy is observed for wide range of simulations, it has been observed that there is a systematic worsening of the predictions at high strain rates, the response becoming too soft under these conditions. Even if this is not a catastrophic effect, it is interesting to go deeper and understand the reasons of such a behavior. This will be done with the help of the numerical FE simulations. Effectively, these enable to get helpful information of the microscopic fields within each constituent of the composite.

A first source of error could come from the adopted homogenization scheme (Mori-Tanaka). This is known for giving good predictions at low volume fractions of the reinforcement phase but is less satisfying at higher ones. Effectively, an effect of the volume fraction of particles has been observed (figures 6.6a - 6.6b). However, differences between FE and mean-field predictions are noticeable only at high volume fractions so that this cannot explain the strain rate effect.

Another source of error might come from the definition of per phase reference states for homogenization schemes. In our implementation of the affine formulation, the reference equivalent stress is evaluated from the average stress tensor instead of the volume average of the equivalent stress field. Significant

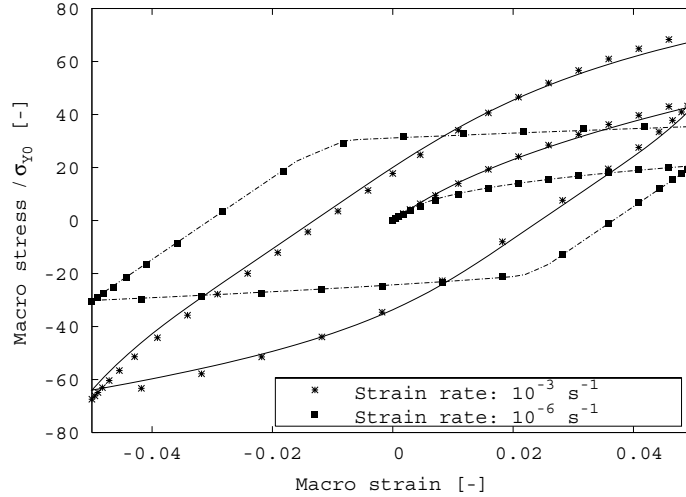


Figure 6.10: Cyclic uniaxial tension - compression test on a cell reinforced by 30% of stiff elasto-viscoplastic spherical inclusions. Comparison between direct 3D FE analysis of RVE and affine homogenization formulation. Specified strain rates are for the two loading paths while their opposites are used for unloading.

differences between these two evaluations exist for high levels of heterogeneity of the fields. This is illustrated on figure 6.11 for the accumulated plasticity for a cross section of the RVE at the end of one cycle of uniaxial loading. Especially in the matrix, the non uniformity is evident and is particularly high along the direction of traction (direction 1) where inclusions are close to each others. With the help of the local fields obtained by FE, the volumetric cumulative probability of accumulated plastic strain (volume fraction of a phase where the local accumulated plastic strain is smaller than a given value) enables to give a qualitative measure of the heterogeneity level. This is plotted at the end of the first cycle on figure 6.12a for the matrix and 6.12b for the inclusions. In both phases, the accumulated plastic strain is lower at high strain rates due to the stiffer response as the strain rate increases. Also, accumulated plastic strain is much more homogeneous at high strain rates than at lower ones. This would suggest that deterioration of the quality of the predictions at high strain rates is not linked to heterogeneity effects. Since precision is much better in the matrix, extending the affine formulation by taking into account second-order moments of the stress tensor would not increase significantly the quality of the predictions.

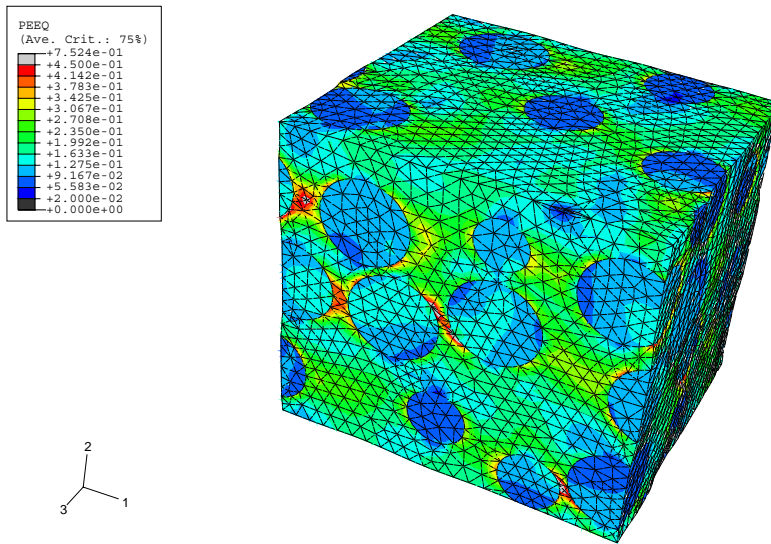
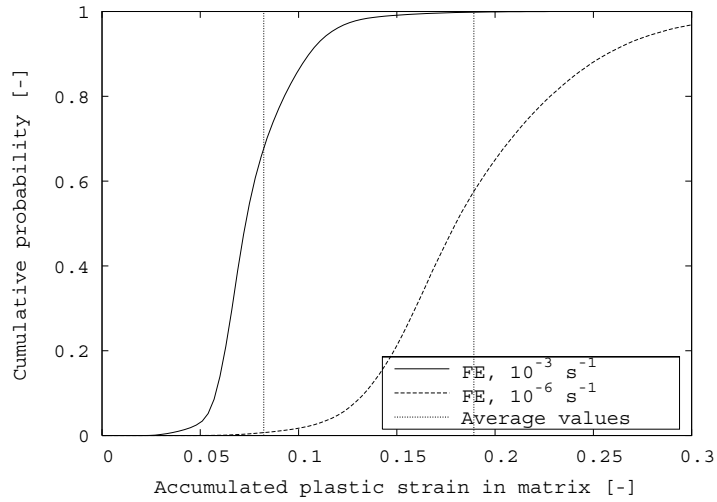
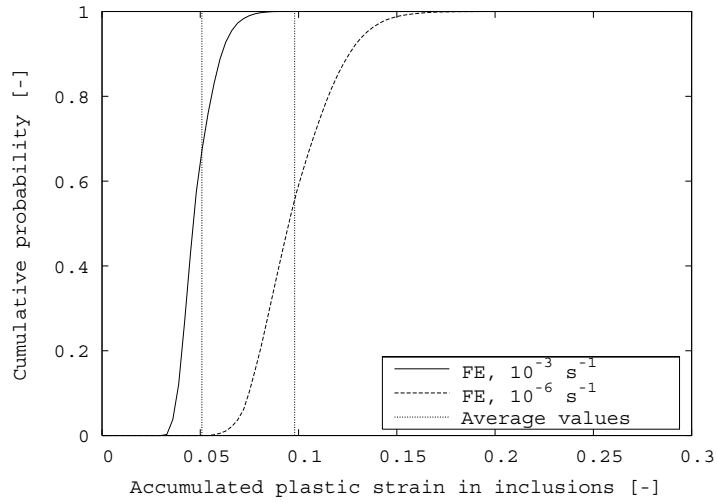


Figure 6.11: Cyclic uniaxial tension - compression test - cell reinforced by 30% of stiff elasto-viscoplastic spherical inclusions. Contour plot of the accumulated plastic strain field.



(a) Cumulative probability in the matrix.



(b) Cumulative probability in the inclusions.

Figure 6.12: Measurement of the heterogeneity of the accumulated plastic strain field at the end of one cycle of uniaxial tension-compression.

An analysis of the per phase reference stresses is now performed. For the affine formulation, these are given from the average stress in the phase. For the FE simulations, relation (5.60) enables to compute the volume average of the

$\dot{\epsilon}$ [s^{-1}]	Predictive method	p [-] in matrix	p [-] in incl.
10^{-6}	FE	0.1892	0.0980
	Homogenization	0.1949	0.0653
10^{-3}	FE	0.0823	0.0508
	Homogenization	0.0818	0.0394

Table 6.1: Accumulated plastic strain in the matrix and the inclusions at low and high strain rates obtained by homogenization and FE (volume average of the local field) at the end of one cycle.

equivalent stress in matrix. Similarly, this can be computed in the inclusions. These are plotted on figure 6.13 for a matrix reinforced by 30% of inclusions. This shows that the reference stress in the inclusions is underestimated while the ones in the matrix are acceptable. This observation is even more pronounced at high strain rates (figure 6.13b). Consequently, the accumulated plastic strain in the spherical inclusions given by the affine model is also underestimated (table 6.1). This result is surprising because it should lead to an overestimation of the stiffness of inclusions, which should lead to the same result for the composite. However, the effective composite behavior given by the affine model follows the opposite trend, so the differences between the model and the simulations cannot be attributed to this factor.

As explained in sections 5.3.1 and 6.3.3, a general implementation of the incremental and affine formulation gives too stiff macroscopic predictions. In order to solve this problem, various methods to reduce the matrix stiffness have been proposed (5.3.6). The one adopted for the affine formulation was to use an isotropic extraction of the matrix modulus for the computation of the Eshelby's tensor only while all the other computations are made with the anisotropic tensor. This technique is denoted *EshIso* in the following. Other stiffness reduction methods which gave satisfying results in elasto-plasticity (section 5.4.1) are to use this isotropic tensor for the computation of the Hill's tensor (*PIso*) only or for all the computations (*AllIso*). Such isotropisation techniques might have a considerable impact on the final prediction. Effective responses of these three methods are reported on figure 6.14a (volume fraction: 30%, strain rate: $10^{-3} s^{-1}$). This shows that the adopted isotropisation (*EshIso*) underestimates the macroscopic predictions (as observed on figure (6.6b)) and the two other methods (*PIso* and *AllIso*) give slightly better results. The differences in the predictions are closely related to the evaluation of the reference stress in each phase as illustrated on figures 6.14b-6.14c. Very good accuracy of the predictions in the matrix are preserved whatever isotropisation technique is used while this is strongly improved in the inclusions by using either *PIso* or *All Iso*. Once again, this shows the crucial issue of a good choice of the affine modulus (isotropic or not) of the matrix to obtain accurate predictions of the effective

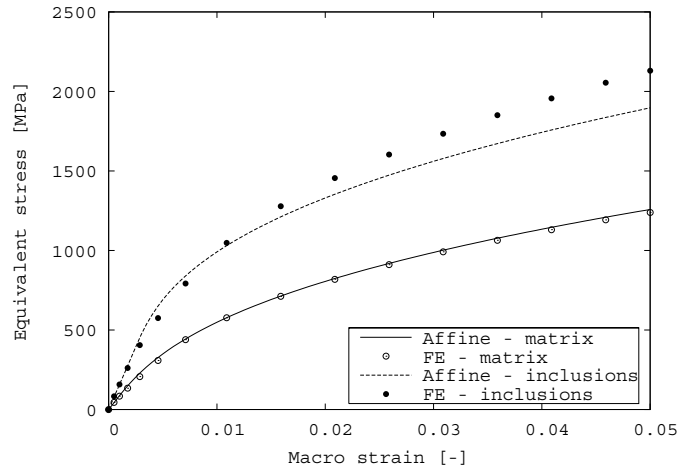
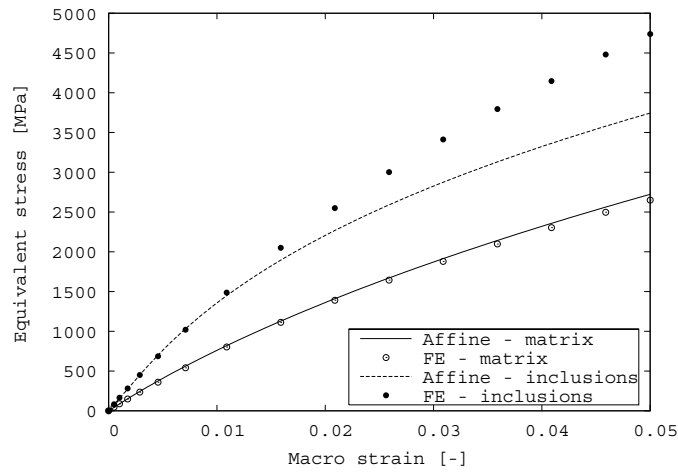
(a) Strain rate: 10^{-6} s^{-1} .(b) Strain rate: 10^{-3} s^{-1} .

Figure 6.13: Evolution of the von Mises equivalent stress in both phases.

properties.

Finally, it should be noted that the collocation points needed for the numerical inversion of the Laplace transform in the simulations presented in figure 6.14 are slightly different than those used in all previous simulations in this chapter in order to better take into account the interaction law. This numerical modification (which only has a small influence if the isotropic part of the affine moduli

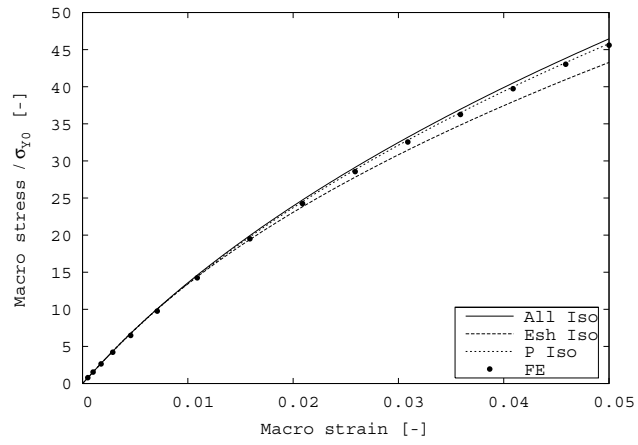
is only used to compute Eshelby's tensor) is necessary to obtain accurate results when Hill's tensor is computed with these isotropic moduli. Unfortunately, the mixture of very large times and very low collocation points leads to numerical problems at low strain rates and the non-linear localization tensorial equation (6.22) cannot be solved. Thus, for practical purposes, the affine homogenization model based on the isotropic projection of the affine modulus to compute only Eshelby's tensor has to be used to simulate the mechanical response of elasto-viscoplastic composites.

6.5 Conclusions

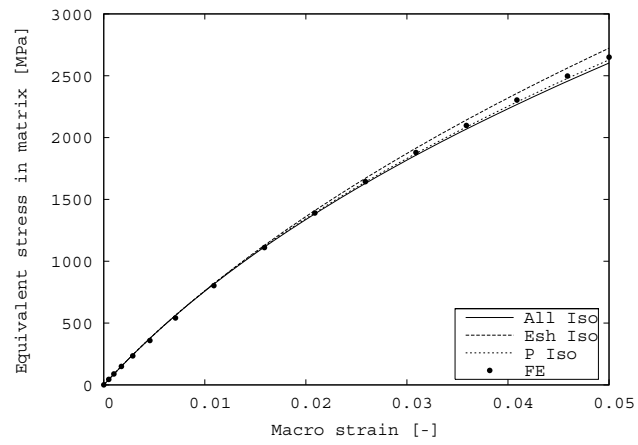
This chapter dealt with the affine formulation in the context of elasto-viscoplasticity. This formulation linearizes each phase's elasto-viscoplastic constitutive model into a fictitious linear thermo-elastic relation defined in the Laplace-Carson domain. At this stage, classical homogenization schemes valid in thermo-elasticity can be applied, from which the macroscopic response can be computed at the end of the time step. Our implementation includes a complete treatment of the internal variables.

The method enables to deal with various loadings, including cyclic, shear and relaxation tests. Influence of the shape of the reinforcements, the way to compute the macroscopic response and the influence of the homogenization scheme were also presented. Other simulations illustrate the viscous effects and when these become negligible, the elasto-plastic response is well retrieved.

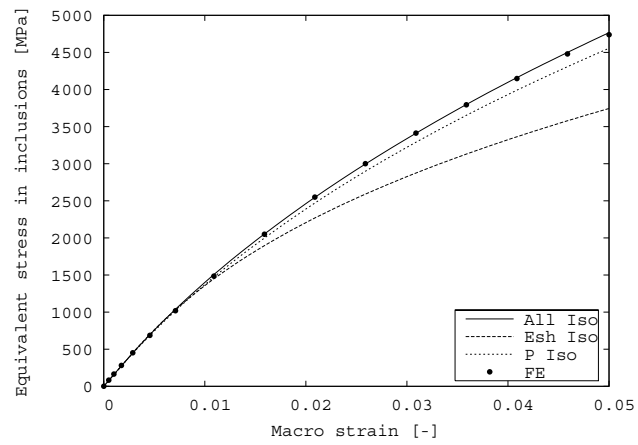
The accuracy of the affine homogenization method was assessed by comparison with results obtained by the numerical simulation of a three-dimensional representative volume element of the composite microstructure. Macroscopic predictions of the affine homogenization model were excellent in composites with different volume fraction of spheres, subjected to different loading conditions as well as to monotonic and cyclic deformation, particularly at low strain rates. However, accuracy of the predictions decreased systematically as the strain rate increased, the homogenization scheme giving a slightly softer response than the numerical simulations. The detailed information of the stress and strain microfields given by the finite element simulations was used to analyze the source of this error, which was traced to the use of an isotropic extraction of the matrix affine modulus to compute Eshelby's tensor. It was found that better predictions at high strain rates could be obtained if the same isotropic extraction was used to determine Hill's tensor (instead of Eshelby's tensor) but the numerical problems associated with the numerical inversion of the Laplace-Carson transform did not make advisable to use this latter approach.



(a) Macroscopic predictions.



(b) Predictions in the matrix.



(c) Predictions in the inclusions.

Figure 6.14: Comparison of various isotropisation methods.

Chapter 7

Conclusions

Throughout this thesis, we have investigated some important aspects of the numerical prediction of elasto-plastic and elasto-viscoplastic inclusion-reinforced composites and proposed some original improvements. To carry this out, two techniques have been examined: mean-field homogenization schemes and finite element simulations.

We first adapted the finite element technique for the analysis of composites. The major advantage of such analysis is the accuracy of its predictions and the possibility of knowing the state of deformation at any point of the representative volume element, although this can only be done at a high computational cost. Furthermore, on the contrary to other methods, it can deal easily with any constitutive behavior for any phase. Based on existing developments for sphere reinforced materials, we extended the technique to inclusions with a spheroidal (ellipsoidal with an axis of revolution) shape which enables to deal with a much wider category of composites. To do this, we first generated geometries with randomly dispersed and non overlapping inclusions. Due to the imposition of periodic boundary conditions, both the geometry and the mesh must also be periodic. This guarantees a limited size of the RVE. A geometrical study proved the required homogeneity and transverse isotropy of the cell in the case of aligned inclusions. The numerical analysis showed that for inclusions with a low aspect ratio, 30 of them were enough to reproduce correctly the behavior of the material. High attention was devoted to the mesh quality so that precision of the microscopic fields was guaranteed, which is of first importance when taking damage into account. Finite element simulations are a fantastic tool for validation purpose of other simplified but much faster homogenization schemes.

Main part of this work is devoted to development of mean-field homogenization schemes for elasto-plastic and elasto-viscoplastic composites. First of all, these are presented in the context of linear thermo-elastic or viscoelastic materials and relies on the Eshelby's result. Accuracy of these models is checked

against experimental results and finite element simulations and a good correlation was found between these models. This has a great impact on subsequent developments since this consists of a subproblem of homogenization schemes in the nonlinear regime.

First extension to nonlinear materials is done in the context of two-phase elasto-plastic composites. In order to apply homogenization schemes developed for linear elastic materials, an incremental linearization of the local constitutive equations is carried out. This is done over several time steps and has the advantage of following the loading path so that it can handle any loading history, including cyclic and non proportional ones. However, this general approach is known to be too stiff. In order to circumvent this problem, we suggested several stiffness reduction methods. First of all, this was studied on a theoretical point of view and the dependence of various tensors used during the homogenization step (Hill, Hill's constraint and the effective tangent operators) with respect to the matrix tangent modulus was examined. Previous results have shown that Hill's tensor \mathbf{P} decreases (in the meaning of quadratic forms) with the matrix modulus while Hill's constraint tensor \mathbf{C}^* and the effective operator $\bar{\mathbf{C}}$ are increasing with it. In order to make use of these properties, several matrix modulus tensors are considered: the original anisotropic one \mathbf{C}_0^{ani} and the extraction of its isotropic or transverse isotropic parts. The softest modulus is obtained with a special isotropisation technique in a direction orthogonal to the normal to the yield surface in the stress space. Similarly, our proposed transverse isotropisation technique relies on a projection on the subspace of transversely isotropic tensors and a stiffness reduction in the same direction. Dependence of the different tensors on the matrix modulus combined with all the proposed stiffness reduction methods enable to perform various predictions. It has been noted that the previously used evaluation of the Eshelby's tensor \mathcal{E} with the special isotropisation technique \mathbf{C}_0^{IsoSpe} can sometimes give non physical predictions, which is due to the loss of major symmetries of the Hill's tensor \mathbf{P} . After numerous validation tests, we recommend the computation of the Hill's tensor \mathbf{P} with the special isotropic matrix modulus \mathbf{C}_0^{IsoSpe} . Unfortunately, this special method is not applicable to all constitutive models. Spectacular improvements have also been obtained with the transversely isotropic extraction method ($\mathbf{C}_0^{TrIsoSpe}$) but this still relies on a fitting parameter which reduces its scope of applications.

Still in the context of elasto-plasticity, a comparison between the secant formulation (per phase reference state defined from either first order or second order moment of the stress tensor), the incremental formulation and finite element simulations has been carried out. This showed that best predictions are obtained with the second order secant homogenization schemes. Incremental formulation also gives satisfying predictions and has the major advantage of remaining valid with general plasticity models (e.g.: kinematic hardening) and non-proportional loadings (e.g.: cyclic). Difference between first and second

order methods are especially noticeable when high plastic strain localization occurs and when uniaxial traction test is performed along the direction of the aligned ellipsoids. However, several difficulties for capturing correctly the per phase average strain and stress is still a major problem when dealing with mean-field homogenization schemes. Some of these problems are due to the use of isotropisation technique or the second order secant method.

Major developments of this thesis concern the affine formulation developed for elasto-viscoplastic composites. The main improvement with previous implementations of the method is that it enables to deal with internal parameters. Such formulation transforms the local elasto-viscoplastic constitutive laws into form-similar linear thermo-viscoelastic relations. With the help of the Laplace-Carson transform, these are reduced to linear thermo-elastic ones in the Laplace domain where the homogenization procedure can be applied. In order to solve the localization problem, some numerical inversions are required. Due to the hereditary nature of the constitutive laws, an iterative process must be carried out over several time steps. In order to limit the memory cost, a special attention has been paid to the development of efficient algorithms. Our implementation enables to simulate several loadings including cyclic, relaxation and creep tests, different hardening and viscoplastic laws and several homogenization schemes. Finally, a confrontation with 3D finite element method showed a good accuracy. However, a deterioration of the predictions has been observed as the strain rate increases. This is mainly coming from the isotropisation method.

This thesis showed the general efficiency of mean-field homogenization schemes to capture correctly macroscopic behavior. This has been done for difficult nonlinear behaviors such as elasto-plasticity and elasto-viscoplasticity. Among the future improvements of homogenization methods are:

- Increasing the quality of the microscopic predictions obtained with mean-field methods is a great challenge. This could be done by considering other reference states for the phases of the linear comparison composite. For example, making use of the second order moment of the stress tensor with the incremental formulation is still an open subject.
- Solving some of the limitations of Eshelby-based mean-field homogenization models such as the ellipsoidal shape of the inclusions, the availability of information on the strain localization and the impossibility to model percolation or clustering effects. The latter problem could maybe be solved by considering a decomposition of the two-phase composite into several regions, each one having a different volume fraction of inclusions. Such material can be considered as a multi-phase composite in which each region corresponds to a two-phase composite.
- Modeling size effects which are important when dealing with nanocom-

posites and are not considered by finite element and mean-field homogenization schemes. A solution could be the introduction of a characteristic length in the model.

- Considering damage (inclusion fracture, interface decohesion, . . .). This firstly requires a good accuracy of the predictions at the microscopic scale. Anyway, since detailed microscopic fields are not available with these methods, it must be done in a statistical way. Using an additional internal parameter in the affine formulation could be a solution.
- Dealing with the thermal coupling which is especially useful when performing simulations of a complete process of elasto-viscoplastic composites.

Finally, it is stressed out that even if finite element simulations are realizable on a representative volume element of the microstructure, this is far from being possible if this problem is coupled to a simulation on the macroscopic structure. So, even if computational power is increasing every day, the use of mean-field homogenization schemes are the only way to solve such problems and guarantees a bright future to these methods.

Appendix A

Expressions of the Eshelby's tensor

Analytical formulae of the Eshelby's tensor were introduced by Eshelby [30] for isotropic materials and spheroids. Later, Withers [108] extended the expressions to transversely isotropic medium, with the restriction that the direction of anisotropy has the same orientation as the aligned reinforcements. In all other cases (ellipsoidal inclusions and/or anisotropic material), a numerical evaluation of the tensor is necessary and was implemented by Gavazzi and Lagoudas [34].

A.1 Isotropic matrix

Hereafter are given the non-nil components of the Eshelby's tensor for spheroids of aspect ratio Ar embedded in an isotropic matrix (expressions are picked up from Friebel [32]). Reinforcements are aligned along the direction 1.

$$\begin{aligned} S_{1111} &= \frac{1}{2(1-\nu)} \left[2(1-\nu)(1-g) + g - Ar^2 \frac{3g-2}{Ar^2-1} \right], \\ S_{2222} = S_{3333} &= \frac{1}{4(1-\nu)} \left[2(2-\nu)g - \frac{1}{2} - (Ar^2 - \frac{1}{4}) \frac{3g-2}{Ar^2-1} \right], \end{aligned}$$

$$\begin{aligned}
S_{1122} = S_{1133} &= \frac{1}{4(1-\nu)} \left[4\nu(1-g) - g + Ar^2 \frac{3g-2}{Ar^2-1} \right], \\
S_{2233} = S_{3322} &= \frac{1}{4(1-\nu)} \left[-(1-2\nu)g + \frac{1}{2} - \frac{1}{4} \frac{3g-2}{Ar^2-1} \right], \\
S_{2211} = S_{3311} &= \frac{1}{4(1-\nu)} \left[-(1-2\nu)g + Ar^2 \frac{3g-2}{Ar^2-1} \right], \\
S_{1212} = S_{1313} &= \frac{1}{4(1-\nu)} \left[(1-\nu)(2-g) - g + Ar^2 \frac{3g-2}{Ar^2-1} \right], \\
S_{2323} &= \frac{S_{2222} - S_{1122}}{2},
\end{aligned} \tag{A.1}$$

where:

$$\begin{aligned}
g &= \frac{Ar}{(Ar^2-1)^{3/2}} \left[Ar(Ar^2-1)^{1/2} - \cos^{-1} Ar \right] \text{ for } 0 < Ar < 1, \\
g &= \frac{Ar}{(1-Ar^2)^{3/2}} \left[\cosh^{-1} Ar - Ar(1-Ar^2)^{1/2} \right] \text{ for } 1 < Ar < \infty.
\end{aligned} \tag{A.2}$$

Eshelby's tensor has the minor symmetries ($S_{ijkl} = S_{jikl} = S_{ijlk} = S_{jilk}$) but not the major ones ($S_{ijkl} = S_{klij}$).

For the particular case of spherical inclusions, previous equations become invalid and require a study of these functions around $Ar = 1$. This gives:

$$\begin{aligned}
S_{1111} = S_{2222} = S_{3333} &= \frac{7-5\nu}{15(1-\nu)}, \\
S_{1122} = S_{1133} = S_{2233} &= \frac{5\nu-1}{15(1-\nu)}, \\
S_{1212} = S_{1313} = S_{2323} &= \frac{4-5\nu}{15(1-\nu)}.
\end{aligned} \tag{A.3}$$

A.2 Transversely isotropic matrix

Eshelby's results are based on the solution of a point force applied inside an infinite solid. Solution of this problem is given by the elastic Green's functions. An explicit solution of the Green's function in a general anisotropic medium is possible only if a sixth-order algebraic equation has six different roots. For transversely isotropic materials this condition is reduced to (direction of anisotropy is 1):

$$(C_{1111}C_{3333})^{1/2} - C_{1133} - C_{2323} \neq 0. \tag{A.4}$$

Analytical point force solution for an infinite transversely isotropic solid was given by Pan and Chou [76].

Starting from the solution of this problem, Withers [108] developed the expression of Eshelby's tensor for transversely isotropic medium under the condition that the direction of anisotropy is the same as the aligned inclusions. Components of this tensor are function of several constants and two integrals over the volume of the ellipsoid. Developments of Withers remain valid only if expression (A.4) is positive. However, when performing all the computations with complex calculus, one can prove that the integrals in the two cases are complex conjugate and equals. They are thus real as well as the final result of the Eshelby's tensor.

Appendix B

Laplace-Carson transform and its inversion

B.1 Laplace-Carson transform

The Laplace-Carson transform is defined by:

$$[\mathcal{L}(f)]_{(s)} = f^*(s) = s \int_0^{\infty} f(t)e^{-st} dt. \quad (\text{B.1})$$

It is thus the classical Laplace transform multiplied by the Laplace variable s . Main advantages of this transform are that a constant remains a constant, the time derivative of one of the members in a convolution product disappears under this transform and the transform of a Stieljes type convolution product is reduced to a single contraction between the transform of the two operands. Some basic Laplace-Carson transforms are given in table B.1.

B.2 Laplace-Carson inversion

The collocation method proposed by Scharperly [90] for numerical inversion of the Laplace-Carson transform is adopted. Main advantages of this method are the ease of its implementation, its efficiency and the analytical form of the result so that the time function can be evaluated at any time.

Consider an expression $f^*(s)$ known in the Laplace domain. A development of the unknown time function into a Dirichlet series for a particular choice of basis functions gives:

$$f(t) = A + Bt + \sum_{k=1}^{k=M} b_k \underbrace{(1 - e^{-t/\theta_k})}_{\text{Basis functions}}. \quad (\text{B.2})$$

$f(t)$	$f^*(s)$	Conditions
a	a	$s > 0$
at	a/s	$s > 0$
e^{at}	$\frac{s}{s-a}$	$s > a$
$\cos(\omega t)$	$\frac{s^2}{s^2 + \omega^2}$	-
$\delta(t - c)$	se^{-cs}	-
$H(t - c)$	e^{-cs}	-
$af(t) + bg(t)$	$af^*(s) + bg^*(s)$	-
$A \otimes B$	$\frac{1}{s}A^*(s) : B^*(s)$	-
$A \odot B$	$A^*(s) : B^*(s)$	-

Table B.1: Basic Laplace-Carson transforms.

Main advantage of this decomposition is that its Laplace-Carson transform is known analytically:

$$f^*(s) = A + \frac{B}{s} + \sum_{k=1}^{k=M} b_k \underbrace{\frac{1}{1 + s\theta_k}}_{\text{Transf. basis funct.}}, \quad (\text{B.3})$$

where θ_k are given relaxation times chosen equispaced on a logarithmic scale. Bounds and length of this interval can have a considerable impact on the results.

In expression (B.3), A and B are limit values which can be evaluated from the known function in the Laplace or time domain:

$$A = \lim_{s \rightarrow +\infty} f^*(s) = \lim_{t \rightarrow 0} f(t), \quad (\text{B.4})$$

$$B = \lim_{s \rightarrow 0} s f^*(s) = \lim_{t \rightarrow +\infty} \frac{f(t)}{t}. \quad (\text{B.5})$$

The only unknowns in expression (B.3) are the factors b_k . In order to calculate them, the function in the Laplace domain is evaluated at M collocation points $s_l = 1/\theta_l$:

$$f^*(s_l) = A + \frac{B}{s_l} + \sum_{k=1}^{k=M} b_k \frac{1}{1 + s_l \theta_k}, \quad 1 \leq l \leq M. \quad (\text{B.6})$$

Typically, around 20 points are enough. Better precision can be obtained when increasing the number of collocation points but the system then becomes larger and can even get close to singular. For computing the factors b_k , a linear system of size M must be solved. Once the M unknowns b_k are found, the time function (B.2) can be evaluated at any time.

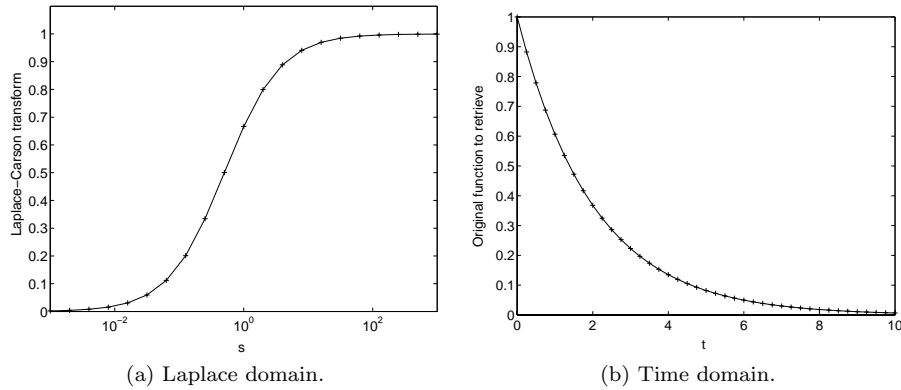


Figure B.1: Numerical inversion of the transform of a decreasing exponential - 20 collocation points.

A possible extension is to choose other basis functions from the proposed ones, with the condition that their transform must be known analytically. Ideally, the choice of basis functions should be such that their transform is as form-similar as possible to the function in the Laplace domain. When inverting tensorial functions, the evolution of each component is considered individually. If polycrystals are modeled, a large amount of Laplace inversions has to be carried out due to numerous individual crystals. In this case, Brenner *et al.* [15] proposed a simplified direct inversion which can reduce considerably the required CPU time. However, this technique is not used in this work since it reduces also the precision of the inversion and the CPU time is not a critical issue for two-phase materials.

Examples of numerical inversions As validation of the collocation method, several inversions of Laplace functions are made for which the transform is known a priori.

- $f(t) = e^{-t/2}, \quad f^*(s) = \frac{s}{s+\frac{1}{2}}$

This function is quite regular and results of the inversion are reported on figure B.1. For this first test, 20 collocation points are considered (noted with the sign '+' on the figure B.1a). Continuous line is always the plot of the analytical functions (known in the Laplace domain, unknown and solution of this problem in the time domain). Crosses on figure B.1b are obtained from the development in series evaluated at several times. For such regular function, an excellent accuracy of this inversion is observed.

- $f(t) = H(t - 2), \quad f^*(s) = e^{-2s}$

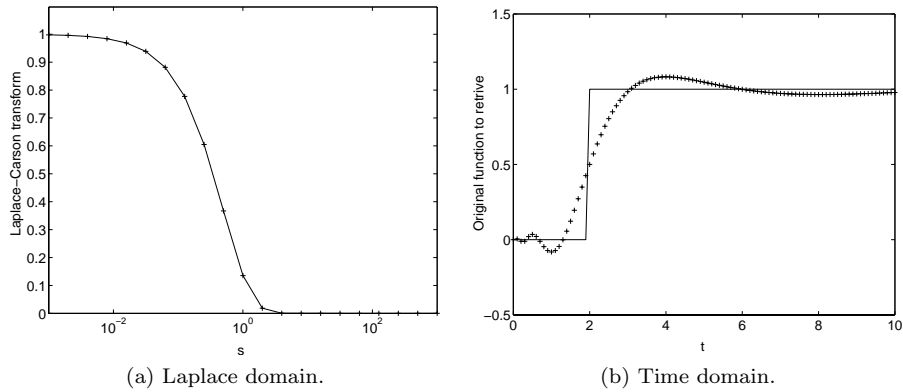


Figure B.2: Numerical inversion of the transform of the step function - 20 collocation points.

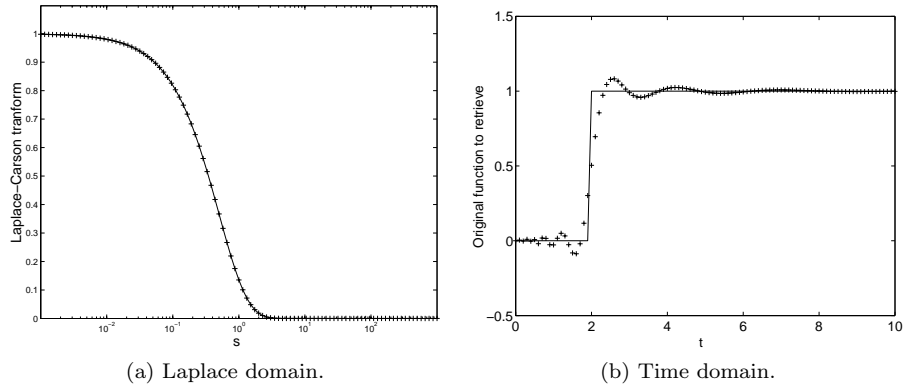


Figure B.3: Numerical inversion of the transform of the step function - 100 collocation points.

A step function is now considered. At first, 20 collocation points are used for the inversion. Figure B.2b shows that the capture of the step isn't that good. When using 100 collocation points (figure B.3b) instead of 20, much better results are obtained. However, even if it might be tempting to consider as many collocation points as possible, several problems arise in this case. First one is that when rising the number of points, this increases the size of the linear system. Since solving a system of size n has a cost of n^3 operations, the complexity is growing up quickly. Another one is that increasing the size of the system leads to a singular matrix.

- $f(t) = \cos(t)$, $f^*(s) = \frac{s}{s^2+1}$

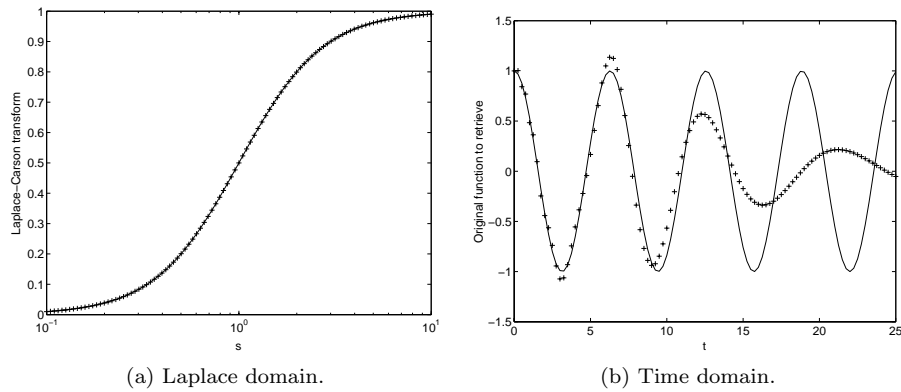


Figure B.4: Numerical inversion of the transform cosine function - 100 collocation points.

This last test considers the periodic cosine function. Figure B.4b shows that 2 complete periods are correctly captured. However, it is impossible to retrieve all the periods because basis functions considered in this case are decreasing exponentials so that the cosine function is reconstructed from balanced exponentials ! A much better choice would be to select other basis functions.

Appendix C

Incremental evaluation of a convolution product

Consider a time-dependent fourth order tensor $\mathbf{F}(t)$ obtained after a numerical inversion of its Laplace-Carson transform so that it is written under the form (B.2). This tensor is convoluted with a second-order tensor written in rate form $\dot{\boldsymbol{\varepsilon}}$. Such operation occurs in the computation of the macroscopic response at various times of a linear viscoelastic composite and in the localization problem of a heterogeneous elasto-viscoplastic material. Main goal of this section is to compute the convolution product at a limited memory cost. For this, consider a time interval $[t_n, t_{n+1}]$. The convolution product is already computed up to t_n and the strain history is known up to the end of the current time step ($t_{n+1} = t_n + \Delta t$). Taking into account all this information, the development hereafter enables to perform the computation of the convolution product at the end of the time step.

$$\begin{aligned} [\mathbf{F} \otimes \dot{\boldsymbol{\varepsilon}}]_{(t_{n+1})} &= \int_0^{t_{n+1}} \mathbf{F}(t_{n+1} - u) : \dot{\boldsymbol{\varepsilon}}(u) du \\ &= \mathbf{A} : \int_0^{t_{n+1}} \dot{\boldsymbol{\varepsilon}}(u) du + \mathbf{B} : \int_0^{t_{n+1}} (t_{n+1} - u) : \dot{\boldsymbol{\varepsilon}}(u) du \\ &\quad + \int_0^{t_{n+1}} \sum_{k=1}^M \mathbf{b}_k (1 - e^{-(t_{n+1}-u)s_k}) : \dot{\boldsymbol{\varepsilon}}(u) du \end{aligned}$$

$$\begin{aligned}
[\mathbf{F} \otimes \dot{\bar{\varepsilon}}]_{(t_{n+1})} &= \left(\mathbf{A} + t_{n+1}\mathbf{B} + \sum_{k=1}^M \mathbf{b}_k \right) : (\bar{\varepsilon}(t_{n+1}) - \bar{\varepsilon}(0)) \\
&\quad - \mathbf{B} : \int_0^{t_{n+1}} u \dot{\bar{\varepsilon}}(u) du \\
&\quad - \sum_{k=1}^M \mathbf{b}_k : \int_0^{t_{n+1}} e^{-(t_{n+1}-u)s_k} \dot{\bar{\varepsilon}}(u) du, \tag{C.1}
\end{aligned}$$

where $s_k = \frac{1}{\theta_k}$. But:

$$\begin{aligned}
\int_0^{t_{n+1}} u \dot{\bar{\varepsilon}}(u) du &= [u\bar{\varepsilon}(u)]_0^{t_{n+1}} - \int_0^{t_{n+1}} 1\bar{\varepsilon}(u) du \\
&= t_{n+1}\bar{\varepsilon}(t_{n+1}) - \int_0^{t_{n+1}} \bar{\varepsilon}(u) du \\
&= t_{n+1}\bar{\varepsilon}(t_{n+1}) - \int_0^{t_n} \bar{\varepsilon}(u) du \\
&\quad - \frac{\Delta t}{2}(\bar{\varepsilon}(t_n) + \bar{\varepsilon}(t_{n+1})), \tag{C.2}
\end{aligned}$$

and:

$$\begin{aligned}
\int_0^{t_{n+1}} e^{-(t_{n+1}-u)s_k} \dot{\bar{\varepsilon}}(u) du &= \left[e^{-(t_{n+1}-u)s_k} \bar{\varepsilon}(u) \right]_0^{t_{n+1}} \\
&\quad - s_k \int_0^{t_{n+1}} e^{-(t_{n+1}-u)s_k} \bar{\varepsilon}(u) du \\
&= \bar{\varepsilon}(t_{n+1}) - e^{-t_{n+1}s_k} \bar{\varepsilon}(0) \\
&\quad - s_k \int_0^{t_{n+1}} e^{-(t_{n+1}-u)s_k} \bar{\varepsilon}(u) du. \tag{C.3}
\end{aligned}$$

Rearranging these terms gives:

$$\begin{aligned}
[\mathbf{F} \otimes \dot{\bar{\varepsilon}}]_{(t_{n+1})} &= \mathbf{A} : \bar{\varepsilon}(t_{n+1}) + \frac{\Delta t}{2} \mathbf{B} : (\bar{\varepsilon}(t_n) + \bar{\varepsilon}(t_{n+1})) \tag{C.4} \\
&\quad + \mathbf{B} : \int_0^{t_n} \bar{\varepsilon}(u) du \\
&\quad + \sum_{k=1}^M s_k \mathbf{b}_k : \int_0^{t_{n+1}} e^{-(t_{n+1}-u)s_k} \bar{\varepsilon}(u) du \\
&\quad - \left[\mathbf{A} + t_{n+1}\mathbf{B} + \sum_{k=1}^M \mathbf{b}_k - \sum_{k=1}^M \mathbf{b}_k e^{-t_{n+1}s_k} \right] : \bar{\varepsilon}(0).
\end{aligned}$$

Evolving parameters from one time-step to another one are: $\mathbf{A}, \mathbf{B}, \mathbf{b}_k, t_{n+1}$. A last term still must be evaluated:

$$\begin{aligned}
\int_0^{t_{n+1}} e^{-(t_{n+1}-u)s_k} \bar{\epsilon}(u) du &= \int_0^{t_n} \underbrace{e^{-(t_{n+1}-u)s_k} \bar{\epsilon}(u)}_{e^{-(t_n+\Delta t-u)s_k} \bar{\epsilon}(u)} du \\
&+ \int_{t_n}^{t_{n+1}} e^{-(t_{n+1}-u)s_k} \bar{\epsilon}(u) du \\
&= e^{-\Delta t s_k} \int_0^{t_n} e^{-(t_n-u)s_k} \bar{\epsilon}(u) du \\
&+ \int_{t_n}^{t_{n+1}} e^{-(t_{n+1}-u)s_k} \bar{\epsilon}(u) du. \quad (\text{C.5})
\end{aligned}$$

In this case, using again a trapezoidal integration rule is quite bad for large values of s_k . This is due to the linear approximation of the integral containing the sharp exponential. This problem can be tackled if $\dot{\bar{\epsilon}}(u)$ is considered as constant on each time-step. On the considered time interval, this gives:

$$\bar{\epsilon}(u) = \bar{\epsilon}(t_n) + (u - t_n) \dot{\bar{\epsilon}}. \quad (\text{C.6})$$

Second integral in (C.5) can be rewritten as:

$$\begin{aligned}
&\int_{t_n}^{t_{n+1}} e^{-(t_{n+1}-u)s_k} \bar{\epsilon}(u) du \\
&= \int_{t_n}^{t_{n+1}} e^{-(t_{n+1}-u)s_k} (\bar{\epsilon}(t_n) + (u - t_n) \dot{\bar{\epsilon}}) du \\
&= (\bar{\epsilon}(t_n) - t_n \dot{\bar{\epsilon}}) e^{-t_{n+1}s_k} \int_{t_n}^{t_{n+1}} e^{us_k} du + \dot{\bar{\epsilon}} e^{-t_{n+1}s_k} \int_{t_n}^{t_{n+1}} u e^{us_k} du \\
&= (\bar{\epsilon}(t_n) - t_n \dot{\bar{\epsilon}}) \frac{e^{-t_{n+1}s_k}}{s_k} (e^{t_{n+1}s_k} - e^{t_n s_k}) + \dot{\bar{\epsilon}} e^{-t_{n+1}s_k} \left[\frac{e^{us_k}}{s_k} \left(u - \frac{1}{s_k} \right) \right]_{t_n}^{t_{n+1}} \\
&= (\bar{\epsilon}(t_n) - t_n \dot{\bar{\epsilon}}) \frac{1 - e^{(t_n - t_{n+1})s_k}}{s_k} \\
&\quad + \dot{\bar{\epsilon}} e^{-t_{n+1}s_k} \left(\frac{e^{t_{n+1}s_k}}{s_k} \left(t_{n+1} - \frac{1}{s_k} \right) - \frac{e^{t_n s_k}}{s_k} \left(t_n - \frac{1}{s_k} \right) \right) \\
&\quad \quad \quad \dot{\bar{\epsilon}} \left(\frac{1}{s_k} \left(t_{n+1} - \frac{1}{s_k} \right) - \frac{e^{(t_n - t_{n+1})s_k}}{s_k} \left(t_n - \frac{1}{s_k} \right) \right) \\
&= \frac{1}{s_k} \left[\bar{\epsilon}(t_n) (1 - e^{-\Delta t s_k}) + \dot{\bar{\epsilon}} \left(\Delta t + \frac{e^{-\Delta t s_k} - 1}{s_k} \right) \right] \\
&= \frac{1}{s_k} \left[\bar{\epsilon}(t_{n+1}) - \bar{\epsilon}(t_n) e^{-\Delta t s_k} + (\bar{\epsilon}(t_{n+1}) - \bar{\epsilon}(t_n)) \frac{e^{-\Delta t s_k} - 1}{s_k \Delta t} \right]. \quad (\text{C.7})
\end{aligned}$$

Appendix D

Computation details of the affine formulation

D.1 Solution of the internal variables' constitutive equation

The linearized equation of internal variables is given by (6.11):

$$\dot{p}(t) = \dot{p}(t_n) + \mathbf{l}(\tau) : [\boldsymbol{\sigma}(t) - \boldsymbol{\sigma}(t_n)] + q(\tau)[p(t) - p(t_n)]. \quad (\text{D.1})$$

Let's prove that the following expression is a solution of (D.1):

$$p(t) - p(t_n) = \hat{p}(\tau, t) + \int_0^t e^{(t-u)q(\tau)} \mathbf{l}(\tau) : \boldsymbol{\sigma}(u) du, \quad (\text{D.2})$$

$$\begin{aligned} \hat{p}(\tau, t) &= q^{-1}(\tau)[e^{(t-t_n)q(\tau)} - 1][\dot{p}(t_n) - \mathbf{l}(\tau) : \boldsymbol{\sigma}(t_n)] \\ &\quad - \int_0^{t_n} e^{(t-u)q(\tau)} \mathbf{l}(\tau) : \boldsymbol{\sigma}(u) du. \end{aligned} \quad (\text{D.3})$$

Let's first recall the theorem which allows to switch the derivative and the integral of a function:

$$\frac{\partial}{\partial t} \int_{a(t)}^{b(t)} f(t, x) dx = \int_{a(t)}^{b(t)} \frac{\partial}{\partial t} f(t, x) dx + f(t, b(t)) \frac{d}{dt} b(t) - f(t, a(t)) \frac{d}{dt} a(t). \quad (\text{D.4})$$

With the help of (D.4), the derivative of (D.2) is given by:

$$\begin{aligned} \dot{p}(t) &= [e^{(t-t_n)q(\tau)}][\dot{p}(t_n) - \mathbf{l}(\tau) : \boldsymbol{\sigma}(t_n)] + q(\tau) \int_{t_n}^t e^{(t-u)q(\tau)} \mathbf{l}(\tau) : \boldsymbol{\sigma}(u) du \\ &\quad + \mathbf{l}(\tau) : \boldsymbol{\sigma}(t). \end{aligned} \quad (\text{D.5})$$

Expression of the proposed solution (D.2) can be rearranged to get an expression of the integral in function of p :

$$\begin{aligned} & \int_{t_n}^t e^{(t-u)q(\tau)} \mathbf{l}(\tau) : \boldsymbol{\sigma}(u) du \\ = & p(t) - p(t_n) - q^{-1}(\tau) [e^{(t-t_n)q(\tau)} - 1] [\dot{p}(t_n) - \mathbf{l}(\tau) : \boldsymbol{\sigma}(t_n)]. \end{aligned} \quad (\text{D.6})$$

Inserting this result in (D.5) gives:

$$\begin{aligned} \dot{p}(t) = & [e^{(t-t_n)q(\tau)}] [\dot{p}(t_n) - \mathbf{l}(\tau) : \boldsymbol{\sigma}(t_n)] + q(\tau)(p(t) - p(t_n)) \\ & - [e^{(t-t_n)q(\tau)} - 1] [\dot{p}(t_n) - \mathbf{l}(\tau) : \boldsymbol{\sigma}(t_n)] + \mathbf{l}(\tau) : \boldsymbol{\sigma}(t). \end{aligned} \quad (\text{D.7})$$

Rearranging the terms gives:

$$\dot{p}(t) = \mathbf{l}(\tau) : \boldsymbol{\sigma}(t) + \dot{p}(t_n) - \mathbf{l}(\tau) : \boldsymbol{\sigma}(t_n) + q(\tau)(p(t) - p(t_n)). \quad (\text{D.8})$$

This result is the same as the differential equation (D.1), the proposed solution is thus acceptable. Continuity conditions are also respected:

$$\begin{aligned} \dot{p}(t = t_n) &= \dot{p}(t_n), \\ p(t = t_n) &= p(t_n). \end{aligned} \quad (\text{D.9})$$

D.2 Linear viscoelastic expressions

The solution in $\hat{p}(\tau, t)$ of the integral equation (6.15) is inserted in equation (6.10) and gives the initial expression reported hereafter. Main goal is to rewrite such complex expression under one similar to a linear thermo-viscoelastic constitutive law by introducing the Stieljes-type convolution product. The final result is given below, a proof of the equivalence between the initial and final result is given afterwards.

Initial expression:

$$\begin{aligned} \forall t \geq t_n : \dot{\boldsymbol{\epsilon}}^{(1)}(t) &= \mathbf{S} : \dot{\boldsymbol{\sigma}}(t) + \mathbf{m}(\tau) : \boldsymbol{\sigma}(t) \\ & \quad + \mathbf{n}(\tau) \int_0^t e^{(t-u)q(\tau)} \mathbf{l}(\tau) : \boldsymbol{\sigma}(u) du + \dot{\boldsymbol{\epsilon}}^{0(1)}(\tau, t), \\ \dot{\boldsymbol{\epsilon}}^{0(1)}(\tau, t) &= \dot{\boldsymbol{\epsilon}}^{in}(t_n) - \mathbf{m}(\tau) : \boldsymbol{\sigma}(t_n) + \hat{p}(\tau, t) \mathbf{n}(\tau). \end{aligned} \quad (\text{D.10})$$

Final expression:

$$\dot{\boldsymbol{\epsilon}}^{(2)}(t) = [\mathbf{S}_\tau \odot \dot{\boldsymbol{\sigma}}]_{(\tau, t)} + \dot{\boldsymbol{\epsilon}}^{0(2)}(\tau, t). \quad (\text{D.11})$$

Expressions of the creep modulus \mathbf{S}_τ and eigenstrain rate tensor $\dot{\boldsymbol{\varepsilon}}^0$ are:

$$\begin{aligned} \mathbf{S}_\tau(\tau, t) &= \mathbf{S} + \mathbf{m}(\tau)t \\ &\quad - q^{-1}(\tau) : \left[t + q^{-1}(\tau) \left(1 - e^{t q(\tau)} \right) \right] \mathbf{n}(\tau) \otimes \mathbf{l}(\tau), \end{aligned} \quad (\text{D.12})$$

$$\begin{aligned} \dot{\boldsymbol{\varepsilon}}^{0(2)}(\tau, t) &= \dot{\boldsymbol{\varepsilon}}^{in}(t_n) - \mathbf{m}(\tau) : \boldsymbol{\sigma}(t_n) + \mathbf{n}(\tau) \hat{p}(\tau, t) \\ &\quad + \dot{\boldsymbol{\varepsilon}}(\tau, t) [1 - H(t - t_n)] + \hat{\boldsymbol{\varepsilon}}^0(\tau, t, \boldsymbol{\sigma}(0)), \end{aligned} \quad (\text{D.13})$$

$$\begin{aligned} \dot{\boldsymbol{\varepsilon}}(\tau, t) &= \dot{\boldsymbol{\varepsilon}}^{in}(t) - \dot{\boldsymbol{\varepsilon}}^{in}(t_n) - \mathbf{m}(\tau) : (\boldsymbol{\sigma}(t) - \boldsymbol{\sigma}(t_n)) \\ &\quad - \mathbf{n}(\tau) \left[\hat{p}(\tau, t) + \int_0^t e^{(t-u)q(\tau)} \mathbf{l}(\tau) : \boldsymbol{\sigma}(u) du \right], \end{aligned} \quad (\text{D.14})$$

$$\hat{\boldsymbol{\varepsilon}}^0(\tau, t, \boldsymbol{\sigma}(0)) = \left[\mathbf{m}(\tau) - \mathbf{n}(\tau) q^{-1}(\tau) \mathbf{l}(\tau) + \mathbf{n}(\tau) q^{-1}(\tau) e^{tq(\tau)} \mathbf{l}(\tau) \right] : \boldsymbol{\sigma}(0),$$

where H is the Heavyside step function. This expression is valid for any time (later or prior to the linearization time t_n). Note that if $t \leq t_n$, expression (D.11) is reduced to:

$$\dot{\boldsymbol{\varepsilon}}(t) = \underbrace{\mathbf{S} : \dot{\boldsymbol{\sigma}}(t)}_{\dot{\boldsymbol{\varepsilon}}^{el}(t)} + \dot{\boldsymbol{\varepsilon}}^{in}(t). \quad (\text{D.15})$$

Equivalence of the two expressions. In the final expression $\dot{\boldsymbol{\varepsilon}}^{0(2)}$, the Stijles-type convolution product \odot is defined as:

$$\begin{aligned} [\mathbf{S}_\tau \odot \dot{\boldsymbol{\sigma}}]_{(\tau, t)} &= \frac{d}{dt} \left[\int_0^t \mathbf{S}_\tau(\tau, t-u) : \dot{\boldsymbol{\sigma}}(u) du \right] \\ &= \int_0^t \frac{d\mathbf{S}_\tau}{du}(\tau, u) : \dot{\boldsymbol{\sigma}}(t-u) du + \mathbf{S}_\tau(\tau, 0) : \dot{\boldsymbol{\sigma}}(t), \end{aligned} \quad (\text{D.16})$$

where the theorem (D.4) has been used to invert the derivative and the integral. Compliance terms are given by:

$$\begin{aligned} \frac{d\mathbf{S}_\tau}{du}(\tau, u) &= \mathbf{m}(\tau) - q^{-1}(\tau) [1 - q^{-1}(\tau) q(\tau) e^{uq(\tau)}] \mathbf{n}(\tau) \otimes \mathbf{l}(\tau) \\ &= \mathbf{m}(\tau) - q^{-1}(\tau) \mathbf{n}(\tau) \otimes \mathbf{l}(\tau) \\ &\quad + q^{-1}(\tau) e^{uq(\tau)} \mathbf{n}(\tau) \otimes \mathbf{l}(\tau), \end{aligned} \quad (\text{D.17})$$

and:

$$\mathbf{S}_\tau(\tau, 0) = \mathbf{S}. \quad (\text{D.18})$$

Expression (D.17) enables to compute the integral in (D.16). Integrals of

the three terms are evaluated separately:

$$\begin{aligned}
\int_0^t \mathbf{m}(\tau) : \dot{\boldsymbol{\sigma}}(t-u) du &\stackrel{y=t-u}{=} - \int_t^0 \mathbf{m}(\tau) : \dot{\boldsymbol{\sigma}}(y) dy \\
&= \int_0^t \mathbf{m}(\tau) : \dot{\boldsymbol{\sigma}}(y) dy \\
&= \mathbf{m}(\tau) : [\boldsymbol{\sigma}(y)]_{y=0}^{y=t} \\
&= \mathbf{m}(\tau) : (\boldsymbol{\sigma}(t) - \boldsymbol{\sigma}(0)), \tag{D.19}
\end{aligned}$$

$$\int_0^t -q^{-1}(\tau) \mathbf{n}(\tau) \mathbf{l}(\tau) : \dot{\boldsymbol{\sigma}}(t-u) du = q^{-1}(\tau) \mathbf{n}(\tau) \mathbf{l}(\tau) : (\boldsymbol{\sigma}(0) - \boldsymbol{\sigma}(t)), \tag{D.20}$$

$$\begin{aligned}
&\int_0^t q^{-1}(\tau) e^{uq(\tau)} \mathbf{n}(\tau) \mathbf{l}(\tau) : \dot{\boldsymbol{\sigma}}(t-u) du \\
&\stackrel{\text{by parts}}{=} [-q^{-1}(\tau) e^{uq(\tau)} \mathbf{n}(\tau) \mathbf{l}(\tau) : \boldsymbol{\sigma}(t-u)]_{u=0}^{u=t} \\
&\quad - \int_0^t q^{-1}(\tau) q(\tau) e^{uq(\tau)} \mathbf{n}(\tau) \mathbf{l}(\tau) : (-\boldsymbol{\sigma}(t-u)) du \\
&\stackrel{s \equiv t-u}{=} -q^{-1}(\tau) e^{tq(\tau)} \mathbf{n}(\tau) \mathbf{l}(\tau) : \boldsymbol{\sigma}(0) + q^{-1}(\tau) e^{0 \cdot q(\tau)} \mathbf{n}(\tau) \mathbf{l}(\tau) : \boldsymbol{\sigma}(t) \\
&\quad - \int_t^0 e^{(t-s)q(\tau)} \mathbf{n}(\tau) \mathbf{l}(\tau) : \boldsymbol{\sigma}(s) ds. \tag{D.21}
\end{aligned}$$

Inserting all these results in the final expression (D.11) gives:

$$\begin{aligned}
\dot{\boldsymbol{\varepsilon}}^{(2)}(t) &= \mathbf{S} : \dot{\boldsymbol{\sigma}}(t) + \mathbf{m}(\tau) : \boldsymbol{\sigma}(t) - q^{-1}(\tau) \mathbf{n}(\tau) \mathbf{l}(\tau) : \boldsymbol{\sigma}(t) \\
&\quad + q^{-1}(\tau) \mathbf{n}(\tau) \mathbf{l}(\tau) : \boldsymbol{\sigma}(t) + \int_0^t e^{(t-u)q(\tau)} \mathbf{n}(\tau) \mathbf{l}(\tau) : \boldsymbol{\sigma}(u) du \\
&\quad + \dot{\boldsymbol{\varepsilon}}^{in}(t_n) - \mathbf{m}(\tau) : \boldsymbol{\sigma}(t_n) + \hat{p}(\tau, t) \mathbf{n}(\tau) \\
&\quad + [1 - H(t - t_n)] \left[\dot{\boldsymbol{\varepsilon}}^{in}(t) - \dot{\boldsymbol{\varepsilon}}^{in}(t_n) - \mathbf{m}(\tau) : (\boldsymbol{\sigma}(t) - \boldsymbol{\sigma}(t_n)) \right. \\
&\quad \left. - \left(\hat{p}(\tau, t) + \int_0^t e^{(t-u)q(\tau)} \mathbf{l}(\tau) : \boldsymbol{\sigma}(u) du \right) \mathbf{n}(\tau) \right]. \tag{D.22}
\end{aligned}$$

This result is equivalent to the initial expression so that expressions (D.10) and (D.11) are the same.

D.3 Linear thermo-elastic expressions

The linear viscoelastic formulation (6.17) with eigenstrain is given by:

$$\dot{\boldsymbol{\varepsilon}}(t) = [\mathbf{S}_\tau \odot \dot{\boldsymbol{\sigma}}]_{(\tau, t)} + \dot{\boldsymbol{\varepsilon}}^0(\tau, t). \tag{D.23}$$

Its Laplace-Carson transform is:

$$\dot{\boldsymbol{\varepsilon}}^*(s) = \underbrace{\mathbf{S}_\tau^*(\tau, s)}_{\text{Term I}} : \dot{\boldsymbol{\sigma}}^*(s) + \underbrace{\dot{\boldsymbol{\varepsilon}}^{0*}(\tau, s)}_{\text{Term II}}. \quad (\text{D.24})$$

This expression is similar to the constitutive law of a linear thermo-elastic material. Terms I and II still must be evaluated.

Term I Expression $\mathbf{S}_\tau(\tau, t)$ is given in equation (D.12). Its Laplace-Carson transform is:

$$\begin{aligned} \mathbf{S}_\tau^*(\tau, s) &= \mathbf{S} + \frac{\mathbf{m}(\tau)}{s} - \frac{q^{-1}(\tau)\mathbf{n}(\tau) \otimes \mathbf{l}(\tau)}{s} \\ &\quad - q^{-1}(\tau)q^{-1}(\tau)\mathbf{n}(\tau) \otimes \mathbf{l}(\tau) + \frac{sq^{-1}(\tau)q^{-1}(\tau)\mathbf{n}(\tau) \otimes \mathbf{l}(\tau)}{s - q(\tau)} \\ &= \mathbf{S} + \frac{\mathbf{m}(\tau)}{s} + \frac{\mathbf{n}(\tau) \otimes \mathbf{l}(\tau)}{s(s - q(\tau))}. \end{aligned} \quad (\text{D.25})$$

This is valid only if $s > \max(0, q(\tau)) = 0$.

Term II Expression of $\dot{\boldsymbol{\varepsilon}}^0(\tau, t)$ is given in equation (D.13). It is separated in four terms as follow:

$$\begin{aligned} \dot{\boldsymbol{\varepsilon}}^0(\tau, t) &= \underbrace{\dot{\boldsymbol{\varepsilon}}^{in}(t_n) - \mathbf{m}(\tau) : \boldsymbol{\sigma}(t_n)}_{\text{Term A}} + \underbrace{\hat{p}(\tau, t)\mathbf{n}(\tau)}_{\text{Term B}} + \underbrace{\dot{\boldsymbol{\varepsilon}}(\tau, t)[1 - H(1 - t_n)]}_{\text{Term C}} \\ &\quad + \underbrace{\left[\mathbf{m}(\tau) - \mathbf{n}(\tau)q^{-1}(\tau)\mathbf{l}(\tau) + \mathbf{n}(\tau)q^{-1}(\tau)e^{tq(\tau)}\mathbf{l}(\tau) \right] : \boldsymbol{\sigma}(0)}_{\text{Term D}}. \end{aligned} \quad (\text{D.26})$$

Due to the linearity of the Laplace-Carson transform, transforms of terms A, B, C and D are evaluated separately.

Term A

$$[\mathcal{L}(\dot{\boldsymbol{\varepsilon}}^{in}(t_n) - \mathbf{m}(\tau) : \boldsymbol{\sigma}(t_n))]_{(s)} = \dot{\boldsymbol{\varepsilon}}^{in}(t_n) - \mathbf{m}(\tau) : \boldsymbol{\sigma}(t_n). \quad (\text{D.27})$$

Term B

$$[\mathcal{L}(\hat{p}(\tau, t)\mathbf{n}(\tau))]_{(s)} = p^*(\tau, s)\mathbf{n}(\tau). \quad (\text{D.28})$$

Expression of $\hat{p}(\tau, t)$ is given by equation (6.16). Transform of the last term of $\hat{p}(\tau, t)$ is given by:

$$\begin{aligned}
& s \int_0^\infty \int_0^{t_n} e^{(t-u)q(\tau)} \mathbf{l}(\tau) : \boldsymbol{\sigma}(u) du e^{-st} dt \\
&= \int_0^{t_n} s \int_0^\infty e^{t(q(\tau)-s)-uq(\tau)} dt \mathbf{l}(\tau) : \boldsymbol{\sigma}(u) du \\
&= -\frac{s}{q(\tau)-s} \mathbf{l}(\tau) : \int_0^{t_n} e^{-uq(\tau)} \boldsymbol{\sigma}(u) du. \tag{D.29}
\end{aligned}$$

This is valid if $s > q(\tau)$. The transform of $\hat{p}(\tau, t)$ is given by:

$$\begin{aligned}
\hat{p}^*(\tau, s) \mathbf{n}(\tau) &= q^{-1}(\tau) \frac{s}{s-q(\tau)} e^{-t_n q(\tau)} \dot{p}(t_n) \mathbf{n}(\tau) \\
&\quad - q^{-1}(\tau) \frac{s}{s-q(\tau)} e^{-t_n q(\tau)} \mathbf{l}(\tau) : \boldsymbol{\sigma}(t_n) \mathbf{n}(\tau) \\
&\quad - q^{-1}(\tau) \dot{p}(t_n) \mathbf{n}(\tau) + q^{-1}(\tau) \mathbf{l}(\tau) : \boldsymbol{\sigma}(t_n) \mathbf{n}(\tau) \\
&\quad + \frac{s}{q(t_n)-s} \mathbf{l}(\tau) : \int_0^{t_n} e^{-uq(\tau)} \boldsymbol{\sigma}(u) du \mathbf{n}(\tau). \tag{D.30}
\end{aligned}$$

Term C Laplace-Carson transform of term C is now examined. Expression of $\dot{e}(\tau, t)$ is given by equation (D.14). Due to the Heavyside function, integral of the Laplace-Carson transform is limited up to $t = t_n$ instead of $t = \infty$ and will be denoted:

$$[\mathcal{L}^{0 \rightarrow t_n}(\dot{\mathbf{e}}^{in}(t))]_{(s)} = s \int_0^{t_n} \dot{\mathbf{e}}^{in}(t) e^{-st} dt. \tag{D.31}$$

Transform of several terms of $\dot{e}(\tau, t)$ can be easily evaluated:

$$\begin{aligned}
[\mathcal{L}^{0 \rightarrow t_n}(\dot{\mathbf{e}}(t_n))]_{(s)} &= s \int_0^{t_n} \dot{\mathbf{e}}^{in}(t_n) e^{-st} dt \\
&= s \dot{\mathbf{e}}^{in}(t_n) \left[\frac{-e^{-st}}{s} \right]_0^{t_n} \\
&= \dot{\mathbf{e}}^{in}(t_n) (1 - e^{-st_n}), \\
[\mathcal{L}^{0 \rightarrow t_n}(\mathbf{m}(\tau) : \boldsymbol{\sigma}(t))]_{(s)} &= s \mathbf{m}(\tau) : \int_0^{t_n} \boldsymbol{\sigma}(t) e^{-st} dt, \\
[\mathcal{L}^{0 \rightarrow t_n}(\mathbf{m}(\tau) : \boldsymbol{\sigma}(t_n))]_{(s)} &= \mathbf{m}(\tau) : \boldsymbol{\sigma}(t_n) (1 - e^{-st_n}), \\
[\mathcal{L}^{0 \rightarrow t_n}(\mathbf{n}(\tau) \hat{p}(\tau, t))]_{(s)} &= \mathbf{n}(\tau) [\mathcal{L}^{0 \rightarrow t_n}(\hat{p}(\tau, t))]_{(s)}. \tag{D.32}
\end{aligned}$$

In this last equation, things are becoming a little bit more complex since $\hat{p}(\tau, t)$ is given by equation (6.16):

$$\begin{aligned}\hat{p}(\tau, t) &= q^{-1}(\tau) \left[e^{(t-t_n)q(\tau)} - 1 \right] [\dot{p}(t_n) - \mathbf{l}(\tau) : \boldsymbol{\sigma}(t_n)] \\ &\quad - \int_0^{t_n} e^{(t-u)q(\tau)} \mathbf{l}(\tau) : \boldsymbol{\sigma}(u) du.\end{aligned}\quad (\text{D.33})$$

Firstly, let's evaluate a preliminary integral:

$$\begin{aligned}\left[\mathcal{L}^{0 \rightarrow t_n} (e^{(t-t_n)q(\tau)}) \right]_{(s)} &= s \int_0^{t_n} e^{(t-t_n)q(\tau)} e^{-st} dt \\ &= s \int_0^{t_n} e^{(q(\tau)-s)t} e^{-t_n q(\tau)} dt \\ &= s \left[\frac{e^{(q(\tau)-s)t} e^{-t_n q(\tau)}}{q(\tau) - s} \right]_0^{t_n} \\ &= s \frac{e^{-st_n} - e^{-q(\tau)t_n}}{q(\tau) - s}.\end{aligned}\quad (\text{D.34})$$

This gives the transform of the last term of $\hat{p}(\tau, t)$:

$$\begin{aligned}s \int_0^{t_n} \int_0^{t_n} e^{(t-u)q(\tau)} \mathbf{l}(\tau) : \boldsymbol{\sigma}(u) du e^{-st} dt \\ &= \int_0^{t_n} s \int_0^{t_n} e^{(t-u)q(\tau)} e^{-st} dt \mathbf{l}(\tau) : \boldsymbol{\sigma}(u) du \\ &= \int_0^{t_n} s \left[\frac{e^{t(q(\tau)-s)-uq(\tau)}}{q(\tau) - s} \right]_0^{t_n} \mathbf{l}(\tau) : \boldsymbol{\sigma}(u) du \\ &= \int_0^{t_n} \frac{s}{q(\tau) - s} (e^{t_n(q(\tau)-s)-uq(\tau)} - e^{-uq(\tau)}) \mathbf{l}(\tau) : \boldsymbol{\sigma}(u) du \\ &= \frac{s}{q(\tau) - s} \mathbf{l}(\tau) : \int_0^{t_n} e^{-uq(\tau)} \boldsymbol{\sigma}(u) du (e^{t_n(q(\tau)-s)} - 1).\end{aligned}\quad (\text{D.35})$$

Finally, the modified Laplace-Carson transform of (D.32) is given by:

$$\begin{aligned}\left[\mathcal{L}^{0 \rightarrow t_n} (\hat{p}(\tau, t) \mathbf{n}(\tau)) \right]_{(s)} &= q^{-1}(\tau) s \frac{e^{-st_n} - e^{-q(\tau)t_n}}{q(\tau) - s} \dot{p}(t_n) \mathbf{n}(\tau) \\ &\quad - q^{-1}(\tau) s \frac{e^{-st_n} - e^{-q(\tau)t_n}}{q(\tau) - s} \mathbf{l}(\tau) : \boldsymbol{\sigma}(t_n) \mathbf{n}(\tau) \\ &\quad + \frac{s}{q(\tau) - s} \mathbf{l}(\tau) : \int_0^{t_n} e^{-uq(\tau)} \boldsymbol{\sigma}(u) du (e^{t_n(q(\tau)-s)} - 1) \mathbf{n}(\tau).\end{aligned}$$

Last term of (D.14) can be transformed as:

$$\begin{aligned} & \left[\mathcal{L}^{0 \rightarrow t_n} \mathbf{l}(\tau) : \int_0^t e^{(t-u)q(\tau)} \boldsymbol{\sigma}(u) du \mathbf{n}(\tau) \right]_{(s)} \\ &= s \int_0^{t_n} \mathbf{l}(\tau) : \int_0^t e^{(t-u)q(\tau)} \boldsymbol{\sigma}(u) du e^{-st} dt \mathbf{n}(\tau). \end{aligned} \quad (\text{D.36})$$

Regrouping all the partial transform, one get the one of $\dot{e}(\tau, t)$:

$$\begin{aligned} & [\mathcal{L}(\dot{e}(\tau, t)[1 - H(t - t_n)])]_{(s)} \\ &= s \int_0^{t_n} \dot{\boldsymbol{\epsilon}}^{in}(t) e^{-st} dt - \dot{\boldsymbol{\epsilon}}^{in}(t_n)(1 - e^{-st_n}) - s \mathbf{m}(\tau) : \int_0^{t_n} \boldsymbol{\sigma}(t) e^{-st} dt \\ & \quad + \mathbf{m}(\tau) : \boldsymbol{\sigma}(t_n)(1 - e^{-st_n}) \\ & \quad - q^{-1}(\tau) s \frac{e^{-st_n} - e^{-q(\tau)t_n}}{q(\tau) - s} \dot{\mathbf{p}}(t_n) \mathbf{n}(\tau) \\ & \quad + q^{-1}(\tau) \mathbf{l}(\tau) : \boldsymbol{\sigma}(t_n) s \frac{e^{-st_n} - e^{-q(\tau)t_n}}{q(\tau) - s} \mathbf{n}(\tau) \\ & \quad + q^{-1}(\tau) [\dot{\mathbf{p}}(t_n) - \mathbf{l}(\tau) : \boldsymbol{\sigma}(t_n)] \mathbf{n}(\tau) (1 - e^{-st_n}) \\ & \quad + \frac{s}{q(\tau) - s} \mathbf{l}(\tau) : \int_0^{t_n} e^{-uq(\tau)} \boldsymbol{\sigma}(u) du (e^{t_n(q(\tau)-s)} - 1) \mathbf{n}(\tau) \end{aligned} \quad (\text{D.37})$$

$$- s \mathbf{n}(\tau) : \mathbf{l}(\tau) \int_0^{t_n} \int_0^t e^{(t-u)q(\tau)} \boldsymbol{\sigma}(u) du e^{-st} dt. \quad (\text{D.38})$$

Last term (D.37) can be rewritten as:

$$\begin{aligned} & \mathbf{n}(\tau) : \mathbf{l}(\tau) \int_0^{t_n} \int_0^t e^{(t-u)q(\tau)} \boldsymbol{\sigma}(u) du e^{-st} dt \quad (\text{D.39}) \\ &= \frac{s \mathbf{n}(\tau) : \mathbf{l}(\tau)}{q(\tau) - s} \left[e^{t_n(q(\tau)-s)} \int_0^{t_n} \boldsymbol{\sigma}(u) e^{-uq(\tau)} du - \int_0^{t_n} \boldsymbol{\sigma}(u) e^{-su} du \right]. \end{aligned}$$

This enable to further simplify the sum of (D.37) and (D.38).

Term D Term D can be viewed as a function of $\boldsymbol{\sigma}(0)$. Its Laplace-Carson transform is given by:

$$\begin{aligned} \hat{\boldsymbol{\epsilon}}^{0*}(\tau, s, \boldsymbol{\sigma}(0)) &= \mathbf{m}(\tau) : \boldsymbol{\sigma}(0) - \mathbf{n}(\tau) q^{-1}(\tau) \mathbf{l}(\tau) : \boldsymbol{\sigma}(0) \\ & \quad + \mathbf{n}(\tau) q^{-1}(\tau) \frac{s}{s - q(\tau)} \mathbf{l}(\tau) : \boldsymbol{\sigma}(0). \end{aligned} \quad (\text{D.40})$$

This is valid only if $s > q(\tau)$. Regrouping terms A, B, C and D enables to compute $\hat{\boldsymbol{\epsilon}}^{0*}$. Its final expression is reported in the main text (section 6.3.1).

D.4 Limit values for the Laplace-Carson inversion

For the numerical inversion of the Laplace-Carson transform with a collocation method, two limits of the function are needed. For a function $f(t)$ (denoted $f^*(s)$ in the Laplace domain), these can be evaluated equivalently in the Laplace or time domain:

$$\begin{aligned}\lim_{s \rightarrow \infty} f^*(s) &= \lim_{t \rightarrow 0} f(t), \\ \lim_{s \rightarrow 0} s f^*(s) &= \lim_{t \rightarrow \infty} \frac{f(t)}{t}.\end{aligned}\quad (\text{D.41})$$

In the proposed algorithm to solve the localization problem for two-phase elasto-viscoplastic plastic composite with an affine formulation, the two strain concentration tensors of linear thermo-elasticity have to be inverted: $\mathbf{A}^{\epsilon^*}(\tau, s)$ and $\mathbf{a}^{\epsilon^*}(\tau, s)$. Expressions for the strain concentration tensors used in this section correspond to the Mori-Tanaka homogenization scheme (section 4.2.3) but limit values for other mean-field models can be obtained in a similar way. If the final macroscopic response is computed via the macroscopic relation of linear viscoelasticity (equation (6.24)), macroscopic stiffness and eigenstrain must also be inverted. Limit values of these expressions are given in Pierard [77].

D.4.1 The different functions

In the following, the subscript r refers to the matrix ($r = 0$) or the inclusions ($r = 1$).

General case $\mathbf{C}_0^*(\tau, s) \neq \mathbf{C}_1^*(\tau, s)$

$$\begin{aligned}\mathbf{S}_r^*(\tau, s) &= \mathbf{S}_r + \frac{\mathbf{m}_r(\tau)}{s} + \frac{\mathbf{n}_r(\tau) \otimes \mathbf{l}_r(\tau)}{s(s - q_r(\tau))}, \\ \mathbf{C}_r^*(\tau, s) &= \mathbf{S}_r^{*-1}(\tau, s), \\ \mathcal{E}^*(\tau, s) &: \text{Eshelby's tensor remains finite for any } \nu \neq 0, \\ \mathbf{B}^{\epsilon^*}(\tau, s) &= [\mathbf{I} + \mathcal{E}^*(\tau, s) : ((\mathbf{C}_0^*(\tau, s))^{-1} : \mathbf{C}_1^*(\tau, s) - \mathbf{I})]^{-1}, \\ \mathbf{A}^{\epsilon^*}(\tau, s) &= \mathbf{B}^{\epsilon^*}(\tau, s) : [(1 - v_1)\mathbf{I} + v_1\mathbf{B}^{\epsilon^*}(\tau, s)]^{-1}, \\ \boldsymbol{\varepsilon}_r^{0*}(\tau, s) &: \text{see equation (6.21),} \\ \mathbf{a}^{\epsilon^*}(\tau, s) &= (\mathbf{A}^{\epsilon^*} - \mathbf{I}) : (\mathbf{C}_1^*(\tau, s) - \mathbf{C}_0^*(\tau, s))^{-1} \\ &: [\mathbf{C}_0^*(\tau, s) : \boldsymbol{\varepsilon}_0^{0*}(\tau, s) - \mathbf{C}_1^*(\tau, s) : \boldsymbol{\varepsilon}_1^{0*}(\tau, s)].\end{aligned}\quad (\text{D.42})$$

Particular case Some of these expressions become invalid and have to be reformulated if $\mathbf{C}_1^*(\tau, s) = \mathbf{C}_0^*(\tau, s)$

$$\begin{aligned}
\mathbf{S}_r^*(\tau, s), \mathbf{C}_0^*(\tau, s) \text{ and } \mathcal{E}(\tau, s) &\text{ remain valid and unchanged,} \\
\mathbf{B}^{\epsilon^*}(\tau, s) &= \mathbf{I}, \\
\mathbf{A}^{\epsilon^*}(\tau, s) &= \mathbf{I}, \\
\boldsymbol{\varepsilon}^{0^*}(\tau, s) &\text{ remains valid and unchanged,} \\
\mathbf{a}^{\epsilon^*}(\tau, s) &\text{ becomes invalid.}
\end{aligned} \tag{D.43}$$

In the last expression, when the inclusion's parameters tend to the ones of the matrix, first term of $\mathbf{a}^{\epsilon^*}(\tau, s)$ tends to \mathbf{I} , second one to $\mathbf{0}$ and the contraction of the third and fourth ones tends to $\boldsymbol{\varepsilon}_1^{0^*}(\tau, s) - \boldsymbol{\varepsilon}_0^{0^*}(\tau, s)$. Thus, if $\mathbf{C}_0^*(\tau, s) = \mathbf{C}_1^*(\tau, s)$, $\mathbf{a}^{\epsilon^*}(\tau, s) = \mathbf{0}$.

D.4.2 Limit values for $s \rightarrow \infty$

General case $\lim_{s \rightarrow \infty} \mathbf{C}_0^*(\tau, s) \neq \lim_{s \rightarrow \infty} \mathbf{C}_1^*(\tau, s)$

$$\begin{aligned}
\lim_{s \rightarrow \infty} \mathbf{S}_r^*(\tau, s) &= \mathbf{S}_r, \\
\lim_{s \rightarrow \infty} \mathbf{C}_r^*(\tau, s) &= \mathbf{S}_r^{-1}, \\
\lim_{s \rightarrow \infty} \mathcal{E}^*(\tau, s) &\text{ remains finite,} \\
\lim_{s \rightarrow \infty} \mathbf{B}^{\epsilon^*}(\tau, s) &= \left[\mathbf{I} + \lim_{s \rightarrow \infty} \mathcal{E}^* : (\mathbf{S}_0 : \mathbf{S}_1^{-1} - \mathbf{I}) \right]^{-1}, \\
\lim_{s \rightarrow \infty} \mathbf{A}^{\epsilon^*}(\tau, s) &= \lim_{s \rightarrow \infty} \mathbf{B}^{\epsilon^*}(\tau, s) : (v_1 \lim_{s \rightarrow \infty} \mathbf{B}^{\epsilon^*}(\tau, s) + (1 - v_1)\mathbf{I})^{-1}, \\
\lim_{s \rightarrow \infty} \boldsymbol{\varepsilon}_r^{0^*}(\tau, s) &= \mathbf{m}_r(\tau) : \boldsymbol{\sigma}_r(0), \\
\lim_{s \rightarrow \infty} \mathbf{a}^{\epsilon^*}(\tau, s) &= (1 - v_1) \left(v_1 \lim_{s \rightarrow \infty} \mathbf{B}^{\epsilon^*}(\tau, s) + (1 - v_1)\mathbf{I} \right)^{-1}, \\
&: \left(\lim_{s \rightarrow \infty} \mathbf{B}^{\epsilon^*}(\tau, s) - \mathbf{I} \right) : (\mathbf{S}_1^{-1} - \mathbf{S}_0^{-1})^{-1}, \\
&: (\mathbf{S}_0^{-1} : \mathbf{m}_0(\tau) : \boldsymbol{\sigma}_0(0) - \mathbf{S}_1^{-1} : \mathbf{m}_1(\tau) : \boldsymbol{\sigma}_1(0)). \tag{D.44}
\end{aligned}$$

Limits of the strain concentration tensors can be evaluated just once for all time-steps if $\boldsymbol{\sigma}_0(0) = 0$ and $\boldsymbol{\sigma}_1(0) = 0$. Otherwise, additional time-dependent terms must be considered.

Particular case $\lim_{s \rightarrow \infty} \mathbf{C}_0^*(\tau, s) = \lim_{s \rightarrow \infty} \mathbf{C}_1^*(\tau, s)$

$\lim_{s \rightarrow \infty} \mathbf{S}_r^*(\tau, s)$ and $\lim_{s \rightarrow \infty} \mathbf{C}_r^*(\tau, s)$ remains valid and unchanged.

$$\begin{aligned}
\lim_{s \rightarrow \infty} \mathcal{E}^*(\tau, s) & \quad (\text{remains finite}), \\
\lim_{s \rightarrow \infty} \mathbf{B}^{\varepsilon^*}(\tau, s) & = \mathbf{I} \text{ (simplified),} \\
\lim_{s \rightarrow \infty} \mathbf{A}^{\varepsilon^*}(\tau, s) & = \mathbf{I} \text{ (simplified),} \\
\lim_{s \rightarrow \infty} \varepsilon_r^{0*}(\tau, s) & = \mathbf{m}_r(\tau) : \boldsymbol{\sigma}_r(0) \text{ (unchanged),} \\
\lim_{s \rightarrow \infty} \mathbf{a}^{\varepsilon^*}(\tau, s) & = \mathbf{0} \text{ (undetermined in the general case).} \quad (\text{D.45})
\end{aligned}$$

D.4.3 Limit values for $s \rightarrow 0$

General case $\lim_{s \rightarrow 0} \mathbf{C}_0^*(\tau, s) \neq \lim_{s \rightarrow 0} \mathbf{C}_1^*(\tau, s)$

$$\begin{aligned}
\lim_{s \rightarrow 0} \mathbf{S}_r^*(\tau, s) & = \frac{1}{s(s - q_r(\tau))} [s(s - q_r(\tau))\mathbf{S}_r \\
& \quad + (s - q_r(\tau))\mathbf{m}_r(\tau) + \mathbf{n}_r(\tau) \otimes \mathbf{l}_r(\tau)], \\
\lim_{s \rightarrow 0} \mathbf{C}_r^*(\tau, s) & = \left[\lim_{s \rightarrow 0} \mathbf{S}_r^*(\tau, s) \right]^{-1} \\
& = \lim_{s \rightarrow 0} -s q_r(\tau) [-q_r(\tau)\mathbf{m}_0(\tau) + \mathbf{n}_r(\tau) \otimes \mathbf{l}_r(\tau)]^{-1} \\
& = \mathbf{0}, \\
\lim_{s \rightarrow 0} \mathcal{E}^*(\tau, s) & \quad \text{remains finite since } \lim_{s \rightarrow 0} \mathbf{C}_0^*(\tau, s) = 0, \\
\lim_{s \rightarrow 0} [\mathbf{C}_0^{*-1}(\tau, s) : \mathbf{C}_1^*(\tau, s) - \mathbf{I}] \\
& = \lim_{s \rightarrow 0} \frac{q_1(\tau)}{q_0(\tau)} [s(s - q_0(\tau))\mathbf{S}_0 + (s - q_0(\tau))\mathbf{m}_0(\tau) + \mathbf{n}_0(\tau) \otimes \mathbf{l}_0(\tau)] : \\
& \quad : [s(s - q_1(\tau))\mathbf{S}_1 + (s - q_1(\tau))\mathbf{m}_1(\tau) + \mathbf{n}_1(\tau) \otimes \mathbf{l}_1(\tau)]^{-1} - \mathbf{I} \\
& = \frac{q_1(\tau)}{q_0(\tau)} [\mathbf{n}_0(\tau) \otimes \mathbf{l}_0(\tau) - q_0(\tau)\mathbf{m}_0(\tau)] : [\mathbf{n}_1(\tau) \otimes \mathbf{l}_1(\tau) - q_1(\tau)\mathbf{m}_1(\tau)]^{-1} \\
& \quad - \mathbf{I}. \quad (\text{D.46})
\end{aligned}$$

$$\begin{aligned}
\lim_{s \rightarrow 0} \mathbf{B}^{\varepsilon^*}(\tau, s) & = \lim_{s \rightarrow 0} \left[\underbrace{\mathbf{I} + \underbrace{\mathbf{S}^*(\mathbf{I}, \mathbf{C}^{*iso}(\tau, s))}_{\text{Finite}} : \underbrace{(\mathbf{C}_0^{*-1} : \mathbf{C}_1^* - \mathbf{I})}_{\text{Finite}}}_{\text{Finite}} \right]^{-1}. \\
\lim_{s \rightarrow 0} s \mathbf{A}^{\varepsilon^*}(\tau, s) & = \underbrace{s \lim_{s \rightarrow 0} \mathbf{H}^{\varepsilon^*}(\tau, s)}_{\text{Finite}} : \underbrace{[v_0 \mathbf{I} + v_1 \lim_{s \rightarrow 0} \mathbf{H}^{\varepsilon^*}(\tau, s)]^{-1}}_{\text{Finite}} \\
& = \mathbf{0}. \quad (\text{D.47})
\end{aligned}$$

$$\begin{aligned}
\lim_{s \rightarrow 0} \boldsymbol{\varepsilon}_r^{0*}(\tau, s) &= \dot{\boldsymbol{\varepsilon}}_r^{in}(\tau) - q^{-1}(\tau) \dot{p}(\tau) \mathbf{n}(\tau) + q^{-1}(\tau) \mathbf{l}(\tau) : \boldsymbol{\sigma}(\tau) \mathbf{n}(\tau) \\
&- \left(\int_0^\tau e^{(\tau-t)q(\tau)} \mathbf{l}(\tau) : \boldsymbol{\sigma}(t) dt \right) \mathbf{n}(\tau) \\
&+ \mathbf{m}(\tau) : \boldsymbol{\sigma}(0) - \mathbf{n}(\tau) q^{-1}(\tau) \mathbf{l}(\tau) : \boldsymbol{\sigma}(0). \tag{D.48}
\end{aligned}$$

Remains finite!

$$\begin{aligned}
&\lim_{s \rightarrow 0} [\mathbf{C}_1^*(\tau, s) - \mathbf{C}_0^*(\tau, s)]^{-1} : [\mathbf{C}_0^*(\tau, s) : \boldsymbol{\varepsilon}_0^{0*}(\tau, s) - \mathbf{C}_1^*(\tau, s) : \boldsymbol{\varepsilon}_1^{0*}(\tau, s)] \\
&= \lim_{s \rightarrow 0} s^{-1} [-q_1(\tau) (-q_1(\tau) \mathbf{m}_1(\tau) + \mathbf{n}_1(\tau) \otimes \mathbf{l}_1(\tau))^{-1} \\
&\quad + q_0(\tau) (-q_0(\tau) \mathbf{m}_0(\tau) + \mathbf{n}_0(\tau) \otimes \mathbf{l}_0(\tau))^{-1}]^{-1} \\
&: s [-q_0(\tau) (-q_0(\tau) \mathbf{m}_0(\tau) + \mathbf{n}_0(\tau) \otimes \mathbf{l}_0(\tau))^{-1} : \boldsymbol{\varepsilon}_0^{0*} \\
&\quad + q_1(\tau) (-q_1(\tau) \mathbf{m}_1(\tau) + \mathbf{n}_1(\tau) \otimes \mathbf{l}_1(\tau))^{-1} : \boldsymbol{\varepsilon}_1^{0*}]. \tag{D.49}
\end{aligned}$$

s^{-1} and s can be simplified each others and this limit is thus finite.

$$\begin{aligned}
\lim_{s \rightarrow 0} s \mathbf{a}^{\varepsilon^*}(\tau, s) &= s v_0 \underbrace{\left[v_1 \lim_{s \rightarrow 0} \mathbf{B}^{\varepsilon^*}(\tau, s) + v_0 \mathbf{I} \right]^{-1}}_{\text{Finite}} : \underbrace{\left[\lim_{s \rightarrow 0} \mathbf{B}^{\varepsilon^*}(\tau, s) - \mathbf{I} \right]}_{\text{Finite}} \\
&: \underbrace{\left[\mathbf{C}_1^*(\tau, s) - \mathbf{C}_0^*(\tau, s) \right]^{-1} : [\mathbf{C}_0^*(\tau, s) : \boldsymbol{\varepsilon}_0^{0*}(\tau, s) - \mathbf{C}_1^*(\tau, s) : \boldsymbol{\varepsilon}_1^{0*}(\tau, s)]}_{\text{Finite}} \\
&= \mathbf{0}. \tag{D.50}
\end{aligned}$$

The two required limits are thus nil for all times.

Particular case $\lim_{s \rightarrow 0} \mathbf{C}_0^*(\tau, s) = \lim_{s \rightarrow 0} \mathbf{C}_1^*(\tau, s)$.

$\lim_{s \rightarrow 0} \mathbf{S}_r^*(\tau, s)$, $\lim_{s \rightarrow 0} \mathbf{C}_r^*(\tau, s)$ and $\lim_{s \rightarrow 0} \mathcal{E}^*(\mathbf{I}, \mathbf{C}^{*iso}(\tau, s))$ remain valid and unchanged.

$$\begin{aligned}
\lim_{s \rightarrow 0} \mathbf{H}^{\varepsilon^*}(\tau, s) &= \mathbf{I}, \\
\lim_{s \rightarrow 0} s \mathbf{F}^*(\tau, s) &= \mathbf{0} \text{ (unchanged)}, \\
\lim_{s \rightarrow 0} \boldsymbol{\varepsilon}_r^{0*}(\tau, s) &\text{ (unchanged)}, \\
\lim_{s \rightarrow 0} s \mathbf{a}^{\varepsilon^*}(\tau, s) &= \mathbf{0} \text{ (unchanged)}. \tag{D.51}
\end{aligned}$$

Appendix E

Tensile tests

This appendix examines the required additional loop for tensile test. This is necessary when considering loading cases such as uniaxial tension, biaxial tension, hydrostatic pressure, creep, . . . Only the two first cases are examined here. The proposed algorithm is for a strain driven approach so that imposition of the required conditions on the stress tensor is not trivial a priori. For example, in the case of a tensile test, $\Delta\varepsilon_{11}$ is given over a time step (if traction is performed along direction 1) but the other components of the strain increment are unknown. This iterative procedure is required at each time step. Hereafter, $\bar{\mathbf{C}}$ designates the tangent modulus.

E.1 Uniaxial tensile test

At the end of a time-step, the system should be form similar to:

$$\begin{pmatrix} \Delta\sigma_{11} & 0 & 0 \\ 0 & 0 & 0 \\ 0 & 0 & 0 \end{pmatrix} = \bar{\mathbf{C}} : \begin{pmatrix} \Delta\varepsilon_{11} & 0 & 0 \\ 0 & \Delta\varepsilon_{22} & 0 \\ 0 & 0 & \Delta\varepsilon_{33} \end{pmatrix},$$

$\Delta\sigma_{22}$ and $\Delta\sigma_{33}$ are nil only for particular values of the unknowns $\Delta\varepsilon_{22}$ and $\Delta\varepsilon_{33}$. Starting form arbitrary values for these components, an iterate Newton-Raphson scheme is used. The two functions to varnish are written as:

$$\begin{aligned} \Delta\sigma_{22} &= \bar{C}_{2211}\Delta\varepsilon_{11} + \bar{C}_{2222}\Delta\varepsilon_{22} + \bar{C}_{2233}\Delta\varepsilon_{33} = 0, \\ \Delta\sigma_{33} &= \bar{C}_{3311}\Delta\varepsilon_{11} + \bar{C}_{3322}\Delta\varepsilon_{22} + \bar{C}_{3333}\Delta\varepsilon_{33} = 0. \end{aligned} \quad (\text{E.1})$$

The Newton-Raphson system can thus be written as:

$$\begin{bmatrix} \Delta\sigma_{22} \\ \Delta\sigma_{33} \end{bmatrix}^{it} + \begin{bmatrix} \bar{C}_{2222} & \bar{C}_{2233} \\ \bar{C}_{3322} & \bar{C}_{3333} \end{bmatrix}^{it} : \begin{bmatrix} \Delta\varepsilon_{22}^{it+1} - \Delta\varepsilon_{22}^{it} \\ \Delta\varepsilon_{33}^{it+1} - \Delta\varepsilon_{33}^{it} \end{bmatrix} = 0.$$

$\Delta\varepsilon_{33}^{it+1}$ can be isolated from the first equation:

$$\Delta\varepsilon_{33}^{it+1} = \Delta\varepsilon_{33}^{it} - \frac{1}{\bar{C}_{2233}^{it}} \Delta\sigma_{22}^{it} - \frac{1}{\bar{C}_{2233}^{it}} \bar{C}_{2222}^{it} (\Delta\varepsilon_{22}^{it+1} - \Delta\varepsilon_{22}^{it}). \quad (\text{E.2})$$

Inserting this result into the second one gives:

$$\Delta\sigma_{33}^{it} + \bar{C}_{3322}^{it} (\Delta\varepsilon_{22}^{it+1} - \Delta\varepsilon_{22}^{it}) - C_{3333}^{it} \left(\frac{\Delta\sigma_{22}^{it}}{C_{2233}^{it}} + \frac{C_{2222}^{it}}{C_{2233}^{it}} (\Delta\varepsilon_{22}^{it+1} - \Delta\varepsilon_{22}^{it}) \right) = 0,$$

which can be rewritten as:

$$(\Delta\varepsilon_{22}^{it+1} - \Delta\varepsilon_{22}^{it}) \left(\bar{C}_{3322}^{it} - \frac{C_{3333}^{it} C_{2222}^{it}}{C_{2233}^{it}} \right) + \Delta\sigma_{33}^{it} - \frac{C_{3333}^{it}}{C_{2233}^{it}} \Delta\sigma_{22}^{it} = 0. \quad (\text{E.3})$$

Final expression of the new iteration of the strain increments are given by:

$$\begin{aligned} \Delta\varepsilon_{22}^{it+1} &= \Delta\varepsilon_{22}^{it} + \left(\bar{C}_{3322}^{it} - \frac{C_{3333}^{it} C_{2222}^{it}}{C_{2233}^{it}} \right)^{-1} \left(\frac{C_{3333}^{it}}{C_{2233}^{it}} \Delta\sigma_{22}^{it} - \Delta\sigma_{33}^{it} \right), \\ \Delta\varepsilon_{33}^{it+1} &= \Delta\varepsilon_{33}^{it} - \frac{\Delta\sigma_{22}^{it}}{\bar{C}_{2233}^{it}} - \frac{\bar{C}_{2222}^{it}}{\bar{C}_{2233}^{it}} (\Delta\varepsilon_{22}^{it+1} - \Delta\varepsilon_{22}^{it}). \end{aligned} \quad (\text{E.4})$$

Initialization of the strain increments can be given by:

$$\begin{aligned} \Delta\varepsilon_{11}^1 &\text{ given,} \\ \Delta\varepsilon_{22}^1 &= -0.49\Delta\varepsilon_{11}^1, \\ \Delta\varepsilon_{33}^1 &= -0.49\Delta\varepsilon_{11}^1. \end{aligned} \quad (\text{E.5})$$

E.2 Biaxial tensile test

At the end of a time-step, the system should be form similar to:

$$\begin{pmatrix} \Delta\sigma_{11} & 0 & 0 \\ 0 & \Delta\sigma_{22} & 0 \\ 0 & 0 & 0 \end{pmatrix} = \bar{C} : \begin{pmatrix} \Delta\varepsilon_{11} & 0 & 0 \\ 0 & \Delta\varepsilon_{22} & 0 \\ 0 & 0 & \Delta\varepsilon_{33} \end{pmatrix}.$$

Only the last component of the stress matrix is not trivially satisfied. In this case, the problem is thus reduced to find the solution of a single equation:

$$\Delta\sigma_{33} = \bar{C}_{3311} : \Delta\varepsilon_{11} + \bar{C}_{3322} : \Delta\varepsilon_{22} + \bar{C}_{3333} : \Delta\varepsilon_{33}. \quad (\text{E.6})$$

Solving this equation with the Newton-Raphson method gives:

$$\Delta\sigma_{33}^{it} + \bar{C}_{3333} : (\Delta\varepsilon_{33}^{it+1} - \Delta\varepsilon_{33}^{it}) = 0. \quad (\text{E.7})$$

The new iteration of the strain increment is finally given by:

$$\Delta\varepsilon_{33}^{it+1} = \Delta\varepsilon_{33}^{it} - \frac{\Delta\sigma_{33}^{it}}{\bar{C}_{3333}}. \quad (\text{E.8})$$

Appendix F

A short introduction to Affinistan

Affinistan is the main software developed during this thesis. It enables to predict the behavior of two phase elasto-viscoplastic composites. This is done with an affine linearization of the local constitutive law and predictions are obtained with a mean-field homogenization scheme. Even if not mandatory, Affinistan comes with its graphical user interface which enables to describe easily both materials, the loading conditions and some numerical parameters. Furthermore, a basic post processor handles with plots. Possibilities offered by the software are briefly presented hereafter.

F.1 Input section

The input section is divided into four main windows (see figure F.1). First and second ones describe both phases of the material. A third one is devoted to the mean-field homogenization scheme and the loading parameters. The last section specifies some optional parameters. Furthermore, a main toolbar offers some global options.

F.1.1 Toolbar

Here is a basic description of the buttons of the main toolbar.

- New: Reinitialize all the fields as when launching the software.
- Load: Enable to load an input (.dat) file for a simulation with Affinistan.

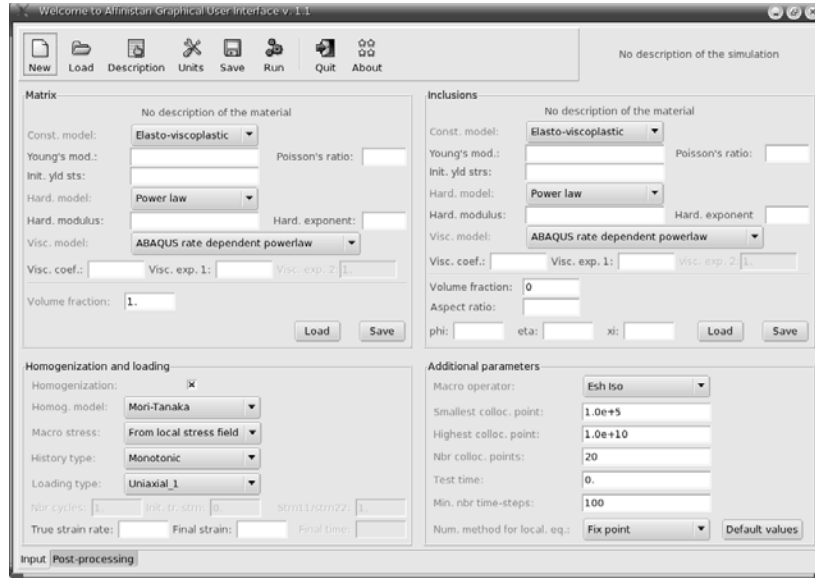


Figure F.1: Input section of Affinistan.

- Description: Give a description of both materials and of the simulation. These fields appear in the input window of the graphical user interface and in comments of the .dat file.
- Units: Define the global unit system (for stress, time and angles). A modification induces an optional automatic correction of the already filled fields.
- Save: Write the corresponding .dat file of the current simulation.
- Run: Run a simulation. If not done previously, the user is prompted to save the simulation. Some checks are made if the fields are filled correctly (each field label correctly filled is green if correct or red otherwise).
- Quit: Exit Affinistan.
- About: Give informations about the software.

F.1.2 Matrix and inclusions sections

- Const. model: Select the constitutive model: linear elastic, elasto-plastic or elasto-viscoplastic. For linear elastic materials, the initial yield stress is set very high and for elasto-plastic ones, the viscosity is set very low.

- Young's mod.: Young's modulus (E).
- Poisson's ratio: Poisson's ratio (ν).
- Init. yld str: Initial yield stress (σ_Y).
- Hard. model: Hardening model: power law, exponential law or Swift law. The two first models are presented in section 6.1.
- Hard. modulus: Hardening modulus (k).
- Hard. exponent: Hardening exponent (n).
- Visc. model: Model for the viscoplastic function (g_v): Norton (see Doghri [24]), three-parameters creep model of ABAQUS [1], the viscous model defined by Li and Weng ([58]) or the ABAQUS rate-dependent power law [1]. Some of these models are presented in section 6.1.
- Visc. coef.: Viscoplastic coefficient.
- Visc. exp. 1: First viscoplastic exponent.
- Visc. exp. 2: Second viscoplastic exponent.
- Volume fraction: Volume fraction of each phase. If modified, volume fraction of the other phase is corrected accordingly.
- Aspect ratio: Aspect ratio of the spheroidal inclusions.
- Phi, eta and xi: Euler angles to describe the orientation of the inclusions with respect to the direction of traction. If aligned, all angles are nil.
- Load: Load a material properties file (.mat).
- Save: Save a material properties file (.mat).

F.1.3 Homogenization and loading section

- Homogenization: If checked, allows to define a heterogeneous material. Otherwise, only simulations on the matrix can be performed.
- Homog. model: Select the homogenization model: Voigt, Reuss, Mori-Tanaka, three-phases generalized self consistent (for spherical inclusions only) and interpolative model.
- Macro stress: Computation of the macroscopic stress response: average from local stress fields or from a linearized macroscopic constitutive law (suspended in the last version of Affinistan).

- History type: Monotonic, cyclic, relaxation or creep loading.
- Loading type: Prescribed strain, uniaxial traction along direction 1, biaxial traction along directions 1 and 2 or shear test in the plane 1/2.
- Nbr cycles: Specify the number of cycles if the loading history is cyclic.
- Init. tr. strain: Initial true strain if loading history is relaxation. Initial true stress if loading history is creep.
- Strn11/strn22: Strain ratio between directions 1 and 2 if loading type is biaxial.
- True strain rate: Constant true strain rate during all the simulation.
- Final strain.
- Final time: Computed from the two previous values.

F.1.4 Additional parameters section

- Macro operator: Select the way to compute the macroscopic operator (see section 5.3): only Eshelby's tensor is computed from an isotropic extraction of the affine modulus of the matrix or only the Hill's tensor P or all the computations.
- Smallest colloc. point: Smallest collocation point. Used in the numerical inversion of the Laplace-Carson transform.
- Highest colloc. point: Highest collocation point.
- Nbr colloc. points: Number of collocation points. These are equispaced on a logarithmic scale between the smallest and highest value.
- Test time: Reference time at which debugging information is written in several files. Inactive if nil.
- Min. nbr time-steps: Minimum number of time steps during the simulation.
- Num. method for local. eq.: Numerical method to solve the localization method: fixed point or Newton-Raphson.
- Default values: Reset all the fields of this section to their default values.

F.2 Post processing section

This section is used to plot or save figures. In addition to a new toolbar, it enables to add curves to the curves list (figure F.2) and to set some parameters for the layout of the figure (figure F.3).

F.2.1 Toolbar

- New figure: Delete all the curves from the curve list.
- View figure: Plot the curves list and the specified parameters for the layout. This figure is shown with the Gnuplot software for several seconds.
- Save figure: Save the current figure in a postscript format.
- Save script: Save the Gnuplot script corresponding to the current figure.
- Quit: Exit Affinistan.
- About: Give informations about the software.

F.2.2 Add curve section

A maximum of 20 curves can be plotted on the same figure.

- Select data source: Add a curve either from the last simulation or from a selected data file. If 'From simulation' is selected, the type of curve must be selected (macroscopic, in the matrix, in the inclusions, matrix alone or inclusions alone). Corresponding variables to be plotted must also be selected. If 'From file' option is selected the user is prompted to select the corresponding file and the column numbers of this file to be plotted.
- Curve label: Give a label to the current curve.
- Select line style: Select the line style. This option is only valid when saving the script.
- Select point style: Select the point style. This option is only valid when saving the script.

F.2.3 Set figure layout section

Enable to fix the layout of the figure. All these fields are optional.

- Figure title: Give a title to the figure.
- X Axis label: Give a label to the X axis.

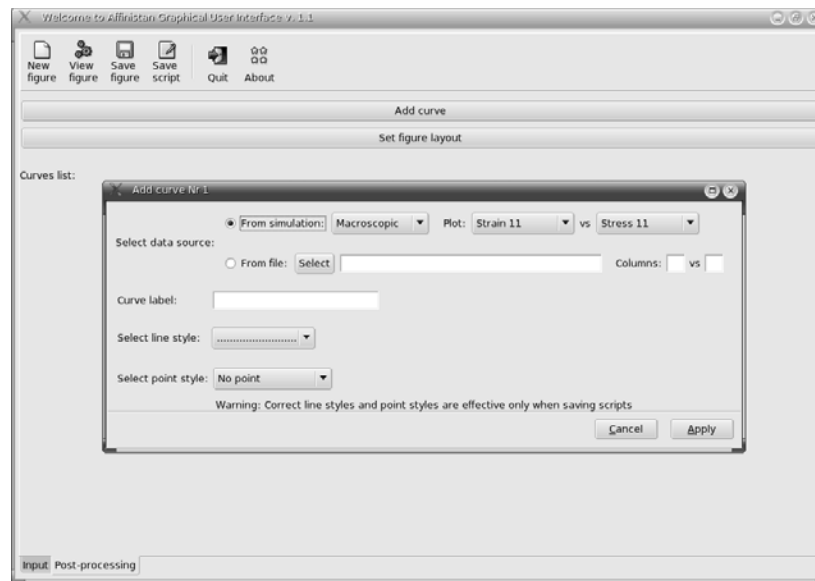


Figure F.2: Add curve section of Affinistan.

- Y Axis label: Give a label to the Y axis.
- X range: Define a range for the X axis.
- Y range: Define a range for the Y axis.
- Legend position: Select a corner of the figure for the legend position.

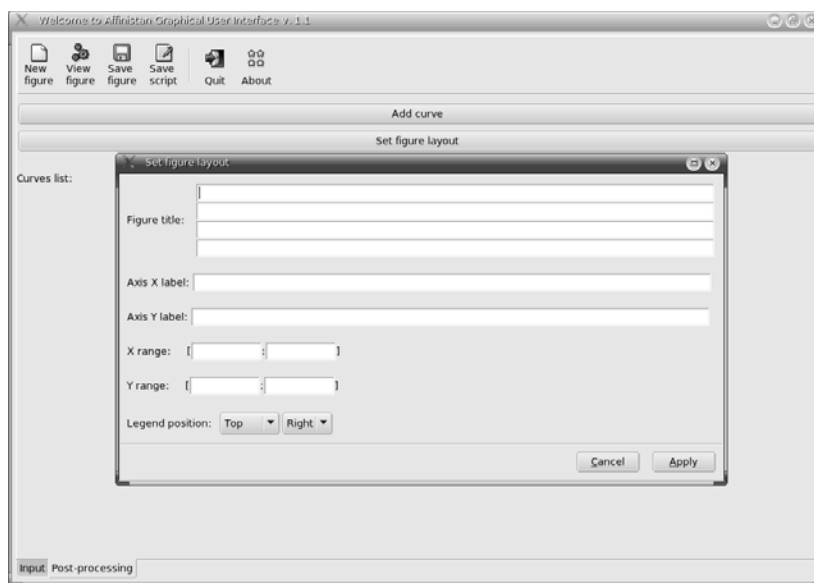


Figure F.3: Set figure layout section of Affinistan.

Appendix G

Notations and units

Fourth order tensors

Symbol	Definition	Units
\mathbf{m}	$\frac{\partial \dot{\boldsymbol{\varepsilon}}^{in}}{\partial \boldsymbol{\sigma}}$	$\frac{1}{s \cdot Pa}$
\mathbf{A}^ϵ	Strain concentration tensor ($\boldsymbol{\varepsilon}_1 = \mathbf{A}^\epsilon : \bar{\boldsymbol{\varepsilon}}$)	-
\mathbf{B}^ϵ	Strain concentration tensor ($\boldsymbol{\varepsilon}_1 = \mathbf{A}^\epsilon : \boldsymbol{\varepsilon}_0$)	-
\mathbf{C}	Elastic or tangent operator	Pa
\mathbf{C}^*	Hill's constraint tensor	Pa
\mathbf{C}^{alg}	Algorithmic tangent operator	Pa
\mathbf{C}^{ep}	Continuum tangent operator (el.-pl.)	Pa
\mathbf{C}^{in}	Continuum tangent operator (el.-visc.pl.)	Pa
\mathbf{C}^s	Secant stiffness operator	Pa
\mathbf{D}^ϵ	Strain concentration tensor ($\boldsymbol{\varepsilon}(x) = \mathbf{D}^\epsilon : \bar{\boldsymbol{\varepsilon}}$)	-
\mathbf{D}^σ	Stress concentration tensor ($\boldsymbol{\sigma}(x) = \mathbf{D}^\sigma : \bar{\boldsymbol{\sigma}}$)	-
\mathbf{G}	Relaxation tensor	Pa
\mathbf{I}^{vol}	Volumetric unit tensor	-
\mathbf{I}^{dev}	Deviatoric unit tensor	-
\mathbf{I}	Unit tensor	-
\mathbf{J}	Creep tensor	$1/Pa$
\mathbf{P}	Hill's tensor	$1/Pa$
\mathbf{S}	Compliance	$1/Pa$
\mathcal{E}	Eshelby's tensor	-

Second order tensors

Symbol	Definition	Units
l	$\frac{\partial g_v}{\partial \sigma}$	$\frac{1}{s.Pa}$
n	$\frac{\partial \dot{\epsilon}^n}{\partial p}$	1/s
G	Displacement gradient	-
N	Normal to the yield surface in stress space	-
α	Thermal expansion	1/K
1	Unit tensor	-
ϵ	Strain	-
ϵ^e	Elastic strain	-
ϵ^p	Plastic strain	-
ϵ^{th}	Thermal strain	-
ϵ^*	Eigenstrain	-
ϵ^∞	Far field strain	-
σ	Stress	Pa
τ	Polarization tensor	Pa

Scalars

Symbol	Definition	Units
f	Yield function	Pa
g_v	Viscoplastic function	1/s
p	Accumulated plastic strain	-
q	$\frac{\partial g_v}{\partial p}$	1/s
v_1	Volume fraction of inclusions	-
w	Stress potential	Pa
E	Young's modulus	Pa
G	Lamé Coefficient	Pa
$R(p)$	Hardening function	Pa
S	Surface	m ²
T	Temperature	K
V	Volume	m ³
$\dot{\gamma}$	Plastic multiplier	-
κ	Bulk modulus	Pa
λ	Lamé coefficient	Pa
μ	Shear modulus	Pa
ν	Poisson's ratio	-
σ_{eq}	Equivalent stress	Pa
σ_{eq}^{tr}	Trial equivalent stress after an elastic time step	Pa
σ_Y	Initial yield stress	Pa

Vectors

Symbol	Definition	Units
\mathbf{n}	Normal to a surface	-
\mathbf{t}	Stress	Pa
\mathbf{u}	Displacement	m
\mathbf{x}	Position	m

Symbols

Symbol	Definition
\tilde{x}_r	Reference state in phase r
$\langle x \rangle_{\omega_r}$	Average value over phase r
$\langle x \rangle_{\omega}$	Average value over all the volume
\bar{x}	Macroscopic value
$\mathbf{C} > \mathbf{0}$	$\boldsymbol{\varepsilon} : \mathbf{C} : \boldsymbol{\varepsilon} > 0$ for all $\boldsymbol{\varepsilon}$
Δx	Variation
\otimes	Convolution product
\odot	Stieljes-type convolution product
x^*	Laplace-Carson transform
$[\mathcal{L}(x)]_{(s)}$	Laplace-Carson transform of an expression
s	Laplace variable
x_0	Refers to the matrix
x_1	Refers to the inclusions
\mathbf{x}^{dev}	Deviatoric part of the tensor
x^{eff}	Effective value
\dot{x}	Time derivative
\otimes	Tensorial product
:	Contraction over two indices
::	Contraction over four indices

Bibliography

- [1] ABAQUS[®]. *A general-purpose finite element software*. ABAQUS Inc., Pawtucket, RI, USA, 2005.
- [2] ABOUDI, J. Micromechanical analysis of composites by the method of cells. *Appl. Mech. Rev.* *42* (1989), 193–221.
- [3] ABOUDI, J., PINDERA, M.-J., AND ARNOLD, S. Linear thermo-elastic higher-order theory for periodic multiphase materials. *J. Appl. Mechanics* *68* (2001), 697–707.
- [4] ABOUDI, J., PINDERA, M.-J., AND ARNOLD, S. Higher-order theory for periodic multiphase materials with inelastic phases. *Int. J. Plasticity* *19*, 6 (2003), 805–847.
- [5] BEDNARCYK, B., ARNOLD, S., ABOUDI, J., AND PINDERA, M.-J. Local field effects in titanium matrix composites subject to fiber-matrix debonding. *Int. J. Plasticity* *20* (2004), 1707–1737.
- [6] BENSOUSSAN, A., LIONS, J., AND PAPANICOLAOU, G. *Asymptotic analysis for periodic structures*. North Holland, Amsterdam, 1978.
- [7] BENVENISTE, Y. A new approach to the application of Mori-Tanaka’s theory in composite materials. *Mech. Materials* *6*, 2 (1987), 147–157.
- [8] BERVEILLER, M., AND ZAOUÏ, A. An extension of the self-consistent scheme to plastically-flowing polycrystals. *J. Mech. Phys. Solids* *26* (1979), 325–344.
- [9] BÖHM, H., AND HAN, W. Comparisons between three-dimensional and two-dimensional multi-particle unit cell models for particle reinforced metal matrix composites. *Modeling and Simulation in Materials Science and Engineering* *2* (2001), 47–65.

-
- [10] BORNERT, M. *Morphologie microstructurale et comportement mécanique; caractérisations expérimentales, approches par bornes et estimations autocohérentes généralisées*. Phd thesis, Ecole Nationale des Ponts et Chaussées, 1996.
- [11] BORNERT, M. *Homogénéisation des milieux aléatoires: bornes et estimations*, vol. 1. Hermes Science, Paris, 2001, ch. 5, pp. 133–221.
- [12] BORNERT, M., STOLTZ, C., AND ZAOUÏ, A. A morphologically representative pattern-based bounding in elasticity. *J. Mech. Phys. Solids* 44 (1996), 307–331.
- [13] BOWLES, D., AND TOMPKINS, S. Prediction of coefficients of thermal expansion for unidirectional composites. *J. Comp. Mat.* 23 (1989), 370–388.
- [14] BRENNER, R., CASTELNAU, O., AND BADEA, L. Mechanical field fluctuations in polycrystals estimated by homogenization techniques. *Proc. Roy. Soc. Lond. A* 460 (2004), 3589–3612.
- [15] BRENNER, R., MASSON, R., CASTELNAU, O., AND ZAOUÏ, A. A “quasi-elastic” affine formulation for the homogenised behaviour of nonlinear viscoelastic polycrystals and composites. *Eur. J. Mech. A/Solids* 25 (2002), 943–960.
- [16] BUDIANSKI, B., AND WU. Theoretical prediction of plastic strains of polycrystals. In *Proc. of the 4th U.S. National Congress of Applied Mechanics, ASME* (1962), pp. 1175–1185.
- [17] BURYACHENKO, V. The overall elastoplastic behavior of multiphase materials with isotropic components. *Acta Mech.* 119 (1996), 93–117.
- [18] CHABOCHE, J., AND KANOUTÉ, P. Sur les approximations ‘isotrope’ et ‘anisotrope’ de l’opérateur tangent pour les méthodes tangentés, incrémentale et affine. *C. R. Acad. Sci. Paris* (2003), 857–864.
- [19] CHABOCHE, J., KANOUTÉ, P., AND ROOS, A. On the capabilities of mean-field approaches for the description of plasticity in metal matrix composites. *Int. J. Plasticity* 21, 7 (2005), 1409–1434.
- [20] CHRISTMAN, T., NEEDLEMAN, A., AND SURESH, S. An experimental and numerical study of deformation in metal-ceramic composites. *Acta Metall.* 37, 11 (1989), 3029–3050.
- [21] CHUNG, P., TAMMA, K., AND NAMBURU, R. Asymptotic expansion homogenization for heterogeneous media: computational issues and applications. *Composite part A* 32, 9 (2001), 1291–1301.

- [22] DEBOTTON, G., AND PONTE CASTAÑEDA, P. Variational estimates for the creep behavior of polycrystals. *Proc. Roy. Soc. Lond. A* 448 (1995), 421–442.
- [23] DIGIMAT. *A software for the linear and nonlinear multi-scale modeling of heterogeneous materials*. e-Xstream engineering, Louvain-la-Neuve, Belgium, 2006.
- [24] DOGHRI, I. *Mechanics of deformable solids. Linear, nonlinear, analytical and computational aspects*. Springer, Berlin, 2000.
- [25] DOGHRI, I., AND FRIEBEL, C. Effective elasto-plastic properties of inclusion-reinforced composites. Study of shape, orientation and cyclic response. *Mech. Materials* 37, 1 (2005), 45–68.
- [26] DOGHRI, I., AND OUAAR, A. Homogenization of two-phase elasto-plastic composite materials and structures. Study of tangent operators, cyclic plasticity and numerical algorithms. *Int. J. Solids Struct.* 40, 7 (2003), 1681–1712.
- [27] DOGHRI, I., AND TINEL, T. Micromechanical modeling and computation of elasto-plastic materials reinforced with distributed-orientation fibers. *Int. J. Plasticity* 21, 10 (2005), 1919–1940.
- [28] DRUGAN, W., AND WILLIS, J. A micromechanics-based nonlocal constitutive equations and estimates of representative volume element size for elastic composites. *J. Mech. Phys. Solids* 44 (1996), 497–524.
- [29] DVORAK, G. Transformation field analysis of inelastic composite materials. *Proc. Roy. Soc. Lond. A* 437 (1992), 311–327.
- [30] ESHELBY, J. The determination of the elastic field of an ellipsoidal inclusion, and related problems. *Proc. Roy. Soc. Lond. A* 241 (1957), 376–396.
- [31] FREDERICO, S., GRILLO, A., AND HERZOG, W. A transversely isotropic composite with a statistical distribution of spheroidal inclusions: a geometrical approach to overall properties. *J. Mech. Phys. Solids* 52, 10 (2004), 2309–2327.
- [32] FRIEBEL, C. *Modélisation et Simulation micro-macro de matériaux composites. Etude de l'influence des renforts (matériau, forme et orientation)*. Graduation report, Université Catholique de Louvain, Belgium, 2002.
- [33] FRIEBEL, C., DOGHRI, I., AND LEGAT, V. General mean-field homogenization schemes for viscoelastic composites containing multiple phases of coated inclusions. *Int. J. Solids Struct.* 43, 9 (2006), 2513–2541.

-
- [34] GAVAZZI, A., AND LAGOUDAS, D. On the numerical evaluation of eshelby's tensor and its application to elastoplastic fibrous composites. *Comp. Mech.* 7 (1990), 13–19.
- [35] GHOSH, S., LEE, K., AND MOORTHY, S. Multiple scale analysis of heterogeneous elastic structures using homogenization theory and Voronoi cell finite element method. *Int. J. Solids Struct.* 32, 1 (1995), 27–62.
- [36] GHOSH, S., LEE, K., AND MOORTHY, S. Two scale analysis of heterogeneous elastic-plastic materials with asymptotic homogenization and Voronoi cell finite element model. *Comput. Methods Appl. Mech. Engrg.* 132, 1-2 (1996), 63–116.
- [37] GONZÁLEZ, C., SEGURADO, J., AND LLORCA, J. Numerical simulation of elasto-plastic deformation of composites: evolution of stress micro-fields and implications for homogenization models. *J. Mech. Phys. Solids* 52, 7 (2004), 1573–1593.
- [38] HASHIN, Z., AND SHTRIKMAN, S. A variational approach to the theory of the elastic behaviour of multiphase materials. *J. Mech. Phys. Solids* 11 (1963), 127–140.
- [39] HERVÉ, E., AND ZAOUI, A. n -layered inclusion-based micromechanical modelling. *Int. J. Engrg. Sci.* 31 (1993), 1–10.
- [40] HERVÉ, E., AND ZAOUI, A. Elastic behavior of multiply coated fiber-reinforced composites. *Int. J. Engrg. Sci.* 33 (1995), 1419–1433.
- [41] HILL, R. Elastic properties of reinforced solids: some theoretical principles. *J. Mech. Phys. Solids* 11 (1963), 357–372.
- [42] HILL, R. Continuum micro-mechanics of elastoplastic polycrystals. *J. Mech. Phys. Solids* 13, 2 (1965), 89–101.
- [43] HILL, R. A self-consistent mechanics of composite materials. *J. Mech. Phys. Solids* 13, 4 (1965), 213–222.
- [44] HOM, C. Three-dimensional finite element analysis of plastic deformation in a whisker-reinforced metal matrix composite. *J. Mech. Phys. Solids* 40, 5 (1992), 991–1008.
- [45] JANSSON, S. Homogenized nonlinear constitutive properties and local stress concentration for composites with periodic internal structure. *Int. J. Solids Struct.* 29, 17 (1992), 2181–2200.
- [46] JIANG, M., JASIUK, I., AND OSTOJA-STARZEWSKI, M. Apparent elastic and elastoplastic behavior of periodic composites. *Int. J. Solids Struct.* 39 (2002), 199–212.

- [47] JIANG, M., OSTOJA-STARZEWSKI, M., AND JASIUK, I. Scale-dependent bounds on effective elastoplastic response of random composites. *J. Mech. Phys. Solids* 49 (2001), 655–673.
- [48] JU, J. Consistent tangent moduli for a class of viscoplasticity. *J. Engrg. Mech.-ASCE* 116, 8 (1990), 1764–1779.
- [49] KANG, G.-Z., AND GAO, Q. Tensile properties of randomly oriented short $\delta - \text{Al}_2\text{O}_3$ fiber reinforced aluminum alloy composites: II. Finite element analysis for stress transfer, elastic modulus and stress-strain curve. *Composite part A* 33, 5 (2002), 657–667.
- [50] KANIT, T., FOREST, S., GALLIET, I., MOUNOURY, V., AND JEULIN, D. Determination of the size of the representative volume element for random composites: statistical and numerical approach. *Int. J. Solids Struct.* 40, 13-14 (2003), 3647–3679.
- [51] KOUZNETSOVA, V. Computational homogenization. Micromechanics graduate course lecture notes, Eindhoven, November 2004.
- [52] KOUZNETSOVA, V., GEERS, M., AND BREKELMANS, W. Multi-scale constitutive modelling of heterogeneous materials with a gradient-enhanced computational homogenization scheme. *Int. J. Num. Meth. Engrg.* 54 (2002), 1235–1260.
- [53] KOUZNETSOVA, V., GEERS, M., AND BREKELMANS, W. Multi-scale second-order computational homogenization of multi-phase materials: a nested finite element solution strategy. *Comput. Methods Appl. Mech. Engrg.* 193 (2004), 5525–5550.
- [54] KRÖNER, E. Zur plastischen verformung des vielkristalls. *Acta Metall.* 9, 2 (1961), 155–161.
- [55] LEVIN, V. Thermal expansion coefficients of heterogeneous materials. *Mekh. Tverd. Tela* 8 (1967), 38–94.
- [56] LEVY, A., AND PAPAIZIAN, J. Tensile properties of short fiber-reinforced SiC/Al composites: Part II. Finite element analysis. *Metall. Trans. A* 21, 2 (1990), 411–420.
- [57] LI, G., AND PONTE CASTAÑEDA, P. *Variational estimates for the elastoplastic response of particle-reinforced metal-matrix composites*, vol. 47. American Society of Mechanical Engineers, 1994, pp. S77–S94.
- [58] LI, J., AND WENG, G. A secant viscosity approach to the time-dependent creep of an elasto-viscoplastic composite. *J. Mech. Phys. Solids* 45, 7 (1997), 1069–1083.

- [59] LI, J., AND WENG, G. A unified approach from elasticity to viscoelasticity to viscoplasticity of particle-reinforced solids. *Int. J. Plasticity* 14, 1-3 (1998), 193–208.
- [60] LI, J., AND WENG, G. Creep of a composite with dual viscoplastic phases. *Compos. Science and Technology* 58, 11 (1999), 1803–1810.
- [61] LIELENS, G. *Micro-Macro Modeling of Structured Materials*. Phd thesis, Université Catholique de Louvain, Belgium, 1999.
- [62] LIELENS, G., PIROTTE, P., COUNIOT, A., DUPRET, F., AND KEUNINGS, R. Prediction of thermo-mechanical properties for compression moulded composites. *Composite part A* 29, 1-2 (1998), 63–70.
- [63] LIN, A., AND HAN, S.-P. On the distance between two ellipsoids. *SIAM J. Opt.* 13, 1 (2002), 298–308.
- [64] LLORCA, J., AND SEGURADO, J. Three-dimensional multiparticle cell simulations of deformation and damage in sphere-reinforced composites. *Mater. Sci. Eng. A* 365, 1-2 (2004), 267–274.
- [65] LUSTI, H., HINE, P., AND GUSEV, A. Direct numerical predictions for the elastic and thermoelastic properties of short fiber composites. *Compos. Science and Technology* 62 (2002), 1927–1934.
- [66] MASSON, R. *Estimations non linéaires du comportement global de matériaux hétérogènes en formulation affine*. Phd thesis, Ecole Polytechnique, Paris, France, 1998.
- [67] MASSON, R., BORNERT, M., SUQUET, P., AND ZAOUÏ, A. An affine formulation for the prediction of the effective properties of nonlinear composites and polycrystals. *J. Mech. Phys. Solids* 48, 6-7 (2000), 1203–1227.
- [68] MASSON, R., AND ZAOUÏ, A. Self-consistent estimates for the rate-dependent elasto-plastic behavior of polycrystalline materials. *J. Mech. Phys. Solids* 47, 7 (1999), 1543–1568.
- [69] MOLINARI, A., CANOVA, G., AND AHZI, S. A self consistent approach at the large deformation polycrystal viscoplasticity. *Acta Metall.* 35, 12 (1987), 2983–2994.
- [70] MOULINEC, H., AND SUQUET, P. A fast numerical method for computing the linear and nonlinear properties of composites. *C. R. Acad. Sci. Paris II* 318 (1994), 1417–1423.
- [71] MOULINEC, H., AND SUQUET, P. *A FFT-based numerical method for computing the mechanical properties of composites from images of their microstructure*. Kluwer Academic Publ., Dordrecht, 1995, pp. 235–246.

- [72] NETGEN. *An automatic three-dimensional tetrahedral mesh generator*. Joachim Schöberl, Johannes Kepler University, Linz, Austria, 2004.
- [73] OSTOJA-STARZEWSKI, M. Material spatial randomness: From statistical to representative volume element. *Prob. Eng. Mech.* 21 (2006), 112–132.
- [74] PALEY, M., AND ABOUDI, J. Micromechanical analysis of composites by the generalized cells model. *Mech. Materials* 14, 2 (1992), 127–139.
- [75] PALMYRA. *A finite-element software for heterogeneous micro-structures*. MatSim GmbH, Zurich, Switzerland, 2001.
- [76] PAN, Y., AND CHOU, T. Point force solution for an infinite transversely isotropic solid. *J. Appl. Mechanics* 43, 4 (1976), 608–612.
- [77] PIERARD, O. *Micro/macro study of reinforced polymers and polymeric composites. Mathematical modeling and numerical simulation of elasto-viscoplastic behavior and thermal coupling*. DEA graduation report, Université Catholique de Louvain, Belgium, 2004.
- [78] PIERARD, O., AND DOGHRI, I. An enhanced affine formulation and the corresponding numerical algorithms for the mean-field homogenization of elasto-viscoplastic composites. *Int. J. Plasticity* 22, 1 (2006), 131–157.
- [79] PIERARD, O., AND DOGHRI, I. A study of various estimates of the macroscopic tangent operator in the incremental homogenization of elasto-plastic composites. *Int. J. Mult. Comp. Engrg.* (2006). Accepted for publication.
- [80] PIERARD, O., FRIEBEL, C., AND DOGHRI, I. Mean-field homogenization of multi-phase thermo-elastic composites: a general framework and its validation. *Compos. Science and Technology* 64, 10-11 (2004), 1587–1603.
- [81] PIERARD, O., GONZÁLEZ, C., SEGURADO, J., LLORCA, J., AND DOGHRI, I. Micromechanics of elasto-plastic materials reinforced with ellipsoidal inclusions. *Mech. Materials* (2006). Submitted for publication.
- [82] PIERARD, O., LLORCA, J., SEGURADO, J., AND DOGHRI, I. Micromechanics of particle-reinforced elasto-viscoplastic composites: finite element simulations versus affine homogenization. *Int. J. Plasticity* (2006). Submitted for publication.
- [83] PONTE CASTAÑEDA, P. The effective mechanical properties of nonlinear isotropic composites. *J. Mech. Phys. Solids* 39 (1991), 45–71.

- [84] PONTE CASTAÑEDA, P. Exact second-order estimates for the effective mechanical properties of nonlinear composite materials. *J. Mech. Phys. Solids* 44, 6 (1996), 827–862.
- [85] PONTE CASTAÑEDA, P. Second-order homogenization estimates for nonlinear composites incorporating field fluctuations: I-theory. *J. Mech. Phys. Solids* 50, 4 (2002), 737–757.
- [86] PONTE CASTAÑEDA, P. Variational methods in nonlinear homogenization. In *Approche multi-échelles en mécanique des matériaux* (Aussois, 2006), MECAMAT.
- [87] PONTE CASTAÑEDA, P., AND WILLIS, J. The effect of spatial distribution on the effective behavior of the composite materials and cracked media. *J. Mech. Phys. Solids* 43 (1995), 1919–1951.
- [88] POVIRK, G. Incorporation of microstructural information into models of two-phase materials. *Acta Metall. Mater.* 43, 8 (1995), 3199–3206.
- [89] SANCHEZ-PALENCIA, E. *Non homogeneous media and vibration theory - lecture notes in physics 127*. Springer, Berlin, 1980.
- [90] SCHAPERLY, R. Approximate methods of transform inversion in viscoelastic stress analysis. In *Proceedings of the 4th US National Congress on Applied Mechanics* (1962), vol. 2, pp. 1075–1085.
- [91] SCHOLES, J. Solution of the problem b6 of the 1st putnam, 1938. <http://www.kalva.demon.co.uk/putnam/psoln/psol3813.html>, 2002.
- [92] SEGURADO, J., AND LLORCA, J. A numerical approximation to the elastic properties of sphere-reinforced composites. *J. Mech. Phys. Solids* 50, 10 (2002), 2107–2121.
- [93] SEGURADO, J., AND LLORCA, J. A computational micromechanics study of the effect of interface decohesion on the mechanical behavior of composites. *Acta Mater.* 53 (2005), 4931–4942.
- [94] SUQUET, P. Overall properties of nonlinear isotropic composites. *C. R. Acad. Sci. Paris Iib* 320 (1995), 563–571.
- [95] SUQUET, P. *Effective properties of nonlinear composites*, vol. 377. Springer-Verlag, Udine, Italy, 1997, pp. 197–264.
- [96] SUQUET, P., AND BORNERT, M. *Rappels de calcul tensoriel et d'élasticité*, vol. 2. Hermes Science, Paris, 2001, ch. 5, pp. 171–202.

- [97] SUQUET, P., AND PONTE CASTAÑEDA, P. Small-contrast perturbation expansions for the effective properties of nonlinear composites. *C. R. Acad. Sci. Paris II 317* (1993), 1515–1522.
- [98] TAKAO, Y., AND TAYA, M. The effect of variable fiber aspect ratio on the stiffness and thermal expansion coefficients of a short fiber composite. *J. Comp. Mat. 21* (1987), 140–156.
- [99] TORQUATO, S. Morphology and effective properties of disordered heterogeneous media. *Int. J. Solids Struct. 35* (1998), 2385–2406.
- [100] TUCKER, C., AND LIANG, E. Stiffness predictions for unidirectional short-fiber composites: Review and evaluation. *Compos. Science and Technology 59* (1999), 655–671.
- [101] VAN ES, M. *Polymer-clay Nanocomposites. The importance of particle dimensions*. PhD thesis, Technische Universiteit Delft, The Netherlands, 2001.
- [102] WALPOLE, L. On bounds for the overall elastic moduli of inhomogeneous systems -I. *J. Mech. Phys. Solids 14* (1966), 151–162.
- [103] WALPOLE, L. Elastic behavior of composite materials: theoretical foundations. *Adv. in Appl. Mech. 21* (1981), 169–242.
- [104] WEISSENBEK, E., BÖHM, H., AND RAMMERSTORFER, F. Micromechanical investigations of arrangement effects in particle reinforced metal matrix composites. *Comput. Mat. Science 3* (1994), 263–278.
- [105] WENG, G. The theoretical connection between Mori-Tanaka and the Hashin-Shtrikman-Walpole bounds. *Int. J. Engrg. Sci. 28* (1990), 1111–1120.
- [106] WIDOM, B. Random sequential adsorption of hard spheres to a volume. *J. Chem. Phys. 44* (1966), 3884–3894.
- [107] WILLIS, J. Bounds and self-consistent estimates for the overall moduli of anisotropic composites. *J. Mech. Phys. Solids 28* (1977), 185–202.
- [108] WITHERS, P. The determination of the elastic field of an ellipsoidal inclusion in a transversely isotropic medium and its relevance to composite materials. *Philosophical Magazine A 59*, 4 (1989), 759–781.
- [109] YI, Y.-M., PARK, S.-H., AND YOUN, S.-K. Asymptotic homogenization of viscoelastic composites with periodic microstructures. *Int. J. Solids Struct. 35*, 17 (1996), 2039–2055.
- [110] ZAOUÏ, A. Continuum micromechanics: Survey. *J. Engrg. Mech.-ASCE 128*, 8 (2002), 808–816.